Miha Luntinen

Consecutive Transients Method for Plasma Diagnostics of Electron Cyclotron Resonance Ion Sources

UNIVERSITY OF JYVÄSKYLÄ

FACULTY OF MATHEMATICS
AND SCIENCE

Miha Luntinen

Consecutive Transients Method for Plasma Diagnostics of Electron Cyclotron Resonance Ion Sources

JYVÄSKYLÄN YLIOPISTO
UNIVERSITY OF JYVÄSKYLÄ

Editors
Ilari Maasilta
Department of Physics, University of Jyväskylä
Päivi Vuorio
Open Science Centre, University of Jyväskylä

ABSTRACT

Luntinen, Miha
Consecutive Transients Method
for Plasma Diagnostics of
Electron Cyclotron Resonance Ion Sources

Electron cyclotron resonance ion sources (ECRISs) have been pivotal for modern experimental nuclear physics in extending the range of known nuclides on the nuclear chart. In recent years, the use of radioactive ion beams (RIBs) of highly charged heavy ions has become vital for nuclear physics research. Many of the isotopes have half-lives shorter than 1 s, and as the half-lives decrease nuclear decay begins to degrade the RIB intensity.

ECRISs are used as charge breeding devices for RIBs: The ECRIS is modified to accept an input beam of low charge state ions, produced e.g. by the ISOL-method. The injected ions are captured by the magnetically confined plasma sustained in the ion source, and subsequently ionized to high charge states via multiple collisions with the plasma electrons. The ions exit the plasma stochastically, and a portion of them become available for beam formation and are extracted from the ion source by means of electric fields for post-acceleration.

To meet the challenge of producing RIBs with ever shorter half-lives, ECRIS researchers require advanced plasma diagnostic methods to study the charge breeding times and the underlying physical processes. In this thesis, we present the Consecutive Transients (CT) method developed for this purpose. It extends the continuum of transient material injection methods dating back to the 1990s. Like its predecessors, the CT-method is based on pulsed injection of material into the plasma, and study of the time series of the extracted beam currents arising as a consequence. It improves the previous methods by implementing a model based data analysis, which minimizes the number of assumptions — importantly, it requires no presupposed model for ion confinement. We describe the derivation of the model, the computational procedures, and the experimental campaigns undertaken to establish and test the method.

The plasma electron density n_e and average energy $\langle E_e \rangle$, and the characteristic times of ionization τ_{inz}, charge exchange τ_{cx} and ion confinement τ_{conf} are obtained as results. We show that the CT-method is sensitive enough to study variations in these plasma parameters as the ECRIS operating condition is changed, and to identify bottlenecks in the charge breeding process. The hierarchy of τ_{conf}, τ_{inz}, τ_{cx} for highly charged ion production is refined. The uncertainty sources are investigated, and avenues for the improvement of result precision are identified.

It was found that $n_e \sim 5 \times 10^{11} \mathrm{cm}^{-3}$, $\langle E_e \rangle \sim 100$ eV–1 keV. The characteristic times ranged from 1 ms to ~ 10 ms. All plasma parameters were found to be charge state dependent, reflecting the spatial distribution of ion populations in the non-equilibrium plasma.

Keywords: ECRIS, Charge Breeding, Ion confinement, Ionization, Charge exchange

TIIVISTELMÄ (ABSTRACT IN FINNISH)

Luntinen, Miha
Peräkkäisten transienttien diagnostiikkamenetelmä
elektronisyklotroniresonanssi-ionilähdeplasmoille

Elektronisyklotroniresonanssi-ionilähteet (ECRIS) ovat olleet avaintekijänä modernin kokeellisen ydinfysiikan laajentaessa ydinkartan tunnettujen ydinten kirjoa. Viime vuosina korkeasti varattujen radioaktiivisten raskasionisuihkujen (RIB) käytöstä on tullut tärkeää ydinfysiikan tutkimuksessa. Näiden isotooppien puoliintumisajat ovat usein lyhyempiä kuin 1 s, minkä seurauksena ydinhajoaminen alkaa heikentää suihkun intensiteettiä.

ECRIS:jä käytetään varauksenkasvattajina RIB:ille. Tällöin ECRIS muokataan vastaanottamaan esimerkiksi ISOL-menetelmällä tuotettu matalavarauksinen ionisuihku. Ionilähteen magneettisesti vangittu plasma kaappaa sinne syötetyt ionit, jotka ionisoituvat korkeille varausasteille törmäyksissä plasman elektronien kanssa. Ionit poistuvat plasmasta satunnaisprosessin kautta, ja osa niistä päätyy alueelle, josta ne päätyvät osaksi hiukkassuihkua ja edelleen jatkokiihdytettäväksi.

Jotta voitaisiin varmistaa entistä lyhytikäisempien RIB:ien tuottaminen, ECRIS-tutkijat tarvitsevat kehittyneitä plasmadiagnostiikkamenetelmiä varauksenkasvattamisaikojen, sekä niihin vaikuttavien fysikaalisten prosessien tutkimiseksi. Tässä väitöskirjassa esittelen tätä tarkoitusta varten kehitetyn peräkkäisten transienttien (CT) menetelmän. Se on 1990-luvulle ulottuvan transienttisten materiaalisyöttömenetelmien jatkumon uusin jäsen, joka parantaa aiempia menetelmiä hyödyntämällä mallipohjaista data-analyysimenetelmää. Menetelmän taustalla on aiempaa vähemmän oletuksia — erityisesti ionien säilöntämallia ei tarvitse etukäteen olettaa. Kuvailen mallin teoreettisen johtamisen, laskennalliset menetelmät, sekä menetelmän kehittämiseksi ja testaamiseksi suoritetut mittauskampanjat.

Menetelmän tuloksina saadaan plasman elektronien tiheys n_e ja keskienergia $\langle E_e \rangle$, sekä ionisaation, varauksenvaihdon ja ionien säilönnän karakteriset ajat (τ_{inz}, τ_{cx}, τ_{conf}). Osoitan, että CT-menetelmä on riittävän herkkä havaitsemaan näiden plasmaparametrien muutoksia ionilähteen operointiparametreja säädettäessä, sekä paljastamaan pullonkauloja varauksenkasvatusketjussa. Tarkennan korkeasti varattujen ionien tuoton vaatimaa hierarkiaa τ_{inz}, τ_{cx}, ja τ_{conf} välillä. Tarkastelen menetelmän epävarmuuslähteitä, ja tunnistan keinoja tulosten tarkkuuden parantamiseksi.

Tulokset näyttävät, että tyypillisesti $n_e \sim 5 \times 10^{11} \mathrm{cm}^{-3}$, ja $\langle E_e \rangle \sim 100$ eV–1 keV CB-ECRIS plasmassa. Karakteristiset ajat vaihtelevat välillä 1 ms ja noin 10 ms varausasteen funktiona. Kaikkien plasmaparametrien havaittiin olevan varausasteriippuvaisia, mikä kertoo ionipopulaatioiden avaruudellisesta jakaumasta plasmassa, jossa vallitsee termodynaaminen epätasapainotila.

Avainsanat: ECRIS, Varauksen jalostaminen, Ionien säilöntä, Ionisaatio, Varauksenvaihto

Author   Miha Luntinen
                  Department of Physics,
                  University of Jyväskylä
                  Finland

Supervisor   Hannu Koivisto
                  Department of Physics,
                  University of Jyväskylä
                  Finland

Reviewers   Alessio Galatà
                  Istituto Nazionale di Fisica Nucleare — Laboratori Nazion-
                  ali di Legnaro
                  Italy

                  Fredrik Wenander
                  CERN
                  Switzerland

Opponent   Oliver Kester
                  TRIUMF
                  Canada

"Kun ollaan luvattu, että tehdään hommat, niin tehdään ne kunnolla, eikä vähän sinne päin. Ja viime kädessä laitetaan hyvä kiertämään, jotta tulevilla sukupolvilla olisi paremmat oltavat."

Juustoportti

PREFACE

I would like to express my thanks to my supervisors, Hannu Koivisto and Olli Tarvainen. Hannu for guiding me through this PhD endeavor and for the opportunity to do my PhD project in the ion source group, as well as shared wisdom both in worklife and actual life related matters. I further thank Olli for introducing me to the complexities of plasma physics in the first place through the plasma physics course, the first research project and the Master's thesis. A great big thank you is also in order to Olli for finding the time to give his expert comments and suggestions to this thesis, which have enabled its timely completion, despite his cramped schedule. In addition to Hannu and Olli, over the course of the last seven (?) years I've also received support and guidance in ion sourcery from my wonderful colleagues Risto, Ville and Taneli. It has been a pleasure to work with you all.

I owe a special thanks to Julien Angot, who conducted the experimental work pertaining to this thesis, and with whom we first brainstormed the idea for the CT-method. Julien's contributions were also pivotal in the development of the numerical routines, and the original conception of the optimization approach was due to him. It has been said that Julien would, and I quote, "mine the rare materials from bedrock by himself" to ensure the success of a measurement campaign. I have seen this to be true.

Thanks are also due to the (extended) Holvi-collaboration for the many lunches and an intellectually emancipated office environment. Thank you each and all for all the serious and less serious discussions. I would also like to thank Janne for making me run up and down the badminton court, which has been beneficial to both my humility and cardiovascular system.

Most importantly: I owe my mental health to my better half Tiia and my two energetic children Verna and Aarni. Thanks also to Tiia for looking after the kids and enabling me to push this thesis over the finish line. Thank you for the support and balance that you bring into my life.

Finally, I extend my gratitude to the reviewers of this thesis and my esteemed opponent. Thank you for taking the time to read this thing that has occupied such a large fraction of my life for such a long time.

Jyväskylä, January 2024
Miha Luntinen

LIST OF INCLUDED ARTICLES

PI   J Angot, M Luntinen, T Kalvas, H Koivisto, R Kronholm, L Maunoury, O Tarvainen, T Thuillier, V Toivanen *Method for estimating charge breeder ECR ion source plasma parameters with short pulse 1+ injection of metal ions*. Plasma Sources Science and Technology **30** 035018 (2021) .

PII   M Luntinen, J Angot, O Tarvainen, V Toivanen, T Thuillier, H Koivisto *Measurement of ionization, charge exchange and ion confinement times in charge breeder ECR ion sources with short pulse 1+ injection of metal ions*. Journal of Physics: Conference Series **2244** 012009 (2022) .

PIII   M Luntinen, V Toivanen, H Koivisto, J Angot, T Thuillier, O Tarvainen, G Castro *Diagnostics of highly charged plasmas with multicomponent 1+ ion injection*. Physical Review E **106** 055208 (2022) .

PIV   M Luntinen, J Angot, H Koivisto, O Tarvainen, T Thuillier, G Castro *The effects of electron energy distribution and ionization cross section uncertainty on charge breeder ion source diagnostics with pulsed 1+ injection*. Physical Review E **30** 073904 (2023) .

PV   J Angot, O Tarvainen, H Koivisto, M Luntinen, T Thuillier, V Toivanen *Diagnostics of charge breeder electron cyclotron resonance ion source plasma with consecutive transients method*. Manuscript submitted **XX** X-XX (2023).

Author's contribution

The Author has performed the numerical analyses of Publications PI–PV. The Author had a leading role in the interpretation of the results for PI–PIV and in writing the manuscripts for Publications PI– PIV. The Author contributed in a supporting role to the interpretation of the results of PV, and manuscript preparation. The Author is responsible for the numerical routines established in PI–PV which comprise the ct-analyzer, and the relevant code repository up to the present version (January 28, 2024).

CONTENTS

INTRODUCTION

Laboratory experiments on nuclear physics consist of bombarding a target nucleus with a projectile nucleus which has been accelerated to an energy high enough to cause a reaction (such as fission, fusion or Coulomb excitation), whose properties, e.g. emitted particles and radiation, nuclear mass, size, shape, or half-life are then studied by the nuclear physicists. These particles are produced using an ion source. A popular source for medium to highly charged heavy ions in such a setting is the Electron Cyclotron Resonance Ion Source — ECRIS [1].

The ECRIS has found its place in the industrial and medical applications as well, serving e.g. as a reliable ion source for cancer treatment using heavy ions [2]–[4]. Its operation is based on the magnetic confinement, and microwave heating of the plasma[1] electrons and stepwise ionization via electron impact. ECRISs are able to produce stable and intense beams of medium to high charge state heavy ions with high efficiency, and the high quality of the output beam can be maintained continuously for hundreds of hours [5], [6].

In recent decades, the nuclear physics community has geared towards the use of radioactive ion beams (RIBs) [7]. They enable, for example, further exploration of the properties of nuclei in the yet unexplored regions of the nuclear chart, critical to the development and testing of fundamental nuclear theories for the modeling of nucleosynthesis of heavy elements in neutron stars [8]. More recently, an ECRIS-based concept has been developed for the study of nuclear decay (among other things) in conditions approximating the stellar environment [9], [10]. This is of great interest to nuclear astrophysics, as certain otherwise stable isotopes (e.g. ^{163}Dy) become radioactive when ionized to high charge states [11].

Many isotopes of interest are not available naturally on Earth as they have short (order of 1 s and less) half-lives. Instead, they need to be produced in conjunction with the experiments, and in some cases subsequently accelerated to attain an energy required by the experiment. This needs to happen within a time span short compared to the half-life — lest radioactive decay renders the number of particles produced too small to enable the experiment.

Acceleration of the RIBs to the energy range required for the nuclear physics experiments with existing accelerators requires the particles to be ionized to a medium to high charge state. This is because in a linear accelerator the kinetic energy (per unit length) obtained for an accelerated particle scales proportionally to the charge state q, and in a cyclotron in proportion to q^2/m. A machine is therefore needed which takes as its input a relatively low intensity beam of singly charged radioactive particles, rapidly ionizes them to a medium to high charge state, and outputs intense, stable beams. One solution is employing the ECRIS as a "charge breeder" between the source of radioactive, singly charged ions and the accelerator.

As the isotopes in the RIBs depart from the valley of stability, their half-lives decrease. In order to produce high intensity charge bred beams with ever shorter half-lives

---

[1]　Plasma — "the 4$^{\text{th}}$ state of matter" — is a conglomerate of ions, electrons and neutral atoms and/or molecules, whose dynamics are dominated by electromagnetic effects.

the performance of ECRISs needs to be continually enhanced. In particular, knowledge of the time scales involved in the production of different ionic charge states for various isotopes are necessary to estimate the yields of RIBs, and to guide the operation and development of the ion source. The Consecutive Transients (CT) diagnostics method presented in this thesis has been developed for this purpose.

The CT-method is based on pulsed injection of a stable isotope (often used as a proxy for a radioactive isotope of the same species) into a plasma sustained in the ECRIS. The extracted higher charge state beams' time series are taken as inputs of the CT-method, while the control signal of the injected 1+ pulse is used as a timestamp for the transients to set $t_0 = 0$ s. A model based optimization procedure is then used to seek out the electron density and average energy, as well as the characteristic times of ionization, charge exchange and ion confinement compatible with the time series. The electron density and average energy are attributes of the support plasma, which — along with other ion source properties such as the magnetic field structure — are considered to fix the characteristic times of the probe species.

This thesis is organized as follows: In Section 1 we present the basic functioning of the ECRIS as a source of multicharged ions, and the physical foundation required for understanding the data analysis. Sections 2, 3, and 4 relate to the CT-method itself: The balance equation underlying the analysis is elaborated in Section 2, while the general experimental arrangements for the application of the method are detailed in Section 3. The structure of the code developed to handle the model based data analysis is presented in Section 4. The experimental campaigns that were undertaken to establish the CT-method are presented in Section 5 along with the key results derived from them. Section 6 concludes the thesis with a review of the method, its application and future outlook.

1 THE ELECTRON CYCLOTRON RESONANCE ION SOURCE

Figure 1 shows a schematic view of the ECR ion source. Electrons in an ECRIS are trapped in a magnetic bottle, typically formed as a superposition of two solenoidal magnetic mirrors at the ends of the plasma chamber[1] and a hexapole field providing radial confinement, which form closed magnetic field isosurfaces. The field is designed to fulfill the so-called "scaling laws" [12], i.e. a set of semi-empirical rules for the magnetic field structure which have been found to ensure a good performance of the source — i.e. higher intensity beams of highly charged ions. The magnetic field intensity B decreases towards the center of the plasma chamber until a minimum value B_{min}. Newest generation of ECRISs use superconducting coils to enable higher frequency ECR heating, allowing a higher plasma density to be achieved.

Microwaves are injected into the plasma chamber typically via a wave guide. The microwave frequency is selected based on the magnetic field configuration so that on one of the isosurfaces (called the ECR surface) the electron gyromotion about the field lines is in resonance with the electric field. When this condition is met, efficient energy transfer from the electric field to the electrons can occur, while ions remain relatively cold. The heating improves the magnetic confinement of the electrons (until very high energies, where RF-induced pitch angle scattering begins to degrade the confinement)[2], which leads to an accumulation of energetic electrons inside the ECR surface. This hot electron population is important for the electrostatic trapping of highly charged ions, as discussed in Section 1.5.

The electrons whose energies exceed the ionization potential of the vaporous atoms fed into the plasma chamber begin to strip these atoms off their electrons in a stepwise manner via electron-impact ionization. This stepwise ionization is contested primarily by charge exchange between ions and neutral atoms, which necessitates a low pressure of the injected gas. The produced ions leak out of the plasma at a rate governed by their confinement time, and the portion of ions that are lost into the extraction region, become available for beam formation. The ion source is maintained at a constant, positive high voltage of some tens of kilovolts which accelerates the lost ions along the beamline and towards post-acceleration.

In the following sections we provide some physics background for the ECRIS operation summarized above, before describing the use of ECRIS as a charge breeder for radioactive ions. We then discuss the problem of ECRIS plasma diagnostics and give a brief review of other transient methods as a segue to the CT-method. For further and more in depth reading on the topic of ECR ion sources, we guide the reader to Refs. [1], [15] and references therein. The charge breeding relevant sections are recapitulations from the comprehensive review presented in Ref. [16].

---

[1]   Multiple coils may be used, but the simplest configuration relies on two coils only.

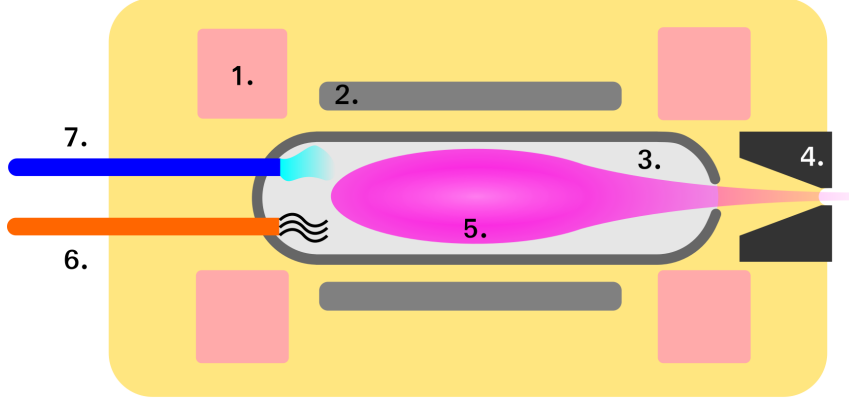[2]   See e.g. Refs. [13], [14] and Section 1.2

FIGURE 1   Schematic of the ECRIS and its core components: (1.) the solenoids and (2.) the permanent magnets forming the magnetic field structure, (3.) the plasma chamber, (4.) the extraction electrodes, (5.) the plasma, whose electrons are heated by microwaves supplied via (6.) the waveguide, and (7.) a pipe for neutral gas input.

1.1   ECR heating

The detailed ECR heating process is complicated from both a physical and mathematical point of view, and the interested reader will find a comprehensive account of ECR heating and its intricacies in Ref. [1]. The following exposition summarises its key features.

The plasma electrons are heated by microwaves, launched into the magnetic field within the plasma chamber typically via a waveguide. The heating microwave frequency f is selected based on the design of the magnetic field, so that on one of the B-isosurfaces (termed the ECR surface, B_{ECR}) the condition

$$2\pi f = \omega_{ce} = \frac{eB}{m_e \gamma},\tag{1}$$

is met, i.e. the electron orbital motion at angular velocity ω_{ce} around the magnetic field lines is in resonance with the oscillating electric field of the microwave. Here, γ is the Lorentz-factor

$$\gamma = \left(1 - \frac{v^2}{c^2}\right)^{-1/2}.\tag{2}$$

This gives for the ECR surface that

$$B_{\mathrm{ECR}} = 2\pi f \gamma m_e / e.\tag{3}$$

For electrons, γ exceeds 1.05 at energies above ~ 25 keV. Given a (classical) Maxwell-Boltzmann EED with $kT = 5$ keV (typical for warm electrons in an ECRIS plasma), the fraction of particles with energy above 25 keV is less than 2 %. Classical equations may thus be used to a good approximation, but it should be kept in mind that electrons in an ECRIS may obtain relativistic energies. This affects e.g. the location of the ECR surface, as can be seen from Eq. (3).

In a simplified model, the plasma can be considered a high-pass filter for microwaves [1]. The microwave propagation through the plasma is then constrained by
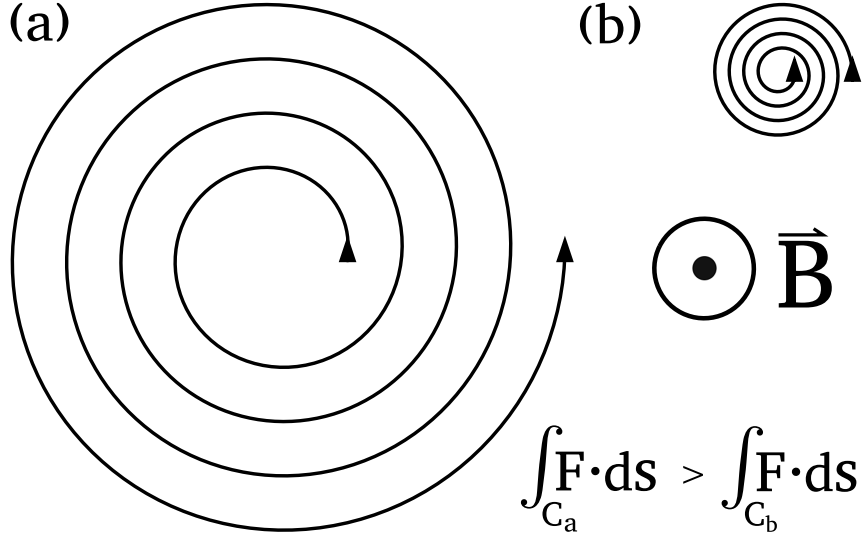
FIGURE 2   Illustration of an electron entering the ECR in (a) an accelerating phase, and (b) a decelerating phase. The magnetic field points out of the page, and the arrowheads indicate the direction of motion of the electron. The work done by the electric field on the particle is greater in case (a) than in case (b).

the condition

$$2\pi f > \omega_{pe} = \left(\frac{n_e e^2}{\varepsilon_0 m_e}\right)^{1/2} \tag{4}$$

where ε_0 is the vacuum permittivity and the γ-factor is omitted. The ω_{pe} is the plasma electron frequency [1], which describes the oscillatory motion of the electrons with respect to the ions arising due to the Coulomb attraction between them. We stress that this is an intentional oversimplification and in reality the wave propagation is affected by the magnetic field and polarization of the microwave. In particular, a right-hand polarized wave which propagates parallel to a decreasing magnetic field can reach the ECR resonance regardless of the plasma density. This makes it possible to attain plasma densities in excess of the critical density, i.e. an overdense plasma [1]. In a minimum-B ECRIS the magnetic field is complex, and thus fulfilling this condition is non-trivial. In particular, in the case of a 14 GHz ECRIS, where the plasma dimensions are comparable to the wavelength of the microwave, it is debatable whether we have a propagating wave or whether it is better modeled as a damped resonant cavity [17]. With these caveats in mind, Eq. (4) provides a good approximation for the upper limit of the electron density for a given frequency f:

$$n_e < \frac{(2\pi f)^2 \varepsilon_0 m_e}{e^2} \equiv n_{e,c}, \tag{5}$$

which defines the critical density $n_{e,c}$. As an example, $n_{e,c}$ for 14.5 GHz microwaves is $2.6 \times 10^{12} \text{cm}^{-3}$. As can be seen from Eq. (5), the maximum plasma density scales with the square of the heating frequency. In existing ECR ion sources, these frequencies range from 2.45 GHz to 18 GHz for room temperature sources, and up to 28 GHz for superconducting sources [18].

Depending on the phase difference between the cyclotron motion of the electron and the electric field of the microwave, the electron will be either accelerated or decelerated as it enters the B_{ECR}. The electrons which get accelerated will have a larger cyclotron radius

around the field line and, consequently, a longer orbit than those that get decelerated — as illustrated in Fig. 2. This results in more work being done on the electrons that gain energy than the amount of negative work done on the ones that lose energy, resulting in a net energy gain and a stochastic heating of the plasma. As a consequence of the heating, there arise two or three electron populations with distinct temperatures [19], [20], a cold (5 eV $\lesssim \langle E_e \rangle \lesssim$ 50 eV), warm (1 keV $< \langle E_e \rangle <$ 10 keV) and a hot (10 keV $\lesssim \langle E_e \rangle \lesssim$ 100 keV) population [19]–[25]. The EED is often assumed to be described by a classical Maxwell-Boltzmann distribution which, as a function of speed v, is:

$$g(v) = \left(\frac{m}{2\pi kT}\right)^{3/2} 4\pi v^2 e^{-\frac{mv^2}{2kT}}, \tag{6}$$

where m is particle mass and T the temperature of the population which can be shown to be related to the average energy by $\langle E \rangle = 3T/2$. The validity of this assumption is important for the CT-method, since the EED needs to be specified for the analysis (to compute the ionization rate coefficients). The consequences are discussed in Section 5.2.

It is shown in Ref. [13] that the energy gain to the parallel and perpendicular velocity components (w.r.t. the magnetic field), as the electron exchanges energy with the microwave, are given by

$$\Delta v_\parallel = \frac{eE}{m_e} \frac{v_\perp}{v_\phi} \sqrt{\frac{\pi}{\omega' v_\parallel}} \tag{7}$$

$$\Delta v_\perp = \frac{eE}{m_e} \left(1 - \frac{v_\parallel}{v_\phi}\right) \sqrt{\frac{\pi}{\omega' v_\parallel}}, \tag{8}$$

respectively. Here ω' is the derivative of the cyclotron frequency ω_c axially i.e. the electron cyclotron frequency is expanded as $\omega_c \approx \omega(z_R) + \omega'(z - z_R)$, where z_R is the location of the resonance. The phase velocity of the microwave is v_ϕ and E is the electric field. It can be deduced from Eqs. (7) and (8) that

$$\Delta v_\perp > \Delta v_\parallel \Leftrightarrow v_\phi > v_\perp + v_\parallel, \tag{9}$$

meaning that at velocities less than the phase velocity of the microwave, the energy gain is to $v_\perp$ mainly. At higher velocities the heating will mostly increase $v_\parallel$, which causes diffusion into the loss cone in velocity space. This is referred to as *RF-induced pitch angle scattering*.

Due to the selective heating of the perpendicular velocity component, the electron velocity distribution can be strongly anisotropic, i.e. $\langle v_\perp \rangle \gg \langle v_\parallel \rangle$. As a consequence, the ECRIS plasma is predisposed to kinetic (electron cyclotron) instabilities [26]–[30], which arise under certain operating conditions — the threshold between stable and unstable modes being mainly determined by the solenoidal magnetic field [26]. These instabilites are driven by the hot electrons [26], whose transverse momentum is released during the instability [31]. The onset of the instability is marked by increased microwave and x-ray emission from the plasma, followed by a burst of electrons from the plasma. In the extracted beam current the instability manifests as large amplitude oscillations with a period of a few milliseconds, i.e. the period of the instability [28], [30]. Owing to the fluctuating plasma density it is paramount to ensure a stable operating mode when applying the CT-method.

1.2 Magnetic confinement of electrons

To model charged particle confinement in a magnetic bottle, consider a particle with charge Q and mass m orbiting about a magnetic field line in a spatially slowly varying field $\vec{B}$. The gyromotion of the particle forms a current loop

$$I = \frac{|Q|\omega_c}{2\pi}, \tag{10}$$

where ω_c is the cyclotron frequency

$$\omega_c = \frac{|Q|B}{m}. \tag{11}$$

The current loop encloses an area $A = \pi\rho_L^2$, where ρ_L is the Larmor-radius

$$\rho_L = \frac{v_\perp}{\omega_c}. \tag{12}$$

Here $v_\perp$ is the velocity component perpendicular to $\vec{B}$. We can write for the kinetic energy W

$$W = W_\perp + W_\parallel \tag{13}$$

dividing the kinetic energy to $W_\perp$ and $W_\parallel$ associated with the particle velocity perpendicular and parallel to the magnetic field, respectively.

The current loop has an associated magnetic dipole moment whose magnitude is (using Eqs. (10), (11), and (12))

$$\mu = |\vec{\mu}| = IA = \frac{W_\perp}{B}. \tag{14}$$

As per the right hand rule, the dipole moment $\vec{\mu}$ caused by I is opposite to the B-field[3].

Magnetic confinement is also predicated on the condition that the gyrofrequency of the charged particle be much greater than the collision frequency — otherwise the magnetic dipole moment is not well-defined as frequent collisions would perturb the helical particle orbit. In other words, magnetic confinement requires that

$$\omega_c \gg \omega_{\text{coll}}, \tag{15}$$

where ω_{coll} incorporates all collision channels which might disturb the particle trajectory, and depends on the energy of the collision via the cross section. For (warm and hot) electrons in an ECRIS, this condition is met under normal operating conditions [1].

In the absence of collisions and electric fields μ and W are conserved [1], [32]. For the parallel component, then

$$W_\parallel(x) = W_0 - \mu B(x). \tag{16}$$

One can see that the $W_\parallel$ is expended as the particle moves towards increasing B — meaning that the parallel velocity component decreases and the electron may be reflected if it

---

3   This is the cause of the diamagnetic property of plasma.

becomes zero. From Eq. (16) it is apparent that a particle with a greater μ will be reflected at a lower B. The point of reflection is called the *mirror point* of the particle, and as a consequence of the ECR heating the mirror points of hot electrons are shifted towards the B_{ECR}, i.e. the plasma core.

Defining the pitch angle α between $v_\perp$ and $v_\parallel$ so that

$$\begin{cases} v_\parallel = v \cos(\alpha) \\ v_\perp = v \sin(\alpha) \end{cases} \tag{17}$$

we have that

$$W_\perp = \frac{1}{2} m v_\perp^2 = W_0 \sin^2(\alpha) \tag{18}$$

and the magnetic moment may be written

$$\mu = \frac{W_\perp}{B} = \frac{W_0 \sin^2(\alpha)}{B}. \tag{19}$$

Hence, from the conservation of μ, it can be shown that as the particle moves from point x_1 to x_2

$$\frac{\sin^2(\alpha_1)}{\sin^2(\alpha_2)} = \frac{B(x_1)}{B(x_2)}. \tag{20}$$

If the minimum of B is at x_1, and the particle is reflected at the throat of the magnetic mirror at x_2, i.e. $W_\parallel(x_2) = 0$ and $\alpha_2 = \pi/2$, we get

$$\sin(\alpha_1) = \sqrt{\frac{B_{\text{min}}}{B_{\text{max}}}} = \sqrt{\frac{1}{R}}, \tag{21}$$

where R is the so-called mirror ratio. The angle α_1 is then the minimum pitch angle for a particle to be confined. Any particles with pitch angles smaller than α_1 will escape.

The angle α_1 defines a loss cone in velocity space: particles outside the loss cone will remain magnetically confined until their pitch angle is modified (e.g. by collisions or RF-induced pitch angle scattering) so that they enter the loss cone, at which point they rapidly escape confinement. Contrarily, ECR heating mainly increases the component $v_\perp$, transferring the electron farther from the loss cone and improving confinement. The loss cone is illustrated in Fig. 3.

Cold electrons experience frequent collisions with neutrals, which rapidly scatter them into the loss cone, resulting in a positive *plasma potential* ϕ which retards electrons and accelerates ions. Note that in the presence of a plasma potential $\phi > 0$, the loss cone is truncated so that only electrons with large enough speeds can leave the plasma. The fluxes of positive and negative charge thus equilibrate, and the quasi-neutrality of the plasma is maintained. This is further discussed in Section 1.5. Hot electrons are magnetically well confined, residing far outside the loss cone due to their large $v_\perp$. They are located mainly inside the ECR surface, improving the confinement of ions within the core plasma (see Section 1.5). They also experience relatively few collisions and are thus not easily scattered into the loss cone. Their confinement is primarily affected by RF-induced pitch angle scattering and kinetic instabilities [28]–[30].
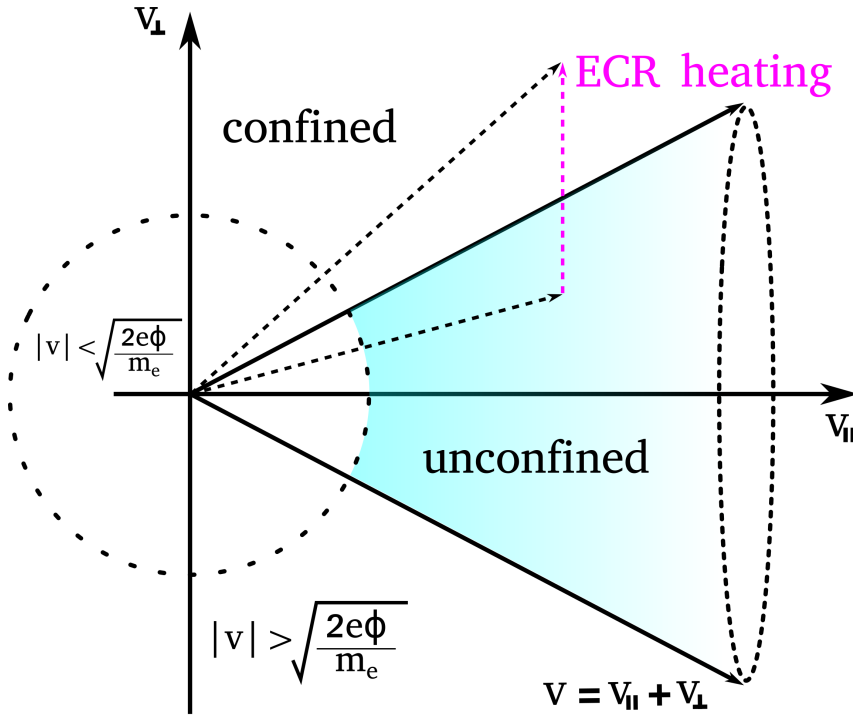
FIGURE 3   Loss cone in velocity space.

1.3   Collisions in an ECR plasma

Collisions between the different particles which constitute the ECRIS plasma are a key part of both the plasma confinement and the production of multiply charged ions: Collisions disrupt the confinement of electrons and depending on the plasma conditions they either improve or worsen the confinement of ions, as discussed in Section 1.5. The balance equation, which lies at the heart of the CT-method, is a zero-dimensional[4] model for ion production based on collision processes between plasma particles. The balance equation is introduced in Section 1.4. In the following we list the collision processes relevant for ion production in ECRIS plasmas, loosely following Ref. [15].

The plasma particles, neutral atoms, ions and electrons, are in constant motion and their mutual interaction affects the particle trajectories and energies — *elastic collisions* — but possibly also the internal state(s) of the interacting particles — *inelastic collisions*. A collision between particles A and B may increase the energies of the electrons bound in the atomic electron shells, a process referred to as *excitation*:

$$A + B \rightarrow A + B^* \rightarrow A + B + \gamma \tag{22}$$
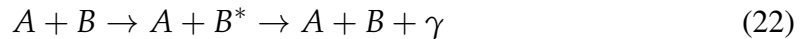
where B^* denotes B in an excited state. Long lived excited states are referred to as isomeric states. Excitation states decay emitting photons (γ) which are useful for e.g. optical diagnostics [33], [34].

If the collision imparts a sufficient amount of energy onto a bound electron, the resultant energy may exceed its binding energy (i.e. the ionization potential), freeing the

---

4   I.e. it is independent of spatial coordinates.

10

electron and *ionizing* the target. For example an electron[5] colliding with an ion of charge state q:

$$e^- + A^q \rightarrow A^{q+1} + 2e^-. \tag{23}$$

The ionization may also proceed via an autoionizing excited state:

$$e^- + A^q \rightarrow A^{q*} + e^- \rightarrow A^{q+1} + 2e^-, \tag{24}$$
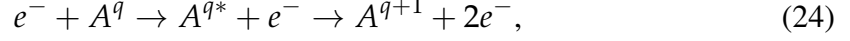
i.e. through an unbound excitation state, which spontaneously emits an electron and is typically short-lived. *Multiple ionization*, i.e. ejection of $k > 1$ electrons, in a single impact, is also possible:

$$e^- + A^q \rightarrow A^{q+k} + (1+k)e^- \tag{25}$$
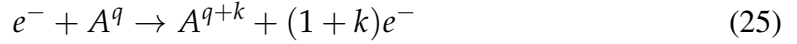
although decreasingly likely with increasing k.

It is also possible for the colliding particles to exchange one or more electrons in a process termed *charge exchange*. Due to the Coulomb repulsion between like-charged ions and the increasing binding energy of the electrons, this process is most probable between neutral atoms and ions. The general charge exchange process can be written:

$$A^q + B^g \rightarrow A^{q\pm k} + B^{g\mp k} \tag{26}$$

where $k \geq 1$, but the transfer of just a single electron is most probable.

It is also possible for an ion to capture a free electron, if the electron velocity is less than that characteristic of the orbital electrons. The *recombination* process proceeds as:

$$e^- + A^q \rightarrow A^{q-1} + \gamma, \tag{27}$$

with the emission of a photon γ.

Probabilities, rates and rate coefficients.[6]

Figure 4 shows an electron flux impinging on a target of stationary collision centers[7]. The electron flux density

$$\Gamma = n_e v_e \tag{28}$$

where n_e is the electron density and v_e is the speed of the electrons. The density of collision centers being n_i and the thickness of the target dx we can write

$$d\Gamma = -\Gamma \sigma n_i dx \tag{29}$$

where σ is the *cross section* of a collision center. The cross section measures the probability of a given event to occur, and it can be understood geometrically to represent the cross sectional area as seen by the impacting projectile defined by

$$\sigma = \pi \rho^2, \tag{30}$$

---

[5] Ion-impact ionization is possible in principle, but in an ECRIS the ions do not attain energies high enough to play a significant role in ionization.

[6] Treatment adapted from Ref. [35]

[7] To a good approximation, ions in an ECR plasma can be taken to be stationary compared to electrons, as the ion energies are much lower than those of electrons — on top of being at least three orders of magnitude more massive.
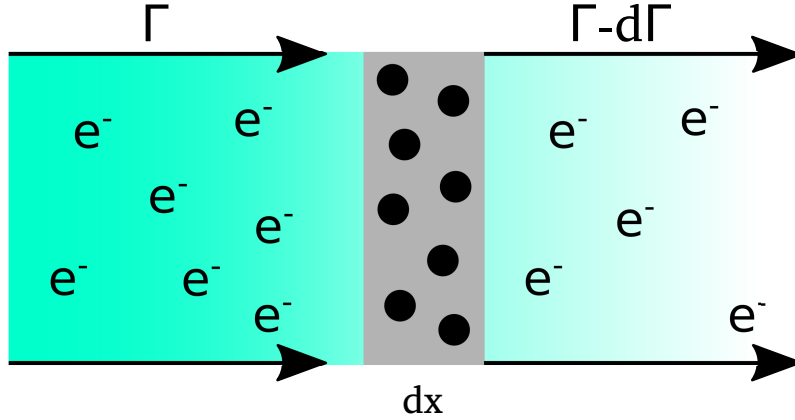
FIGURE 4   Illustration of an electron flux Γ impinging on a target of collision centers having a width dx.

where ρ is the maximum size of the impact parameter with which the event may still occur. The cross section (the maximum ρ) is dependent on the relative speed of the interacting particles. In the case of the stationary collision centers ($v_i \approx 0$) the relative speed may be replaced by v_e. From Eq. (29) one solves

$$\Gamma(x) = \Gamma_0 e^{-\sigma n_i x} \tag{31}$$

i.e. the flux decays as it impinges into the target. The mean free path is defined through the constant

$$\lambda \equiv (\sigma n_i)^{-1} \tag{32}$$

and inherits the speed dependence from the cross section.

It is possible to define a collision rate (i.e. the inverse of the mean time between collisions, τ) based on the relative speed v and the mean free path:

$$\nu \equiv 1/\tau \equiv v/\lambda = n_i \sigma v. \tag{33}$$

Suppose then that the electron energy within the flux is described by a distribution function g. The average collision rate can be computed as an average over the speeds:

$$\langle \nu \rangle = n_i \int_0^\infty g(v)\sigma(v)v\,dv = n_i \langle \sigma v \rangle \tag{34}$$

where the distribution average of σv

$$\langle \sigma v \rangle \equiv \int_0^\infty g(v)\sigma(v)v\,dv \tag{35}$$

is referred to as the rate coefficient. Here the normalization of the distribution g is taken as

$$\int_0^\infty g(v)\,dv = 1 \tag{36}$$

but it can be normalized equally well such that an integral over the speeds gives the electron density n_e, as is often done in the literature.

1.4 Multiply charged ion production

As the electrons gain kinetic energy, they become able to break up the molecules and ionize the atoms of the neutral gas (e.g. O_2, He, H_2, Ar ...) which is fed into the plasma chamber. The ionization proceeds in a stepwise manner, and is counteracted by charge exchange between ions and neutral atoms. The charge state distribution (for a given species of ion) within an ECRIS plasma is modeled by the balance equation [36], [37]

$$
\begin{aligned}
\frac{\mathrm{d}n^q}{\mathrm{d}t} = {} & n_e \left\langle \sigma v \right\rangle^{\mathrm{inz}}_{q-1 \to q} n^{q-1} - n_e \left\langle \sigma v \right\rangle^{\mathrm{inz}}_{q \to q+1} n^q \\
& n_0 \left\langle \sigma v \right\rangle^{\mathrm{cx}}_{q+1 \to q} n^{q+1} - n_0 \left\langle \sigma v \right\rangle^{\mathrm{cx}}_{q \to q-1} n^q \qquad \forall q \in \{0, 1, 2, \ldots, Z\} \\
& - \frac{n^q}{\tau^q_{\mathrm{conf}}},
\end{aligned}
\tag{37}
$$

which defines a set of coupled differential equations over all charge states q up to Z i.e. the proton number of the species. The coupling is illustrated in Fig. 5. Equation (37) (or a variation of it) is the basis of the transient methods for plasma diagnostics in Refs. [38]–[42] and has been used in simulations of ion charge state distributions in ECRIS plasmas [36], [37], [43], [44].

Equation (37) describes the time evolution of the ion density n^q: The charge state q is supplied by stepwise electron-impact ionization from lower states at a volumetric rate $n_e \left\langle \sigma v \right\rangle^{\mathrm{inz}}_{q-1 \to q} n^{q-1}$ and charge exchange between ions and neutrals from higher states at a volumetric rate $n_0 \left\langle \sigma v \right\rangle^{\mathrm{cx}}_{q+1 \to q} n^{q+1}$. The population is depleted by ionization to higher states and charge exchange to lower states at volumetric rates $n_e \left\langle \sigma v \right\rangle^{\mathrm{inz}}_{q \to q+1} n^q$ and $n_0 \left\langle \sigma v \right\rangle^{\mathrm{cx}}_{q \to q-1} n^q$, respectively, as well as by ion losses from the plasma, which are encapsulated in the loss term $n^q / \tau^q_{\mathrm{conf}}$. The loss term defines the ion population confinement time τ^q_{conf}, comprising all possible ion loss channels (see Section 1.5). In steady-state ion losses are in balance with ion production, and Eq. (37) yields zero. Note that this requires a steady supply of material into the plasma.

In conditions relevant for ECRIS operation, the aforementioned five channels are most relevant for ion production. A more precise model would have to account for *(i)* double ionization ($q \to q + 2$) and higher; *(ii)* electron-ion recombination; *(iii)* charge exchange between ions; *(iv)* wall recycling, i.e. ions previously lost from the plasma being sputtered back into the plasma as neutral atoms; and *(v)* ionization from metastable excitation states. It also needs to be noted that the balance equation is inherently a zero-dimensional model which does not account for any anisotropies in particle or energy distributions.

To a good approximation *(i)* may be neglected, as the cross section for the double ionization process is usually at least an order of magnitude lower than that of single ionization, and the cross section for the ejection of 3 or more electrons is even smaller [45]. Recombination *(ii)* does not play a significant part in conditions relevant for ECRIS operation owing to the low cross sections at the relevant energies [45]. It may, however, affect the production rates of very highly charged ions: For example, the total recombination
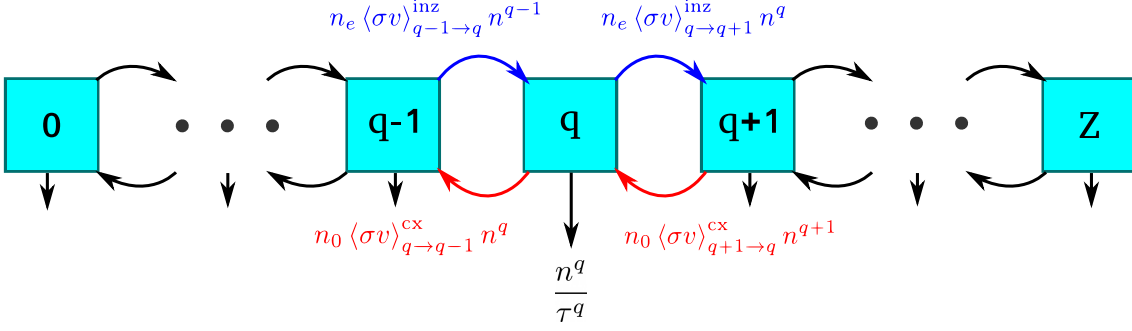
FIGURE 5   Schematic of the stepwise ionization process described by the balance equation.

rate coefficient for Ar^{18+} at 10 keV electron temperature (MB distribution) is roughly 10^{-12} cm^3s^{-1} [46], which is on the same order of magnitude as the ionization rate coefficient of Ar^{17+} [47] at the same temperature. Ion-ion charge exchange *(iii)* is suppressed compared to ion-neutral charge exchange due to the combined effects of the Coulomb repulsion between the two positive ions, and the increase of the binding energy of the outer electrons for higher charge states. Wall recycling *(iv)* can be ignored when millisecond pulses of a metallic element are introduced — as is the case in the experimental campaigns pertaining to this work — since the contribution to the extracted beam from wall recycled metals remains small even after weeks of conditioning [48]. The presence of metastable excited states *(v)* can boost the ionization probability of some charge states if the metastable state has a lifetime on the order of magnitude of the average time between ionizing collisions. Such long-lived states are rare, but may be populated in the plasma, and emissions from these states can be probed by spectroscopic methods [49].

The Golovanivsky plot

Ion production in the ECRIS occurs mainly through stepwise ionization (from one charge state to the next) via multiple consecutive electron-ion collisions [1]. Golovanivsky [50] expressed the condition for the production of charge state q ions as

$$n_e \tau_{\mathrm{conf}}^q \geq \left[\langle \sigma v \rangle_{q \to q+1}^{\mathrm{inz}} \right]^{-1} \tag{38}$$

Here n_e is the electron density, τ_{conf}^q the ion confinement time, $\sigma = \sigma_{q \to q+1}^{\mathrm{inz}}$ the cross section of electron-impact ionization from charge state q to $q+1$, and v is the relative speed between the electron and ion[8]. The rate coefficient is computed as an average over the electron energy distribution (EED), which in the case of a Maxwell-Boltzmann distribution may be parametrized by the temperature T_e, or more generally by the average energy $\langle E_e \rangle$ of the distribution. Golovanivsky considered the inequality for hydrogen-like ions at the optimum temperature T_e^{opt}, i.e. at the maximum of the rate coefficient. As only one ionization channel is considered, the inequality yields an upper limit for the product of $n_e \tau_{\mathrm{conf}}^q$ required for production of fully stripped ions at a given T_e^{opt} (or $\langle E_e \rangle^{\mathrm{opt}}$). The resultant "Golovanivsky plot" is shown in Fig. 6.

---

[8]   Essentially the electron speed, as the relatively much more massive ions are nearly stationary compared to the electrons.
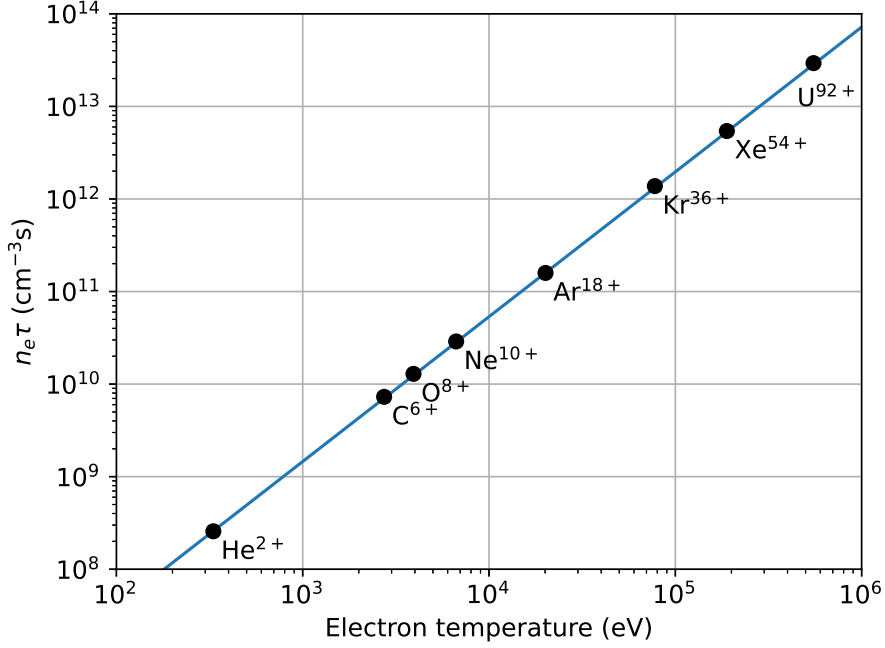
FIGURE 6   The Golovanivsky plot for the plasma product $n_e\tau$ necessary to produce fully
stripped ions as a function of the electron temperature. Data from Ref. [18].

The inequality (38) may be expressed in terms of the characteristic times of ion
confinement and ionization as

$$\tau_{\text{conf}}^{q} \geq \tau_{\text{inz}}^{q} = \left[n_e \left\langle \sigma v \right\rangle_{q \to q+1}^{\text{inz}} \right]^{-1} \tag{39}$$

i.e. the condition for significant $(q \to q+1)$ ionization rates is that the ion confinement
time is longer than the ionization time. A further condition for multiply charged ion
production is that there must be no significant charge decreasing processes. In typical
ECRIS operating conditions this means charge exchange between ions and neutrals must
be minimized, i.e. that the charge exchange time is long compared to the confinement
time.

$$\left[n_0 \left\langle \sigma v \right\rangle_{q \to q-1}^{\text{cx}} \right]^{-1} = \tau_{\text{cx}}^{q} \geq \tau_{\text{conf}}^{q} \tag{40}$$

Here, n_0 is the neutral atom density, and the rate coefficient is that of charge exchange
between neutrals and ions at charge state q.

1.5   Ion confinement

The "plasma product" $n_e\tau_{\text{conf}}^{q}$ defined by the inequality (38) quantifies the impor-
tance of τ_{conf}^{q} for a high performance ECRIS. To produce highly charged ions (HCIs),
good confinement of ions is a necessity. Paradoxically, a well performing ECRIS also
requires the ion confinement time to be small so that the ions, once produced, may leak

out and become available for beam formation. In the charge breeding context this balance becomes even more delicate, as the radioactive ions must be extracted before a large fraction of them decay.

Many different models have been suggested to describe ion confinement in an ECRIS plasma, but none are applicable throughout the whole range of ECRIS operating conditions [51]. Depending on the tune[9] of the ion source, the plasma properties may vary by a lot, affecting the particle energies and densities, and consequently the charge state distributions, spatial distributions of particles, the plasma potential, and so on — all factors that affect the confinement times predicted by the models. In addition, the plasma properties vary spatially, making it almost nonsensical to apply any single model to the problem of ion confinement.

It is probably most realistic to consider, that the totality of the confinement properties are dictated by a combination of the different models, and that the part played by each model assumes a different importance as the tune is adjusted, and that ions in different spatial regions of the source are subject to different confinement schemes.

The different confinement regimes can be classified according to the ion collisionality [52], [53]

$$\eta \equiv \frac{t_{\text{bounce}}}{t_{\text{collision}}}, \tag{41}$$

where t_{bounce} is the ion "bounce time", i.e. the time it takes for an ion to bounce between the magnetic mirrors[10], and $t_{\text{collision}}$ is the time between successive collisions. Different confinement models are justified based on the magnitude of η. These regimes are *(i)* non-collisional, $\eta \ll 1$, *(ii)* moderately collisional, $\eta \sim 1$, and *(iii)* highly collisional, $\eta \gg 1$. Furthermore, Rognlien and Cutler showed in Ref. [52] that cases *(i)* and *(ii)* can be treated as one regime, where $\eta \lesssim 1$.

$\eta \lesssim 1$: Electrostatic confinement[11]

It was first suggested decades ago that in an ECRIS there exists a potential dip $\Delta\phi < 0$ in the otherwise positive plasma potential profile ϕ — similarly to open-mirror fusion devices. This potential dip arises in the plasma core as a consequence of the buildup of hot electrons, which are well-confined due to their larger dipole moment μ and lower collision frequency. The dip is located spatially near the B_{ECR}, because the ECR heating brings the mirror points of the hot electrons close to the ECR zone. This potential dip presents an electrostatic barrier to the positively charged ions, trapping them until they attain a sufficiently high kinetic energy to overcome the barrier.

In this confinement scheme, the ion confinement time may be expressed as a linear combination of characteristic ion confinement times under frequent ($\eta \sim 1$) and infre-

---

9   The configuration of operating parameters (gas input, microwave heating power and frequency, magnetic field configuration,...) set for the source are colloquially referred to as the source "tune."

10   NB: if the ion collision time is less than the gyration time around a magnetic field line, ions are not magnetically confined and the bounce time is poorly defined. In this case η should be interpreted as the number of collisions the ion experiences as it transits through the plasma.

11   Adapted from Refs. [15], [52], [53]

quent ($\eta \ll 1$) collisions[12] [52]

$$\tau = \tau_1 + \tau_2 \tag{42}$$

where for frequent collisions

$$\tau_1 = RL\sqrt{\frac{\pi m}{2T_i}}e^{eq|\Delta\phi|/T_i} \tag{43}$$

with L being the characteristic plasma (half-)length, and for infrequent collisions

$$\tau_2 = \frac{G}{(1 + T_i/2eq|\Delta\phi|)\nu_{ii}}\frac{eq|\Delta\phi|}{T_i}e^{eq|\Delta\phi|/T_i}. \tag{44}$$

In Eq. (44)

$$G = \sqrt{\pi}\frac{R+1}{2R/\ln(2R+2)} \tag{45}$$

and R is the mirror ratio. The ion-ion collision frequency here is the ion-ion Spitzer[13] scattering frequency [53]

$$\nu_{ii} = 174 \times 10^3 \frac{q^2}{\sqrt{M}T_i^{3/2}}\sum_{q'}n^{q'}q'^2 \tag{46}$$

The frequency ($[\nu_{ii}] = 1/s$) is computed for a given ion of mass M ($[M] = u$, u being the atomic mass unit) having a temperature T_i ($[T_i] = eV$)[14] common to all ions in the plasma. The expression in Eq. (42) was derived in the context of open magnetic traps, which served as a precursor to the ECRIS [52], [54], [55]. In ECRIS conditions τ_2 is negligible compared to τ_1 due to the high ion collision frequency, and to a good approximation $\tau \approx \tau_1$.

The key property of Eq. (43) is that the confinement time increases exponentially with the ion charge state. This is because the electrostatic barrier experienced by an ion is the greater, the bigger its charge is, which provides increasingly strong confinement for HCIs. For example, a charge state q ion needs an energy greater than $q\Delta\phi$ to scale the potential barrier. An increased ion temperature, on the other hand, causes the confinement time to decrease as the more energetic the ion population is, the larger fraction of the ions may escape the confines of the dip.

An increasing amount of indirect evidence implies that such a potential dip exists. Direct measurement of the potential profile is as yet infeasible without perturbing the plasma and corrupting the experiment. Experimental measurements of ion beam emittances as well as spatially resolved ion beam profiles indicate that HCIs originate closer to the beamline axis than lower charge state ions [56]–[60]. Simulations [45], [61] of ion trajectories corroborate these inferences, and in Ref. [62] simulations of the plasma density resulted in a plasma potential profile with two potential dips ($\Delta\phi \approx -0.02$ V) which

---

[12] NB: The direct addition (as opposed to addition of the inverses) of the times is valid since τ_1 and τ_2 represent different limits of the same process (as opposed to two distinct processes).

[13] I.e. the rate at which multiple small-angle scatterings accumulate to a 90° rotation of the velocity. NB that Ref. [15] uses a different collision frequency.

[14] Owing to their high collisionality, the ions are considered to have a Maxwellian energy distribution.

formed at the turning points of the hot electrons along the plasma chamber axis. Furthermore, the anomalously high ion temperatures reported in Ref. [33] support a confinement model which yields long enough confinement times to enable considerable ion heating via electron drag. From these considerations it would appear that the HCIs are generated in a potential dip where they are confined until they obtain energies high enough to overcome the potential barrier.

$\eta \gg 1$: **Spatial diffusion**[15]

Whenever there is a density gradient in a macroscopic property of a gas, diffusion can occur, the effect of which is to restore homogeneity. For example, a non-uniform particle distribution gives rise to a flux of particles from high density regions to regions of low particle density.

Confinement time in the spatial diffusion regime [53] can be approximated through

$$\tau \approx \frac{L^2}{D}, \tag{47}$$

where L is the characteristic length of the plasma, and D is the diffusion coefficient [1], [32], [35], which describes the ease of motion through the plasma for a given particle — a larger D meaning faster diffusion.

Although an ECRIS plasma may not be weakly ionized — particularly in the core region — the most important features of diffusion are best illustrated modeling it as such. In the absence of an applied magnetic field, diffusion is impeded by interparticle collisions as they decrease the mean free path. In such a plasma, the diffusion coefficients for electrons and ions are given by

$$D_e = k_B T_e / m_e \nu_e \tag{48}$$
$$D_i^q = k_B T_i^q / m_i \nu_i \tag{49}$$

where $\nu_{e/i}$ are the electron and ion collision frequencies, respectively. Both exact and limiting forms of ν_e and ν_i can be found e.g. in Ref. [63]. Generally speaking, in the ECRIS plasma environment $\nu_i \gg \nu_e$. It can be seen that the light, energetic electrons diffuse faster than the massive, cool and highly collisional ions in the absence of a magnetic field (and parallel to magnetic field lines).

In contrast, the diffusion of charged particles across a magnetic field is eased by collisions: The magnetic field prohibits a charged particle from free movement perpendicular to the field line, forcing it on a helical orbit. Collisions disrupt this orbit, randomising the velocity and allowing the charged particle to jump from one field line to another. The diffusion coefficients perpendicular to the field are modified so that

$$D_{e,\perp} = \frac{\nu_e^2}{\nu_e^2 + \omega_{ce}^2} D_e \tag{50}$$

$$D_{i,\perp}^q = \frac{\nu_i^2}{\nu_i^2 + \omega_{ci}^2} D_i^q \approx D_i^q, \tag{51}$$

---

[15] See also [1], [20], [32], [53]

where $\omega_{ci/ce}$ is the cyclotron frequency of Eq. (11). The diffusion coefficient parallel to the B-field remains unchanged: $D_\parallel = D$. From this it is evident that the ions diffuse more rapidly across the field lines, than the weakly collisional electrons.

Any deviation from charge-neutrality will give rise to a plasma potential ϕ and an associated electric field, which accelerates the slower species and evens out the diffusion rates until the net flow of charge from the plasma is zero. This mode of diffusion is termed *ambipolar diffusion*. In an ECRIS the plasma potential is positive as, in absence of ϕ, the electrons exit the plasma fastest. This leads to a build-up of a net positive charge in the plasma, which propels the ions until the loss rates equilibrate. Typical values of the plasma potential range from 10 V to 100 V, with best performances (i.e. highest extracted HCI currents) found at around 20 V [64], [65].

In the case of perfect ambipolar diffusion in a weakly ionized plasma, the diffusion coefficient is given by [32], [66]

$$D_a = \frac{k_B(T_e + T_i)}{m_e \nu_e + m_i \nu_i} \tag{52}$$

common to both electrons and ions. Equation (52) shows that the cool, massive ($m_i \gg m_e$) and highly collisional ($\nu_i \gg \nu_e$) ions of the ECR plasma slow down the diffusion rate.

The following expressions for confinement time are available in the literature: For ions Eq. (47) gives in the direction along the plasma chamber axis (see [20] and references therein)

$$\tau_{\text{conf}}^q = 7.1 \times 10^{-20} L q \ln \Lambda \sqrt{A} \frac{n_e q_{eff}}{T_i^{5/2}} \tag{53}$$

for diffusion without ambipolar effects — i.e. random walk diffusion. Here the characteristic length L is the half length of the plasma, $\ln \Lambda$ the Coulomb logarithm (a constant $\approx$ 10–20 regardless of the source tuning), A is the ion mass number, and

$$q_{eff} = n_e^{-1} \sum n^q q^2 \tag{54}$$

the effective charge of the plasma.[16] The units are

$$[\tau] = \text{s}; [L] = \text{cm}; [n_e] = \text{cm}^{-3}; [T_i] = \text{eV}.$$

Equation (53) indicates that the ion confinement time grows when the size, effective charge, and density of the plasma increase. This is due to the increased number of collisions which hinder ion diffusion parallel to the magnetic field. A strong inverse dependence on temperature is also apparent, and results from decreased collisions.

Ref. [20] suggests that the ambipolar confinement time be derived through the ion mobility so that

$$\tau_{\text{conf}}^q = \frac{L}{\mu_i E} \tag{55}$$

---

[16]   NB that Eq. (54) should be $\Sigma n^q q^2 = n_e \langle q^2 \rangle / \langle q \rangle$ PI, but the original form is given here.

where $E = -\nabla\phi$ the ambipolar electric field ($[E]$ = V/cm) and

$$\mu_i = \frac{|q|e}{m_i v_i}. \tag{56}$$

This leads to an expression of the form

$$\tau^q_{\text{conf}} = 7.1 \times 10^{-20} L q \ln\Lambda \sqrt{A} \frac{n_e q_{eff}}{T_i^{3/2} E}. \tag{57}$$

The units and other coefficients are as in Eq. (53).

Equation (57) implies, that a larger plasma potential (greater E) and higher ion temperatures decrease the confinement time. The more massive the ion and the larger the plasma chamber, the longer the confinement time. The increase of τ^q_{conf} with $n_e q_{eff}$ is due to collisions inhibiting particle motion in the parallel direction.

An alternative spatial diffusion regime confinement model has also been suggested [67]

$$\tau^q_{\text{conf}} = \frac{L^2 m_i}{K_\parallel \tau_{ij} T_i} e^{eq|\Delta\phi|/T_i}, \tag{58}$$

where τ_{ij} is the unlike ion collision time, and $K_\parallel$ is a constant "shape factor" which depends on the axial plasma profile. This scheme has been considered suitable for overdense ECR plasmas [1]. Equation (58) results from solving the parallel diffusion equation assuming the ion density and the plasma potential to have similar parallel gradient lengths. It was suggested in Ref. [67] that for highly charged ions there occurs a change in confinement scheme from the moderately collisional case described by Eq. (43) to spatial diffusion per Eq. (58) at a threshold pressure. In PI we made a similar inference, discussed in Section 5.1, where an apparent change in confinement scheme was observed between low and high charge state ions.

Magnetic confinement of ions

Ions are subject to the same restoring force arising from the minimum-B structure as the electrons, but their much larger mass and lower energy cause their gyrofrequencies to be smaller and collision frequencies greater, respectively. Hence the collisionality disrupts their magnetic confinement, as the condition expressed in Eq. (15) is less likely to be met in ECRIS conditions. Traditionally, ions have been considered almost completely unmagnetized [20], but recent evidence suggests that low charge state ions may be magnetically confined [68], [69] PI, whereas for HCIs this is definitely not the case.

In Ref. [33] it was found that ions in an ECRIS plasma have a charge state dependent temperature in the range 5 eV–28 eV, with the highest temperatures obtained for the highest charge states. In Fig. 7 oxygen plasma is considered as an example. The ion-ion Spitzer scattering frequencies of Eq. (46) $O^+ \to O^{8+}$ are compared to the cyclotron frequency of O^+ at $B = 0.5$ T, $n_e = 5 \times 10^{11}$ cm^{-3} and $q_{eff} = 4.5$. From the Figure it appears, that the condition $\omega_{ci} \gg \omega_{coll}$ may be satisfied for low charge ions if they attain an energy in excess of $\sim$5 eV.
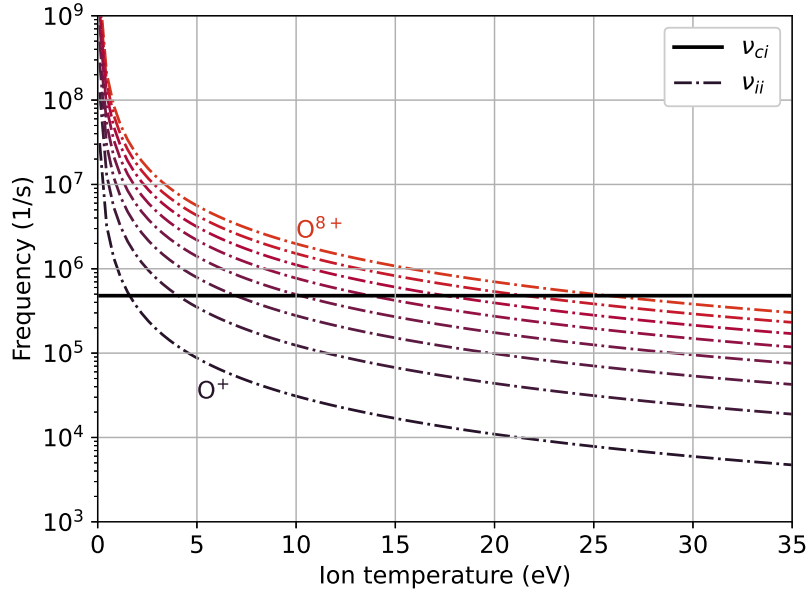
FIGURE 7 Spitzer 90 degree scattering times and the cyclotron frequency ($\nu_{ci} = \omega_{ci}/2\pi$) for oxygen.) The ν_{ci} are computed for O^+ and the ν_{ii} are calculated for $O^+ \rightarrow O^{8+}$ with $n_e = 5 \times 10^{11}$ cm^{-3} and $q_{eff} = 4.5$ at $B = 0.5$ T. Ions with $\nu_{ii} < \nu_{ci}$ can be magnetically confined.

Altogether the ion confinement model depends on the plasma conditions (such as temperature and density) which vary spatially. As the distribution of ions in the plasma is also spatially non-uniform, we expect that the total confinement time is formed through a combination of these models.

Confinement time and ion heating via electron drag

The interplay of ion confinement and ion temperatures was investigated in Ref. [33]. We adapt the treatment here to illustrate the effect of ion confinement on the ion temperatures considering a situation where we have previously established ion populations in the steady-state. The different ion populations each have temperatures T_i^q, and ions escape the plasma at a rate governed by the confinement time τ_{conf}, unique to each population. All ion losses are in balance with the amount of material introduced to the plasma, i.e. the population densities do not change. The ions are presumed to obtain their energy solely from the electrons, and we will neglect energy transfer between ions. This makes the model unsuitable for studying gas-mixing [20], [70] effects in particular, where the energy transfer between ions is key. It also causes an overestimation of the HCI temperatures. A more precise treatment can be found in the Ref. [33].

Ion heating via electron-ion collisions (i.e. "electron drag") can be modeled by [20]

$$\frac{\mathrm{d}\left(\frac{3}{2}n_i^q T_i^q\right)}{\mathrm{d}t} = \frac{3}{2}n_e \frac{T_e - T_i^q}{\tau_e^{e \rightarrow q}} - \sum_{q'} \frac{3}{2}n_i^q \frac{T_i^q - T_i^{q'}}{\tau_{ii}^{q \rightarrow q'}} - \frac{3}{2}n_i^q \frac{T_i^q}{\tau_{\text{conf}}^q}, \tag{59}$$

where the first term on the right-hand-side describes the energy transferred from the elec-

trons to ions of charge state q at a rate determined by the *energy equipartition rate* [20]

$$\frac{1}{\tau_e^{e \to q}} \sim \nu_e^{e \to q} \simeq \frac{3.2 \times 10^{-9} \ln \Lambda}{T_e^{3/2}} \frac{n_i^q q^2}{A} \qquad (\text{s}^{-1}, \text{eV}, \text{cm}^{-3}), \qquad (60)$$

with $\ln \Lambda$ the Coulomb logarithm, A, n_i^q the mass number and density of the ion, respectively. The second term describes energy transferred from ion to ion via collisions at a rate determined by the ion-ion collision frequency. The collision frequency was approximated by [20]

$$\frac{1}{\tau_{ii}^{q \to q'}} \sim \nu_{ii} \simeq \frac{6.8 \times 10^{-8} \ln \Lambda}{\left(T_i^q\right)^{3/2}} \frac{q^2}{\sqrt{A}} n_e q_{eff} \qquad (\text{s}^{-1}, \text{eV}, \text{cm}^{-3}). \qquad (61)$$

The effect of the second term is to distribute energy between ions. Finally, the third term describes the energy carried out of the plasma by ions exiting it at a rate governed by the confinement time.
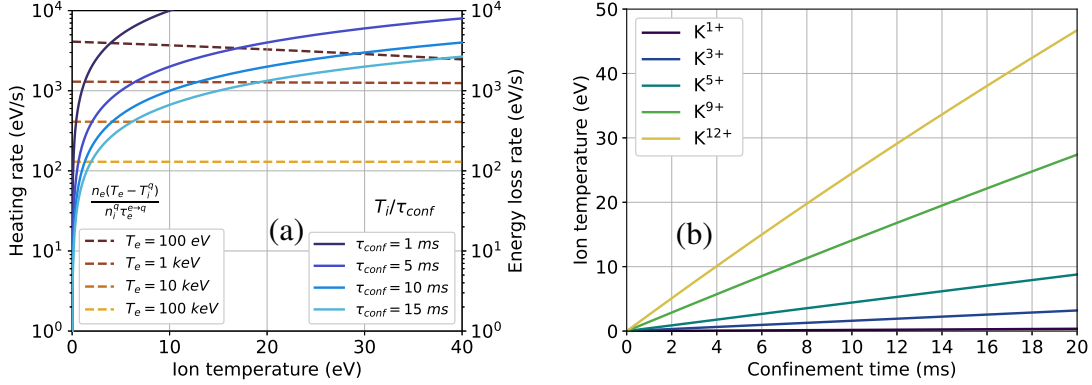

FIGURE 8 $^{39}\text{K}^{10+}$ heating rates resulting from electron drag at different electron temperatures, and the energy loss rate with varying τ_{conf} as a function of ion temperature (a) and the predicted steady-state ion temperatures as a function of ion confinement time for various charge states of ^{39}K when $T_e = 500$ eV (b).

To provide concreteness to these time scales, in Fig. 8 (a) we divide Eq. (59) by $\frac{3}{2n_i^q}$ and plot the first (heating) term $n_e \left(T_e - T_i^q\right) \nu_e^{e \to q} / n_i^q$ for different T_e as a function of T_i. The other parameters were chosen to be $n_e = 5 \times 10^{11}$ cm^{-3}, $\ln \Lambda = 10$, $A = 39$ and $q = 10+$ (i.e. $^{39}\text{K}^{10+}$). The corresponding energy loss rates — as given by the third term T_i / τ_{conf} — with different τ_{conf} are also plotted.

If we disregard the energy transfer between ions then in steady-state (i.e. $\frac{d}{dt} = 0$) the heating rate and the energy loss rate balance out and we have

$$\frac{n_e \left(T_e - T_i^q\right)}{n_i^q \tau_e^{e \to q}} = \frac{T_i^q}{\tau_{\text{conf}}^q}. \qquad (62)$$

That means, the points of Fig. 8 (a), at which the heating term and the energy loss term cross, correspond to the steady-state ion temperature for the chosen T_e and τ_{conf}. Solving this equation for T_i^q gives the ion temperature in steady-state. The T_i^q have been plotted

in Fig. 8 (b) for various charge states of ^{39}K as a function of τ_{conf} given $T_e = 500$ eV, and the other parameters are as in (a). It is apparent that the confinement model plays a key role in determining the ion temperatures: The ion temperature can increase only up to the point where ions exit the plasma at a rate which exactly balances the energy passed to the ions from the electrons. The stronger the confinement, the higher will be the ion temperature. From Fig. 8 we can also see, that as T_e increases, the T_i decreases. This is due to the increasing energy equipartition time, $\tau_{\text{e}}^{e \rightarrow q}$.

1.6 Charge Breeding of radioactive ion beams

Radioactive isotopes are produced primarily via two methods: in-flight separation (IF) [71], and isotope separation on-line (ISOL) [72]. These two methods produce radioactive ions with kinetic energies in the GeV/A and keV/A ranges, respectively[17]. To access energies in the MeV/A region one relies on acceleration of the radioactive ions generated with the ISOL method — i.e. "post-acceleration." Post-acceleration is achieved by means of dedicated accelerators such as cyclotrons and linear accelerators (linacs), in which the energy per nucleon of the post-accelerated ions scales in proportion to the charge state q of the injected ion: In the case of a cyclotron the scaling is $\propto (q/A)^2$, and with linacs $\propto q/A$. Accordingly, it is important to ionize the radioactive species up to a suitable charge state to obtain the desired final beam energy — a process referred to as "charge breeding."

There are three primary charge breeding methods: Gas-jet/foil stripping, Electron Beam Ion Source (EBIS) charge breeder, and Charge Breeder Electron Cyclotron Resonance Ion Source (CB-ECRIS) [16]. In each case the low energy, singly charged ion beam is injected into the charge breeding device and extracted downstream of it as a beam of multiply charged ions (i.e. the N+ beam), and guided into the post-accelerator. The charge breeder type is selected according to the specifications desired by the output beam, which may include the desired charge state distribution (CSD), the charge breeding time, beam intensity, emittance, and operation mode (pulsed vs. continous).

When it comes to producing Radioactive Ion Beams (RIBs), the key parameter is the charge breeding time — i.e. the time between injection of the singly charged ion, and the extraction of the same ion at charge state q [73]. If the charge breeding time is too long, the beam intensity will degrade due to radioactive decay, potentially rendering the extracted beam unusable for the experiment. The efficiency of the charge breeding process is measured by the charge breeding efficiency

$$\eta^{q+} = \frac{I^{q+}}{qI^{1+}} \tag{63}$$

Where I^{1+} and I^{q+} are the injected singly charged and extracted q charge state ion beam currents, respectively. The global efficiency is obtained as the sum $\Sigma_q \eta^{q+}$.

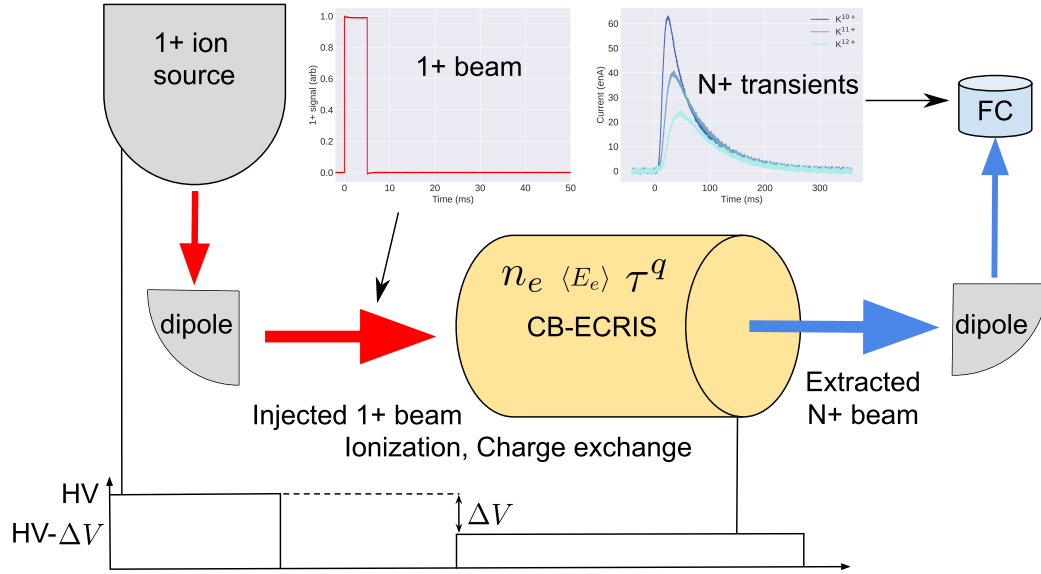[17] Energy per nucleon, A being the mass number of the isotope.

FIGURE 9   Simplified schematic of the charge breeding setup using an ECRIS.

ECRIS as a charge breeder

The conventional minimum-B ECRIS design lends itself conveniently for use as a charge breeder [16]: The required modifications are to fit in suitable injection optics to allow a beam of singly charged ions to be deposited into the plasma sustained in the ECRIS, and rearranging the microwave injection.

Figure 9 presents a schematic of the charge breeding process using an ECRIS. The 1+ ion beam is guided to the ECRIS via a dipole magnet which q/m-analyses the 1+ beam, separating the charge states of a given element. The source of 1+ ions and the ECRIS are biased to the same positive high voltage, but due to the positive potential of an ECRIS, the ion source potential is adjustable by $\Delta V \in [-100 \text{ V}, 0 \text{ V}]$. The value of ΔV is adjusted to maximize the capture efficiency of the 1+ ions in the support plasma[18].

A large fraction ($\sim 60\,\%$) of the injected 1+ beam particles are stopped and captured by the support plasma [74]. The captured particles are then ionized to higher charge states in a process described in more detail in Section 1.4. A portion of the ions exits through the extraction aperture and become available for beam formation. The ECRIS high voltage along with ion optical elements extracts the ions from the source downstream towards post-acceleration. A dipole magnet is generally used to separate the different charge state ions based on their charge-to-mass -ratios q/m and to select the desired charge state. Both electrostatic and magnetic ion optical elements are used to maximize the transport efficiency.

---

18   In this context, the plasma sustained within the source is referred to as the "support" or "buffer" plasma. Molecular hydrogen and helium are typical choices for the support gas species for charge breeding purposes.

1.7 Methods for ECRIS plasma diagnostics

ECRIS plasma diagnostics (See Refs. [18], [75] for comprehensive reviews) are focused on the metrics which affect the source performance — namely the electron density n_e, the EED, and ion confinement properties such as ion temperature and the plasma potential distribution. Arguably the most important qualifying factor of a diagnostic tool in the ECRIS context is its invasiveness — i.e. the amount by which the applied diagnostic affects the properties of the plasma discharge which it aims to measure. This constraint effectively limits the usable methods to those which measure emissions (particles and/or radiation) which arise naturally from the plasma in the operating mode. Such methods include but are not limited to: Measurement of the extracted beam CSD using a Faraday Cup; Optical emission spectroscopy for ion densities in plasma and ion temperatures, plasma bremsstrahlung and energy resolved escaping electron flux measurements for the EED (indirect and direct measurements, respectively), 1+ beam injection for measuring the ion collision frequency, and the retarding field analyzer for determining the plasma potential. For measuring ion confinement times, transient methods measuring plasma ion emissions have been developed. For the plasma energy content, measurements of the plasma diamagnetic effect can be used.

Diamagnetic loop measurements [76] are relevant here, as they probe the plasma energy content (or energy density) as does the CT-method. In diamagnetism experiments a conducting loop of wire is wound around the plasma so that the field lines of the externally applied B-field pass orthogonally through the plane spanned by the loop. When the microwave power is switched on/off, a voltage is induced in the loop.

The induced signal V_{loop} is related to the plasma energy density $n_0 kT$:

$$n_0 kT = \frac{B_0 \int_0^t V_{\text{loop}} \mathrm{d}t}{\pi \mu_0 N r_0^2}.$$

(64)

Here $n_0 kT$ is the average energy density due to all charged particles present in the plasma, B_0 is the intensity of the externally applied magnetic field, N is the number of turns in the loop, r_0 the maximum radius of the plasma and μ_0 the vacuum permeability. Equation (64) assumes that the plasma density decays exponentially with radial distance from the axis, and that the plasma exists in ideal magnetohydrodynamic equilibrium.

Measuring absolute energy content values is challenging, and the method is best suited for revealing trends as a function of the operating parameters of the source (i.e. parameter sweeps), and for investigating the time scales of plasma relaxation to steady state after a perturbation has been induced.

In diamagnetic loop measurements of Ref. [76] it was found that the plasma energy density increases logarithmically with the absorbed microwave power. The energy density was found to saturate rapidly as a function of the neutral pressure, and that the plasma energy density increases with the ratio $B_{\text{min}}/B_{\text{ECR}}$.

Transient material injection methods

Transient methods are a minimally invasive class of diagnostics based on injecting a probe signal into the ion source, and monitoring the corresponding plasma response to it, or the influence of the plasma on the probe signal. The response may again be either radiation or particle emissions. The work in this thesis contributes to a subcategory of transient methods, where a small amount of ions are pulsewise injected into the support plasma sustained in an ECRIS, where the ions or neutrals are captured and subjected to the ionization processes. The system's response is monitored by measuring the extracted ion beam current transients of the injected material, and their time series are analyzed by models which seek to describe the ion creation and loss processes involved in the balance equation (37).

Pardo *et al.* [38] conducted the first transient material injection measurements in an ECRIS. They used laser ablation [77] to produce a pulse of bismuth ions into an ECRIS plasma. The extracted high charge state current transients were then measured and fitted by a model which incorporated the electron-impact ionization and charge exchange processes, but not ion confinement. The experimental methodologies were expanded by Vondrasek *et al.* in their measurements of the transient rise times in Ref. [78]. Later, Imanaka *et al.* [39] conducted experiments (again using laser ablation to produce the injection pulse) where the ion confinement time was also accounted for in the model employed. A necessary assumption of their approach was that the ion confinement time scales linearly with the charge state — an assumption based on an experimental campaign by Douysset *et al.* [21] where the confinement times were deduced from steady-state ion fluxes. More recently, transient experiments were done by Neben *et al.* [40], [41] using pulsed sputtering [79] as the injection method. Here, the authors approximated the plasma charge state distribution as sharply peaked around a given charge state q, so that ion densities for charge states $q' > q + 2$ and $q' < q - 2$ were zero. This simplifying assumption led to an exponential fitting function for the beam current transients, with the same model as in Ref. [39].

The aforementioned experimental campaigns each yielded increasingly accurate postdictions of the plasma electron density, electron temperature, plasma neutral density and ion confinement time, within the confines of the assumptions built into the data analysis models. Common to all the works mentioned is the in-built assumption, that the extracted beam current CSD (I^q) is the same as the CSD in-plasma (n^q). While the extraction current CSD provides a rough image of the plasma CSD [80], the proportionality $I^q \propto n^q / \tau_{\mathrm{conf}}^q$ should be accounted for in a precise model: It has been shown in gas-mixing effect studies that while the ion density may increase, a much smaller increase of the corresponding beam current may be observed [34] highlighting the key role played by ion confinement in HCI production; The usual assumption of a Maxwell-Boltzmann distribution for the EED is also made in each case. While it is known that the EED of the escaping electron flux is strongly non-Maxwellian [25], the actual plasma EED is hitherto unknown, and remains a possible source of systematic error; The methods also require the support plasma to remain unperturbed by the injected probe pulse, but using laser ablation and sputtering, it is not possible to precisely estimate the amount of material injected. Furthermore, the literature values of electron-impact ionization cross sections (and con-

sequently also the rate coefficients) are subject to very large uncertainties which have not been taken into consideration in as of yet any analysis.

The work presented in this thesis builds on the aforementioned works, and seeks to improve the analysis model, to minimize the method invasiveness by controlling the amount of material injected, to do away with the presupposed Maxwell-Boltzmann distributed EED and to account for the uncertainty of the cross section data. Assumptions regarding the ion confinement time and ion densities are evaded. With a parsimony of assumptions an experimental and computational procedure is developed for acquiring the characteristic times of ionization τ_{inz}^q, charge exchange τ_{cx}^q and ion confinement τ_{conf}^q for HCIs. Estimates of the electron density n_e and the average energy of the presupposed EED $\langle E_e \rangle$ are also obtained.

2 THEORETICAL FRAMEWORK

2.1 Derivation of the current balance equation

The balance equation (37) cannot be directly used to describe the extracted beam currents, as it is a model for the ion densities within the confined plasma. This section recapitulates the derivation of the corresponding equation for the beam currents, as derived in PI. The extraction current can be related to the ion density by the expression [21], [81]

$$I^q = F_B \kappa L S \frac{eqn^q}{\tau_{\mathrm{conf}}^q} \tag{65}$$

where κ is the beamline transmission efficiency [82], L is the length of the plasma chamber and S the size of the extraction aperture. We have added a constant factor F_B, which depends on the magnetic field configuration, and which determines what fraction of escaped ions ends up in the plasma volume corresponding to the extraction region. Expression (65) can be substituted into Eq. (37), and making the assumption that the constants κ, F_B, L and S are charge state independent — or at the very least they vary slowly with q — they can be divided away from the resultant equation.

The plasma length L is a constant on the order of the size of the ECR surface, but we have not determined the charge state dependencies of S, F_B, or κ. They could, in principle, be measured and accounted for in the calculations. It has been found [56], for example, that the effective size of the extraction aperture S, has a charge state dependence: For higher charge states of a given ion S is smaller, but the variation of S with q becomes less pronounced for higher charge states. This is attributed to the fact that HCIs originate closer to the chamber axis. The coefficient F_B is often taken to be $1/2$, which corresponds to symmetric magnetic mirrors and totally axial ion losses. For our experiments, the extraction mirror was typically weaker, corresponding to a larger loss cone on the extraction side of the ion source. A greater number of electrons (and ions as a consequence of ambipolar diffusion) is then lost towards the extraction, but to be precise, one should also determine what fraction of these ions ends up in a region which maps into the extraction aperture. For highly charged ions the losses are primarily along the chamber axis, as evident from the experiments in Refs. [56], [57], [59], [60].

The ion confinement time is often divided in components parallel and perpendicular to the magnetic field, so that

$$\frac{1}{\tau_{\mathrm{conf}}} = \frac{1}{\tau_\parallel} + \frac{1}{\tau_\perp}, \tag{66}$$

where the confinement times $\tau_\parallel$ and $\tau_\perp$ characterize the probability for ions to be lost from the plasma either along or across magnetic field lines, respectively. It has been shown [83], [84] that ions are lost primarily along the magnetic field, i.e. that $\tau_\perp \gg \tau_\parallel$. The confinement time is then closely approximated by the parallel component.

With the definitions

$$a_q = n_e \langle \sigma v \rangle^{\text{inz}}_{q-1 \to q} \frac{q}{q-1} \frac{\tau^{q-1}_{\text{conf}}}{\tau^q_{\text{conf}}} \tag{67}$$

$$b_q = \left(n_e \langle \sigma v \rangle^{\text{inz}}_{q \to q+1} + n_0 \langle \sigma v \rangle^{\text{cx}}_{q \to q-1} + 1/\tau^q_{\text{conf}} \right) \tag{68}$$

$$c_q = n_0 \langle \sigma v \rangle^{\text{cx}}_{q+1 \to q} \frac{q}{q+1} \frac{\tau^{q+1}_{\text{conf}}}{\tau^q_{\text{conf}}} \tag{69}$$

we obtain for the beam currents

$$\frac{\mathrm{d}I^q}{\mathrm{d}t} = a_q I^{q-1} - b_q I^q + c_q I^{q+1}, \tag{70}$$

which we dub the "current balance equation." Given an unperturbed plasma (i.e. constant $\langle E_e \rangle$, n_e, n_0), Eq. (70) can be used to model the time evolution of the extracted beam currents. The coefficients a_q, b_q and c_q can be considered constant and be determined by fitting Eq. (70) to experimentally measured beam current transients. The fitting procedure will be detailed in Section 4.

2.2 Deconvolution of the characteristic times

By algebraic manipulation of Eqs. (67), (68) and (69) one can obtain an expression depending only on n_e and $\langle E_e \rangle$ and the parameters a_q, b_q and c_q:

$$\frac{q}{q+1} \frac{a_{q+1}}{n_e \langle \sigma v \rangle^{\text{inz}}_{q \to q+1}}$$
$$= \frac{b_{q+1} - n_e \langle \sigma v \rangle^{\text{inz}}_{q+1 \to q+2} - \frac{a_{q+1} c_q}{n_e \langle \sigma v \rangle^{\text{inz}}_{q \to q+1}}}{b_q - n_e \langle \sigma v \rangle^{\text{inz}}_{q \to q+1} - \frac{a_q c_{q-1}}{n_e \langle \sigma v \rangle^{\text{inz}}_{q-1 \to q}}} \tag{71}$$

where the $\langle E_e \rangle$ dependence arises through the ionization rate coefficients. Equation (71) has an infinitude of solutions, but the set of solutions can be constrained on physical grounds by limiting the n_e and $\langle E_e \rangle$ ranges to those plausible to be found within the ECRIS.

Using the solutions of Eq. (71) the confinement time can be solved from:

$$\tau^q_{\text{conf}} = \left(b_q - n_e \langle \sigma v \rangle^{\text{inz}}_{q \to q+1} - \frac{a_q c_{q-1}}{n_e \langle \sigma v \rangle^{\text{inz}}_{q-1 \to q}} \right)^{-1}. \tag{72}$$

The charge exchange time can be computed using

$$\tau^q_{\text{cx}} = \left[n_0 \langle \sigma v \rangle^{\text{cx}}_{q \to q-1} \right]^{-1} = \left(b_q - n_e \langle \sigma v \rangle^{\text{inz}}_{q \to q+1} - 1/\tau^q_{\text{conf}} \right)^{-1} \tag{73}$$

And the ionization time can be computed using the n_e and $\langle E_e \rangle$ values from the definition

$$\tau^q_{\text{inz}} = \left[n_e \langle \sigma v \rangle^{\text{inz}}_{q \to q+1} \right]^{-1} \tag{74}$$

3 EXPERIMENTAL METHODS

The CT-method requires pulsed material injection into the plasma of a charge breeder. The amount of material injected during a pulse should be controlled as best as possible and minimized to avoid perturbing the support plasma. The plasma needs to be allowed to relax between pulses, erasing the history of the material injection. These conditions were met by employing square 1+ injection pulses with pulse widths less than 10 ms, 1 Hz repetition rates, and rise and fall times of 2 μs and 60 μs, respectively, in Publications PI–PV. Nevertheless, the support plasma perturbation should be evaluated separately for each experimental campaign. We used the evolution of the support plasma CSD under continuous injection mode (in particular the intensities of the high charge states) as a measure of the support plasma perturbation. As an example, in PI the extraction currents of high charge states of oxygen — found as an impurity in the support plasma — dropped by < -5.4 % when K^+ was injected in continuous mode at an intensity of 740 nA. As a consequence we inferred in PI that the effect of 5 ms injection pulses at this intensity was negligible. The effects of varying the pulse width were found to be small compared to other uncertainty sources up to 100 ms in PIV.

The charge breeder should be prepared with a low Z support plasma such as helium or hydrogen, and having as few impurities as possible, to avoid q/m overlaps between the support plasma and the injected species. This is because the method requires at least five consecutive charge states' extraction current transients to be measured (which yields characteristic time data for three charge states), and overlaps with the support plasma may cause unwanted modifications of the transient shape, corrupting the measurement. This condition for the support gas may be relaxed if the transients can be separated with enough resolution, for example using a high resolution dipole magnet or time of flight separation. As the model developed in Section 2 does not incorporate fly-through and in-flight ionized ions, which are not captured by the support plasma, the lowest charge states ($q = 1+, 2+, 3+$) should be neglected. A metallic element should be used to minimize wall recycling effects, which are also not included in the analysis model.

3.1 Material injection

Different injection methods may be used to inject a square material pulse into the ECRIS. At least sputtering, laser ablation and 1+ injection have been used in previous transient experiments [38]–[41]. In our setup 1+ injection was the natural choice as it pre-existed as part of the LPSC test bench, which was used for the experimental campaigns of this thesis. The test bench will be described in more detail in Section 3.2. 1+ injection also happens to be the most advantageous out of the three in terms of its non-invasiveness. It is also the injection method which is relevant for charge breeding of RIBs and hence the natural choice for a diagnostic method in this context.

A key benefit of the 1+ injection method is that it allows the precise measurement of the injected beam intensity, i.e. it allows the user to determine the amount of material

injected into the source. This is a great advantage of 1+ injection compared to, for example, sputtering or laser ablation which are methods used to inject neutral metallic atoms into the support plasma. Sputtering [79] is achieved by inserting a metallic probe biased to a negative voltage near the plasma periphery. The probe will then attract positive ions, which collide with the probe causing probe material to be sputtered into the plasma. In laser ablation [77], a laser beam is used to heat a metallic element and to evaporate the target material which passes into the plasma. In either case it is not possible to precisely control the amount of material injected into the plasma. If, however, the experimenter is assured that the perturbation on the plasma is minimal there is no reason to rule out either as a viable injection method.

In the case of sputtering one must also take into account the perturbation on the plasma due to the electric field of the negatively biased probe. To mitigate the perturbation of the support plasma, one could try using amplitude modulation of the material injection pulse: The experiment is set up otherwise as usual, but material injection is sustained in a continuous mode at an amplitude A_0. The pulsing is then realized as a small square-mode perturbation $\Delta A(t)$ on top of A_0, so that $A(t) = A_0 + \Delta A(t)$. This technique is applicable at least in the case of sputtering and 1+ injection [73], but possibly laser ablation as well. For 1+ injection the amplitude modulation can be realized by using electrostatic deflectors to deflect the 1+ beam only slightly off axis (A_0) in the continuous injection mode, and to pulse the beam by returning it onto the axis ($\Delta A(t)$).

Charge breeder ECRISs are built to accommodate 1+ injection [85], [86] as a part of their normal functioning. For charge breeding purposes, a (radioactive) beam of singly charged ions is generally produced through in flight separation or isotope separation on-line methods. Usually the viability of these beams is tested — and research and development of charge breeders is conducted — on a test bench, where stable isotopes are used as proxies for the radioactive species (e.g. K^{39} in place of K^{38}). These proxy beams may be produced for example via thermal emission from a pellet containing the desired isotope, followed by surface ionization [87].

A composite pellet may be desired if no-stop injection of multiple ion species is required, as in the case of PII. Using such a pellet, the desired ion species (e.g. K/Na) may be selected using the 1+ dipole magnet without having to switch off the charge breeder in between, as would be the case if a single component pellet were used. This enables probing the same plasma using multiple ion species without having to worry about finding precisely the same source tune after switching off the plasma — most often a hopeless endeavor due to the internal uncertainties associated with the operating parameters of the ion source. Although the CT-method probes the properties of the support plasma, the probe species have different electron shell configurations which allowed us to decrease the uncertainty of the CT-method results in Ref. [II], using multi-species injection, as discussed in Section 5.

The 1+ beam is stopped and captured by the plasma potential [88] of the support plasma, where they become ionized through the process described in Section 1. The singly charged particle needs to be injected into the plasma with a kinetic energy on the order of the plasma potential to achieve optimum deceleration and capture. For this purpose, the ECRIS is biased to a potential $V - \Delta V$ (with respect to ground), where V is the high voltage of the ECRIS and ΔV is on the order of ϕ. The plasma potential ϕ and, hence,

the optimum value of ΔV depends on the source tune, and it is adjusted on a case-by-case basis so that maximum capture efficiency is achieved. The slowed down ions may then be further slowed by collisions with the support plasma ions until they are captured in the potential dip in the plasma core.

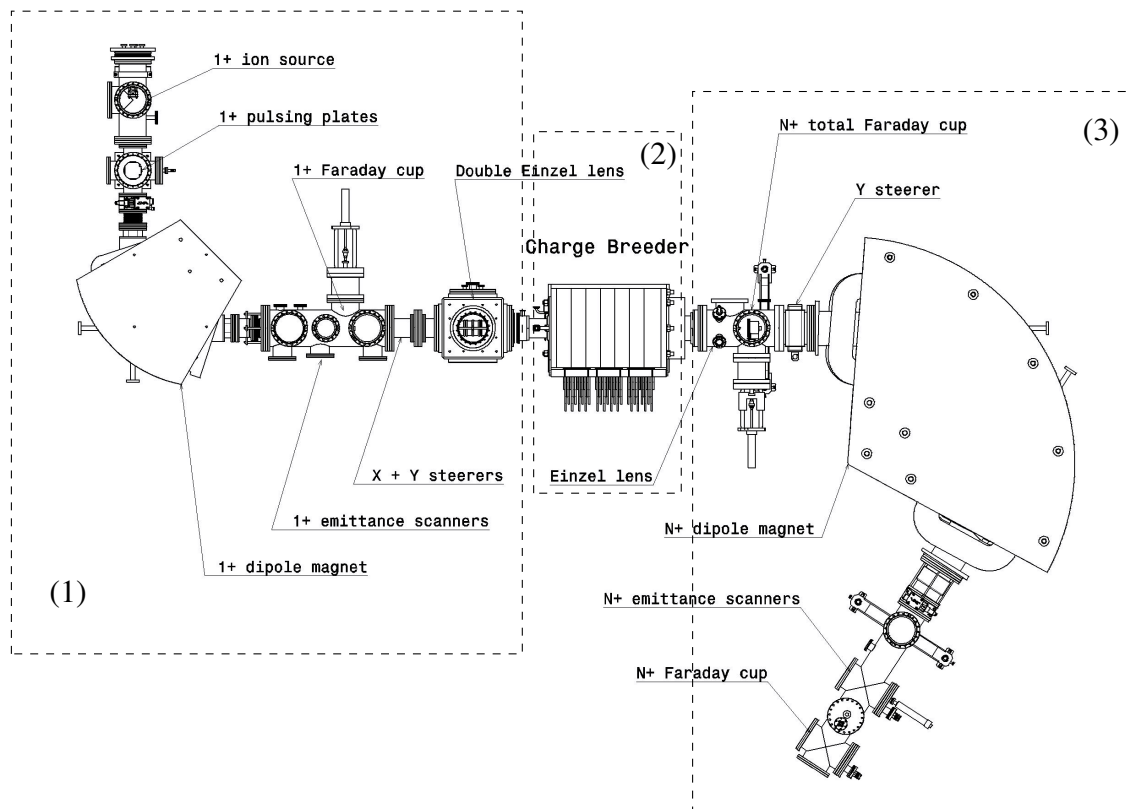## 3.2 The LPSC test bench configuration

FIGURE 10   The LPSC 14.5 GHz CB-ECRIS test bench.

Figure 10 shows a blueprint of the charge breeding beamline of the LPSC 14.5 GHz CB-ECRIS test bench [73], [74]. The setup can be divided in three parts: (1) The beamline upstream of the charge breeder, (2) the charge breeder itself, and (3) the beamline downstream of the charge breeder.

Upstream

Starting from the upstream direction from the Charge Breeder (upper left in Fig. 10), the 1+ ion source (Heat Wave Labs ion gun [87]) is used to generate the beam of singly charged ions to be charge bred in the CB-ECRIS. The 1+ pulsing plates consist of a pair of electrostatic deflectors, which enable the redirection of the singly charged ion beam to a beam dump by means of a high voltage. The 1+ dipole magnet is used to purify the 1+ beam of any higher charge states or impurities according to the q/m-ratio of the particles.

TABLE 1   Typical operating parameter values for the charge breeder. The magnetic field values at ion source injection, the minimum-B, and extraction (B_{inj}, B_{min}, B_{ext}, respectively); A typical microwave heating power (heating frequency 14.5 GHz); Support gas species; Background vacuum pressure in the source injection region without plasma (P_{inj}); The accelerating high voltage, i.e. the ion source bias; and the ΔV value. The tabulated values are directive and do not correspond to any of the experimental campaigns.

Parameter	value
B_{inj} (T)	1.58
B_{min} (T)	0.45
B_{ext} (T)	0.83
Microwave power (W)	500
Support gas species	He/H_2
P_{inj} ($\times 10^{-8}$ mbar)	10
Accelerating high voltage (kV)	20
ΔV (V)	-4

After the dipole magnet, there are the 1+ emittance scanners and the 1+ Faraday Cup (FC), which enable the measurement of the emittance and current of the 1+ ion beam, respectively. The X+Y steerers (electromagnets) are used to deflect the beam in the X and Y directions transverse to the beamline axis. The double Einzel lens is used for focusing the beam before injection into the Charge Breeder. These ion optical elements are used to optimize the 1+ beam for injection into the CB-ECRIS.

The Charge Breeder

At the time of the experiments, the LPSC 14 GHz PHOENIX-type charge breeder was based on a conventional, room-temperature ECRIS. Its hexapole magnet had a radial magnetic field of 0.8 T on the magnetic poles at the plasma chamber wall, when the solenoids were not energized, and a soft iron plug was installed in the injection end of the source (under vacuum) providing increased axial magnetic field intensity [89]. The charge breeder had a three coil configuration (injection, middle, and extraction coils), which enabled the variation of B_{inj}, B_{min}, and B_{ext} almost independently. The source had an 8 mm diameter plasma electrode aperture, and the background vacuum pressure at injection was measured to be 2.5×10^{-8} mbar. High 1+ capture efficiencies of 50 % – 60 % have been reported for the source [82], [87]. Global charge breeding efficiencies of 41.8 %, and 62.7 % (corresponding to K^{9+} efficiencies of 8.9 % and 20.4 %, respectively) were obtained depending on the source tuning and conditioning in PI, and PII. Typical accelerating high voltage for the charge breeder was around 20 kV. The plasma was heated with 14.5 GHz microwaves from a Klystron using direct waveguide injection. Typical source operating parameters are tabulated in Table 1.

Downstream

Downstream of the Charge Breeder, there is another Einzel lens for focusing the extracted ion beam. The N+ FC allows the measurement of the total (i.e. not q/m-separated) extracted beam current and the Y steerer can be used to steer the beam in the Y-direction, and match it for injection into the N+ dipole magnet. The N+ dipole is used to mass analyze the extracted ion beam, and select the desired ion species based on the q/m-ratio. Finally, the N+ emittance scanners and FC allow the determination of the emittance and measurement of the current of the charge bred ion beam, respectively.

4 THE COMPUTATIONAL PROCEDURE

Based on the theoretical framework in Section 2, we developed a set of analysis and post-processing routines which were used in the analysis of the experimental data of the Publications PI–PV. These routines form the numerical tool "CT-analyzer," which is openly available at https://github.com/misapema-jyfl/ct-analyzer.

Figure 11 depicts the workflow of the CT-analyzer. The input data are fed to the data parsing module, which parses the 1+ and N+ signals to a form expected by the next module. The RK4 fitting script fits Eq. (70) to the transient time series, and produces as its output the parameters a_q, b_q and c_q. These are then passed to the electron density and energy optimization module whose outputs are the n_e, $\langle E_e \rangle$ solution sets and the corresponding characteristic times τ_{conf}^q, τ_{inz}^q, and τ_{cx}^q. The process is governed by the parameters.yaml file, and the results are collected in csv files. A separate plotting routine produces heatmaps of the solution sets, and plots of the characteristic times as a function of charge state. Another post-processing routine can be used to take multiple solution set outputs and compute the results within their mutual overlap.

This section outlines the main components of the CT-analyzer: Parsing of the input data; fitting of the current balance equation to the measured transient time series; optimization of the $\langle E_e \rangle$ and n_e values; and the solution set overlap method of PIII.
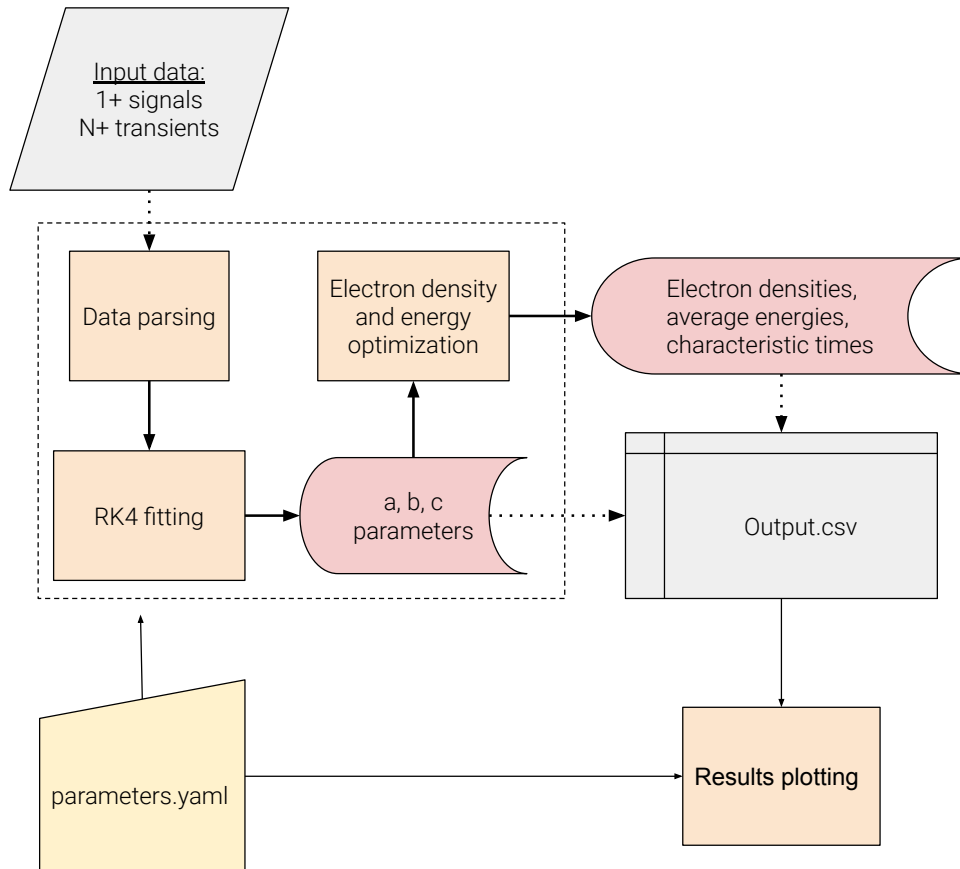

FIGURE 11   The CT-analyzer workflow.

4.1 Data parsing

The data is first parsed to a format which is acceptable for the code. The code expects as unparsed input both an N+ time series and the corresponding 1+ injection pulse signal (or the equivalent for any other material injection pulse). An example is given in Fig. 12. The measurement of the two signals must be concurrent, and they must begin from a certain zero current/voltage (for the N+ time series this corresponds to a quiescent plasma) and the N+ current must be allowed to fully decay to the same background value so that the fits can be made to the complete transient. The parsing routine removes background offset from the N+ time series (if any), and determines the signal noise level without the 1+ injection. A short amount of background current needs to be measured prior to the onset of the 1+ signal for noise determination. A square 1+ pulse is expected.

4.2 RK4 fitting

The coefficients a_q, b_q and c_q are determined by fitting the beam current transients according to Eq. (70). The solution $\mathcal{I}^q$ to the differential equation is computed by a fourth order Runge-Kutta method, so that the beam currents $I^{q-1}(t)$ and $I^{q+1}(t)$ are taken as input. The correct parameters a_q, b_q and c_q minimize the difference between the measured time series $I^q(t)$ and the solution of Eq. (70), $\mathcal{I}^q(t)$. Python's `scipy.optimize.curve_fit` function is used for the fitting with the Trust Region Reflective algorithm, as it supports passing bounds to the parameters — allowing us to constrain the parameters a_q, b_q and c_q to take only positive, i.e. physical values. The goodness-of-fit is quantified by computing the reduced χ^2 value

$$\chi_r^2 = \left(\frac{I^q - \mathcal{I}^q}{\sigma} \right)^2 / (N - 3) \tag{75}$$

where the uncertainty σ is taken to be the noise on top of the time series, determined with 1+ injection off, and N is the number of datapoints in the time series. Typically the χ_r^2 is close to one (indicating a good fit), but the best way to determine the goodness-of-fit is by visual evaluation (i.e. eyeballing). The produced fits are typically very good, but especially for high charge states, for which the signal-to-noise ratio may be very poor, there may be either overshoot or undershoot in the fits. In such a case one may try to apply a Gaussian filter on the input data in an attempt to rectify the fits, it is best way to attempt to improve the signal-to-noise ratio during the experiment — e.g. by taking averages over multiple waveforms, or by increasing the 1+ injection intensity. In our experiments we mitigated the effects of noise by taking waveform averages over 64 waveforms. A representative sample fit is shown in Fig. 12.
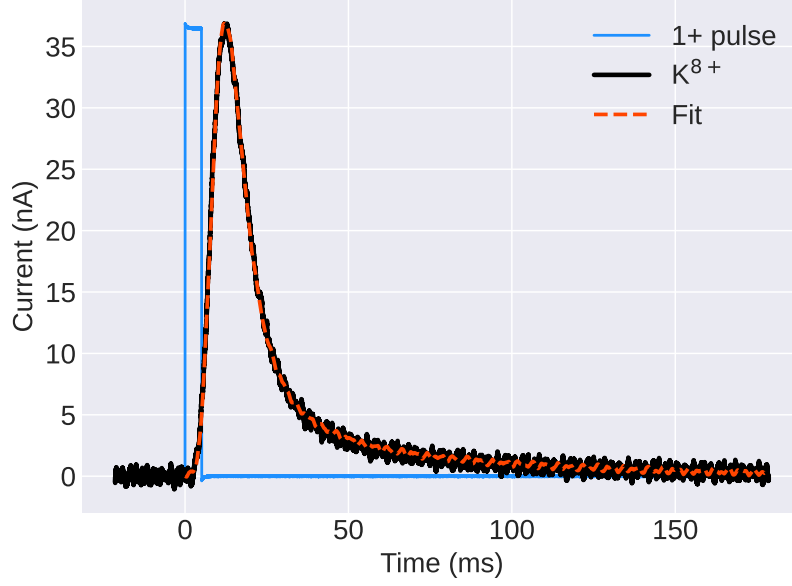
FIGURE 12   A sample input time series of K^{8+} and the corresponding 1+ pulse. The 1+ signal is in arbitrary units, and the fit is produced with the RK4 method.

4.3 Electron density and average energy optimization

The electron density n_e and average energy optimization is done by taking the expression in Eq. (71) and defining a penalty function

$$
F \equiv \left| \frac{q}{q+1} \frac{a_{q+1}}{n_e \langle \sigma v \rangle^{\text{inz}}_{q \to q+1}} \right.
$$

$$
\left. - \frac{b_{q+1} - n_e \langle \sigma v \rangle^{\text{inz}}_{q+1 \to q+2} - \frac{a_{q+1} c_q}{n_e \langle \sigma v \rangle^{\text{inz}}_{q \to q+1}}}{b_q - n_e \langle \sigma v \rangle^{\text{inz}}_{q \to q+1} - \frac{a_q c_{q-1}}{n_e \langle \sigma v \rangle^{\text{inz}}_{q-1 \to q}}} \right| \Bigg/ \tag{76}
$$

$$
\frac{q}{q+1} \frac{a_{q+1}}{n_e \langle \sigma v \rangle^{\text{inz}}_{q \to q+1}}.
$$

As the function (76) has an infinitude of roots, we will obtain a set of solutions $(\langle E_e \rangle , n_e)$ which are consistent with the parameters a_q, b_q and c_q. This set can be constrained on physical grounds by limiting the $(\langle E_e \rangle , n_e)$ ranges to those which can reasonably be expected to occur in an ECRIS.

In PI we argued that the lower limit for the density can be estimated based on the results from 1+ stopping experiments [69] conducted on the same charge breeder which was the workhorse of the experimental campaigns pertaining to this thesis. A conservative lower limit estimate[1] based on those results was chosen to be 1×10^{11} cm^{-3}. The upper limit can be taken to be the critical density (see Eq. (5)) which for 14.5 GHz microwaves is

---

[1]   Performing the 1+ stopping experiment in conjunction with the CT-method experiments could provide a more precise, narrower solution set, which could improve the precision of the characteristic time results.

2.6×10^{12} cm^{-3}. For the lower limit of the average energy of the EED, we choose 10 eV based on the order of magnitude of the plasma potential [64]. The upper limit of 10 keV was set according to Ref. [90]. Within these bounds, we select a dense, logspaced array (1000 elements) of n_e values, and iteratively seek the minimum of the penalty function as a function of $\langle E_e \rangle$. All found $(\langle E_e \rangle, n_e)$- points corresponding to penalty function minima are collected.

Monte Carlo method for the uncertainty

Experimental measurements of ionization cross sections are conducted e.g. using the method of intersecting beams [91]. As a consequence of e.g. low signal to noise ratios [92], some of the currently available experimental cross section data have considerable relative uncertainty associated with it — this is particularly true for higher charge states and near to electron shell closures — for example in Ref. [47] a 200 % relative uncertainty is given for the ionization process

$$e^- + K^{8+} \rightarrow K^{9+} + 2e^-,$$
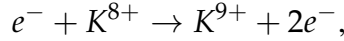
which proceeds from the closed electron shell of K^{8+}. We employ the semi-empirical formula introduced in Ref. [92] and data from Ref. [47] to compute the ionization cross section. The effects of this uncertainty on the CT-method results are studied in PIII.

We use a Monte Carlo method to sample the experimental uncertainties. In the beginning of the $(\langle E_e \rangle, n_e)$ optimization, we generate a set of bias coefficients whose values are within the experimental uncertainties, and apply this bias to the rate coefficients so that

$$\langle \sigma v \rangle^{\text{inz}}_{q \rightarrow q+1} \rightarrow \langle \sigma v \rangle^{\text{inz}}_{q \rightarrow q+1} \times (1 + \mathcal{B}_q) \tag{77}$$

where $\mathcal{B}^q$ is the bias coefficient. The random variable $\mathcal{B}_q$ is chosen from a uniform distribution within the experimental uncertainty bounds reported for $\delta\sigma^{\text{inz}}_{q \rightarrow q+1}$, i.e. $\mathcal{B}_q \sim U(-\delta\sigma, \delta\sigma)$. We then carry out the aforementioned minimization process for the penalty function with all the generated biases (1000 samples adequately covers the uncertainty space). In addition, to better cover the $(\langle E_e \rangle, n_e)$ space, at the beginning of each Monte Carlo iteration we also displace the elements in the n_e array by small random amounts, so that no two iterations use precisely the same array, resulting in fewer gaps in the solution set.

Usual solution sets have $\sim 10^4$ $(\langle E_e \rangle, n_e)$ pairs. Within this set, we choose an upper limit for the penalty function F_{upper} so that the number of solutions satisfying $F < F_{\text{upper}}$ is on the order of thousands. Typically we can set $F_{\text{upper}} = 1 \times 10^{-6}$ or better. An example solution set is shown in Fig. 13. The heat map is produced by counting the number of solutions falling into each bin of a 200×200 logspaced grid, and normalizing to the maximum number. The $\langle E_e \rangle$ and n_e distributions have been projected onto the x and y margins of the Figure, respectively.

Characteristic time computation

Within the obtained $(\langle E_e \rangle, n_e)$ set we compute the characteristic times of ionization, charge exchange and confinement according to Equations (72), (73), and (74). We
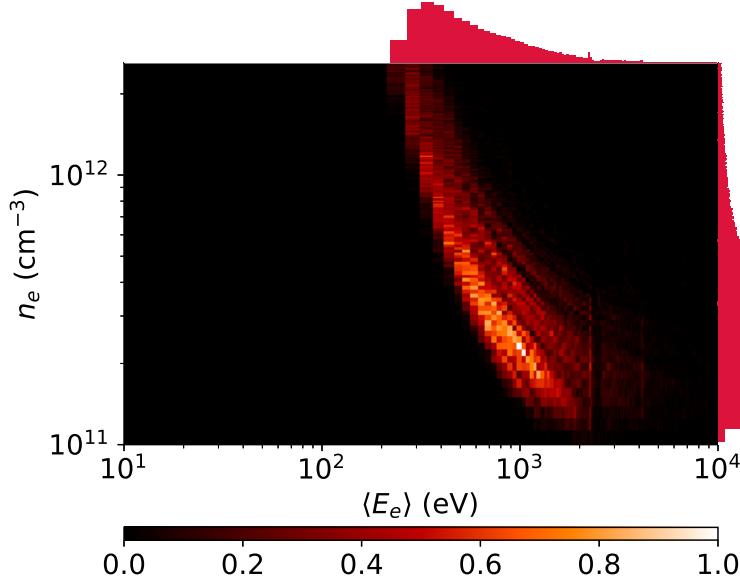
FIGURE 13 An example heat map of an $(\langle E_e \rangle, n_e)$ solution set obtained for K^{9+} through the penalty function minimization. The normalization is done to the maximum density. The $\langle E_e \rangle$ and n_e distributions are projected onto the appropriate margins.

then require their values to satisfy

$$
\begin{cases}
\tau_{\text{conf}}^q & > 0, \\
\tau_{\text{inz}}^q & > 0, \quad \text{and} \\
\tau_{\text{cx}}^q & > 0
\end{cases}
\tag{78}
$$

while negative solutions are discarded.

This computation yields a distribution of solutions for each characteristic time, an example of which is shown for the confinement time of $^{41}K^{9+}$ in the experimental campaign of Ref. [93]. Due to the asymmetry typical for the distributions, we have adopted the following convention for expressing our results: The median (represented by the solid red line in Fig. 14) is taken as the data point τ, while the asymmetric uncertainty is quantified by the upper and lower bounds (dashed red lines in Fig. 14) which enclose 34.1 % of all solutions in the distributions, respectively. Altogether the upper and lower bounds thus contain 68.2 % of all solutions, similar to the standard deviation of a Gaussian distribution.

To make the minimization process computationally more efficient, the rate coefficients of electron-impact ionization are computed beforehand as functions of $\langle E_e \rangle$, and interpolation functions are used in their place. Figure 15 illustrates this for K^{8+}. In subfigure (a) the cross section for ionization from 8+ to 9+ ($\sigma_{8+\to9+}^{\text{inz}}$) is plotted with the Maxwell-Boltzmann distribution (g_{MB}) with $\langle E_e \rangle = 1000$ eV. The corresponding rate coefficient $\langle \sigma v \rangle_{8+\to9+}^{\text{inz}}$ is the area under the curve $g_{\text{MB}}\sigma_{8+\to9+}^{\text{inz}}v$ (a function of speed/energy) shown in blue. This process is repeated for a multitude g_{MB} with varying $\langle E_e \rangle$, a selection of which is scatter plotted in subfigure (b). An interpolation function is generated from these points (crimson line). The interpolation function can then be used
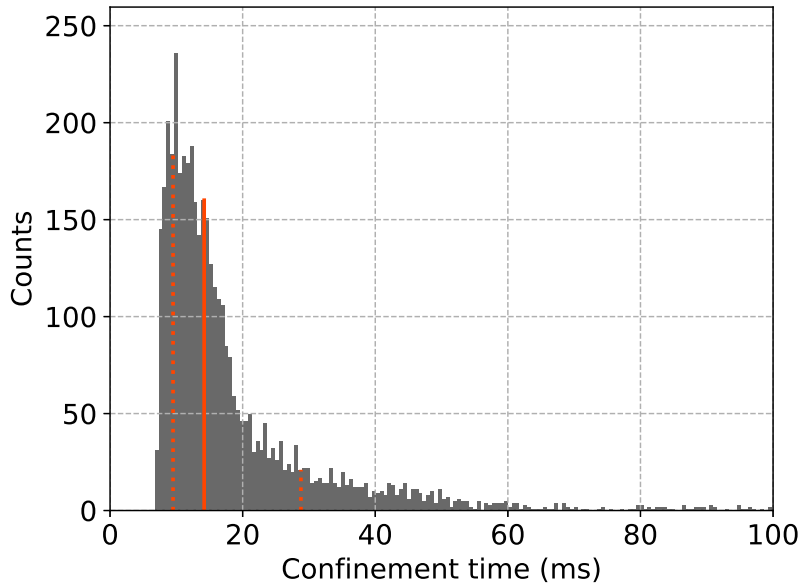
FIGURE 14   An example distribution for the confinement time of $^{41}\text{K}^{9+}$. Reproduced with permission from PIII, Copyright © 2022 American Physical Society.

in the numerical analysis to quickly evaluate $\langle\sigma v\rangle^{\text{inz}}_{8+\to 9+}$ as a function of $\langle E_e\rangle$. Similar interpolation functions are generated for all charge states.

4.4   Solution set overlap

The solution sets obtained for different ion populations (species and/or charge state) from the optimization procedure for n_e and $\langle E_e\rangle$ can be multiplied together to obtain their mutual overlap. This was utilized in Publication PIII: Singly charged potassium and sodium were injected into a support plasma upheld in a CB-ECRIS by heating a two-component pellet at the 1+ ion source. The resultant time series were analyzed with the CT method and overlaps of the ($\langle E_e\rangle$, n_e) solution sets were taken for the high charge states of the two species. Overlapping the solution sets is justified if/when the ion populations in question can be argued to originate from the same region of the plasma, i.e that they experience a plasma with the same n_e and $\langle E_e\rangle$.

An example of the overlap technique is given in Fig. 23. Subfigure (a) shows the outer borders of the solution sets of K^{9+}, K^{10+} and Na^{7+}. Multiplying these solution sets yields the overlap, the heat map of which is shown in subfigure (b). In this case, the much smaller solution set of Na^{7+} greatly reduces the number of valid solutions obtained using potassium only.

Taking the overlap generally reduces the uncertainty bounds of the resultant n_e, $\langle E_e\rangle$ and characteristic time values. In case of two component injection it allows one to circumvent some of the experimental uncertainty of $\sigma^{\text{inz}}_{q\to q+1}$, as the two different species will have different ionization cross sections — owing to their differing electron configurations.
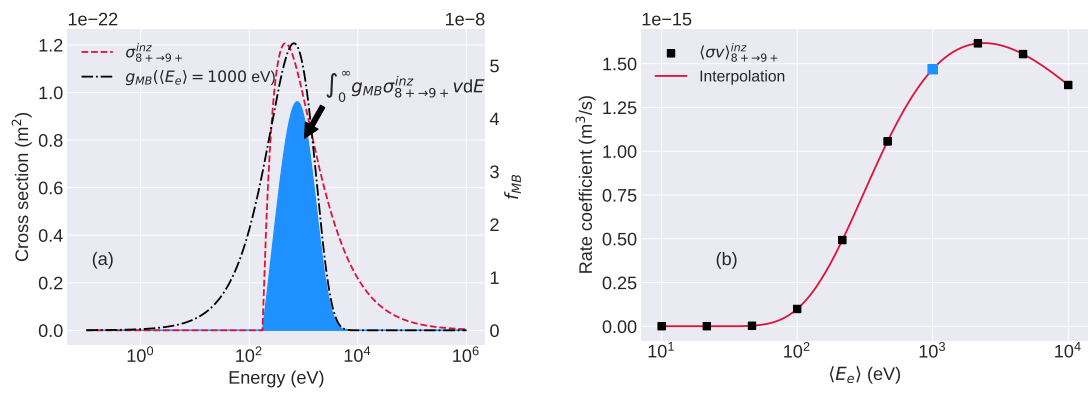
FIGURE 15   Example of calculating an interpolation function for the rate coefficient of elec-
tron impact ionization of K^{8+}. In (a) the Maxwell-Boltzmann distribution ($\langle E_e \rangle =$
1000 eV) is plotted with the electron-impact ionization cross section. The blue
filled area corresponds to the rate coefficient, also highlighted as the blue marker in
(b). The rate coefficient and an interpolation are plotted as functions of $\langle E_e \rangle$ in (b).

5 EXPERIMENTAL CAMPAIGNS AND RESULTS

The ion production process is governed by the balance equation (37), which in the case of RIBs is amended by an extra term to account for the nuclear decay:

$$
\begin{aligned}
\frac{\mathrm{d}n^q}{\mathrm{d}t} = {} & n_e \left\langle \sigma v \right\rangle^{\mathrm{inz}}_{q-1 \to q} n^{q-1} - n_e \left\langle \sigma v \right\rangle^{\mathrm{inz}}_{q \to q+1} n^q \\
& n_0 \left\langle \sigma v \right\rangle^{\mathrm{cx}}_{q+1 \to q} n^{q+1} - n_0 \left\langle \sigma v \right\rangle^{\mathrm{cx}}_{q \to q-1} n^q \qquad \forall q \in \{0,1,2,\ldots,Z\} \\
& - \frac{n^q}{\tau^q_{\mathrm{conf}}} - \frac{n^q}{\tau_{\mathrm{decay}}},
\end{aligned}
\tag{79}
$$

where the decay time τ_{decay} is related to the half-life $T_{1/2}$ by $\tau_{\mathrm{decay}} = T_{1/2} / \ln(2)$. To precisely estimate the beam current of the RIB by means of a proxy, the balance equation needs to be solved as a function of time. This necessitates the characteristic times of ionization, charge exchange and ion confinement to be determined. For the solution of Eq. (79), then, the characteristic times for the radioactive ion would be presumed to be those of the proxy isotope: E.g. tuning the CB-ECRIS for optimum production of $^{39}\mathrm{K}^{q+}$, and estimating the attainable extraction beam current of $^{52}\mathrm{K}^{q+}$, which is unstable with a half-life of 110 ms. This procedure would not only facilitate the source tuning, but save costs as well, since the radioisotopes can be expensive to produce.

Another benefit obtained from a knowledge of the characteristic times is the potential to identify bottlenecks in the ion production chain, which can serve as a guide for the future development of the ion source. As an example, both a large charge exchange rate and a small ionization rate may cause inefficient ion production, but cures to these problems are different: Ionization can be boosted by increasing n_e, and possibly $\langle E_e \rangle$; Charge exchange, on the other hand, can be mitigated by decreasing the neutral density or changing the support gas species to one with a greater ionization potential. The confinement time also plays a critical role in ion production because it governs the rate at which ions become available for beam formation. Optimization of the confinement properties, too, is dependent on our ability to measure the confinement time.

We present here results from five experimental campaigns which were undertaken to develop and test such a method. First, in Section 5.1 we discuss the development of the CT-method in Publication PI. Second, the uncertainty sources investigated in PIV are discussed in Section 5.2. Third, in Section 5.3 we present results from the campaign presented in PII, where CT-method was applied in two different configurations corresponding to distinct source tunes and differing charge breeding efficiencies. Fourth, in Section 5.4, we discuss the findings in PIII, where we studied the effects of applying the CT-method with multi-component injection. Finally, fifth, in Section 5.5 we present and discuss the parametric dependencies of the observables yielded by the CT-method in PV.

5.1 Development of the CT-method

The existing transient injection methods (discussed in Section 1.7) which probe the characteristic times were based directly on the balance equation for the ion densities in-plasma. As discussed in Section 1, the extraction beam current depends on both the ion density and the confinement time, so we introduced this relationship to the balance equation. We then realized that in order to work with the resultant coupled differential equation for the beam currents, Eq. (70), at least five consecutive beam current transients would need to be handled simultaneously to yield results for a given charge state ion population: To obtain the characteristic times, n_e and $\langle E_e \rangle$ of an ion population X^{q+} the extraction beam current transients corresponding to X^{q-2}, X^{q-1}, X^q, X^{q+1}, and X^{q+2} must be measured.

We therefore designed an experimental campaign to deliver suitable data for developing a computational method for the solution of Eq. (70) and to compute the characteristic times from the coefficients a_q, b_q, c_q (Eqs. (67), (68), (69), respectively). During this campaign the consecutive transients method was developed, and the results were published in PI.

The computational procedure was discovered through a process of trial and error. Initially, we attempted to ascribe a singular ($\langle E_e \rangle$, n_e) value to the entire plasma, but this approach failed. We found instead, that we had to allow each different charge state ion population to correspond to their own n_e and $\langle E_e \rangle$. This implied that the ion populations had sufficiently distinct spatial distributions, that each population could be assumed to originate from a region of plasma with different plasma parameters.

The spatial distributions were reflected in the resultant ($\langle E_e \rangle$, n_e)-solution sets where a drift towards higher $\langle E_e \rangle$ and n_e was observed as a function of q, as shown in Fig. 16. The finding that the ion populations and plasma conditions are spatially localized is not new. It is known, for example, that the hot electrons are well confined in the plasma core regions — as discussed in Sections 1.2 and 1.5. It was also discussed in Section 1.5 that evidence [33], [45], [56]–[62] points to the fact that higher charge state ions originate closer to the plasma chamber axis, while lower charge state ions come from the plasma periphery. In other words, HCIs accumulate in the potential dip(s) which forms as a consequence of well-confined hot electron pileup in the plasma, and lower charge state ions originate from layers which are localized radially outward from the axis — i.e. the ion populations assume a "nested-layer"-structure.

Because of this nested-layer structure — whereby the ion populations are localized to distinct plasma regions — and the fact that the ($\langle E_e \rangle$, n_e)-optimization requires data for only three neighboring charge states at a time[1], the CT-method yields results with a spatial dependency, even though it is based on a zero-dimensional model, which has been an unexpected benefit of the CT-method.

Figure 17 shows the characteristic times obtained in PI as functions of charge state q. Importantly, a charge state dependence of the confinement time was obtained without assuming one beforehand, as was necessary for the analysis in Ref. [39]. In the results

---

[1] I.e. the fitting coefficients a_q, b_q, c_q for three consecutive charge states. The five neighboring q transients are necessary to obtain said a_q, b_q, c_q.
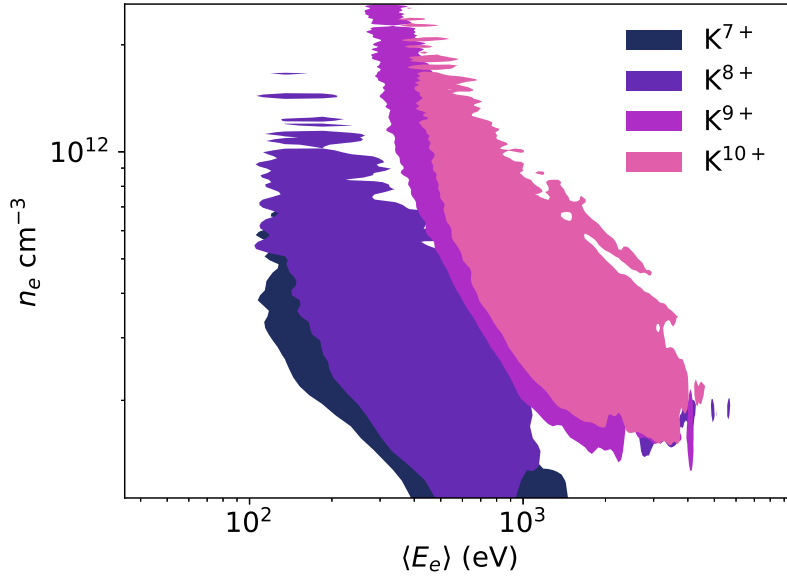
FIGURE 16   Solution sets of K^{7+}, K^{8+}, K^{9+}, K^{10+}. Adapted from PV under the license CC BY 4.0 DEED.

pertaining to PI, the confinement time seemed to obey a power law whereby $\tau^q_{\text{conf}} \propto q^{2.5}$ rather than a linear increase with q (as one might expect from ambipolar confinement, Eq. (57)).

The ionization time was seen to increase with charge state, which is to be expected since the ionization cross section diminishes with q due to the increasing ionization potential. The shell closure between K^{8+} and K^{9+} was observed in τ^q_{inz} as a distinct jump between the charge states.

For τ^q_{cx}, we got the intuitive result that for low q charge exchange plays only a small role, as evidenced by the relatively long characteristic times, $\tau^{6+}_{\text{cx}} \approx 30$ ms and $\tau^{5+}_{\text{cx}} \approx 400$ ms. A minimum of τ^q_{cx} was found around K^{8+}, i.e. the τ_{cx} increased for higher q, even though the ion-neutral charge exchange cross section increases with q. This was attributed to the decrease of neutral density due to the poor penetration of neutrals into the plasma core as evident from Ref. [45]. These findings were in agreement with the increase of the energy content $n_e \langle E_e \rangle$ as a function of q.

As evident from Fig. 17, the CT-method was found to yield considerable uncertainty estimates — in particular to the high charge states. It was surmised that this was due at least in part to the uncertainty inherited from the ionization cross sections taken from the literature. This was investigated systematically in PIV.

5.2   Method uncertainties

The CT-method relies on the primary assumption, that the balance equation (37) accurately describes the time evolution of the ion densities within the plasma. This contains of course the implicit assumption that the parameters n_e, $\langle E_e \rangle$, n_0 and τ^q_{conf} are constants
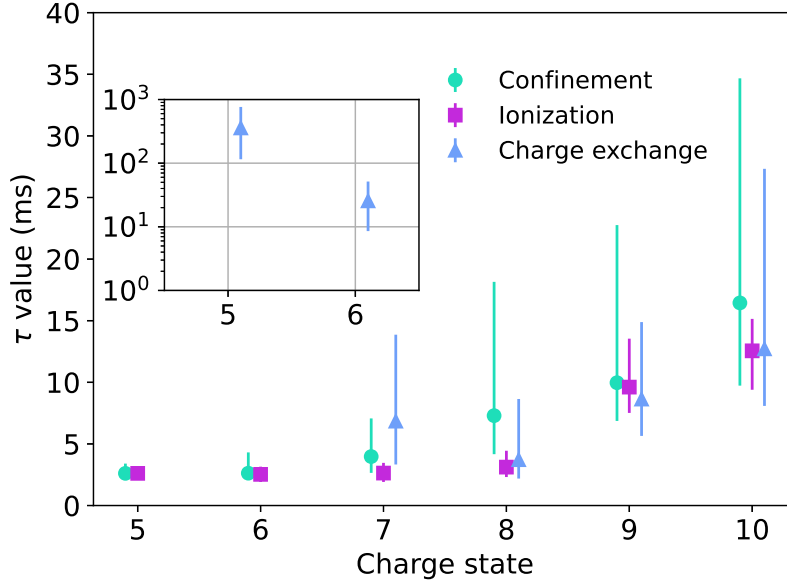
FIGURE 17   Characteristic times of ion confinement, ionization and charge exchange. Adapted with permission from PI © IOP Publishing Ltd. All rights reserved.

as a function of time. We are ensured of this by considering the electron density and EED to be fixed by the support plasma, and by making certain that the injected 1+ pulse does not cause a significant perturbation to the plasma state. These uncertainty sources are associated with the experimental setup, and need to be controlled for in conjunction with the experiments. In PIV we set out to study uncertainty arising from the analysis method itself, i.e. uncertainty inherited from adopted literature values and/or associated with assumptions made in the computations.

From the balance equation we derived the current balance equation (70) which is used for making a fit to the extracted beam current transients I^q and to obtain the fitting parameters a_q, b_q, c_q. By means of algebraic manipulation, we obtained the penalty function (76) whose solution yields a set of points $\langle E_e \rangle$ and n_e, which may be used to calculate the characteristic times.

Use of the penalty function, however, requires the evaluation of the rate coefficients $\langle \sigma v \rangle^{\mathrm{inz}}$. For this we require the ionization cross sections $\sigma^{\mathrm{inz}}_{q \to q+1}$, which we have taken from the literature in the form of the semi-empirical formula provided in Refs. [47], [92]. As stated previously these data contain in some cases significant uncertainties, which is naturally inherited by the results of the CT-method.

In the absence of more precise cross section data, we performed a hypothetical investigation in which we arbitrarily — but systematically — curtailed the $\delta\sigma^{\mathrm{inz}}_{q \to q+1}$. Assuming that the cross section uncertainty was systematic (i.e. not dependent on the relative speed v), this amounted to applying a constant bias to the rate coefficients. The uncertainty estimation is carried out using the Monte Carlo approach explained in Section 4.3, but here we adjust the procedure by adding a constant bias coefficient A_q:

$$\langle \sigma v \rangle^{\mathrm{inz}}_{q \to q+1} \to \langle \sigma v \rangle^{\mathrm{inz}}_{q \to q+1} \left(A_q + B_q \right). \tag{80}$$

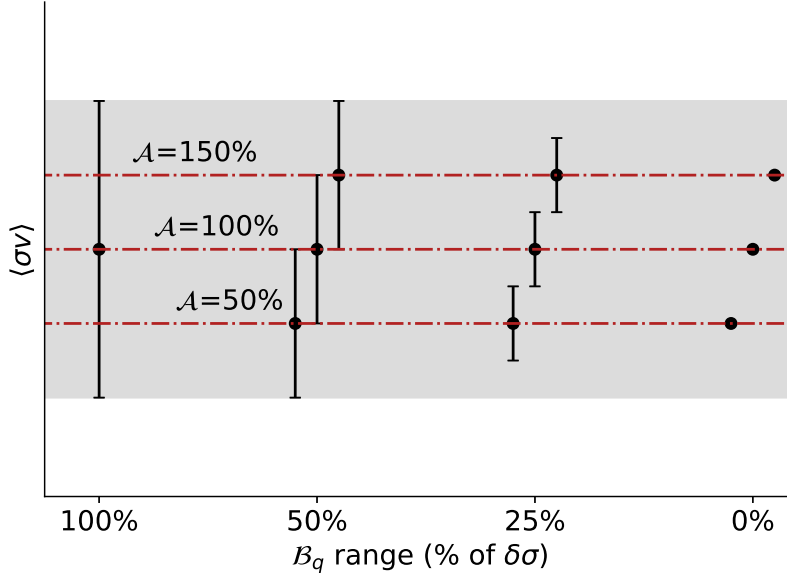Here, B_q is again selected from a uniform distribution within the uncertainty bounds re-

FIGURE 18   Example of the effect of an arbitrary curtailment of $\langle\sigma v\rangle$ as a function of B_q range for different A_q values. A_q adjusts the location of the true value of $\langle\sigma v\rangle$, while restricting B_q limits the relative uncertainty around the true value. Reprinted from PIV, with the permission of AIP Publishing.

ported for the cross section $\sigma^{\text{inz}}_{q\to q+1}$, i.e.

$$B_q \sim U(-\delta, +\delta), \tag{81}$$

but by arbitrarily curtailing δ to a chosen fraction of the true uncertainty, we were able to simulate the effect of sharper uncertainty bounds around the "true value" $\langle\sigma v\rangle^{\text{inz}}_{q\to q+1}$. The coefficient A_q on the other hand enabled us to adjust the true value itself ($A_q = 1$ and $B_q \sim U(-\delta\sigma^{\text{inz}}_{q\to q+1}, \delta\sigma^{\text{inz}}_{q\to q+1})$ corresponding, of course, to the literature values). The effect of the choice of A_q and B_q is illustrated in Fig. 18.

We also need a functional form of the EED to compute the integral in Eq. (35) which defines the rate coefficient. Many experiments [25], [30], [94], [95] have been conducted to measure the EED of the electrons escaping the plasma confinement (LEED): Directly by means of energy-resolved spectroscopy using the dipole magnet and indirectly via bremsstrahlung emissions. Through these experiments it has been found that the LEED is strongly non-Maxwellian, but the precise EED within the ECRIS plasma is as yet unknown. In particular, the EED of the strongly confined hot electron component is not known, and the traditional assumption of a Maxwellian EED could thus affect the results of the CT-method via the rate coefficients.

Thus far we had employed a Maxwellian distribution of particle speeds, but in the following analysis we implemented both a kappa distribution [96] and a double Maxwellian distribution formed as the sum of two Maxwellian functions. The kappa distribution is given by

$$g_\kappa = \frac{2v^2}{(\kappa w_\kappa^2)^{3/2}} \frac{\Gamma(\kappa + 1)}{\Gamma(\kappa - 1/2)\,\Gamma(3/2)} \left(1 + \frac{v^2}{\kappa w_\kappa^2}\right)^{-(\kappa+1)}, \tag{82}$$

where the thermal velocity

$$w_\kappa = \sqrt{\frac{(2\kappa - 3)\, kT_{eq}}{\kappa m}}, \tag{83}$$

with T_{eq} the equivalent temperature, Γ the gamma function and κ the spectral index. Decreasing the value of κ has the effect of increasing the contribution of the tail-end of the kappa-distribution to the total EED. As $\kappa \to \infty$ the kappa distribution approaches a Maxwellian.

The double Maxwellian distribution was defined as

$$g\left(v; \langle E_e \rangle\right) = n_e \left[f_c g_c \left(v; \langle E_{e,c} \rangle\right) + f_h g_h \left(v; \langle E_{e,h} \rangle\right) \right] \tag{84}$$

where g_c and g_h are Maxwellian distributions (see Eq. (6)) parametrized by the average energies $\langle E_{e,c} \rangle$, and $\langle E_{e,h} \rangle$ of the cold/warm and hot electron populations, respectively. The coefficients

$$0\,\% < f_c < 100\,\%, \qquad \text{and} \tag{85}$$

$$f_h = 100\,\% - f_c \tag{86}$$

determine the electron fractions assigned to the cold/warm populations, respectively. The average energy of the hot electron component, $\langle E_{e,h} \rangle$ is fixed while $\langle E_{e,c} \rangle$ of the cold/warm population is allowed to vary.

The kappa and double Maxwellian distributions are compared to the standard Maxwell-Boltzmann distribution as functions of electron energy in Fig. 19 (a) and (b) with different values of κ and f_h, respectively.
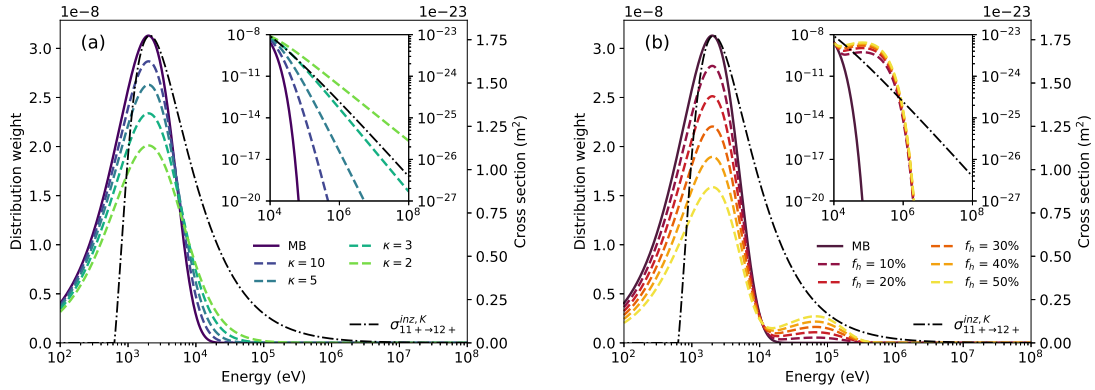

FIGURE 19   Comparisons of the Maxwell-Boltzmann distribution to the kappa (a) and double Maxwellian distribution (b) with varying spectral index and hot electron fractions, respectively. The distributions are plotted as functions of the electron energy so that the most probable energy is 2 keV. The average energy of the hot electron population in (b) is 100 keV. The insets plot the high energy tails of the distributions. The electron-impact ionization cross section of K^{11+} is plotted for reference. Reprinted from PIV, with the permission of AIP Publishing.

In Ref. [97] it was found that an abrupt, 50 % decrease in escaping electron flux results from switching off the microwave heating power. It was deduced that this occurs

because there is no more rf-induced pitch-angle scattering, which primarily affects the warm and hot electrons ($\langle E_e \rangle \in [10\,\text{keV}, 100\,\text{keV}]$. Based on this, we set as the "worst-case-scenario" that $\langle E_{e,h} \rangle = 100\,\text{keV}$, and $f_{h,\text{max}} = 50\%$, i.e. restricting $50\,\% \geq f_c$.

By computing the ionization rate coefficients using Eqs. (82) and (84) we parameterized the rate coefficients with respect to $\langle E_e \rangle$ as described in Section 4 with the simple Maxwellian distribution. We repeated the analysis using different selections of the spectral index κ and hot electron fraction f_h to obtain systematics of the variation of the results as the contribution of the high energy electrons to the EED was changed.

Since this campaign was purely data analysis, no new experimental measurements were required. The data for this campaign was taken from the experiments conducted for PI.

The effect of varying A_q and B_q on the $(\langle E_e \rangle, n_e)$-sets is shown in Fig. 20 for K^{8+}, which has the most pathological uncertainty estimate of 200 % given in the literature. Decreasing A_q causes the solution sets to drift towards higher energy and density. This is to be expected, as a smaller A_q corresponds to a lower $\langle \sigma v \rangle_{q \to q+1}^{\text{inz}}$, and a larger energy content $n_e \langle E_e \rangle$ is needed to reproduce the experimentally measured transients. When constraining the range of B_q we observe that the breadth of the solution sets is reduced. We note, however, that even a complete elimination of uncertainty (i.e. $B_q = 0\%$) will not yield a singular $(\langle E_e \rangle, n_e)$-value, which reflects the fact that the penalty function has an infinite number of solutions.

The reduction of the relative uncertainty represented by B_q is reflected also in the characteristic time values output by the CT-method. With the full literature uncertainty (and $A_q = 100\%$), the relative uncertainty of τ_{conf} for K^{8+} is 200%. With $B_q = 0\%$ this uncertainty becomes 80%. The same behavior is observed for all the characteristic times. It is noteworthy that with $A_q = 100\%, B_q \sim U(-50, 50)\%$, the uncertainty of τ_{conf} actually increases. This is probably an artifact of the artificial nature of the uncertainty curtailment: When we constrain the uncertainty, we may inadvertently focus into an inaccurate value of $\sigma_{q \to q+1}^{\text{inz}}$, which may corrupt our results. For this reason we chose to vary A_q in addition to constraining the range of B_q.

The effect of using a different EED on the $(\langle E_e \rangle, n_e)$-sets is shown for K^{9+} in Fig. 21. It can be seen that both in the case of the kappa distribution and with the double-Maxwellian EED, the greatest change occurs when the hot electron component is largest (i.e. $\kappa = 2$ and $f_h = 50\%$).

The change in the solution sets is less distinct when varying the hot electron contribution by means of the kappa distribution compared to using a double Maxwellian. This is because the contribution of the hot electron population to the total EED is greater in the latter case. When using the kappa distribution, there is no notable difference in the characteristic times. In the double Maxwellian case, as can be seen from Fig. 21 (b), with higher f_h the solution sets get "clipped" from the high density end. This is reflected to a small degree also in the confinement times of the high ($q > 8+$) charge states, which increase by as much as a factor of two. The greatest difference occurs for the confinement time of K^8 which is probably due to the fact that its solution set is the broadest (due to the large uncertainty) and consequently a larger number of $(\langle E_e \rangle, n_e)$-points get clipped from the solution set. The τ_{inz} and τ_{cx} are not likewise affected, and the overall trends
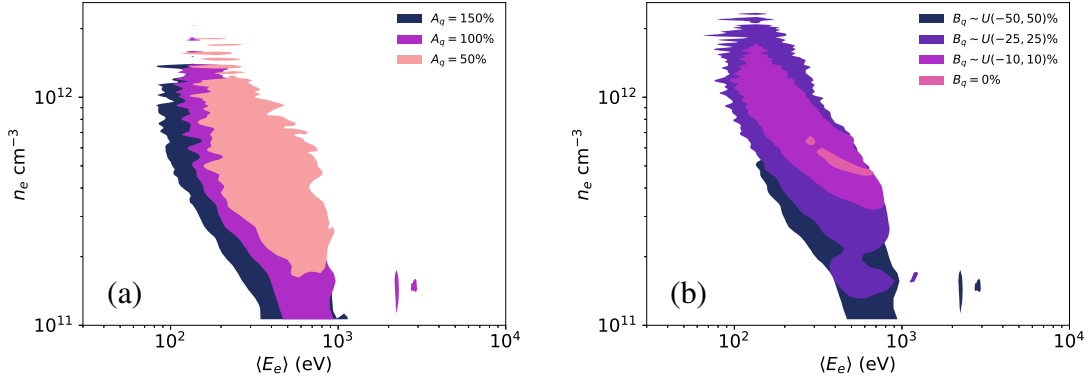
FIGURE 20   Example of the effect of varying the bias coefficients A_q and B_q for K^{8+}. In subfigure (a) the B_q is selected from $U\left(-50, +50\right)\% \times \delta\sigma^{\mathrm{inz}}_{q \to q+1}$, but the coefficient A_q varies. In subfigure (b), $A_q = 100\%$ a constant, but the range from which B_q gets sampled is varied. The range of B_q is given as a percentage of $\delta\sigma^{\mathrm{inz}}_{q \to q+1}$ reported in literature. The results are plotted as a function of $\langle E_{e,c}\rangle$. Adapted from PIV, with the permission of AIP Publishing.
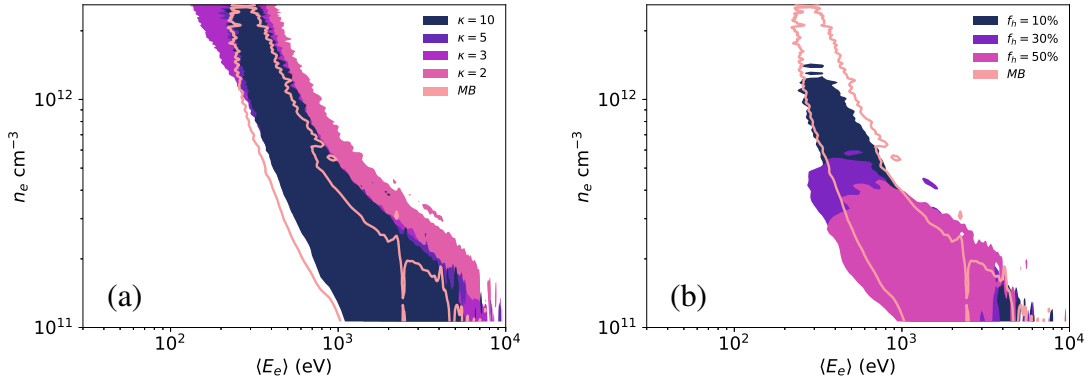
remain the same.

FIGURE 21   Example of the effect of using different presupposed EEDs for the CT-method analysis on the solution sets of K^{9+}. The solution sets for a kappa distribution with different spectral indices κ are plotted in subfigure (a), and solution sets with a double Maxwellian distribution with a varying hot electron component are plotted in (b). The results with the standard Maxwellian EED are superposed in both figures with the empty contour. Adapted from PIV, with the permission of AIP Publishing.

To see an effect in the results due to the choice of the EED, however, the size of the hot electron component needs to be at least $f_h = 10\ \%$. In lieu of precise experimental data, based on the results of Ref. [97] it seems possible that the fraction of hot electrons is as great as 50 %. Therefore, we are lead to conclude that the choice of the presupposed EED does play a role in particular for the determination of the $\left(\langle E_e\rangle, n_e\right)$ solution sets, but that the characteristic times are quite insensitive to it — at least within their admittedly considerable uncertainty bounds.

TABLE 2   Ion source operation parameters in the Former and New configurations corresponding to Publications PI and PII, respectively. PII reproduced under the license CC BY 3.0 DEED, IOP Publishing Ltd. The ΔV values have been appended to this Table.

	Configuration	
Parameter	Former	New
B_{inj} (T)	1.58	1.57
B_{min} (T)	0.45	0.44
B_{ext} (T)	0.83	0.84
Microwave power (W)	504	530
Support gas species	He	H_2
P_{inj} ($\times 10^{-8}$ mbar)	9.0	13.6
K^+ intensity (nA)	710	500
K^+ pulse width (ms)	5	5
ΔV (V)	-3.9	-4.2

We showed that an arbitrary curtailment of the uncertainty bounds can greatly decrease the uncertainty of the CT-method results. This may motivate a more precise determination of the high charge state elecron-ion impact ionization cross sections either theoretically or experimentally. To our best knowledge we have for the first time accounted for the cross section uncertainty in ECRIS plasma diagnostics, and at least in the case of the CT-method the uncertainty propagates to the results in a great degree. It may be of interest to study the effects of the uncertainty inherited by e.g. CSD simulations [61] as well as any experiments which may employ the cross sections in their analysis.

5.3 Application to different source configurations

After the experimental campaign for PI, the LPSC charge breeder tuning and conditioning were optimized. The improvements led to a K^{9+} charge breeding efficiency of 20.4 % — an increase by a factor of two compared to the previous configuration. The source operation parameters corresponding to the source configurations labeled Former (PI) and New (PII), respectively, are given in Table 2. We wanted to ascertain whether or not the method was sensitive enough to reveal differences in plasma parameters between distinct ion source tunes, despite the large result uncertainty. We applied the CT method in the New source tune to compare the plasma parameters between it and the Former operating configuration. Importantly, in the New tuning the support gas species was changed from helium to hydrogen, and the injection pressure increased from 9×10^{-8} mbar to 13.6×10^{-8} mbar (same pressure gauge calibration). Microwave power was increased from 500 W to 530 W. A slightly smaller 1+ injection intensity of 500 nA was used compared to the Former 710 nA. The ΔV was around -4 V in both cases.

The effect of the pressure gauge calibration was not taken into account in PII. The pressure readouts should be corrected so that the H_2 reading is 27.2×10^{-8} mbar and He reading 54×10^{-8} mbar. The neutral densities in these cases are (assuming an ideal gas)

TABLE 3   Table of most probable values of n_e and $\langle E_e \rangle$ between the Former (PI) and New (PII) configurations of the LPSC 14.5 GHz ECRIS. Adapted from PII under the license CC BY 3.0 DEED, IOP Publishing Ltd. The $\langle E_e \rangle$ are rounded to two significant figures for clarity.

Ion	n_e ($\times 10^{11}$ cm^{-3})		$\langle E_e \rangle$ (eV)	
	Former	New	Former	New
K^{5+}	1.0	1.0	100	130
K^{6+}	1.3	1.4	120	120
K^{7+}	1.2	1.0	160	170
K^{8+}	1.4	2.1	150	210
K^{9+}	1.0	2.6	290	360
K^{10+}	1.4	2.5	350	520

approximately the same, because the hydrogen molecules dissociate in the plasma, which doubles the corresponding neutral density.

The effect of the changed operating conditions on the electron density n_e and average energy of the EED $\langle E_e \rangle$, as given by the CT-method, is shown in Table 3. The n_e and $\langle E_e \rangle$ increased clearly for $q = 8+, 9+$ and $10+$, while no change in the values for lower charge states was observed.

Figure 22 shows the difference in the characteristic times overlaid with the charge breeding efficiency change. The relative difference of the characteristic times between the New and Former configurations was calculated so that

$$\Delta\tau = \frac{\tau_{\text{New}}}{\tau_{\text{Former}}} - 1 \tag{87}$$

and expressed in percentages. The evolution of the charge breeding efficiency is given as an absolute percentage change, i.e.

$$\Delta\eta = \eta_{\text{New}} - \eta_{\text{Former}}. \tag{88}$$

The $\Delta\tau$ in the figure were calculated without uncertainty estimation.

It is evident from Fig. 22, that the change in the charge breeding efficiencies occur due to the collective effect of the variation in the characteristic times: The charge exchange time decreases across all measured q, the effect of which is to deplete the high charge states and to supply the lower q populations — which is reflected in the evolution of the charge breeding efficiencies as a significantly increased efficiency for $q \leq 9+$ and a decrease for $q > 10$. The ionization time also decreases, but not as much as τ_{cx}. The decrease of τ_{inz} counteracts the effects of charge exchange in particular for the low q populations. The confinement time of the HCIs, in particular of K^{9+}, is decreased, which enables those ion populations to efficiently escape the plasma confinement, bolstering the corresponding breeding efficiency.

The change in the characteristic times occurred through a combination of effects: *(i)* In the $\langle E_e \rangle$ range suggested by the CT-method, i.e. 100 eV–500 eV, the second ion-
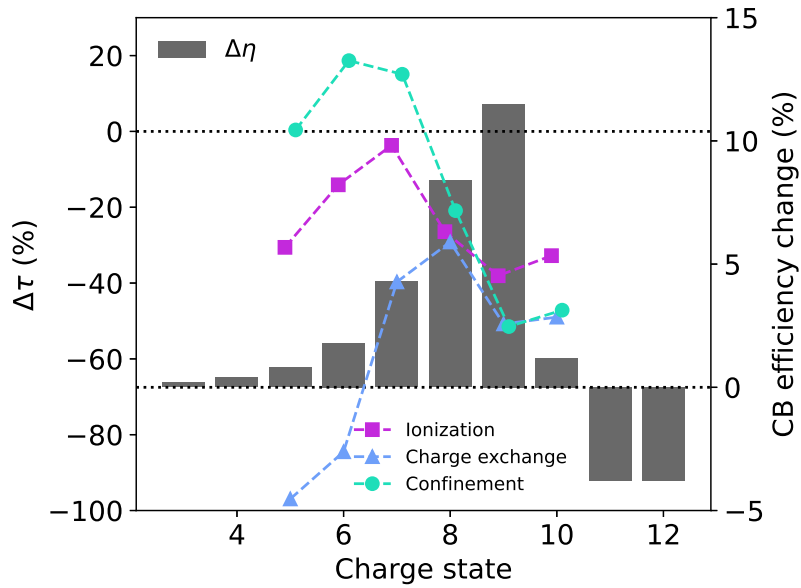
FIGURE 22 The absolute change in charge breeding efficiency $\Delta\eta$ and the relative change $\Delta\tau$ in the characteristic times τ_{conf}, τ_{inz}, and τ_{cx} as functions of charge state. Adapted from PII under the license CC BY 3.0 DEED, IOP Publishing Ltd.

ization rate coefficient of helium is an order of magnitude smaller than that of atomic[2] hydrogen [92]. This and the slightly increased microwave power led to a greater n_e when using hydrogen as the support gas, and a consequent increase in the local energy content, $n_e \langle E_e \rangle$, as well as a shorter τ_{inz} for potassium. *(ii)* The larger charge exchange cross section of hydrogen compared to helium [99] probably caused the decrease in τ_{cx}. No clear cause for the decrease of the confinement time was determined, but *(iii)* the decrease of τ_{conf} for HCIs may have been due to the increased plasma density and a consequent increase of the collision frequency.

We found in this campaign that the CT-method was indeed sufficiently sensitive to enable us to deduce physical causes underlying the changes in the charge breeding efficiency. Nevertheless, the large uncertainty bounds associated with the results still inhibits analysis based on the absolute values of the plasma parameters attained, which restricts us to discussing only the trends in the data.

5.4 Multi-component injection

We decided to attempt to enhance the experimental methods with multi-component 1+ injection. We hypothesized that the HCIs, which originate from the same plasma region, could be used to decrease the size of the $(\langle E_e \rangle, n_e)$-solution sets by taking the mutual overlap of the HCI solution sets. This could then lead to a reduced uncertainty

---

[2] Strictly speaking the dissociation of H_2 should also be accounted for, but the total amount of molecular hydrogen in the plasma is small — at most ≈ 50 % in a 2.45 GHz ECRIS [98]. In the core plasma of an ECRIS for highly charged ions the fraction can be argued to be even lesser.
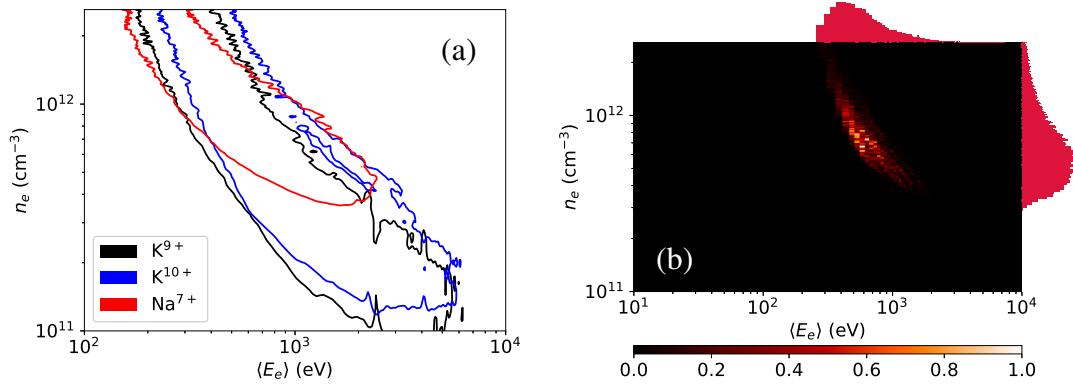
FIGURE 23 Effect of overlapping high charge states' solution sets. Subfigure (a) plots the outer contours of K^{9+}, K^{10+} and Na^{7+} solution sets obtained. The heat map of the corresponding overlap is plotted in subfigure (b). Reprinted with permission from PIII, Copyright © 2022 American Physical Society.

estimate due to smaller $(\langle E_e \rangle, n_e)$-sets. Studying the transients of multiple species could further decrease the uncertainty, because they have different electron configurations — leading to different rate coefficients — and, hence, the same plasma conditions result in different transient time series.

The 1+ ion source is typically loaded with a single component pellet, from which singly charged ions are thermally emitted. Under such a configuration, the pellet needs to be changed every time one wants to change the 1+ species. We circumvented this by loading the 1+ ion source with a custom made pellet comprised of potassium and sodium in a porous, refractory metal dispenser. This enabled us to measure the support plasma properties using the two probe elements — without switching off the charge breeder in between — by selecting the desired 1+ species for injection using the dipole magnet upstream of the charge breeder.

With this amendment to the experimental setup, we measured in Ref. [93] the N+ transients resulting from the injection of K^+ and Na^+ into a hydrogen support plasma. Although it is not possible to state with absolute certainty which ions originate from a given region of plasma, simulations [45] point to the fact that for ions with q above the CSD peak we may assume them to originate from the same plasma volume. We therefore took the overlap of the $(\langle E_e, n_e \rangle)$-solution sets of K^{9+}, K^{10+} and Na^{7+} (the highest charge state of Na for which a solution set was obtained). The outer contours of the solution sets are plotted in Fig. 23 (a) and the heat map of the corresponding overlap is given in subfigure (b). It can be seen that the Na^{7+} solution set effectively restricts those of K^{9+} and K^{10+}.

Tables 4 and 5 tabulate the results. In both tables the relative uncertainty is computed from the asymmetric uncertainties so that

$$\delta x = 100\% \times \frac{\hat{\delta} x + \check{\delta} x}{x} \tag{89}$$

where $\hat{\delta} x > 0$ is the upper, and $\check{\delta} x > 0$ the lower (absolute) uncertainty of $x^{+\hat{\delta}x}_{-\check{\delta}x}$. It is worth noting that typically $\check{\delta} x < \hat{\delta} x$. Therefore, although the relative uncertainty often exceeds 100 % we do not, in fact, obtain negative values as results from the CT-method.

TABLE 4 The plasma parameters n_e and $\langle E_e \rangle$ and the associated uncertainties for high charge states of K and Na, and for their mutual overlap. Adapted with permission from PIII, Copyright © 2022 American Physical Society.

Set	n_e ($\times 10^{11}$ cm^{-3})	δn_e (%)	$\langle E_e \rangle$ (keV)	$\delta \langle E_e \rangle$ (%)
K^{9+}	4^{+10}_{-3}	325	$1^{+1.9}_{-0.6}$	250
K^{10+}	4^{+9}_{-3}	300	$1.3^{+1.8}_{-0.8}$	200
Na^{7+}	7^{+6}_{-3}	130	$0.9^{+4.6}_{-0.5}$	570
Overlap	8^{+8}_{-3}	140	$0.6^{+0.6}_{-0.3}$	150

TABLE 5 The characteristic times and associated relative uncertainties of ion confinement, ionization and charge exchange for high charge states of K and Na both individually and within their mutual overlap. Adapted with permission from PIII, Copyright © 2022 American Physical Society.

	τ_{conf} (ms) ($\delta\tau$ (%))		τ_{inz} (ms) ($\delta\tau$ (%))		τ_{cx} (ms) ($\delta\tau$ (%))	
Set	No overlap	Overlap	No overlap	Overlap	No overlap	Overlap
K^{9+}	10 (140%)	8 (100%)	3.8 (40%)	3.5 (30%)	9 (200%)	16 (85%)
K^{10+}	19 (140%)	16 (100%)	8 (50%)	7 (60%)	8 (100%)	9 (90%)
Na^{7+}	5.4 (55%)	5.7 (50%)	2.8 (25%)	2.8 (25%)	20 (95%)	19 (100%)

The electron densities and average energies are given for the individual ion populations and for their overlap in Table 4. As an example, the $\delta n_e / n_e$ corresponding to K^{10+} decreases from 300 % to 140 %, and $\delta \langle E_e \rangle / \langle E_e \rangle$ decreases from 200 % to 150 %. The corresponding characteristic time values are tabulated in Table 5. The uncertainty computed for the confinement time $\delta\tau^q_{\mathrm{conf}} / \tau^q_{\mathrm{conf}}$ decreases from 140 % to 100 %. It can be seen that taking the overlap reduces the uncertainty of the confinement times in particular. The benefit to the ionization times is lesser due to the already small uncertainties.

In addition to taking the overlap of the high-q states of the two species, we checked the effect of *(i)* overlapping the solution sets of two different isotopes of potassium (^{39}K and ^{41}K), and *(ii)* overlapping the solution sets of high charge states of potassium. The results can be summarized as follows: In case *(i)* there was no effect, as expected. The two isotopes are near in mass and their electron configurations are the same. Therefore, no change in the plasma parameters or uncertainty was expected; In case *(ii)* we also found improvements in the result precision. Taking the mutual overlap of K^{9+}, K^{10+} and K^{11+} reduced the uncertainty of $\langle E_e \rangle$ to 85 % and of n_e to 60 %. Smaller improvements were observed in the characteristic times. Overlapping high charge states of a single species, therefore, can aid in improving the result precision, although it requires the measurement of higher charge state transients, for which the signal-to-noise ratio can be poor.

By probing the plasma with multiple species and applying the overlap-technique to the HCIs, we were able to reduce the uncertainty associated with the HCIs considerably, but the uncertainties remained large regardless. At this stage we had performed initial

tests in arbitrarily curtailing the uncertainty of the ionization cross section data (taken from literature), which suggested that the result precision could be improved if only we had more precise estimates of $\sigma^{\text{inz}}_{q \to q+1}$.

5.5 Parameter dependencies revealed by the CT-method

The ECRIS operating parameters, such as gas injection rate, magnetic field strength, microwave power and frequency, can be viewed as "knobs" that the ion source operator can tune to effect a change in the plasma parameters. The effect of a given operating parameter on the plasma condition is not straightforward, and a change in one set parameter can cause variations in multiple plasma parameters. As an example, increasing the neutral gas injection rate will of course increase the plasma neutral density n_0, but through ionization of the neutrals the electron density n_e will also increase (as well as the ion densities n^q). The change in n_e can further modify the ion temperature (through ion heating via electron drag), the plasma potential ϕ and the potential dip depth $\Delta\phi$. Consequently the ion confinement properties are affected. All this will contribute to a change in the plasma CSD and the extracted beam CSD, which is the object of primary interest for the ion source operator.

Plasma diagnostics are applied to determine the effects that tuning these knobs has on the plasma. A very usual type of experiment is the *parameter sweep*, where the ion source is first tuned to some starting configuration — e.g. optimal production of some high charge state ion beam — and the source tuning is then varied by adjusting just one set parameter. Chosen plasma diagnostic methods are applied in each new configuration to determine the consequent variations in the plasma parameters probed by the diagnostic as a function of the operating parameter.

In PV we performed parameter sweeps of the microwave power, support gas pressure, magnetic field minimum B_{min}, and magnetic field intensity at the extraction B_{ext}. These parameters were chosen as they influence the CSD, and the EED, n_e, n_0 and the plasma confinement properties — i.e. all the plasma parameters within the reach of the CT-method.

We choose the microwave power sweep as a good case study of the parameter sweeps, because it showed clear trends in the plasma parameters, and plasma diamagnetism experiments are available [22] for a comparison of the energy content trends. In the microwave sweep the heating power was varied between 150 W and 600 W. The N+ transients for K^{4+}–K^{12+} were collected and analyzed, leading to the plasma parameters for K^{6+}–K^{10+}. The uncertainties of the CT-method results remain large, and in the following we consider only the median values for clarity of presentation. The focus of the analysis should then be kept in the trends visible in the data, rather than the absolute values. Similar deductions can be made based on the other parameter sweeps.

The variation of the energy content as a function of charge state is plotted in Fig. 24 (a). Note the charge state dependence, which hints at the nested layer spatial distribution of ion populations, as discussed in Section 5.1. Figure 24 (b) plots the energy content obtained through plasma diamagnetism experiments from Ref. [22] for comparison. We

observe that the trends are essentially the same — i.e. an increase with the input power — but the diamagnetism values are approximately an order of magnitude greater than those from the CT-method. This difference may be due to the diamagnetism experiments probing mainly the hot electrons, while the CT-method is sensitive to the electron populations more relevant for ionization. The order of magnitude difference may thus arise if, for example, only 10 % of the electrons are hot electrons.

The increase of the energy content with microwave power is most likely due to the increase of $\langle E_e \rangle$ rather than n_e, as evident from Fig. 25 where the solution sets of K^{10+} are plotted at 150 W and 600 W input power. As shown in the annotations, the n_e remains almost unchanged at approximately 5×10^{11} cm^{-3}, which is typical for ECRIS plasmas, but the $\langle E_e \rangle$ increases from 1 keV to 1.5 keV.
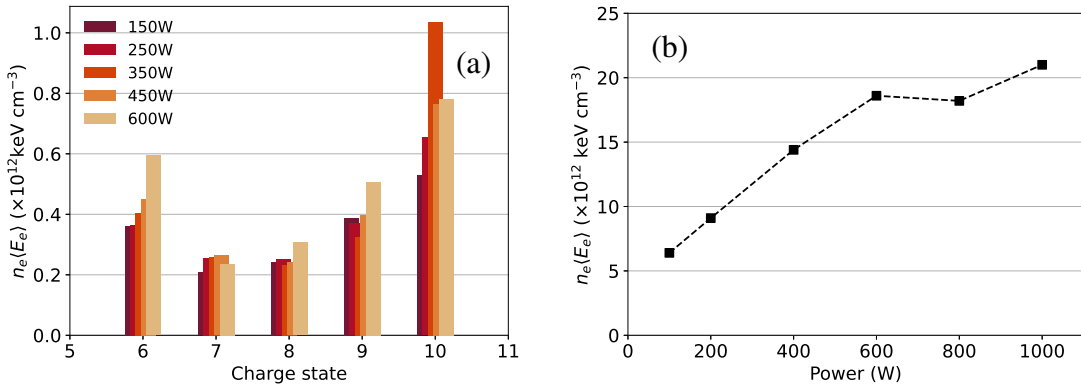

FIGURE 24   Energy contents as functions of charge state for different microwave powers (a), and from diamagnetism measurements. Subfigure (a) from PV reproduced under the license CC BY 4.0 DEED. Subfigure (b) adapted from [22], with the permission of AIP Publishing.

The hierarchy of the characteristic times is of particular interest, since the magnitudes of τ_{conf}, τ_{inz}, and τ_{cx} determine the CSD through the balance equation (37). We deduced in PV that for the production of HCIs, the desired hierarchy between the characteristic times is

$$\tau_{\mathrm{conf}} > \tau_{\mathrm{inz}} \qquad \text{and} \tag{90}$$

$$\tau_{\mathrm{cx}} > \tau_{\mathrm{conf}}. \tag{91}$$

This is of course equivalent to $\tau_{\mathrm{conf}} - \tau_{\mathrm{inz}} > 0$ and $\tau_{\mathrm{cx}} - \tau_{\mathrm{conf}} > 0$.

In Fig. 26 we have plotted the characteristic times ((d), (e), (f)), the charge breeding efficiencies (c), and the values $\tau_{\mathrm{conf}} - \tau_{\mathrm{inz}}$ and $\tau_{\mathrm{cx}} - \tau_{\mathrm{conf}}$ ((a), (b)) as functions of charge state. We note first that the extracted beam CSD (as represented by the breeding efficiency) shifts towards higher charge states as the microwave power is increased. In particular, the efficiencies η^{4+}–η^{8+} first increase up to around 350 W, and subsequently decrease. The efficiencies η^{9+}–η^{12+} increase monotonically as the input power is increased.

Figure. 26 (a) and (b) compare the magnitudes of τ_{conf} to τ_{inz}, and τ_{cx} to τ_{conf}, respectively. The positive regions of the respective subplots correspond to the desirable
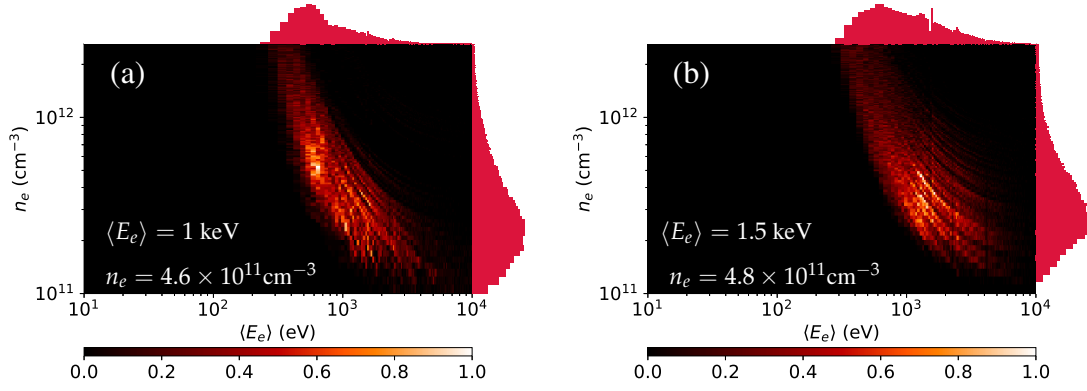
FIGURE 25   Solution sets of K^{10+} at (a) 150 W input power, and (b) 600 W input power. The median values of n_e and $\langle E_e \rangle$ are annotated to the plots. PV reproduced under the license CC BY 4.0 DEED.

cases of Eqs. (90) and (91). We observe in (a) that for the low charge states K^{6+} and K^{7+} the hierarchy degrades slightly as a function of increased power. From subfigures (d) and (e), this is apparently due to mostly to the decrease of the confinement time. For the charge states $\geq K^{8+}$ the hierarchy improves, i.e. $\tau_{\text{conf}} - \tau_{\text{inz}}$ becomes more positive — mostly owing to the decreased τ_{inz}.

On the other hand, Fig. 26 (b) shows that, as the input power is increased, the hierarchy between τ_{cx} and τ_{conf} remains the same up to the highest input power until it suddenly degrades for K^{9+} and K^{10+}. For K^{7+} and K^{8+} there is no apparent change, and the condition improves for K^{6+}. The sudden increase for the high charge states is attributable to the growth of the confinement times τ_{conf} and the simultaneous slight decrease of τ_{cx}.

These observations are in agreement with the obviously increased mean charge state in the CSD of Fig. 26 (c). Moreover, the availability of the characteristic times allows us to identify bottlenecks in the ion production chain. Subfigure (a) suggests, that an increase of the power input might not yield unlimited improvements in the extracted CSD, since the hierarchy of the low charge states has a decreasing trend with power, and could in fact become negative. From (b) we can infer that the CSD could be pushed further towards the higher charge states by either an increased τ_{cx} or a decreased τ_{conf}. Of the two, the charge exchange is under more direct control either by *(i)* decreased neutral gas input or *(ii)* a change of the support gas species to one with a higher first ionization potential.

As a caveat to the preceding analysis, we point out that although the changes in the characteristic times are visible, the considerable uncertainties associated with them prevent us from drawing conclusions on the precise causes behind their evolution with the input power. As a particular example, the increase of τ_{inz} for K^{10+} at high power is counterintuitive, and it is possible that the true values are hidden under the error bounds. There are also evident discontinuities in trends, e.g. in Fig. 26 (a) the K^{9+} hierarchy at 350 W power.

The key takeaways from the experimental campaign pertaining to Publication PV are as follows: We were able to show that the CT-method is sufficiently sensitive to probe

variations in the plasma condition as a function of the source control parameters. Although the uncertainties associated with the CT-method results remain large, the observed trends are in agreement with results obtained using e.g. diamagnetic loop measurements. The method provides information on the characteristic times, which are inaccessible by other methods, and these are shown to provide the ion source operator with critically important knowledge of the bottlenecks which may inhibit the production of HCIs. In particular, the hierarchy of the characteristic times established in PV provides a useful diagnostic for possible avenues of improvement in either the source tuning or even the overall design of the ion source.
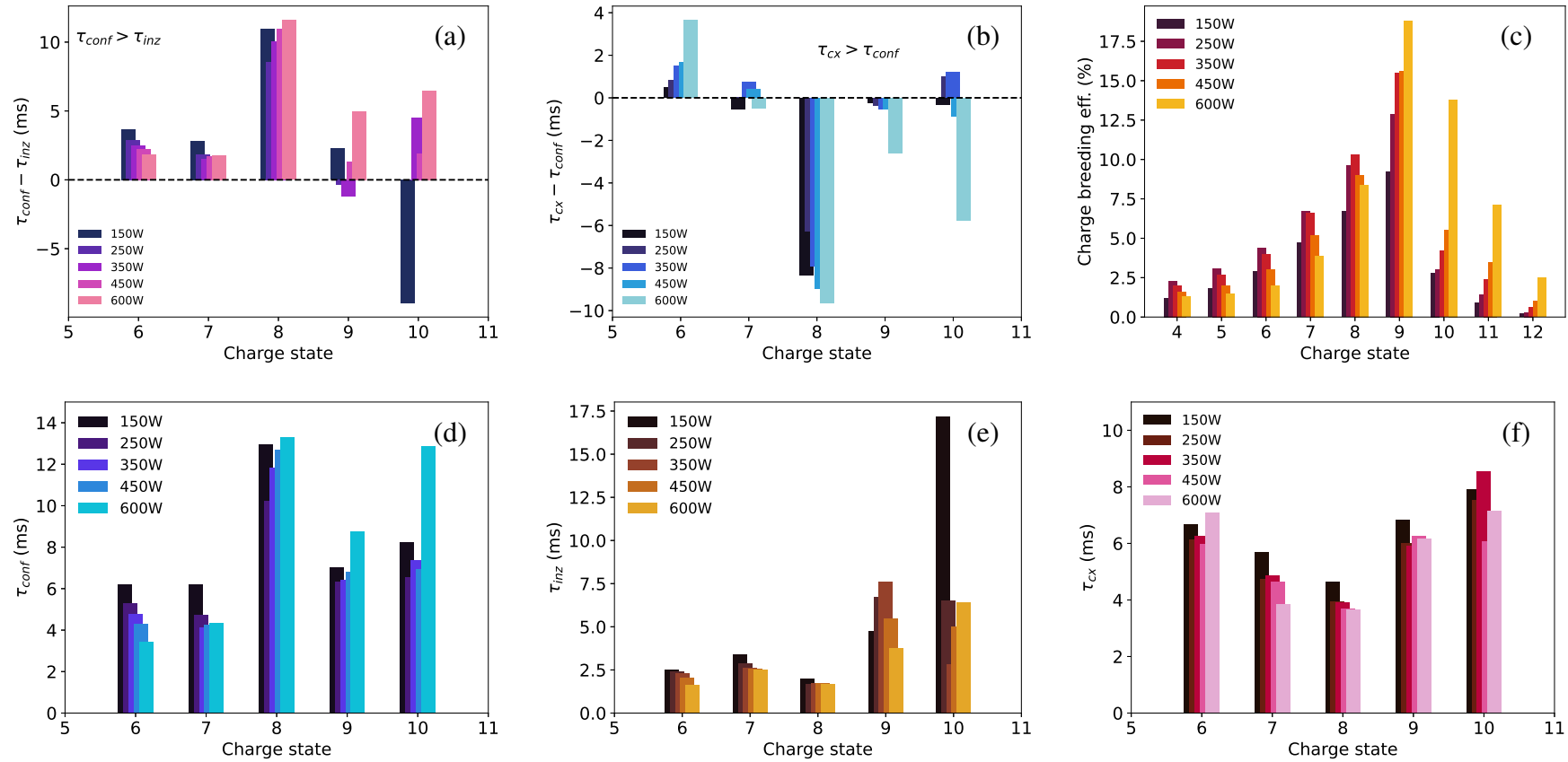
FIGURE 26 The values of $\tau_{\text{conf}} - \tau_{\text{inz}}$, $\tau_{\text{cx}} - \tau_{\text{conf}}$ and the charge breeding efficiencies ((a), (b), (c)); and the characteristic times ((d), (e), (f)) for the microwave power sweep. The regions where $\tau_{\text{conf}} > \tau_{\text{inz}}$ and $\tau_{\text{cx}} > \tau_{\text{conf}}$ — i.e. where efficient HCI production is expected — are indicated in the figures. PV reproduced under the license CC BY 4.0 DEED.

6   CONCLUSION

In the experimental campaigns conducted in Publications PI–PV we have established the Consecutive Transients method for ECRIS plasma diagnostics. The CT-method is the newest edition in a continuum of transient material injection methods which date back to the 1990s. These methods are based on pulsewise injection of a given element into a support plasma sustained in the ECRIS, where the injected particles are captured and ionized to higher charge states. Ultimately, the ions escape plasma confinement and a fraction of them are extracted as ions at charge state q. The corresponding beam current transients thus formed are experimentally measured, and their time series are analyzed. As a result, the plasma electron average energy $\langle E_e \rangle$ and density n_e are obtained, along with the characteristic times of ion confinement, ionization and charge exchange τ_{conf}, τ_{inz}, and τ_{cx}, respectively.

The CT-method is fundamentally similar to the established transient methods in its experimental arrangements. The choice of material injection technique is basically arbitrary, but the 1+ injection system available at the LPSC 14.5 GHz PHOENIX-type charge breeder test bench, which was employed in the experimental campaigns discussed herein, enabled precise regulation of the amount of material injected. It was therefore possible to minimize and control the scale of the perturbation on the support plasma, which is key in ensuring that the plasma parameters do not change due to the experiment. The constancy of the plasma parameters in time is a primary assumption of the CT-method — similarly to the previously established transient methods.

The improvements provided by the CT-method lie in the model based analysis of the extracted beam current transients. The analysis is based on the beam current balance equation (70), which is derived from the ion density balance equation (37) — the foundation of earlier methods. This improvement is critical for the accuracy of the results, because the beam currents are not directly proportional to the ion densities, but rather they are modified by the confinement time so that $I^q \propto n^q / \tau_{\mathrm{conf}}^q$. In contrast, earlier transient methods have essentially presumed that $I^q \propto n^q$, which leads to an underestimation of the HCI densities in particular as the high q ions are more strongly confined than the lower q ions. This is rectified in the CT-method by use of Eq. (70).

In developing the CT-method we strove for a parsimony of assumptions. In particular, we avoided presuming a certain confinement model which would yield τ_{conf}, because it is most likely that no single confinement model suffices to describe the total ion confinement in the (steady-state) non-equilibrium ECRIS plasma. Ultimately, we arrived at an optimization routine which is based on the analysis of multiple (≥ 5) consecutive charge state transients, and which requires a foreknowledge only of the ionization cross sections and the EED. The cross sections are adopted from existing literature, and the EED is presumed to be Maxwellian, although we are not restricted to that choice.

The optimization is done by forming a penalty function $F(\langle E_e \rangle, n_e)$ by algebraic manipulation of the fitting coefficients obtained from fits to the transient time series using Eq. (70). It should be noted that the CT-method is quite sensitive to the noise-to-signal

ratio in the measured transients, and best efforts should be made to minimize it. Especially the high charge state transients, whose signals are low, are prone to yield poor fits which have resulted in rogue data points. The best way to minimize noise is to increase the material injection intensity and the length of the pulse, but care must be taken to simultaneously control the support plasma perturbation to avoid corrupting the experiment.

Through the optimization routine we obtain a set of solutions $(\langle E_e \rangle, n_e)$ for $N-4$ ion populations, where N is the number of consecutive transients measured. These solution sets are constrained using physical constraints, i.e. conservative lower and upper bounds for n_e, and $\langle E_e \rangle$ as implied by existing ECRIS research; and the requirement that each of the characteristic times satisfy $\tau > 0$. This routine enables us to naturally introduce a Monte Carlo method for estimation of the uncertainty originating from the literature values of the ionization cross sections, which can be as high as 200 %. The estimation procedure is simple: The optimization routine is repeated $N \geq 1000$ times, and in each iteration the ionization rate coefficients are biased by a random factor $B_q \sim U(-\delta\sigma, \delta\sigma)$, drawn from the uniform distribution U, where $\delta\sigma$ is the uncertainty of the ionization cross section. The results $(\langle E_e \rangle, n_e)$ are collected from each iteration to yield the final solution set, which thus incorporates solutions obtained by comprehensively sampling the uncertainty bounds.

The CT-method uniquely incorporates the uncertainty of $\sigma^{\mathrm{inz}}_{q \to q+1}$, and we have shown in Ref. [100] that the error propagates to our results in a large degree. We found that by curtailing the cross section uncertainty, great reductions in the plasma parameter results can be achieved. It is likely that other experiments which employ $\sigma^{\mathrm{inz}}_{q \to q+1}$ would also benefit from such an uncertainty estimation, and a revisit of the experimental / theoretical cross section data to sharpen the error estimates may be desirable.

In Publication PIV we also investigated the effect of the presupposed EED. We focused on the effects to the results from varying the high energy tail of the EED, since measurements of the lost electron energy distributions and bremsstrahlung emissions suggest that the hot electron component in the ECRIS plasma may be considerable. We found that the effects were primarily on the $\langle E_e \rangle, n_e$ solution sets, while the characteristic times were less affected. The results of Ref. [100] indicate that the choice of the plasma EED is important for the determination of $\langle E_e \rangle$ and n_e, and its importance is emphasized if the cross section uncertainty can be reduced.

In addition to $\langle E_e \rangle$ and n_e, the characteristic times of ion confinement τ_{conf}, ionization τ_{inz} and charge exchange τ_{cx} are obtained. Due to the large uncertainty bounds it is difficult to draw sound conclusions based on the absolute values of the characteristic times, but Refs. [101] and PV demonstrate that the CT-method is sensitive enough to allow inferences to be made from the trends observed in the plasma parameters changing with the source tune. In particular, Publication PV demonstrated the importance of the hierarchy of the characteristic times (as expressed in Eqs. (90) and (91)), which presents an important new diagnostic for the ECRIS operator for identifying bottlenecks in the ion production process. The Figs. 26 (a) and (b), and the associated discussion in Section 5.5 give an example of this: When $\tau_{\mathrm{conf}} > \tau_{\mathrm{inz}}$ and $\tau_{\mathrm{cx}} > \tau_{\mathrm{conf}}$, HCI production is enhanced.

We have obtained ion confinement times that exceed 10 ms for HCIs, e.g. $^{39}\mathrm{K}^{9+/10+}$ in Fig. 17. With such a τ_{conf}, the simplified electron-drag heating (presented in Sec-

tion 1.5) would enable K^{9+} to be heated to an energy around 15 eV, given $T_e = 500$ eV, $n_e = 5 \times 10^{11}\text{cm}^{-3}$ and $\ln \Lambda = 10$ — consistent with results obtained with the CT-method. This ion temperature is in agreement with that found experimentally for Ar^{9+} ($T_i \approx 12$ eV) in Ref. [33] in a conventional ECRIS using similar microwave heating power and 14 GHz frequency. The charge state dependence of the confinement time found in this work is also mutually corroborative with the charge state dependent ion temperatures of Ref. [33], since in this heating scheme an ion with a longer confinement time will gain more energy from the electrons. We remind the reader that these confinement times were obtained with the simplifying assumption that the ions do not exchange energy between one another. Including this would deplete the temperature of the higher charge states, since the low q ions have shorter τ_{conf}. The analysis was also conducted in the steady-state for established ion populations. It would be interesting to perform a stochastic simulation of the heating of independent ions introduced to the plasma as neutrals or 1+ ions: The ion would be heated by electrons throughout their cumulative lifetime as their charge state gets increased and decreased by ionization and charge exchange — i.e. the ion spends time at different charge states and is hence heated at different rates at different points in its lifecycle, until it finally escapes the plasma. The resultant energy distributions of the lost ions should ideally agree with the model presented here.

Our results suggest that it is possible that the low and high charge states obey different confinement schemes, with the high charge state ions being confined electrostatically in the potential dip within the plasma potential profile. Since the HCIs are highly collisional (collisionality $\eta \gg 1$), the moderately collisional scheme of Eq. (43) does not seem applicable. Nevertheless, the long confinement times of the HCIs could be reproduced by an exponential dependence on the charge state which suggests that Eq. (58) might be suitable, if the $|\Delta\phi|$ is sufficiently large. In Ref. [21], however, the ambipolar confinement model represented by Eq. (57) was found to reproduce the timescales of τ_{conf} determined from ion source end loss fluxes in the steady-state. The transient measurements of Ref. [39] on the other hand also point to confinement times of up to 10 ms (with the caveat of a presumed linear charge state dependence), which support our findings. Long confinement times are also supported by the charge state dependent, high ion temperatures of Ref. [33]. Clearly, more thorough investigations are required.

In PIII we established multi-component injection and solution set overlaps as an amendment to the experimental and computational procedures of the CT-method. Probing the support plasma properties using two different ion species enabled further restricting the solution sets of the HCIs. This lead to a reduction in the uncertainty of the results. This approach also has its drawbacks: Applying the overlap method presented in PIII requires the additional assumption to be made, that the HCIs originate from the same plasma region. While it is well established in both experiments and through simulation results that the HCIs are localized closer to the plasma chamber axis, it is not clear where to draw the line between a low charge ion and a highly charged ion. We have used simulation results to justify the postulate, that ions above the CSD peak can be considered to originate from approximately the same plasma region, but more evidence is needed to totally ascertain this. Additionally, the overlap method can only be employed for a fraction of the measured transients (i.e. those above the CSD peak), while knowledge of the lower charge

states too is required to draw conclusions on the data. Fortunately, the lower charge states have in general lower uncertainties than the HCIs. In principle, multi-component injection could be adapted to use cases where laser ablation or sputtering are used for material injection. One would then use a laser ablation target or sputter probe tip comprised of more than one element.

The original motivation for the development of the CT-method was to determine the total confinement time of an ion injected into a charge breeder ECRIS. This is of great importance for the production of radioactive ion beams where the isotope of interest has a lifetime on the order of a second or less: The ion needs to be charge bred to a high charge state for post-acceleration to energies required for nuclear physics experiments. This charge breeding process must take place in a timescale short compared to the lifetime of the nuclear decay for the isotope, or else the beam intensity necessary for conducting the nuclear physics experiment cannot be achieved.

We have shown that the CT-method can be used to obtain the characteristic times of ion production for a portion of the ion populations whose beam currents are experimentally measurable. To deduce the beam currents of RIBs from the characteristic times of their stable proxy isotopes, one would have to solve the balance equation amended with radioactive decay, i.e. Eq. (79). In effect, the characteristic times of the ion populations inaccessible through the CT-method would have to be extrapolated based on those that can be determined. These would then be substituted into Eq. (79) which can be solved, e.g. using a Runge-Kutta method. The resultant ion densities can then be related to the beam currents via Eq. (65), which describes the proportionality of I^q to n^q.

Such an analysis has not been carried out due to time constraints. If this analysis is undertaken, the results should be compared with those obtained using the traditional charge breeding time (τ_{cb}) measurements such as those presented in Ref. [73]. The measurement of τ_{cb} is much more straightforward, and is equally invasive / non-invasive as the CT-method. If both methods yield similar (and correct) estimates for RIB intensities, the measurement of τ_{cb} should be preferred for that purpose.

In principle, all CB-ECRISs are equipped with the necessary diagnostic tools required to apply the CT-method, since only an appropriate pulsed material injection method and beam current measurement are required. The CT-method has been proven to be suitable at least in the case of 1+ injection, but both pulsed sputtering and laser ablation could be applied in principle. The perturbation on the support plasma may be further mitigated by amplitude modulation. There are indications [42] that the sputtering voltage causes a significant perturbation on the support plasma, which should be mitigated e.g. by means of amplitude modulation. The ct-analyzer, which implements the numerical routines discussed in Section 4, is openly available at https://www.github.com/misapema-jyfl/ct-analyzer.

BIBLIOGRAPHY

[1] R. Geller, *Electron Cyclotron Resonance Ion Sources and ECR Plasmas*. Institute of Physics Publishing, Bristol and Philadelphia, 1996, ISBN: 0-7503-0107-4.

[2] R. Pardo, R. Vondrasek, and J. Bergman, Eds., *Experience at the ion beam therapy center (HIT) with 2 years of continuous ECR ion source operation*, Argonne National Laboratory, Chicago, Illinois USA: Journal of Accelerator Conferences Website, Sep. 2008.

[3] E. Ritter, R. Cee, T. Haberer, A. Peters, A. Silze, T. Winkelmann, G. Zschornack, and G. Zschornack, "Implementation of a superconducting electron beam ion source into the hit ion source test bench", en, *Proceedings of the 5th Int. Particle Accelerator Conf.*, vol. IPAC2014, Germany, 2014. DOI: 10.18429/JACOW-IPAC2014-WEPRO083. [Online]. Available: http://jacow.org/IPAC2014/doi/JACoW-IPAC2014-WEPRO083.html.

[4] T. Kamada, H. Tsujii, E. A. Blakely, J. Debus, W. D. Neve, M. Durante, O. Jäkel, R. Mayer, R. Orecchia, R. Pötter, S. Vatnitsky, and W. T. Chu, "Carbon ion radiotherapy in japan: An assessment of 20 years of clinical experience", *The Lancet Oncology*, vol. 16, no. 2, e93–e100, Feb. 2015. DOI: 10.1016/s1470-2045(14)70412-7. [Online]. Available: https://doi.org/10.1016/s1470-2045(14)70412-7.

[5] C. Andresen, "Characterisation and performance of the CERN ECR4 ion source", in *AIP Conference Proceedings*, Berkeley, California (USA): AIP, 2005.

[6] T. Kövener, D. Küchler, E. Mahner, R. Scrivens, A. Baris, S. Pfeiffer, L. Mourier, and W. Vollenberg, "Experiments to improve the performance of the gts-lhc ecr ion source", *Journal of Physics: Conference Series*, vol. 2244, no. 1, p. 012 020, Apr. 2022. DOI: 10.1088/1742-6596/2244/1/012020. [Online]. Available: https://dx.doi.org/10.1088/1742-6596/2244/1/012020.

[7] W. Gelletly, "Radioactive ion beams: A new window on atomic nuclei", *Proceedings of the American Philosophical Society*, vol. 145, no. 4, pp. 519–554, 2001, ISSN: 0003049X. [Online]. Available: http://www.jstor.org/stable/1558191 (visited on 06/10/2022).

[8] J. J. Cowan, C. Sneden, J. E. Lawler, A. Aprahamian, M. Wiescher, K. Langanke, G. Martínez-Pinedo, and F.-K. Thielemann, "Origin of the heaviest elements: The rapid neutron-capture process", *Rev. Mod. Phys.*, vol. 93, p. 015 002, 1 Feb. 2021. DOI: 10.1103/RevModPhys.93.015002. [Online]. Available: https://link.aps.org/doi/10.1103/RevModPhys.93.015002.

[9] D. Mascali, A. Musumarra, F. Leone, F. P. Romano, A. Galatà, S. Gammino, and C. Massimi, "PANDORA, a new facility for interdisciplinary in-plasma physics", *The European Physical Journal A*, vol. 53, no. 7, Jul. 2017. DOI: 10.1140/epja/i2017-12335-1. [Online]. Available: https://doi.org/10.1140/epja/i2017-12335-1.

[10] D. Mascali, M. Busso, A. Mengoni, S. Amaducci, C. Giuseppe, L. Celona, G. Cosentino, S. Cristallo, P. Finocchiaro, A. Galata, S. Gammino, C. Massimi, M. Maggiore, G. Mauro, M. Maria, E. Naselli, F. Odorici, S. Palmerini, D. Santonocito, and T. Giuseppe, "The PANDORA project: An experimental setup for measuring in-plasma β-decays of astrophysical interest", *EPJ Web of Conferences*, vol. 227, C. Spitaleri, M. L. Cognata, L. Lamia, R. Pizzone, and S. Romano, Eds., p. 01 013, 2020. DOI: 10.1051/epjconf/202022701013. [Online]. Available: https://doi.org/10.1051/epjconf/202022701013.

[11] M. Jung, F. Bosch, K. Beckert, H. Eickhoff, H. Folger, B. Franzke, A. Gruber, P. Kienle, O. Klepper, W. Koenig, C. Kozhuharov, R. Mann, R. Moshammer, F. Nolden, U. Schaaf, G. Soff, P. Spädtke, M. Steck, T. Stöhlker, and K. Sümmerer, "First observation of bound-state β^- decay", *Physical Review Letters*, vol. 69, no. 15, pp. 2164–2167, Oct. 1992. DOI: 10.1103/physrevlett.69.2164. [Online]. Available: https://doi.org/10.1103/physrevlett.69.2164.

[12] D. Hitz, A. Girard, G. Melin, S. Gammino, G. Ciavola, and L. Celona, "Results and interpretation of high frequency experiments at 28 GHz in ECR ion sources, future prospects", *Review of Scientific Instruments*, vol. 73, no. 2, pp. 509–512, Feb. 2002. DOI: 10.1063/1.1429313. [Online]. Available: https://doi.org/10.1063/1.1429313.

[13] A. Girard, C. Perret, G. Melin, and C. Lécot, "Modeling of electron-cyclotron-resonance ion source and scaling laws", *Review of Scientific Instruments*, vol. 69, no. 2, pp. 1100–1102, Feb. 1998. DOI: 10.1063/1.1148588. [Online]. Available: https://doi.org/10.1063/1.1148588.

[14] C. Perret, A. Girard, H. Khodja, and G. Melin, "Limitations to the plasma energy and density in electron cyclotron resonance ion sources", *Physics of Plasmas*, vol. 6, no. 8, pp. 3408–3415, Aug. 1999. DOI: 10.1063/1.873581. [Online]. Available: https://doi.org/10.1063/1.873581.

[15] G. D. Shirkov and G. Zschornack, *Electron Impact Ion Sources for Charged Heavy Ions*. Wiesbaden: Vieweg+Teubner Verlag, 1996. DOI: https://doi.org/10.1007/978-3-663-09896-6.

[16] F. J. C. Wenander, *Charge breeding of radioactive ions*, Comments: 30 pages, contribution to the CAS-CERN Accelerator School: Ion Sources, Senec, Slovakia, 29 May – 8 June 2012, edited by R. Bailey, CERN-2013-007, 2013. DOI: 10.5170/CERN-2013-007.351. arXiv: 1404.0945. [Online]. Available: http://cds.cern.ch/record/1693329.

[17] L. Celona, G. Ciavola, F. Consoli, S. Gammino, F. Maimone, D. Mascali, P. Spädtke, K. Tinschert, R. Lang, J. Mäder, J. Roßbach, S. Barbarino, and R. S. Catalano, "Observations of the frequency tuning effect in the 14ghz caprice ion source", *Review of Scientific Instruments*, vol. 79, no. 2, Feb. 2008, ISSN: 1089-7623. DOI: 10.1063/1.2841694. [Online]. Available: http://dx.doi.org/10.1063/1.2841694.

[18] O. Tarvainen, T. Kalvas, H. Koivisto, R. Kronholm, M. Marttinen, M. Sakildien, V. Toivanen, I. Izotov, V. Skalyga, and J. Angot, "Plasma diagnostic tools for ecr ion sources—what can we learn from these experiments for the next generation sources", *Review of Scientific Instruments*, vol. 90, no. 11, p. 113 321, 2019. DOI: 10.1063/1.5127050.

[19] G. Melin, F. Bourg, P. Briand, J. Debernardi, M. Delaunay, R. Geller, B. Jacquot, P. Ludwig, T. K. N'Guyen, L. Pin, M. Pontonnier, J. C. Rocco, and F. Zadworny, "Some particular aspects of the physics of the ECR sources for multicharged ions", *Review of Scientific Instruments*, vol. 61, no. 1, pp. 236–238, Jan. 1990. DOI: 10.1063/1.1141305. [Online]. Available: https://doi.org/10.1063/1.1141305.

[20] G. Melin, A. G. Drentje, A. Girard, and D. Hitz, "Ion behavior and gas mixing in electron cyclotron resonance plasmas as sources of highly charged ions", *Journal of Applied Physics*, vol. 86, no. 9, pp. 4772–4779, 1999. DOI: 10.1063/1.371442.

[21] G. Douysset 1, H. Khodja, A. Girard, and J. P. Briand, "Highly charged ion densities and ion confinement properties in an electron-cyclotron-resonance ion source", *Phys. Rev. E*, vol. 61, pp. 3015–3022, 3 Mar. 2000. DOI: 10.1103/PhysRevE.61.3015. [Online]. Available: https://link.aps.org/doi/10.1103/PhysRevE.61.3015.

[22] C. Barué, M. Lamoureux, P. Briand, A. Girard, and G. Melin, "Investigation of hot electrons in electron-cyclotron-resonance ion sources", *Journal of Applied Physics*, vol. 76, no. 5, pp. 2662–2670, Sep. 1994. DOI: 10.1063/1.357563. [Online]. Available: https://doi.org/10.1063/1.357563.

[23] N. K. Bibinov, V. F. Bratsev, D. B. Kokh, V. I. Ochkur, and K. Wiesemann, "Spectroscopic determination of the cold electron population in very low pressure ECR discharges in n2/he mixtures", *Plasma Sources Science and Technology*, vol. 14, no. 1, pp. 109–128, 2005. DOI: 10.1088/0963-0252/14/1/014. [Online]. Available: https://doi.org/10.1088/0963-0252/14/1/014.

[24] A. Gumberidze, M. Trassinelli, N. Adrouche, C. I. Szabo, P. Indelicato, F. Haranger, J.-M. Isac, E. Lamour, E.-O. L. Bigot, J. Merot, C. Prigent, J.-P. Rozet, and D. Vernhet, "Electronic temperatures, densities, and plasma x-ray emission of a 14.5 GHz electron-cyclotron resonance ion source", *Review of Scientific Instruments*, vol. 81, no. 3, Mar. 2010. DOI: 10.1063/1.3316805. [Online]. Available: https://doi.org/10.1063/1.3316805.

[25] I. Izotov, O. Tarvainen, V. Skalyga, D. Mansfeld, T. Kalvas, H. Koivisto, and R. Kronholm, "Measurement of the energy distribution of electrons escaping minimum-b ECR plasmas", *Plasma Sources Science and Technology*, vol. 27, no. 2, p. 025 012, Feb. 2018. DOI: 10.1088/1361-6595/aaac14. [Online]. Available: https://doi.org/10.1088/1361-6595/aaac14.

[26] O. Tarvainen, I. Izotov, D. Mansfeld, V. Skalyga, S. Golubev, T. Kalvas, H. Koivisto, J. Komppula, R. Kronholm, J. Laulainen, and V. Toivanen, "Beam current oscillations driven by cyclotron instabilities in a minimum-*b* electron cyclotron resonance ion source plasma", *Plasma Sources Science and Technology*, vol. 23, no. 2, p. 025 020, Apr. 2014. DOI: 10.1088/0963-0252/23/2/025020. [Online]. Available: https://doi.org/10.1088/0963-0252/23/2/025020.

[27] O. Tarvainen, J. Laulainen, J. Komppula, R. Kronholm, T. Kalvas, H. Koivisto, I. Izotov, D. Mansfeld, and V. Skalyga, "Limitations of electron cyclotron resonance ion source performances set by kinetic plasma instabilities", *Review of Scientific Instruments*, vol. 86, no. 2, p. 023 301, 2015. DOI: 10.1063/1.4906804. [Online]. Available: https://doi.org/10.1063/1.4906804.

[28] O. Tarvainen, T. Kalvas, H. Koivisto, J. Komppula, R. Kronholm, J. Laulainen, I. Izotov, D. Mansfeld, V. Skalyga, V. Toivanen, and G. Machicoane, "Limitation of the ECRIS performance by kinetic plasma instabilities (invited)", *Review of Scientific Instruments*, vol. 87, no. 2, 02A703, 2016. DOI: 10.1063/1.4931716. [Online]. Available: https://doi.org/10.1063/1.4931716.

[29] O. Tarvainen, T. Kalvas, H. Koivisto, J. Komppula, R. Kronholm, J. Laulainen, I. Izotov, D. Mansfeld, and V. Skalyga, "Kinetic instabilities in pulsed operation mode of a 14 GHz electron cyclotron resonance ion source", *Review of Scientific Instruments*, vol. 87, no. 2, 02A701, 2016. DOI: 10.1063/1.4931711. [Online]. Available: https://doi.org/10.1063/1.4931711.

[30] I. Izotov, T. Kalvas, H. Koivisto, R. Kronholm, D. Mansfeld, V. Skalyga, and O. Tarvainen, "Broadband microwave emission spectrum associated with kinetic instabilities in minimum-b ECR plasmas", *Physics of Plasmas*, vol. 24, no. 4, p. 043 515, Apr. 2017. DOI: 10.1063/1.4981387. [Online]. Available: https://doi.org/10.1063/1.4981387.

[31] S. V. Golubev and A. G. Shalashov, "Cyclotron-resonance maser driven by magnetic compression of rarefied plasma", *Physical Review Letters*, vol. 99, no. 20, Nov. 2007. DOI: 10.1103/physrevlett.99.205002. [Online]. Available: https://doi.org/10.1103/physrevlett.99.205002.

[32] J. A. Bittencourt, *Fundamentals of plasma physics*. Springer Science & Business Media, 2004.

[33] R. Kronholm, T. Kalvas, H. Koivisto, J. Laulainen, M. Marttinen, M. Sakildien, and O. Tarvainen, "Spectroscopic study of ion temperature in minimum-b ECRIS plasma", *Plasma Sources Science and Technology*, vol. 28, no. 7, p. 075 006, Jul. 2019. DOI: 10.1088/1361-6595/ab27a1. [Online]. Available: https://doi.org/10.1088/1361-6595/ab27a1.

[34] R. Kronholm, T. Kalvas, H. Koivisto, S. Kosonen, M. Marttinen, D. Neben, M. Sakildien, O. Tarvainen, and V. Toivanen, "Ecris plasma spectroscopy with a high resolution spectrometer", *Review of Scientific Instruments*, vol. 91, no. 1, p. 013 318, 2020. DOI: 10.1063/1.5128854.

[35] R. J. Goldston and P. H. Rutherford, *Introduction to Plasma Physics*. London: IOP Publishing Ltd, 1995. DOI: https://doi.org/10.1201/9780367806958.

[36] G. Shirkov, C. Mühle, G. Musiol, and G. Zschornack, "Ionization and charge dispersion in electron cyclotron resonance ion sources", *Nuclear Instruments and Methods in Physics Research Section A: Accelerators, Spectrometers, Detectors and Associated Equipment*, vol. 302, no. 1, pp. 1–5, 1991, ISSN: 0168-9002. DOI: https://doi.org/10.1016/0168-9002(91)90485-9. [Online]. Available: https://www.sciencedirect.com/science/article/pii/0168900291904859.

[37] G. D. Shirkov, "A classical model of ion confinement and losses in ECR ion sources", *Plasma Sources Science and Technology*, vol. 2, no. 4, pp. 250–257, Nov. 1993. DOI: 10.1088/0963-0252/2/4/004. [Online]. Available: https://doi.org/10.1088/0963-0252/2/4/004.

[38] R. C. Pardo, R. Harkewicz, and P. J. Billquist, "Time evolution of charge states in an electron cyclotron resonance ion sources)", *Review of Scientific Instruments*, vol. 67, no. 4, pp. 1602–1605, 1996. DOI: 10.1063/1.1146900.

[39] M. Imanaka, T. Nakagawa, H. Arai, I. Arai, and S. M. Lee, "Plasma diagnostics of liquid he-free sc-ecr ion source (shiva) with use of laser ablation technique", *Nuclear Instruments and Methods in Physics Research Section B: Beam Interactions with Materials and Atoms*, vol. 237, no. 3, pp. 647–655, 2005, ISSN: 0168-583X. DOI: https://doi.org/10.1016/j.nimb.2005.04.105.

[40] D. Neben *et al.*, "Fast Sputtering Measurement Studies using Uranium with the NSCL ECR Ion Sources", in *Proc. of International Workshop on ECR Ion Sources (ECRIS'16), Busan, Korea, August 28 - September 1, 2016*, (Busan, Korea), ser. International Workshop on ECR Ion Sources, Geneva, Switzerland: JACoW, Oct. 2016, pp. 129–133, ISBN: 978-3-95450-186-1. DOI: https://doi.org/10.18429/JACoW-ECRIS2016-WEPP40.

[41] D. Neben, G. Machicoane, G. Parsey, A. Pham, J. Stetson, and J. Verboncoeur, "An Analysis of Fast Sputtering Studies for Ion Confinement Time", in *Proc. of Linear Accelerator Conference (LINAC'16), East Lansing, MI, USA, 25-30 September 2016*, (East Lansing, MI, USA), ser. Linear Accelerator Conference, Geneva, Switzerland: JACoW, May 2017, pp. 475–477, ISBN: 978-3-95450-169-4. DOI: https://doi.org/10.18429/JACoW-LINAC2016-TUPRC032.

[42] M. Marttinen, J. Angot, A. Annaluru, P. Jardin, T. Kalvas, H. Koivisto, S. Kosonen, R. Kronholm, L. Maunoury, O. Tarvainen, V. Toivanen, and P. Ujic, "Estimating ion confinement times from beam current transients in conventional and charge breeder ECRIS", *Review of Scientific Instruments*, vol. 91, no. 1, Jan. 2020. DOI: 10.1063/1.5128546. [Online]. Available: https://doi.org/10.1063/1.5128546.

[43] G. D. Shirkov, "Highly charged ion production in ECR source of heavy ions", 36 p, 1994. [Online]. Available: https://cds.cern.ch/record/276886.

[44] V. Mironov, O. Hohn, S. Runkel, L. Schmidt, G. Shirkov, K. Stiebing, H. Schmidt-B, and A. Schemppó, "Laser ablation plasma injection into the frankfurt 14 ghz ecris", Jan. 1999.

[45] V. Mironov, S. Bogomolov, A. Bondarchenko, A. Efremov, and V. Loginov, "Numerical model of electron cyclotron resonance ion source", *Phys. Rev. ST Accel. Beams*, vol. 18, p. 123 401, 12 Dec. 2015. DOI: 10.1103/PhysRevSTAB.18.123401. [Online]. Available: https://link.aps.org/doi/10.1103/PhysRevSTAB.18.123401.

[46] C. Li, Y. Qu, and J. Wang, "State-selective radiative recombination cross sections of argon ions", *Journal of Quantitative Spectroscopy and Radiative Transfer*, vol. 113, no. 15, pp. 1920–1927, Oct. 2012. DOI: 10.1016/j.jqsrt.2012.05.005. [Online]. Available: https://doi.org/10.1016/j.jqsrt.2012.05.005.

[47] M. A. Lennon, K. L. Bell, H. B. Gilbody, J. G. Hughes, A. E. Kingston, M. J. Murray, and F. J. Smith, "Recommended data on the electron impact ionization of atoms and ions: Fluorine to nickel", *Journal of Physical and Chemical Reference Data*, vol. 17, no. 3, pp. 1285–1363, 1988. DOI: 10.1063/1.555809. [Online]. Available: https://doi.org/10.1063/1.555809.

[48] R. Geller, P. Ludwig, and G. Melin, "Metal ion production in ECRIS (invited)", *Review of Scientific Instruments*, vol. 63, no. 4, pp. 2795–2800, Apr. 1992. DOI: 10.1063/1.1142810. [Online]. Available: https://doi.org/10.1063/1.1142810.

[49] R. Kronholm, T. Kalvas, H. Koivisto, and O. Tarvainen, "Spectroscopic method to study low charge state ion and cold electron population in ECRIS plasma", *Review of Scientific Instruments*, vol. 89, no. 4, Apr. 2018. DOI: 10.1063/1.5023434. [Online]. Available: https://doi.org/10.1063/1.5023434.

[50] K. S. Golovanivsky, *Instruments and Experimental Techniques (New York: Plenum)*, vol. 28, no. 5, p. 98, 1986.

[51] A. A. Ivanov and K. Wiesemann, "Ion confinement in electron cyclotron resonance ion sources (ecris): Importance of nonlinear plasma-wave interaction", *IEEE Transactions on Plasma Science*, vol. 33, pp. 1743–1762, 6 I 2005, ISSN: 00933813. DOI: 10.1109/TPS.2005.860078.

[52] T. Rognlien and T. Cutler, "Transition from pastukhov to collisional confinement in a magnetic and electrostatic well", *Nuclear Fusion*, vol. 20, no. 8, pp. 1003–1011, Aug. 1980. DOI: 10.1088/0029-5515/20/8/007. [Online]. Available: https://doi.org/10.1088/0029-5515/20/8/007.

[53] D. R. Whaley and W. D. Getty, "Ion temperature effects on ion charge-state distributions of an electron cyclotron resonant ion source", *Physics of Fluids B: Plasma Physics*, vol. 2, no. 6, pp. 1195–1203, Jun. 1990. DOI: 10.1063/1.859256. [Online]. Available: https://doi.org/10.1063/1.859256.

[54] V. Pastukhov, "Collisional losses of electrons from an adiabatic trap in a plasma with a positive potential", *Nuclear Fusion*, vol. 14, no. 1, pp. 3–6, Jan. 1974. DOI: 10.1088/0029-5515/14/1/001. [Online]. Available: https://doi.org/10.1088/0029-5515/14/1/001.

[55] ——, "Classical longitudinal plasma losses from open adiabatic traps", in *Reviews of Plasma Physics*, Springer US, 1987, pp. 203–259. DOI: 10.1007/978-1-4613-1777-7_3.

[56] M. A. Leitner, D. Wutte, and C. M. Lyneis, "Design of the extraction system of the superconducting ecr ion source venus*", in *Proceedings of the 2001 Particle Accelerator Conference, Chicago*, P. Lucas and S. Webber, Eds., Argonne National Laboratory, Fermi National Accelerator, and Laboratory Oak Ridge National Laboratory, vol. 5, Chicago, Illinois U.S.A.: IEEE, 2001, pp. 67–69.

[57] D. Wutte, S. Abbott, M. A. Leitner, and C. M. Lyneis, "High intensity metal ion beam production with ecr ion sources at the lawrence berkeley national laboratory", *Review of Scientific Instruments*, vol. 73, no. 2, pp. 521–524, 2002. DOI: 10.1063/1.1425781. eprint: https://doi.org/10.1063/1.1425781. [Online]. Available: https://doi.org/10.1063/1.1425781.

[58] J. Mandin, "Étude expérimentale et simulation des conditions d'extraction d'un faisceau d'ions multichargés d'une source à résonance cyclotronique électronique", Theses, Université de Caen, Dec. 1996. [Online]. Available: http://hal.in2p3.fr/in2p3-00008706.

[59] L. Panitzsch, M. Stalder, and R. F. Wimmer-Schweingruber, "Spatially resolved measurements of electron cyclotron resonance ion source beam profile characteristics", *Review of Scientific Instruments*, vol. 82, no. 3, p. 033 302, 2011. DOI: 10.1063/1.3553013. eprint: https://doi.org/10.1063/1.3553013. [Online]. Available: https://doi.org/10.1063/1.3553013.

[60] L. Panitzsch, T. Peleikis, M. Stalder, and R. F. Wimmer-Schweingruber, "Spatially resolved charge-state and current-density distributions at the extraction of an electron cyclotron resonance ion source", *Review of Scientific Instruments*, vol. 82, no. 9, p. 093 302, 2011. DOI: 10.1063/1.3637462. eprint: https://doi.org/10.1063/1.3637462. [Online]. Available: https://doi.org/10.1063/1.3637462.

[61] V. Mironov and J. P. M. Beijers, "Three-dimensional simulations of ion dynamics in the plasma of an electron cyclotron resonance ion source", *Physical Review Special Topics - Accelerators and Beams*, vol. 12, no. 7, Jul. 2009. DOI: 10.1103/physrevstab.12.073501. [Online]. Available: https://doi.org/10.1103/physrevstab.12.073501.

[62] V. Mironov, S. Bogomolov, A. Bondarchenko, A. Efremov, V. Loginov, and D. Pugachev, "Spatial distributions of plasma potential and density in electron cyclotron resonance ion source", *Plasma Sources Science and Technology*, vol. 29, no. 6, p. 065 010, Jun. 2020. DOI: 10.1088/1361-6595/ab62dc. [Online]. Available: https://doi.org/10.1088/1361-6595/ab62dc.

[63] J. Huba, U. S. O. of Naval Research, and N. R. L. (U.S.), *NRL Plasma Formulary*, ser. NRL publication. Naval Research Laboratory, 2016.

[64] T. Lamy, J. Angot, M. Marie-Jeanne, J. Médard, P. Sortais, T. Thuillier, A. Galatà, H. Koivisto, and O. Tarvainen, "Fine frequency tuning of the phoenix charge breeder used as a probe for ecris plasma", in *Proceedings of ECRIS2010, Grenoble, France*, Jan. 2011.

[65] A. G. Drentje, "Techniques and mechanisms applied in electron cyclotron resonance sources for highly charged ions", *Review of Scientific Instruments*, vol. 74, no. 5, pp. 2631–2645, Apr. 2003. DOI: 10.1063/1.1569408. [Online]. Available: https://doi.org/10.1063/1.1569408.

[66] F. F. Chen, *Introduction to Plasma Physics and Controlled Fusion*. Springer International Publishing, 2016. DOI: 10.1007/978-3-319-22309-4. [Online]. Available: https://doi.org/10.1007%2F978-3-319-22309-4.

[67] C. C. Petty, D. L. Goodman, D. L. Smatlak, and D. K. Smith, "Confinement of multiply charged ions in an electron cyclotron resonance heated mirror plasma", *Physics of Fluids B: Plasma Physics*, vol. 3, no. 3, pp. 705–714, Mar. 1991, ISSN: 0899-8221. DOI: 10.1063/1.859867. [Online]. Available: http://dx.doi.org/10.1063/1.859867.

[68] O. Tarvainen, T. Lamy, J. Angot, T. Thuillier, P. Delahaye, L. Maunoury, J. Choinski, L. Standylo, A. Galatà, G. Patti, and H. Koivisto, "Injected 1+ ion beam as a diagnostics tool of charge breeder ECR ion source plasmas", *Plasma Sources Science and Technology*, vol. 24, no. 3, p. 035 014, May 2015. DOI: 10.1088/0963-0252/24/3/035014. [Online]. Available: https://doi.org/10.1088/0963-0252/24/3/035014.

[69] O. Tarvainen, H. Koivisto, A. Galatà, J. Angot, T. Lamy, T. Thuillier, P. Delahaye, L. Maunoury, D. Mascali, and L. Neri, "Diagnostics of a charge breeder electron cyclotron resonance ion source helium plasma with the injection of $^{23}Na^{1+}$ ions", *Phys. Rev. Accel. Beams*, vol. 19, p. 053 402, 5 May 2016. DOI: 10.1103/PhysRevAccelBeams.19.053402. [Online]. Available: https://link.aps.org/doi/10.1103/PhysRevAccelBeams.19.053402.

[70] A. Drentje, "The ECR ion source and associated equipment at the KVI", *Nuclear Instruments and Methods in Physics Research Section B: Beam Interactions with Materials and Atoms*, vol. 9, no. 4, pp. 526–528, Jul. 1985. DOI: 10.1016/0168-583x(85)90360-x. [Online]. Available: https://doi.org/10.1016/0168-583x(85)90360-x.

[71] D. Morrissey and B. Sherrill, in *In-Flight Separation of Projectile Fragments*. Springer Lecture Notes Phys, Aug. 2004, vol. 651, pp. 113–135, ISBN: 978-3-540-22399-3. DOI: 10.1007/978-3-540-44490-9_4.

[72] M. Lindroos, "Review of ISOL-type Radioactive Beam Facilities", in *Proc. EPAC'04*, (Lucerne, Switzerland, Jul. 2004), JACoW Publishing, Geneva, Switzerland, 2004. [Online]. Available: http://accelconf.web.cern.ch/e04/papers/TUXCH01.pdf.

[73] J. Angot, O. Tarvainen, T. Thuillier, M. Baylac, T. Lamy, P. Sole, and J. Jacob, "Charge breeding time investigations of electron cyclotron resonance charge breeders", *Phys. Rev. Accel. Beams*, vol. 21, p. 104 801, 10 Oct. 2018. DOI: 10.1103/PhysRevAccelBeams.21.104801. [Online]. Available: https://link.aps.org/doi/10.1103/PhysRevAccelBeams.21.104801.

[74] J. Angot, A. Galatà, L. Maunoury, T. Thuillier, M. Baylac, M. Migliore, and P. Sole, "Contaminants reduction in ecr charge breeders by lnl lpsc ganil collaboration", in *ECRIS 2020 proceedings WEZZO02*, 2020.

[75] A. Girard, "Plasma diagnosis related to ion sources (invited)", *Review of Scientific Instruments*, vol. 63, no. 4, pp. 2676–2682, 1992. DOI: 10.1063/1.1143806.

[76] J. Noland, O. Tarvainen, J. Benitez, D. Leitner, C. Lyneis, and J. Verboncoeur, "Studies of electron heating on a 6.4 GHz ECR ion source through measurement of diamagnetic current and plasma bremsstrahlung", *Plasma Sources Science and Technology*, vol. 20, no. 3, p. 035 022, Apr. 2011. DOI: 10.1088/0963-0252/20/3/035022. [Online]. Available: https://doi.org/10.1088/0963-0252/20/3/035022.

[77] R. Harkewicz, J. Stacy, J. Greene, and R. C. Pardo, "Solid material evaporation into an electron cyclotron resonance source by laser ablation", *Review of Scientific Instruments*, vol. 65, no. 4, pp. 1104–1106, 1994. DOI: 10.1063/1.1145078.

[78] R. C. Vondrasek, R. H. Scott, R. C. Pardo, and D. Edgell, "Techniques for the measurement of ionization times in ecr ion sources using a fast sputter sample and fast gas valve", *Review of Scientific Instruments*, vol. 73, no. 2, pp. 548–551, Feb. 2002, ISSN: 1089-7623. DOI: 10.1063/1.1430273. [Online]. Available: http://dx.doi.org/10.1063/1.1430273.

[79] R. Harkewicz, P. J. Billquist, J. P. Greene, J. A. Nolen, and R. C. Pardo, "Ion plasma sputtering as a method of introducing solid material into an electron cyclotron resonance ion source", *Review of Scientific Instruments*, vol. 66, no. 4, pp. 2883–2887, 1995. DOI: 10.1063/1.1146501.

[80] M. Guerra, P. Amaro, C. I. Szabo, A. Gumberidze, P. Indelicato, and J. P. Santos, "Analysis of the charge state distribution in an ECRIS ar plasma using high-resolution x-ray spectra", *Journal of Physics B: Atomic, Molecular and Optical Physics*, vol. 46, no. 6, p. 065 701, Mar. 2013. DOI: 10.1088/0953-4075/46/6/065701. [Online]. Available: https://doi.org/10.1088/0953-4075/46/6/065701.

[81] H. J. West, "Calculation of ion charge state distribution in ecr ion source", Lawrence Livermore National Laboratory, Tech. Rep. UCRL-53391, 1982.

[82] J. Angot, T. Lamy, M. Marie-Jeanne, P. Sortais, and T. Thuillier, "Lpsc phoenix ecr charge breeder beam optics and efficiencies", in *ECRIS 2012 proceedings THYO02*, 2012.

[83] S. C. Jeong, M. Oyaizu, N. Imai, Y. Hirayama, H. Ishiyama, H. Miyatake, K. Niki, M. Okada, Y. X. Watanabe, Y. Otokawa, A. Osa, and S. Ichikawa, "Wall-loss distribution of charge breeding ions in an electron cyclotron resonance ion source", *Review of Scientific Instruments*, vol. 82, no. 3, Mar. 2011, ISSN: 1089-7623. DOI: 10.1063/1.3567802. [Online]. Available: http://dx.doi.org/10.1063/1.3567802.

[84] *Thermal design of refrigerated hexapole 18 GHz ECRIS HIISI*, weommh04, Institute of Applied Physics of the Russian Academy of Sciences, Nizhny Novgorod, Russia: Joint Accelerator Conferences Website (JACoW), Aug. 2014.

[85] R. Geller, C. Tamburella, and J. L. Belmont, "The isol–mafios source (invited)", *Review of Scientific Instruments*, vol. 67, no. 3, pp. 1281–1285, 1996. DOI: 10.1063/1.1146649.

[86] C. Tamburella, J. L. Belmont, G. Bizouard, J. F. Bruandet, R. Geller, G. Gimond, and B. Vignon, "Production of multicharged radioactive ion beams: The 1+ to n+ charge state transformation for the production, ionisation, accélération de faisceaux exotiques project", *Review of Scientific Instruments*, vol. 68, no. 6, pp. 2319–2321, 1997. DOI: 10.1063/1.1148142.

[87] T. Lamy, J. Angot, T. Thuillier, P. Delahaye, L. Maunoury, J. Choinski, L. Standylo, A. Galata, G. Patti, H. Koivisto, and O. Tarvainen, "Experimental activities with the lpsc charge breeder in the european context", in *Proceedings of ECRIS 2014 : the 21st International Workshop on ECR Ion Sources*, Available online http://accelconf.web.cern.ch/AccelConf/ECRIS2014/papers/weobmh01.pdf, Institute of Applied Physics of the Russian Academy of Sciences, Nizhny Novgorod, Russia: Joint Accelerator Conferences Website (JACoW), Aug. 2014, pp. 120–126.

[88] O. Tarvainen, J. Angot, T. Thuillier, M. Migliore, L. Maunoury, and P. Chauveau, "The capture of injected 1+ ions in charge breeder electron cyclotron resonance ion source plasma", *Plasma Sources Science and Technology*, vol. 31, no. 12, p. 125 003, Dec. 2022. DOI: 10.1088/1361-6595/aca713. [Online]. Available: https://doi.org/10.1088/1361-6595/aca713.

[89] J. Angot, T. Thuillier, O. Tarvainen, M. Baylac, J. Jacob, T. Lamy, M. Migliore, and P. Sole, "Recent improvements of the lpsc charge breeder", *poster*, 2017.

[90] C. Perret, PhD thesis, Université Joseph Fourier, Grenoble, 1998.

[91] K. T. Dolder and B. Peart, "Collisions between electrons and ions", *Reports on Progress in Physics*, vol. 39, no. 8, pp. 693–749, Aug. 1976. DOI: 10.1088/0034-4885/39/8/001. [Online]. Available: https://doi.org/10.1088/0034-4885/39/8/001.

[92] K. L. Bell, H. B. Gilbody, J. G. Hughes, A. E. Kingston, and F. J. Smith, "Recommened Data on the Electron Impact Ionization of Light Atoms and Ions", *J. Phys. Chem.*, vol. 12, no. 4, pp. 891–916, 1983.

[93] M. Luntinen, V. Toivanen, H. Koivisto, J. Angot, T. Thuillier, O. Tarvainen, and G. Castro, "Diagnostics of highly charged plasmas with multicomponent 1+ ion injection", *Physical Review E*, vol. 106, no. 5, Nov. 2022. DOI: 10.1103/physreve.106.055208. [Online]. Available: https://doi.org/10.1103/physreve.106.055208.

[94] I. Izotov, O. Tarvainen, V. Skalyga, D. Mansfeld, H. Koivisto, R. Kronholm, V. Toivanen, and V. Mironov, "Measurements of the energy distribution of electrons lost from the minimum b-field—the effect of instabilities and two-frequency heating", *Review of Scientific Instruments*, vol. 91, no. 1, Jan. 2020. DOI: 10.1063/1.5128322. [Online]. Available: https://doi.org/10.1063/1.5128322.

[95] B. Isherwood and G. Machicoane, "Measurement of the energy distribution of electrons escaping confinement from an electron cyclotron resonance ion source", *Review of Scientific Instruments*, vol. 91, no. 2, Feb. 2020. DOI: 10.1063/1.5129656. [Online]. Available: https://doi.org/10.1063/1.5129656.

[96] V. Pierrard and M. Lazar, "Kappa distributions: Theory and applications in space plasmas", *Solar Physics*, vol. 267, no. 1, pp. 153–174, Oct. 2010. DOI: 10.1007/s11207-010-9640-2. [Online]. Available: https://doi.org/10.1007/s11207-010-9640-2.

[97] M. Sakildien, O. Tarvainen, R. Kronholm, I. Izotov, V. Skalyga, T. Kalvas, P. Jones, and H. Koivisto, "Experimental evidence on microwave induced electron losses from ecris plasma", *Physics of Plasmas*, vol. 25, no. 6, p. 062 502, 2018. DOI: 10.1063/1.5029443.

[98] O. Waldmann and B. Ludewigt, "Measurements of beam current density and proton fraction of a permanent-magnet microwave ion source", *Review of Scientific Instruments*, vol. 82, no. 11, Nov. 2011, ISSN: 1089-7623. DOI: 10.1063/1.3660282. [Online]. Available: http://dx.doi.org/10.1063/1.3660282.

[99] H. Knudsen, H. K. Haugen, and P. Hvelplund, "Single-electron-capture cross section for medium- and high-velocity, highly charged ions colliding with atoms", *Physical Review A*, vol. 23, no. 2, pp. 597–610, Feb. 1981, ISSN: 0556-2791. DOI: 10.1103/physreva.23.597. [Online]. Available: http://dx.doi.org/10.1103/PhysRevA.23.597.

[100] M. Luntinen, J. Angot, H. Koivisto, O. Tarvainen, T. Thuillier, and V. Toivanen, "The effects of electron energy distribution and ionization cross section uncertainty on charge breeder ion source diagnostics with pulsed 1+ injection", *Physics of Plasmas*, vol. 30, no. 7, Jul. 2023. DOI: 10.1063/5.0150198. [Online]. Available: https://doi.org/10.1063/5.0150198.

[101] M. Luntinen, J. Angot, O. Tarvainen, V. Toivanen, T. Thuillier, and H. Koivisto, "Measurement of ionization, charge exchange and ion confinement times in charge breeder ECR ion sources with short pulse 1+ injection of metal ions", *Journal of Physics: Conference Series*, vol. 2244, no. 1, p. 012 009, Apr. 2022. DOI: 10.1088/1742-6596/2244/1/012009. [Online]. Available: https://doi.org/10.1088/1742-6596/2244/1/012009.

ORIGINAL PAPERS

PI

METHOD FOR ESTIMATING CHARGE BREEDER ECR ION SOURCE PLASMA PARAMETERS WITH SHORT PULSE 1+ INJECTION OF METAL IONS

by

J Angot, M Luntinen, T Kalvas, H Koivisto, R Kronholm, L Maunoury, O Tarvainen, T Thuillier, V Toivanen

Method for estimating charge breeder ECR ion source plasma parameters with short pulse 1+ injection of metal ions

J. Angot[1,†], M. Luntinen[2,*], T. Kalvas[2], H. Koivisto[2], R. Kronholm[2], L. Maunoury[4], O. Tarvainen[3], T. Thuillier[1], and V. Toivanen[2]

[1]Univ. Grenoble Alpes, CNRS, Grenoble INP, LPSC-IN2P3, 53 Avenue des Martyrs, 38000 Grenoble, France
[2]University of Jyväskylä, Department of Physics, Survontie 9D, 40500 Jyväskylä, Finland
[3]STFC ISIS Pulsed Spallation Neutron and Muon Facility, Rutherford Appleton Laboratory, Harwell, OX11 0QX, UK
[4]Grand Accélérateur National d'Ions Lourds, Boulevard Henri Becquerel, 14000 Caen, France
[†]julien.angot@lpsc.in2p3.fr
[*]misapema@jyu.fi

December 2020

Abstract

A new method for determining plasma parameters from beam current transients resulting from short pulse 1+ injection of metal ions into a Charge Breeder Electron Cyclotron Resonance Ion Source (CB-ECRIS) has been developed. The proposed method relies on few assumptions, and yields local values for the ionisation times $1/n_e \langle \sigma v \rangle_{q \to q+1}^{\mathrm{inz}}$, charge exchange times $1/n_0 \langle \sigma v \rangle_{q \to q-1}^{\mathrm{cx}}$, the ion confinement times τ^q, as well as estimates for the minimum plasma energy contents $n_e \langle E_e \rangle$ and the plasma triple products $n_e \langle E_e \rangle \tau^q$. The method is based on fitting the current balance equation on the extracted beam currents of high charge state ions, and using the fitting coefficients to determine the postdictions for the plasma parameters via an optimisation routine. The method has been applied for the charge breeding of injected K^+ ions in helium plasma. It is shown that the confinement times of K^{q+} charge states range from $2.6^{+0.8}_{-0.4}$ ms to $16.4^{+18.3}_{-6.8}$ ms increasing with the charge state. The ionisation and charge exchange times for the high charge state ions are $2.6^{+0.5}_{-0.5}$ ms–$12.6^{+2.6}_{-3.2}$ ms and $3.7^{+5.0}_{-1.6}$ ms–$357.7^{+406.7}_{-242.4}$ ms, respectively. The plasma energy content is found to be $2.5^{+4.3}_{-1.8} \times 10^{15}$ eV/cm^3.

1

1   Introduction

Minimum-B Electron Cyclotron Resonance Ion Sources (ECRIS) [1] are widely used to produce ion beams for particle accelerators and as charge breeders in ISOL facilities [2], [3]. The performance improvements of these installations are dependent in part on the ECRIS development, which is driven by empirical laws obtained from decades of research and development. Despite recent studies using optical spectroscopy methods [4], [5] and $1+/n+$ diagnostics [6], [7], understanding of the fundamental ECRIS plasma behavior, such as the ion confinement, the electron energy distribution or the plasma electrostatic potential distribution is still imprecise.

In the ECRIS, Highly Charged Ions (HCIs) are created through stepwise electron-impact ionisation, whereas the principal charge decreasing mechanism is due to charge exchange with neutral atoms, which dominates over radiative recombination (Ref. [8] via [9]). The confinement of ions inside the plasma volume determines on one hand the time scale in which an ion may become further ionised, and on the other hand the rate at which the ions escape confinement and become available for beam formation. The plasma characteristic times — the ion confinement time, the ionisation time and charge exchange time — therefore play an important role in obtaining high intensity beams of HCIs. Shorter ionisation times and longer confinement and charge exchange times lead to more efficient HCI production.

Experimentally, only a limited number of physical quantities can be observed, due in part to the fact that access to the plasma is technically challenging owing to the surrounding components, but also because the measurements must be limited to non-invasive methods in order to avoid corrupting the results by perturbing the plasma state. At present this means that one is limited to measuring the plasma radiation emissions, and the particles escaping confinement e.g. by measuring the extracted beam current.

Transient methods for studying the effects of material injection on the extracted beam currents were first proposed by Pardo [10]. These methods consist of pulsed injection of material into the support plasma and analysing the responses observed in the extracted current. Several techniques are used for pulsed material injection, e.g. laser ablation [11], fast gas injection [12] sputtering [12]–[14], and $1+$ injection [7]. A 0D code is then generally used to reproduce the measured beam currents by numerically optimising the plasma parameters involved in a system of differential equations formed by physical models describing the plasma [10], [15], [16].

In this work such transient measurements were conducted using short pulse $1+$ injection of K into a He support plasma of a Charge Breeder ECRIS (CB-ECRIS) [17]. $1+$ injection was chosen, because the number, energy and capture rate of injected particles can be precisely managed by tuning the $1+$ source, contrary to e.g. sputtering where the yield depends on the energy of the ions bombarding the sample and, therefore, on the (unknown) local charge state distribution of the plasma. Alkali metal ions were chosen as the injected species to prevent wall recycling effects, and the helium buffer was used to obtain a clean Charge State Distribution (CSD) with as few overlapping peaks in the q/m spectrum as possible. In the case of a heavier support gas, overlapping peaks should be resolved using a high precision spectrometer or collimation system. A critical reason for using K as the injected species was that the necessary ionisation rate coefficient data was readily available.

We propose a new 0D-approach for analysing the current transients. For this purpose the balance equation governing the time evolution of the ion densities is converted into extraction current formalism, and the resultant differential equation is fitted on three consecutive charge state currents. The obtained fitting parameters are used to calculate the plasma characteristic times,

2

energy content and triple product. Because the fitting is done on only three charge states at a time, the results derived from them are local to the plasma volume where they originate. The basis of the method is laid out in detail in sections 2, and 3, and the experimental methods are described in section 4. As a further improvement to pre-existing 0D-methods, this one can be applied without a priori knowledge of input parameters $(T_e, T_i^q, n_e, n_0, \ldots)$ or assumptions regarding the ion confinement scheme, while still including ionisation, charge-exchange and particle loss channels in the model. This method thus provides important improvements on the approach employed e.g. in Ref. [16], where the ion beam current is taken to represent the plasma internal CSD directly, and the confinement time is assumed to be a linear function of the ion charge state q, which is not the case as per our results.

The scope of this work is to rigorously introduce the novel method which can then later be used for parametric studies, and to describe the experimental and numerical procedures involved[1].

2 Theoretical foundations

The balance equation [1], [18], [19] defines a group of coupled differential equations, which describe the time evolution of the ion population densities in the plasma. For the charge state q the temporal change of the number density, n^q,[2] is given by:

$$
\begin{aligned}
\frac{\mathrm{d}n^q}{\mathrm{d}t} = &+ \langle \sigma v \rangle_{q-1 \to q}^{\mathrm{inz}} \, n_e n^{q-1} - \langle \sigma v \rangle_{q \to q+1}^{\mathrm{inz}} \, n_e n^q \\
&+ \langle \sigma v \rangle_{q+1 \to q}^{\mathrm{cx}} \, n_0 n^{q+1} - \langle \sigma v \rangle_{q \to q-1}^{\mathrm{cx}} \, n_0 n^q \\
&- \frac{n^q}{\tau^q}
\end{aligned}
\tag{1}
$$

Here the rate coefficients $\langle \sigma v \rangle_{q \to q+1}^{\mathrm{inz}}$ and $\langle \sigma v \rangle_{q \to q-1}^{\mathrm{cx}}$ describe ionisation from state q to $q+1$, and charge exchange from state q to $q-1$ respectively. The ionisation is assumed to occur in a stepwise process with electrons (density n_e) and charge exchange with the neutral atoms of the support plasma (density n_0). The last term in the balance equation depicts the actual loss rate of ions from the plasma volume, and defines the confinement time τ^q of the ion population. In our treatment both n_e and n_0 are assumed to be fixed by the supporting He plasma. In the case of a non-metallic injected species, the balance equation should be amended with a term accounting for the wall recycling effect. There are no fundamental reasons for why such a source term could not be included but it would increase the uncertainty. Thus, for the experiments introducing the method we have chosen alkali metal injection.

The reaction rate coefficient is defined as the weighted average

$$
\langle \sigma v \rangle = \int_0^\infty \sigma\,(v)\, v f\,(v)\, \mathrm{d}v,
\tag{2}
$$

where v is the relative speed of the interacting particles, σ the reaction cross section, and f the probability distribution for the relative speed.

---

[1] Access to the numerical code and the data that support the findings of this study are openly available at the following URL/DOI: `https://github.com/misapema-jyfl/popTauPy` (code), doi:10.6084/m9.figshare.13602827.v1 (data)

[2] The subscript i specifying the ion species is omitted as the support plasma perturbation is assumed small enough to be negligible, and the group of differential equations can be written solely for the injected species.

Table 1 – The coefficients for the Voronov semi-empirical analytical equation for the electron-impact ionisation rate coefficient in the case of potassium. δE is the ionisation threshold for the charge state q ion, while P, A, X, and K are experimentally determined fitting coefficients. Data corresponding to ionisation from closed electronic shells are highlighted. Data from Ref. [20].

q	δE (eV)	P	A	X	K
0+	4.3	1	2.02E-07	0.272	0.31
1+	31.6	1	4.01E-08	0.371	0.22
2+	45.8	1	1.5E-08	0.433	0.21
3+	60.9	1	1.94E-08	0.889	0.16
4+	82.7	1	6.95E-09	0.494	0.18
5+	99.4	1	4.11E-09	0.54	0.17
6+	117.6	1	2.23E-09	0.519	0.16
7+	154.7	1	2.15E-09	0.828	0.14
8+	175.8	0	1.61E-09	0.642	0.13
9+	504	1	1.07E-09	0.695	0.13
10+	564.7	1	3.78E-10	0.173	0.3
11+	629.4	0	6.24E-10	0.418	0.33
12+	714.6	1	2.29E-10	0.245	0.28
13+	786.6	1	1.86E-10	0.344	0.23
14+	861.1	0	2.69E-10	0.396	0.37
15+	968	1	1.06E-10	0.912	0.13
16+	1053.4	1	4.24E-11	0.737	0.16
17+	4610.9	0	1.38E-11	0.416	0.34
18+	4934.1	1	3.67E-12	0.555	0.18

In this work, the ionisation rate coefficients of K^{q+} were estimated using the semi-empirical expression by Voronov [20]:

$$\langle \sigma v \rangle_{q \to q+1}^{\text{inz}} = A \frac{1 + P \cdot U^{1/2}}{X + U} U^K e^{-U} \quad \text{cm}^3/\text{s}, \tag{3}$$

with

$$U \equiv \frac{\delta E}{T_e}. \tag{4}$$

Here the coefficients A, P, K and X are empirically determined coefficients from best fits to data, and δE is the ionisation threshold energy. The coefficients are tabulated in Table 1 according to Ref. [20]. It should be noted that Equation (3) and the tabulated coefficients assume the Maxwell-Boltzmann (M-B) distribution. The assumption of a M-B EED is a strong one, but one that is commonly used and mathematically well-defined. Since there is no knowledge of the energy distribution of the confined electrons [21], we have elected to use the rate coefficient formula based on the assumed M-B EED.

The cross section for charge exchange between an ion at charge state q and a neutral atom can be estimated as [4], [22]

$$\sigma_{q \to q-1}^{\text{cx}} = \pi r_0^2 q \left(\frac{I_0}{I} \right)^2 Z_{\text{eff}}, \tag{5}$$

where r_0 is the Bohr radius, I_0 the ionisation potential of hydrogen, I the ionisation potential of the neutral atom, and Z_{eff} [23], [24] its effective proton number as seen by the valence electron after the screening by inner shell electrons has been accounted for. Equation (5) is a geometrical cross section based on the Bohr atomic model.

The $\sigma_{q \to q-1}^{\text{cx}}$ is independent of the interaction energy up to around 10 keV/u [22], which is vastly in excess of the energy that an ion may realistically gain in the ECRIS plasma ($T_i \sim 10$ eV [4], [5]). Therefore, the rate coefficient for charge exchange may be obtained relatively simply as

$$\langle \sigma v \rangle_{q \to q-1}^{\text{cx}} = \sigma_{q \to q-1}^{\text{cx}} \langle v_i^q \rangle = \sigma_{q \to q-1}^{\text{cx}} \sqrt{\frac{8 T_i^q}{\pi m_i}}, \tag{6}$$

where $\langle v_i^q \rangle$ is the average speed of ions given a Maxwell-Boltzmann distribution, and m_i is the ion mass. In the above derivation neutrals were assumed cold relative to the ions.

2.1 Conversion of the balance equation to beam current formalism

The extracted beam current for charge state q can be expressed as [25], [26]

$$I^q = \kappa F_B(2L) S \frac{n^q q e}{\tau^q} \propto \frac{n^q q}{\tau^q}, \tag{7}$$

where κ is the transmission efficiency of the low energy beamline, $2L$ is the length of the plasma chamber, S the area of the extraction aperture, n^q the number density of ions at charge state q, e is the elementary charge, and τ^q the confinement time of the population of ions at charge state q. Equation (7) has been generalized by introducing the constant factor F_B, which depends on the extraction mirror ratio of the magnetic confinement structure. Assuming, that κ, S and L are the same for the consecutive charge states $q-1$, q and $q+1$, they can be absorbed into one constant which disappears upon substitution to the balance equation. The balance equation becomes in the extraction current formalism

$$\begin{aligned}
\frac{\mathrm{d}}{\mathrm{d}t} I^q =& n_e \langle \sigma v \rangle_{q-1 \to q}^{\text{inz}} \frac{q}{q-1} \frac{\tau^{q-1}}{\tau^q} I^{q-1} \\
&- \left(n_e \langle \sigma v \rangle_{q \to q+1}^{\text{inz}} + n_0 \langle \sigma v \rangle_{q \to q-1}^{\text{cx}} + 1/\tau^q \right) I^q \\
&+ n_0 \langle \sigma v \rangle_{q+1 \to q}^{\text{cx}} \frac{q}{q+1} \frac{\tau^{q+1}}{\tau^q} I^{q+1}.
\end{aligned} \tag{8}$$

By defining:

$$a_q = n_e \langle \sigma v \rangle_{q-1 \to q}^{\text{inz}} \frac{q}{q-1} \frac{\tau^{q-1}}{\tau^q} \tag{9}$$

$$b_q = \left(n_e \langle \sigma v \rangle_{q \to q+1}^{\text{inz}} + n_0 \langle \sigma v \rangle_{q \to q-1}^{\text{cx}} + 1/\tau^q \right) \tag{10}$$

$$c_q = n_0 \langle \sigma v \rangle_{q+1 \to q}^{\text{cx}} \frac{q}{q+1} \frac{\tau^{q+1}}{\tau^q}, \tag{11}$$

equation (8) becomes

$$\frac{\mathrm{d}}{\mathrm{d}t} I^q = a_q I^{q-1} - b_q I^q + c_q I^{q+1}. \tag{12}$$

Equation (12) may be used to determine the parameters a_q, b_q, and c_q by fitting to experimentally measured beam current transients $\mathrm{d}I^q/\mathrm{d}t$. This procedure is described in section 3.1. Because the fitting procedure is performed on three consecutive charge states at a time (as opposed to all of the charge states simultaneously), the obtained results correspond to plasma conditions at the location of origin for the charge states in question i.e. the results for each charge state are local.

We assume, that the plasma parameters are constants in time, i.e. that the perturbation on the support plasma caused by the 1+ injection pulse is sufficiently small, for n_e, T_e, n_0, the ion temperatures T_i^q and confinement times τ^q to be determined by the support plasma; rendering a_q, b_q, and c_q constant. The validity of this assumption is discussed in section 6.

2.2　Deconvolution of the characteristic values from the fitting parameters

The definitions (9), (10) and (11) hold for all q. From equation (11) we obtain (by choosing $q \rightarrow q - 1$):

$$c_{q-1} = n_0 \langle \sigma v \rangle_{q \rightarrow q-1}^{\mathrm{cx}} \frac{q-1}{q} \frac{\tau^q}{\tau^{q-1}}, \tag{13}$$

which can be rearranged to obtain

$$n_0 \langle \sigma v \rangle_{q \rightarrow q-1}^{\mathrm{cx}} = \frac{q}{q-1} \frac{\tau^{q-1}}{\tau^q} c_{q-1}. \tag{14}$$

The fraction τ^{q-1}/τ^q can be obtained from equation (9) as

$$\frac{\tau^{q-1}}{\tau^q} = \frac{q-1}{q} \frac{a_q}{n_e \langle \sigma v \rangle_{q-1 \rightarrow q}^{\mathrm{inz}}}. \tag{15}$$

By substituting equations (14) and (15) into equation (10), we obtain an expression for the confinement time:

$$\tau^q = \left. b_q - n_e \langle \sigma v \rangle_{q \rightarrow q+1}^{\mathrm{inz}} - \frac{a_q c_{q-1}}{n_e \langle \sigma v \rangle_{q-1 \rightarrow q}^{\mathrm{inz}}} \right)^{-1}, \tag{16}$$

which is a function of n_e, T_e and the fitting parameters. From equation (15) (making the substitution $q \rightarrow q + 1$) one obtains

$$\frac{q}{q+1} \frac{a_{q+1}}{n_e \langle \sigma v \rangle_{q \rightarrow q+1}^{\mathrm{inz}}} = \frac{\tau^q}{\tau^{q+1}}. \tag{17}$$

The confinement times in Equation (17) can be calculated using Equation (16) (simply substituting $q \rightarrow q + 1$ to obtain τ^{q+1}). This leads to the following equation for n_e and T_e:

$$\frac{q}{q+1} \frac{a_{q+1}}{n_e \langle \sigma v \rangle_{q \rightarrow q+1}^{\mathrm{inz}}} = \frac{b_{q+1} - n_e \langle \sigma v \rangle_{q+1 \rightarrow q+2}^{\mathrm{inz}} - \frac{a_{q+1} c_q}{n_e \langle \sigma v \rangle_{q \rightarrow q+1}^{\mathrm{inz}}}}{b_q - n_e \langle \sigma v \rangle_{q \rightarrow q+1}^{\mathrm{inz}} - \frac{a_q c_{q-1}}{n_e \langle \sigma v \rangle_{q-1 \rightarrow q}^{\mathrm{inz}}}} \tag{18}$$

where the T_e dependence resides in the ionisation rate coefficients. Having determined the coefficients a_q, b_q, and c_q from the experimental data it is possible to search for the allowed pairs of the parameters n_e and T_e which satisfy Equation (18). Mathematically the equation of two unknowns

6

has an infinitude of solutions, but the solution space may be constrained by physical considerations as explained in Section 3. The solution pairs constitute the set of *postdictions* for the possible range of (n_e, T_e) values in the support plasma, which could account for the measured a_q, b_q, c_q coefficients.

The ionisation time $(1/n_e \langle \sigma v \rangle_{q \to q+1}^{\mathrm{inz}})$ can be calculated using the obtained (n_e, T_e)-pairs and Equation (3). One may then also calculate from the definition (10) of the parameter b_q, the characteristic charge exchange time:

$$1/n_0 \langle \sigma v \rangle_{q \to q-1}^{\mathrm{cx}} = \left(b_q - 1/n_e \langle \sigma v \rangle_{q \to q+1}^{\mathrm{inz}} - 1/\tau^q \right)^{-1} \tag{19}$$

Note, that formulas (16), (17), (18), and (19) do not describe physical dependencies of observables on plasma parameters, as they are merely formulas for calculating their values based on the fitting coefficients, and other plasma parameters.

3 Numerical methods

3.1 Determining coefficients a_q, b_q and c_q

Equation (12) can be used to obtain the coefficients a_q, b_q, c_q by fitting to the measurement data, but due to the noise involved in the current measurement, calculating the derivative to make the fits is not practical. We instead used the 4$^{\mathrm{th}}$ order Runge-Kutta method to solve for $\mathfrak{I}^q(t)$ the system

$$\begin{cases} I^{q-1}(t), \\ \dot{\mathfrak{I}}^q(t) = l I^{q-1}(t) - m \mathfrak{I}^q(t) + n I^{q+1}(t), \\ I^{q+1}(t), \end{cases} \tag{20}$$

where I^{q-1} and I^{q+1} are taken from the measurement, and coefficients l, m, n can be varied. The residual of the measured current $I^q(t)$, and $\mathfrak{I}^q(t)$ is then minimised by the least squares method where the l, m and n corresponding to the minimum residue are taken to represent $a_q, b_q,$ and c_q.

3.2 Determining the plasma parameters

In order to find the pairs n_e, T_e, which satisfy the Equation (18), we defined a penalty function, namely the deviation of the two terms set by Eq. (18)

$$F^q(n_e, T_e) \equiv$$

$$\left| \frac{q}{q+1} \frac{a_{q+1}}{n_e \langle \sigma v \rangle_{q \to q+1}^{\mathrm{inz}}} - \frac{b_{q+1} - n_e \langle \sigma v \rangle_{q+1 \to q+2}^{\mathrm{inz}} - \frac{a_{q+1} c_q}{n_e \langle \sigma v \rangle_{q \to q+1}^{\mathrm{inz}}}}{b_q - n_e \langle \sigma v \rangle_{q \to q+1}^{\mathrm{inz}} - \frac{a_q c_{q-1}}{n_e \langle \sigma v \rangle_{q-1 \to q}^{\mathrm{inz}}}} \right| \Bigg/ \frac{q}{q+1} \frac{a_{q+1}}{n_e \langle \sigma v \rangle_{q \to q+1}^{\mathrm{inz}}} \tag{21}$$

which was minimised with the constraints

$$\begin{cases} 0 < \tau^q, \\ 0 < \tau^{q+1}, \\ 0 < 1/n_0 \langle \sigma v \rangle_{q \to q-1}^{\mathrm{cx}}, \\ n_{e,\mathrm{low}} < n_e < n_{e,\mathrm{co}}, \\ T_{e,\mathrm{low}} < T_e < T_{e,\mathrm{high}} \end{cases} \tag{22}$$

7

where τ^q and τ^{q+1} were calculated using Equation (16), and $1/n_0 \langle \sigma v \rangle^{\mathrm{cx}}_{q \to q-1}$ using Equation (19). The first three constraints are intuitive as they merely state that the characteristic times are positive. The upper limit for the support plasma electron density n_e can be taken to be the cut-off density which can be calculated from [1]

$$n_{e,\mathrm{co}} = \frac{\varepsilon_0 m_e (2\pi f)^2}{e^2}, \qquad (23)$$

where ε_0 is the vacuum permittivity, m_e is electron mass, e the elementary charge and f is the frequency of the inbound microwave. For the 14.5 GHz microwaves this value is 2.61×10^{12} cm^{-3}. The lower limit for n_e can be approximated based on the results from Ref. [6], where it was found that the lower limit for n_e increases as a function of the microwave power: Using 14.5 GHz frequency and 470 W microwave power they found $n_{e,\mathrm{low}}$ to be 4.4×10^{11} cm^{-3}. As a conservative lower limit, we take $n_{e,\mathrm{low}} = 1 \times 10^{11}$ cm^{-3} for the 500 W microwave power used herein. The lower limit for the electron temperature is positive and non-zero, and $T_{e,\mathrm{low}} = 10$ eV was chosen as it corresponds to the order of magnitude of the plasma potential [27]. The upper limit $T_{e,\mathrm{high}}$ is set to 10 keV, as according to Ref. [28] (as cited in Ref. [26]) the fraction of electrons having an energy higher than a few keV is between 20 % and 50 %. This corresponds to the warm electron population, which mostly accounts for the ionisation processes within the plasma. Based on an analysis of the solution sets (see supplement A.4) only such minima for which $F^q(n_e, T_e) < 10^{-4}$ were accepted, and solutions leading to negative (i.e. unphysical) results were discarded.

The semi-empirical analytical expression (3) was used to evaluate the necessary rate coefficients. In order to account for the uncertainty of Eq. (3), a Monte Carlo approach was employed, where a random systematic bias — within the uncertainty limits given for the formula — was added to each rate coefficient involved in the function $F^q(n_e, T_e)$. According to Voronov in Ref. [20], the uncertainty of the rate coefficients is 40 % − 60 %.

The flow of the code is illustrated in Figure 1. The algorithm was run using 1000 different, randomized uncertainty biases to ensure that the solution set was sufficiently sampled. The process produces a set of (n_e, T_e)-pairs, which minimise the penalty function within the given constraints. When the confinement times, ionisation times, charge exchange times and plasma energy contents are calculated for each pair, we obtain a distribution of results for each quantity, respectively. We take the median, and the 34.1-percentile below and above the median to represent the results, which corresponds to a one sigma uncertainty for a normal distribution.

The $N+$ pulse response of three consecutive charge states (I^{q-1}, I^q, and I^{q+1}) are necessary to estimate the a_q, b_q, and c_q for any given charge state. To solve Eq. (18), on the other hand, requires the parameters a_q, a_{q+1}, b_q, b_{q+1}, c_{q-1}, and c_q. To obtain them, five neighboring charge state currents must be measured. By extension, given X measured neighboring currents in the CSD, one can obtain a set of solutions for $X - 4$ charge states.

4 Experimental methods

The method consists of injecting short pulses of 1+ ions into a CB-ECRIS plasma and analysing the extracted n+ responses. High 1+ capture efficiencies, ranging between 50 % and 60 %, are typically measured for injected beam intensities up to 1 μA in continuous 1+ injection mode (CW mode) [29], [30]. The optimum 1+ ion capture efficiency is obtained when the velocity of the injected ions is equal to the average velocity of the support plasma ions [31]. It can be finely tuned by adjusting the potential difference ΔV between the source generating the 1+ beam and the charge breeder.
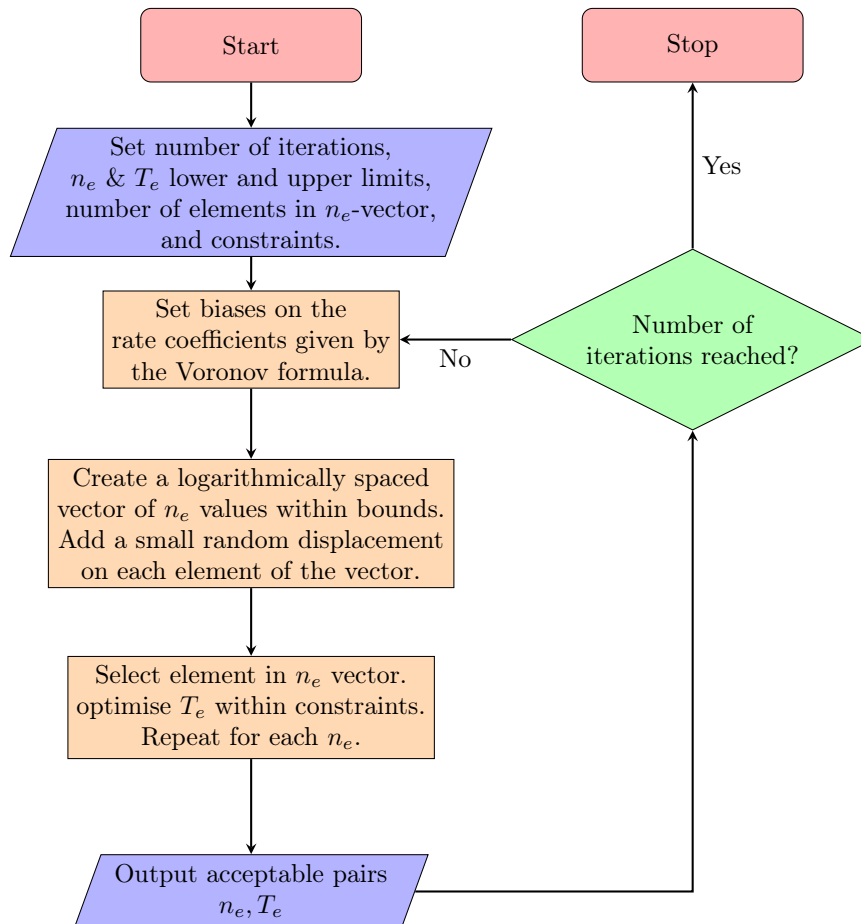
8

Figure 1 – Flowchart of the code designed to search for the acceptable (n_e, T_e)-pairs satisfying Equation (18).

Table 2 – Measured charge breeding efficiencies for charge states between K^+ and K^{12+}.

Ion	K^+	K^{2+}	K^{3+}	K^{4+}	K^{5+}	K^{6+}	K^{7+}	K^{8+}	K^{9+}	K^{10+}	K^{11+}	K^{12+}
Efficiency (%)	9.7	2.7	1.2	1.0	1.1	1.2	1.5	2.7	8.9	10.6	8.5	5.1

The number of injected particles is managed by tuning the 1+ source to produce the chosen 1+ beam intensity in order to minimise the perturbation of the buffer plasma.

4.1   Experimental setup

The measurements were conducted by injecting a K^+ beam into a He support plasma to obtain high charge breeding efficiencies [32]. K was chosen as the injected species because it is an alkali, so there is no recycling of the ions lost on the charge breeder plasma chamber wall into the plasma, and several consecutive charge states, ranging from 1+ to 12+, can be measured. It is also the heaviest alkali for which cross section / rate coefficient data was available.

Experiments were conducted on an upgraded version of the Laboratory of Subatomic Physics & Cosmology (LPSC) 1+→N+ test bench [17], see Figure 2, with respect to the configuration for the short pulse injection studies done previously [7]. After these modifications, which essentially consisted of improving the vacuum, and surface residue mitigation, the background vacuum pressure at injection was 2.5×10^{-8} mbar.

The charge breeder was assembled with a hexapole providing a 0.8 T radial magnetic field strength at plasma chamber wall, on the poles. An additional soft iron plug was mounted under vacuum to increase the axial magnetic field strength at injection [33]. The plasma electrode aperture diameter was 8 mm. For the experiments, the charge breeder was operated at 20 kV extraction voltage with a He plasma, the extracted beams being mass-analysed using the N+ dipole, and measured at the N+ Faraday Cup (FC) (see Fig. 2).

First, the charge breeder was tuned to optimise the K^{10+} efficiency in continuous 1+ injection mode. A 0.71 μA (0.44×10^{13} pps) K^+ beam was produced with the ion gun 1+ source [30]. The K^+ beam was selected by the 1+ beam line dipole magnet and injected into the charge breeder. The electrostatic pulsing system, set just before the 1+ dipole magnet, was used to pulse the 1+ beam into the charge breeder in order to calculate the charge breeding efficiencies taking into account the N+ background.

The ΔV parameter was carefully adjusted to optimise the capture of the injected 1+ ions. The optimum K^{10+} efficiency was found with the charge breeder axial magnetic field strength values of $B_{inj} = 1.58$ T, $B_{min} = 0.45$ T and $B_{ext} = 0.83$ T, the 14.5 GHz microwave power being set at 500 W. The vacuum level at injection was 8.7×10^{-8} mbar and the ΔV was set at -3.9 V. In this configuration, the ECR zone length on the charge breeder axis was simulated to be 122 mm.

Table 2 summarizes the measured charge breeding efficiencies of charge states between K^+ and K^{12+}. For reference, the best efficiency measured for K with He as a support gas was 11.7 % for K^{10+} in the previous test bench configuration [33], i.e. the data were taken in conditions relevant for the charge breeding process.

The influence of the 1+ beam injection on the plasma was checked in continuous mode, comparing the CSD extracted from the CB with and without 1+ injection. Without 1+ injection, the
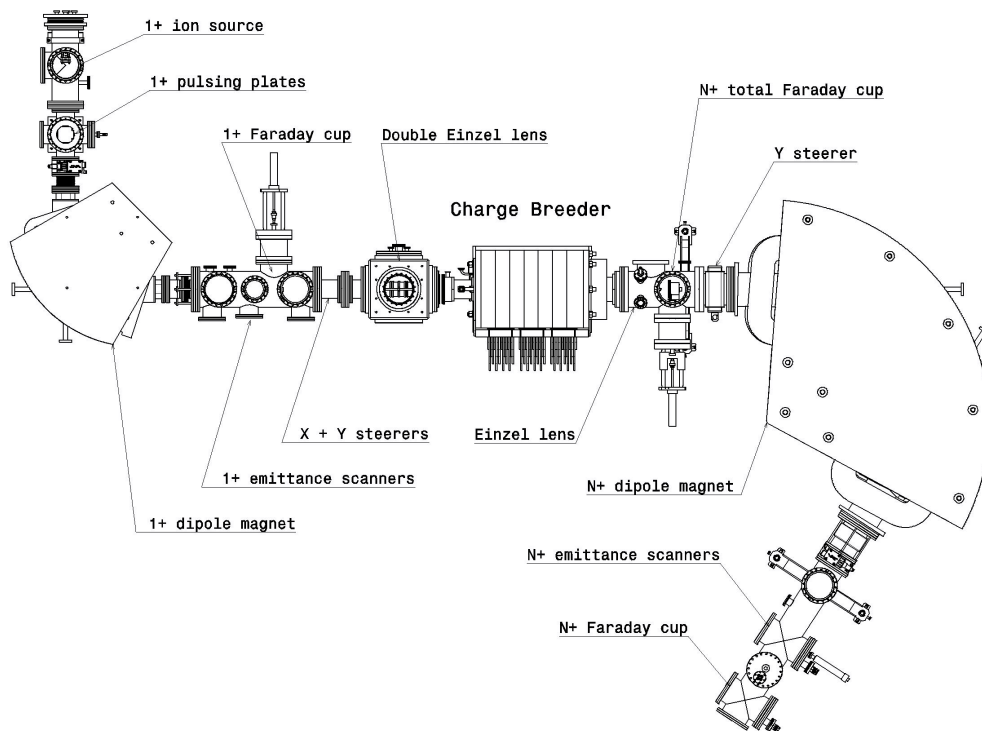
Figure 2 – schematic layout of the 1+ → N+ test bench.

Table 3 – N+ beam intensities I without 1+ beam injection and N+ beam intensities change Δ when injecting K$^+$ beam compared to without injection.

Species	He$^+$/O^{4+}	He^{2+}/H$_2^+$	O$^+$	O^{2+}	O^{3+}	O^{5+}	O^{6+}	O^{7+}
I (μA)	65.2	19.6	2.9	4.1	6.5	22.9	53.1	13.4
Δ (%)	-0.2	-3.6	-0.7	-0.2	-0.3	-2.8	-3.8	-5.4

He$^+$ and He^{2+} beam intensities were 65.2 μA and 19.6 μA, respectively. The measured variations of these peaks when injecting the K$^+$ beam were -0.2 % for He$^+$ and -3.6 % for He^{2+}. It is worth noting that the He$^+$ peak is superimposed with the O^{4+} peak, and He^{2+} peak with H$_2^+$ peak — O and H$_2$ being present in the plasma as contaminants. The estimated total flux of He ions extracted from the CB (with the contaminants contribution subtracted) was 36×10^{13} pps. Therefore, in this continuous mode of operation, the K$^+$ flux amounts to only about 1 % of the support gas extracted ions.

In order to analyse the effect on higher charge states, the change on the oxygen, carbon and nitrogen impurities present in the CSD was also inspected. A slight decrease of the high charge state beam intensities is noticed for O, C and N ion populations with a maximum difference of about -5.4 % for O^{7+} (see Table 3). This CSD modification is attributed to the gas mixing effect, due to the mass difference between the injected ions and the plasma support gas [19], [31]. Taking into account that in continuous mode (i) the flux of injected K$^+$ ions is small compared to the extracted He ions flux (and by extension even smaller compared to the total number of buffer gas ions in the plasma volume) and (ii) the effect on the plasma species is small, we consider here that the 5 ms 1+ beam pulse effect on the support plasma is negligible.

After the aforementioned measurements, the 1+ injection was switched to pulse mode. Short 1+ pulses with a width of 5 ms, corresponding to 2.2×10^{10} particles per pulse, were injected using a square signal to drive the pulsing system. The same pulsing system was used in [7], where the rise and fall front of the command signal were measured to be 2 μs and 60 μs, respectively. The 5 ms duration was chosen to obtain N+ pulse responses with a good signal-to-noise ratio, without accumulation effect [7]. The repetition rate was carefully tuned to leave N+ pulse responses enough time to recover between consecutive pulses. The N+ pulse responses were measured with the N+ FC for charge states ranging from K$^+$ to K^{12+}. The FC was connected to ground via a 5.7 MΩ resistor. An oscilloscope was used to measure the voltage at the resistor ends and to average 64 times the pulse responses before sending the measurements to the command and control computer for saving. It is worth noting that in the CSD, due to the resolution of the N+ spectrometer, K^{11+} and K^{12+} peaks overlapped with the fringes of N^{4+} and O^{5+}, respectively. The change of the O^{5+} and N^{4+} beam intensities in CW mode being -2.8 % and +1.7 % compared to the case without 1+ injection, the effect of these contaminants on the K^{11+} and K^{12+} transients was considered negligible in short pulse mode.

4.2   Measurements and fitting coefficient determination

Figure 3 a) and b) show the N+ pulse responses for charge states from K^{1+} to K^{12+}. The onset time of the 1+ injection pulse was set as $t = 0$. For each N+ pulse response, the background was
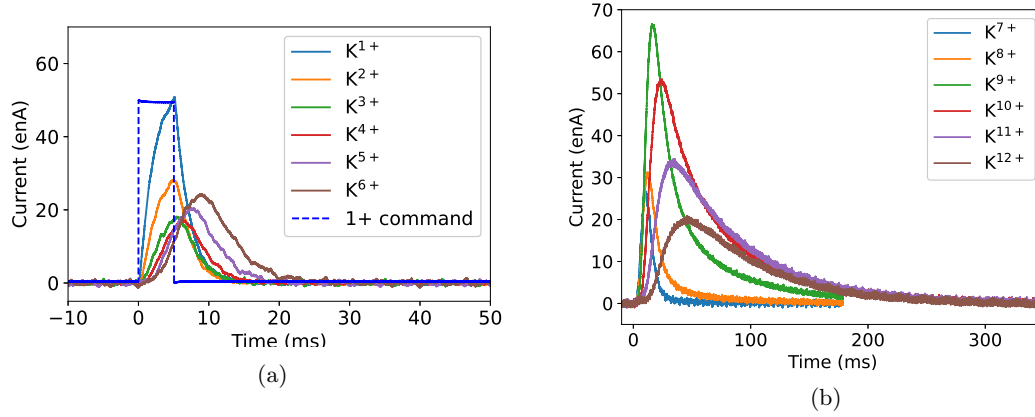
(a)

(b)

Figure 3 – Extracted K^{n+} pulse responses for charge states between a) 1+ to 6+ and b) 7+ to 12+

Table 4 – Calculated a_q, b_q and c_q parameters for K^{4+}–K^{11+}, with an RK4 stepsize of 10 μs, and the corresponding reduced χ^2 values of the fits.

	K^{4+}	K^{5+}	K^{6+}	K^{7+}	K^{8+}	K^{9+}	K^{10+}	K^{11+}
a_q (1/s)	931	996	971	855	793	705	175	132
b_q (1/s)	894	774	846	840	760	326	231	256
c_q (1/s)	2	27	112	136	93	108	117	151
χ^2	1.15	1.01	1.01	1.35	1.68	2.77	1.12	1.26

calculated by making an average of the response before the pulse start. These background values were subtracted from the respective N+ pulse responses.

The method described in 3.1 was applied to estimate the a_q, b_q and c_q parameters from the measured currents. The dependence of the fitting coefficients on the fitting range was checked by limiting the fitting window end point. It was found that for K^{2+} and K^{3+} the coefficients did show a noticeable dependence on the fitting range, while for higher charge states such a dependence was not found. This dependence for low charge states is probably caused by in-flight ionisation effects [34] which are not accounted for by the fitting model. Due to the time dependence, only the parameters for charge states K^{4+} and higher were retained. These values are summarized in Table 4. More details on the fitting range analysis can be found in the supplementary material in A.1. The comparison between the measured K^{n+} pulse responses for charge states between 4+ and 11+ and the best fit curves is presented in supplement A.2.

5 Results

Figure 4 displays the sets of (n_e, T_e)-pairs found to satisfy Equation (18) for charge states K^{5+}–K^{10+} using the method detailed in Section 3.2. Because Equation (18) has two unknowns, no singular solution can be found, and a set of solutions is obtained instead. The optimisation routine was run $N = 1000$ times for each charge state (in order to account for the upto 60 % uncertainty in the ionisation rate coefficients), with an optimum T_e searched for 1000 n_e values in the given range within each iteration. The plasma confinement, ionisation and charge exchange times $(\tau^q, \left[n_e \langle\sigma v\rangle^{\text{inz}}_{q\to q+1}\right]^{-1}, \left[n_0 \langle\sigma v\rangle^{\text{cx}}_{q\to q-1}\right]^{-1})$, were calculated, taking into account the uncertainties issued to the rate coefficients in each iteration. The corresponding energy contents $(n_e \langle E_e\rangle)$, and plasma triple products $(n_e \langle E_e\rangle \tau^q)$ were similarly calculated. It should be noted that because the optimisation is performed for each charge state separately, all values obtained are local and correspond to the plasma volume relevant for the production of the charge state in question. The median values of the characteristic times, energy contents and triple products are plotted in Figures 5, 6 and 7 respectively. In the figures, the errorbars represent the range within which lay 34.1 % of solutions below and above the median value; i.e. the error bars enclose a total of 68.2 % out of all results.

The τ^q values increase as a function of charge state. This is in accordance with the trend found in Ref. [26], although the high charge state confinement times found herein are significantly longer than in their work. For example $\tau^{5+} = 2.6^{+0.8}_{-0.4}$ ms and $\tau^{7+} = 4.0^{+3.1}_{-1.4}$ ms, while $\tau^{8+} = 7.3^{+10.9}_{-3.2}$ ms, and $\tau^{10+} = 16.4^{+18.3}_{-6.8}$ ms. The high charge states are believed to be electrostatically rather than magnetically confined as their collision frequency may exceed their larmor frequency as implied by results for sodium in Ref. [6], and oxygen in Ref. [34]. The ionisation time is level up to charge state 8+ (e.g. $\left[n_e \langle\sigma v\rangle^{\text{inz}}_{5+\to6+}\right]^{-1} = 2.6^{+0.5}_{-0.5}$ ms and $\left[n_e \langle\sigma v\rangle^{\text{inz}}_{7+\to8+}\right]^{-1} = 2.6^{+0.9}_{-0.8}$ ms), but exhibits a kink between $\left[n_e \langle\sigma v\rangle^{\text{inz}}_{8+\to9+}\right]^{-1} = 3.1^{+1.4}_{-0.9}$ ms and $\left[n_e \langle\sigma v\rangle^{\text{inz}}_{9+\to10+}\right]^{-1} = 9.6^{+4.0}_{-2.1}$ ms. This kink corresponds to a shell closure in the electron configuration of potassium, which is also indicated in Table 1. A relatively large uncertainty bound is associated with the charge exchange times. For all except K^{5+} and K^{6+} the median charge exchange times were around 10 ms.

The plasma energy content appears to have no clear charge state dependence, with all values lying around 10^{15} eV/cm^3, the average being $2.5^{+4.3}_{-1.8} \times 10^{15}$ eV/cm^3, indicating that all ions originate from regions of plasma with similar energy content. The triple product on the other hand increases with charge state until a possible saturation around K^{10+}. This charge dependence originates from the corresponding dependence of the confinement times.

6 Discussion

6.1 Method assumptions

In this paper we have presented a new method for calculating plasma characteristic times, along with estimates for the minimum local plasma energy contents and the triple product, from the extracted beam current transients of at least five neighboring charge state ions. The method has been applied to current transients of $K^{4+} - K^{12+}$ (see Fig. 3) obtained from short pulse injection of K^+ into the helium plasma of a CB-ECRIS.

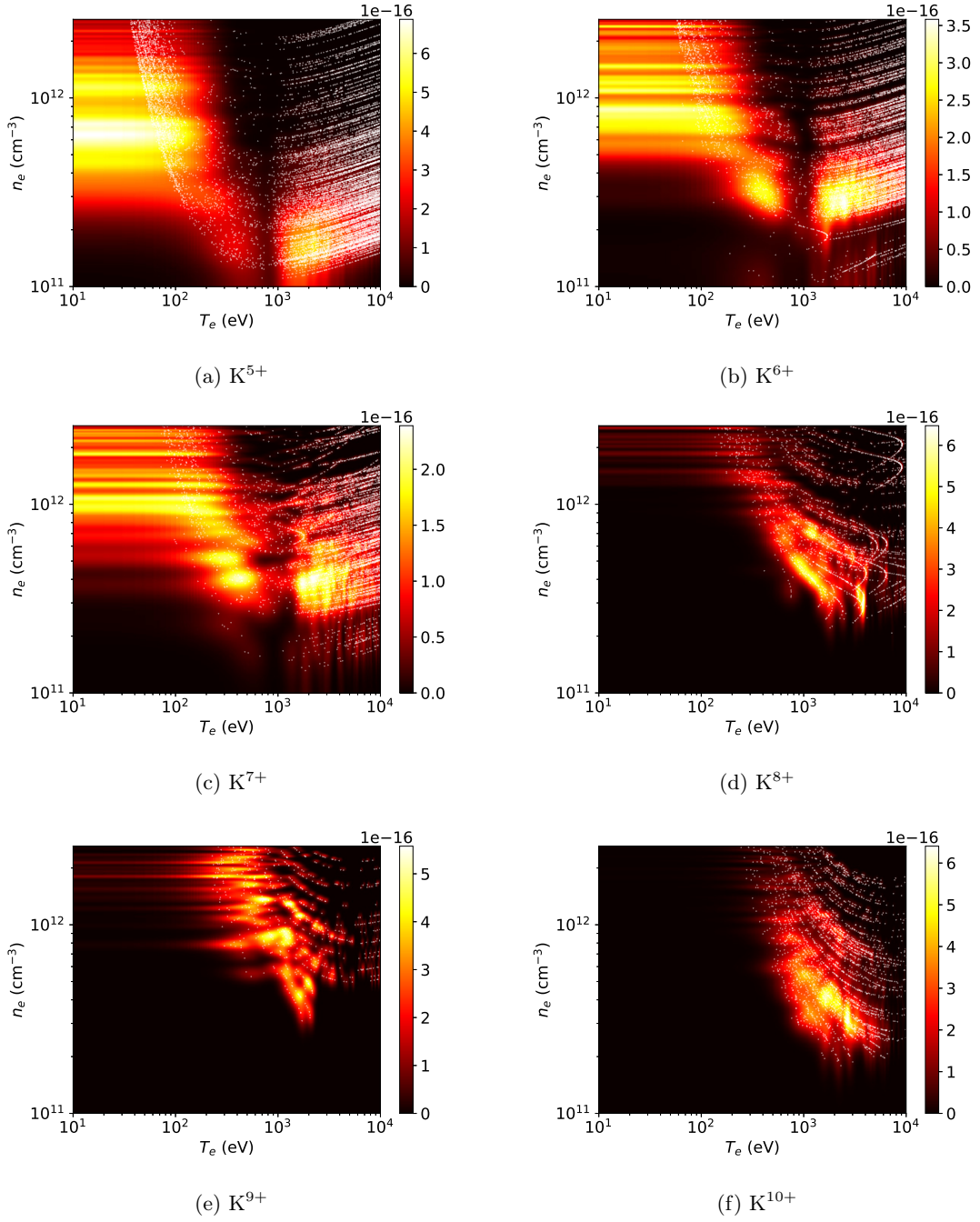The advantage of this method is that it relies only upon a small set of assumptions. We assume

(a) K^{5+}

(b) K^{6+}

(c) K^{7+}

(d) K^{8+}

(e) K^{9+}

(f) K^{10+}

Figure 4 – Probability density plots of the solution sets for K^{5+}–K^{10+} (subfigures (a)–(f)) plotted as heatmaps with an applied gaussian filter. The densities are each normalized such that an integral over the figure area equals to one. The (n_e, T_e)-pairs of each solution set are overlaid on the heatmaps as small white dots.
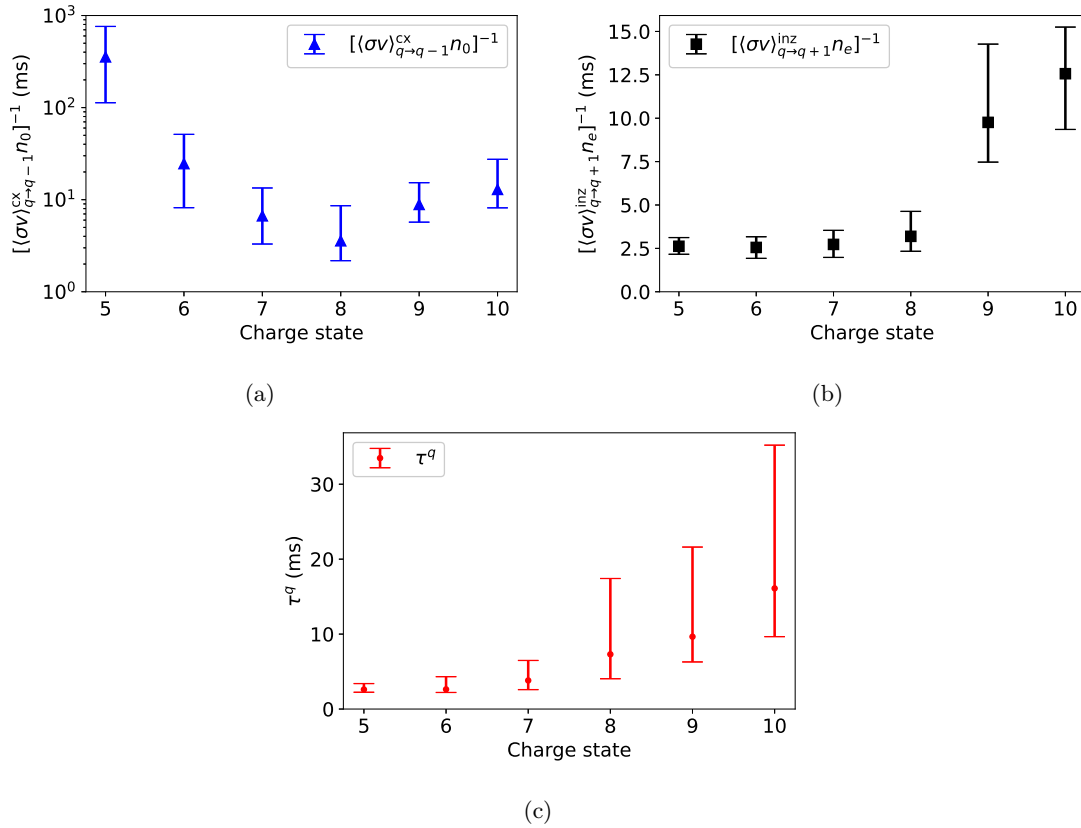
15

(a)

(b)

(c)

Figure 5 – The plasma charge exchange (a), ionisation (b) and confinement times (c) as a function of charge state. Note that subfigure (a) is plotted in logscale.

(i) that the balance equation (1) adequately describes the charge state temporal evolution. Built in to the balance equation is the assumption that the ionisation process is stepwise electron-impact ionisation, and charge exchange takes place predominantly with the neutral atoms n_0. We also make the assumption that (ii) the perturbation caused by the injected species is sufficiently small for the parameters n_e, T_e, and n_0 to be defined by the support plasma. We further assume that (iii) the extracted currents and particle densities are related by Equation (7), where the beamline transmission coefficient κ is assumed to be the same for any three consecutive charge states. These assumptions allow the conversion of the balance equation to the extraction current formalism, yielding equation (8). Finally, the use of Eq. (8) to make fits to the extracted N+ current transients requires us to assume, that (iv) n_e, T_e, n_0 and τ^q are constants — or at least vary only slowly — in time.

Assumption (i) essentially requires, that all other processes except for confinement losses, the stepwise ionisation process, and charge exchange contributing to the CSD time evolution are negligible. This means in effect that wall recycling, secondary ionisation and radiative recombination can be neglected. Using Ar here as a proxy for K — the two elements being neighbours on the

16
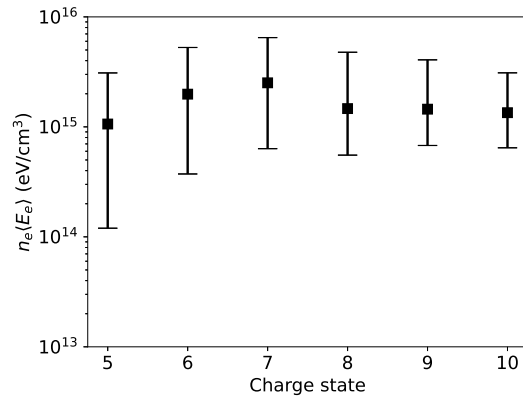
Figure 6 – The local plasma energy content as a function of charge state.
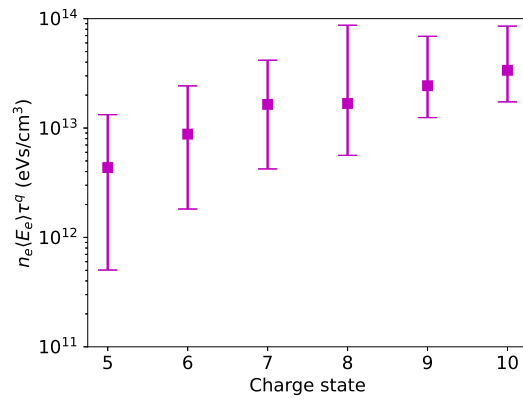
Figure 7 – The local plasma triple product as a function of charge state.

elemental table and K^{1+} having the same electronic shell configuration as neutral Ar — according to experimental data, for example the double ionisation process $Ar^{3+} + e^- \rightarrow Ar^{5+} + 3e^-$ is roughly an order of magnitude less likely than the single ionisation process $Ar^{3+} + e^- \rightarrow Ar^{4+} + 2e^-$ [35], while for higher charge states the difference is even greater. Wall recycling is minimised thanks to potassium being an alkali. Charge exchange with neutrals can be seen to be much more probable than with higher charge state ions, as the cross section decreases according to the inverse square of the ionisation potential — as evident from Eq. (5), and because the low ion temperature does not allow two ions to come close enough to each other for them to exchange charge. Radiative recombination is neglected as a relatively inconsequential process as argued by Mironov *et al.* in Ref. [8] based on the results from Ref. [9]. As noted in section 4.1 we are also safe regarding assumption (*ii*) since the total effect of the K^+ beam injected into the source in CW mode causes a minor (at most $\lesssim 5.4$ % for the oxygen impurity) modification on the support plasma CSD. The total of 2.2×10^{10} particles injected during the 5 ms pulse into the entire plasma volume constitutes a very minor perturbance compared to the buffer plasma density. As regards to assumption (*iii*) Eq. (7) is textbook material [1]. Corresponding equations are used for example by Douysset *et al.* in Ref. [26] and Melin *et al.* in Ref. [19]. The parameters S, L and κ in Eq. (7) are assumed to be the same for any three consecutive charge states. The transmission coefficient κ varies slowly with the charge state, typical transmission of the N+ beamline being around 80 % [29]. If, however, S, L, and κ could be determined for each charge state, they could also be included in the calculations. Defining them for all charge states for the purposes of this method paper was deemed impractical. In the final assumption (*iv*) the constancy of n_e, T_e, and n_0 is justified as the perturbation caused by the K^+ pulse is indeed minimal (c.f. assumption (*ii*)).[3]

With regards to the constancy of τ^q in time, it is known that the ion temperature affects the ion confinement time. According to Ref. [36] the thermal equilibration time of a test particle α streaming into a field of particles β is characterised by the collision frequency

$$\left(\tau_\epsilon^{\alpha/\beta}\right)^{-1} = \nu_\epsilon^{\alpha/\beta} = 1.8 \cdot 10^{-19} \frac{\sqrt{m_\alpha m_\beta} q_\alpha^2 q_\beta^2 n_\beta \ln \Lambda}{(m_\alpha T_\beta + m_\beta T_\alpha)^{3/2}} \qquad (\text{s}^{-1}), \qquad (24)$$

where $m_{\alpha/\beta}$ is mass (g) $q_{\alpha/\beta}$ is the charge state, n_β is particle density (1/cm³), $T_{\alpha/\beta}$ is temperature (eV), and the subscripts α and β refer to the test particle and field particle respectively. Table 5 tabulates the values of $\tau_\epsilon^{\alpha/\beta}$ for different charge states of potassium in a field of either electrons or helium ions; the experimentally obtained confinement times are also tabulated for comparison. The calculations were done for two electron populations separately with temperatures 10 eV and 1000 eV respectively, both with density $n_e = 5 \times 10^{11}$ cm^{-3}. For the calculation in the case of helium the sum over helium charge states was taken, allowing the substitution[4]

$$\sum_q n_{\text{He}}^q q^2 = n_e \frac{\langle q^2 \rangle}{\langle q \rangle}, \qquad (25)$$

where the brackets denote an average value. The CSD determined from the extracted beam currents may be used for a rough estimate of the CSD in plasma [37], and we calculate from the extracted

---

[3]The fitting range analysis provided in the supplementary material (see supplement A.1) also shows that the fitting parameters a_q, b_q and c_q show no time dependence for the charge states 4+ onward, which is in agreement with this assumption.

[4]We note that the often used relation (c.f. Ref. [19]) $\sum_q n^q q^2 = n_e \langle q \rangle$ is incorrect. The derivation of Eq. (25) is given in supplement A.6.

helium currents that $\langle q^2 \rangle / \langle q \rangle \approx 1.2$. The n_e again was set to 5×10^{11} cm^{-3}. A temperature of 10 eV was chosen for He, based on ion temperatures deduced in Ref. [4]. A value of $\ln \Lambda = 10$ was used for all sets, and the test particle temperature was chosen to be 1 eV.

Table 5 shows that the thermal equilibration time between potassium ions and warm electrons is greater than the confinement time, but its thermal equilibration time with the support plasma is less than a millisecond, which means that given a small enough perturbation the potassium ions can be expected to reach thermal equilibrium with the support plasma ions in a time scale much shorter than the duration of the transient. Thus the confinement time may be taken to be a constant in time. For high charge states, however, $\tau_\epsilon^{\alpha/\beta}$ between potassium and cold electrons is on the order of or less than the confinement time, which could enable the temperature of the high charge states of potassium to evolve over the duration of the transient (if the cold electron temperature is higher than the support plasma temperature). On the other hand, in Ref. [7] it was found that the characteristic charge breeding times were not significantly altered by longer injection pulses, which would indicate that this effect is not significant. Nevertheless, the method will be tested in future experiments using long injection pulses, allowing the plasma to reach a new equilibrium (corresponding to continuous mode 1+ injection) after the onset of the 1+ injection. In this new quiescent state the ion temperatures have certainly equilibrated. The method will then be applied to the decaying transient onset to probe the difference between the results in these two cases.

It is also implicitly assumed that the Voronov formula (3) is accurate within the specified uncertainty range. The formula for the rate coefficient presupposes the Maxwell-Boltzmann distribution for the electron energies, and thus affects the method postdictions for T_e. It is known that the energy distribution of escaped electrons is non-Maxwellian [21], and a possible future upgrade to the method could be to redefine the rate coefficient formula using different EEDFs such as the Druyvesteyn, Margenau or kappa distributions [38].

6.2   Results discussion

The necessary conversion of the balance equation to extraction current formalism complicates the procedure of deconvolving the plasma parameters from the measurement data, and causes it to be mathematically impossible to obtain a singular n_e, T_e pair. We have, however, been able to show that the physically allowed n_e, T_e pairs result in plasma characteristic times, energy contents and triple products within a tolerably narrow distribution around a certain median value. This method is a definite improvement over the pre-existing methods thanks to the smaller number of assumptions made in the process, and also due to it relaxing the requirement of a single, global (n_e, T_e) value. To the Authors' best knowledge, this is also the first time that the uncertainty of the ionisation rate coefficients is accounted for in a 0D calculation.

The results indicate that τ^q is not simply linearly dependent on q: A linear fit to the data predicts negative confinement times for the low charge states, which would be unphysical. A power fit of the form $y = 0.04426 \times q^{2.5}$ fits the data with a reduced χ^2 value of 0.47. The fitting is described in more detail in supplement A.7. There is mounting evidence, that the high charge state ions are electrostatically, rather than magnetically confined. The electrostatic confinement model presumes that a potential dip is formed in the plasma potential profile by the well confined hot electron population. This would be in accordance with the nested-layer (or onion) model for ion production in the ECRIS plasma; In the layered view the high charge states are produced in the plasma core, with lower charge states originating from larger radial distance from the chamber axis.

Table 5 – Table of characteristic thermal equilibration times for a test particle $\alpha = \mathrm{K}^{q+}$ ($T_\alpha = 1$ eV) into a field of particles $\beta = \mathrm{e}^-$ / He. The calculation was performed for two electron populations of temperature 10 eV and 1000 eV respectively. For helium $\langle q^2 \rangle / \langle q \rangle$ was 1.2 and the temperature was chosen to be 10 eV. The value $\ln \Lambda = 10$ was used, and the calculations used the same n_e of 5×10^{11} cm^{-3}. The experimentally obtained confinement times τ^q are also tabulated.

| | $\tau_\epsilon^{\alpha/\beta}$ | | | |
| | $\beta = \mathrm{e}^-$ | $\beta = \mathrm{e}^-$ | $\beta = \mathrm{He}$ | |
α	$T_\beta = 10$ eV	$T_\beta = 1000$ eV	$T_\beta = 10$ eV	τ^q
K^+	75.39 ms	75.39 s	747.11 μs	
K^{2+}	18.85 ms	18.85 s	186.78 μs	
K^{3+}	8.38 ms	8.38 s	83.01 μs	
K^{4+}	4.71 ms	4.71 s	46.69 μs	
K^{5+}	3.02 ms	3.02 s	29.88 μs	$2.6^{+0.8}_{-0.4}$ ms
K^{6+}	2.09 ms	2.09 s	20.75 μs	$2.6^{+1.7}_{-0.5}$ ms
K^{7+}	1.54 ms	1.54 s	15.25 μs	$4.0^{+3.1}_{-1.4}$ ms
K^{8+}	1.18 ms	1.18 s	11.67 μs	$7.3^{+10.9}_{-3.2}$ ms
K^{9+}	0.93 ms	0.93 s	9.22 μs	$10.0^{+12.8}_{-3.2}$ ms
K^{10+}	0.75 ms	0.75 s	7.47 μs	$16.5^{+18.3}_{-6.8}$ ms
K^{11+}	0.62 ms	0.62 s	6.17 μs	
K^{12+}	0.52 ms	0.52 s	5.19 μs	

Table 6 – Characteristic collision time $\tau_\epsilon^{\mathrm{K/He}}$ between potassium ions (with temperature 1 eV or 10 eV) and support plasma helium ions (having temperature 1 eV or 10 eV) and the respective gyration times τ_{gyro} about $B = 0.5$ T field intensity. Support plasma was assumed to have $\langle q^2 \rangle / \langle q \rangle = 1.2$ and $n_e = 5 \times 10^{11}$ cm^{-3}.

$T_{\mathrm{K}^{q+}}$ (eV)	$T_{\mathrm{He}} = 1$ eV $\tau_\epsilon^{\mathrm{K/He}}$ (μs)			$T_{\mathrm{He}} = 10$ eV $\tau_\epsilon^{\mathrm{K/He}}$ (μs)			$B = 0.5$ T τ_{gyro} (μs)		
	K^{1+}	K^{5+}	K^{10+}	K^{1+}	K^{5+}	K^{10+}	K^{1+}	K^{5+}	K^{10+}
1	26.9	1.1	0.3	747.1	29.9	6.2	5.2	1.0	0.5
10	67.1	2.7	0.7	851.8	34.1	8.5			

The layer-model is supported by numerical simulations [8], [39], and experimental measurements of ion beam emittance [40], [41]: Such lower beam emittances of HCIs can only be explained by considering them to be extracted from a surface smaller than the plasma electrode aperture [42]. Spatially resolved beam profile measurements [43], [44] have shown that ions with a higher q/m ratio are indeed extracted closer to the beamline axis. The long τ^q values of the high charge states found in this work are commensurate with this view, as they are believed to be formed and trapped in the potential dip, which is formed in the plasma core. The HCIs would reside in the potential dip formed in the plasma core until they have absorbed sufficient energy to overcome the potential barrier. This is also supported by the recent optical measurements which have found ion temperatures in the range of 5 eV–28 eV with a charge state dependence [4].

The necessary condition for magnetic confinement is that the gyration time τ_{gyro} around a field line be shorter than the mean collision time. The gyration time is defined through the cyclotron frequency ω_c such that

$$\frac{1}{\tau_{\mathrm{gyro}}} = \frac{\omega_c}{2\pi} = \frac{qeB}{2\pi m} \tag{26}$$

Here B is the field intensity, and m the particle mass. Table 6 shows the characteristic collision time for certain K ions in a He support plasma, tabulated alongside the gyration time around a field line with $B = 0.5$ T — corresponding to the 14 GHz cold electron resonance field. It can be seen, that even at low temperatures $\tau_\epsilon^{\mathrm{K/He}}$ can exceed the gyration time for low charge state potassium ions, allowing them to be magnetically confined. Meanwhile the collisionality of the HCIs can interfere with the magnetic confinement. In Refs. [34] and [6] similar conclusions have been drawn based on experimental data.

In Refs [13], [14], [45], the confinement time has been studied by exponential fits to the decaying current transients in long pulse material injection mode. In Ref. [14] it is argued that the time constant of the decay represents the cumulative confinement time τ_c^q of an individual particle, rather than the population confinement time τ^q as defined in the balance equation, which is obtained as a result of the method introduced in this work.

Since the determination of both the cumulative confinement time, the charge breeding time and the 90 % extraction time (τ_{CB}, $T_{90\%}$; See e.g. Ref. [7]) is much simpler than carrying out the complete method proposed herein, it should be worth comparing the behavior of these time scales in parameter sweeps. If a correspondence can be established between τ_c^q, τ_{CB}, $T_{90\%}$ and τ^q, one could perform diagnostics of τ^q for a wider variety of elements. The novel method presented herein requires it to be possible to measure multiple neighboring charge states' currents, and to

be able to calculate the rate coefficients for ionisation. The former condition inhibits many gas mixing experiments due to overlapping peaks in the CSD, and the latter is only possible for some of the light elements as cross section data is scarce, and even for those elements the uncertainties on the cross section data can be considerable — the uncertainty reported in Ref. [20] for example is 40 %–60 %. The rate coefficient uncertainty leads to the (n_e, T_e) solution sets becoming "smeared", and consequently, if the cross sectional data were more precise the error bars on the results found using this method could also be reduced.[5]

In Ref. [16] the balance equation for ion densities (Eq. (1)) is fit to the transients of extracted beam intensities in order to determine τ^q, n_e and T_e. The confinement time of the highest charge state ion they find to be on the order of 10 ms. They have also found n_e to be approximately 5×10^{11} cm^{-3}, and T_e around 2 keV–3 keV. The approach in Ref. [16] neglects the current-to-density proportionality $I^q \propto q e n^q / \tau^q$, as proposed by Ref. [25], and further assumes $\tau^q = \tau_{\max} \cdot q / q_{\max}$.

The assumption of the linear q-dependence for τ^q is based on the findings in Ref. [26], which also indicate much shorter confinement times — less than 4 ms for Ar^{16+} and below. In Ref. [26] the confinement time was determined from the saturation currents directly, by using Equation (7), estimating the necessary parameters, κ, S, L, and by determining the population densities n^q using optical spectroscopy methods. These estimations are reported in Ref. [26] to be reliable within a factor on the order of 2. It should be noted, that using the Voronov formula for the ionisation rate coefficient, the electron temperature T_c found in Ref. [26] for the warm electron population, and the highest n_e value of 5.7×10^{11} cm^{-3} found therein, one finds $\left[n_e \langle \sigma v \rangle^{\mathrm{inz}}_{15+ \to 16+} \right]^{-1} \simeq (35 \pm 21)$ ms. If this were true, then for the $\tau^{15+}_{\mathrm{Ar}} < 4$ ms confinement time found in Ref. [26], there should be next to no Ar^{16+} produced[6], since a criterion for appreciable ionisation from q to $q + 1$ is that [1]

$$\tau^q > \left[n_e \langle \sigma v \rangle^{\mathrm{inz}}_{q \to q+1} \right]^{-1} . \tag{27}$$

Hence, there is reason for some doubt concerning the precision of the measurements in Ref. [26].

The present method also produces estimates for the ionisation and charge exchange times in the plasma. For the purposes of HCI production these are extremely important time scales. One wants the ionisation to higher states to occur as quickly as possible, while the charge decreasing charge exchange process should ideally never occur. The lower charge state ions should be confined long enough for them to be ionized to higher states, while the desired HCIs should ideally be immediately ejected to avoid ionisation and charge exchange related losses.

The obtained ionisation times are in agreement with the behavior of the ionisation potential of potassium (tabulated in Table 1), where a shell closure inhibits the ionisation from 9+ to 10+, explaining the discrete jump in ionisation times between $\left[n_e \langle \sigma v \rangle^{\mathrm{inz}}_{8+ \to 9+} \right]^{-1}$ and $\left[n_e \langle \sigma v \rangle^{\mathrm{inz}}_{9+ \to 10+} \right]^{-1}$. It can be seen that τ^q is never smaller than the ionisation time from q to $q + 1$ — satisfying requirement (27).

The charge exchange times are systematically longer than the ionisation times, which is to be expected as the operation of an ECRIS relies on minimising the neutral density. Figure 5 shows that charge exchange may begin to inhibit the production of K^{9+} for example. It is likely that

---

[5]It should be noted that the Voronov formula reproduces the literature values for the rate coefficients to within ~ 10 %, but the literature values themselves have an uncertainty of 40 % $- 60$ %.

[6]Ref. [26] finds two approximately Maxwellian electron populations with temperatures $T_c \simeq 10$ keV and $T_h \simeq 50$ keV, with T_h increasing noticably for higher μW power. In the calculation here, T_c was used as it produced the shorter (more favorable) ionisation time.

in the case of a helium support plasma charge exchange plays a lesser role than it would e.g. if an oxygen support were used, due to the higher ionisation energy of neutral helium (13.62 eV and 24.59 eV respectively). In supplement A.5 the neutral density was deconvoluted from the charge exchange times as a function of the ion temperature, and values on the order of 10^{12} cm^{-3} were found.

Due to the assumption of the M-B EED, which neglects the hot energy tail of the EED, the procedure has yielded an approximation for the minimum plasma energy content. The average energy content has been obtained at the region of origin for the population of each charge state and is plotted in Figure 6. An estimate of the plasma triple product has similarly been obtained and is plotted in Figure 7. Figure 6 indicates that the energy content is more or less the same throughout the plasma, which is in line with the observed increase in ionisation time: The energy content being constant, the increasing ionisation energy required for the production of higher charge states causes an increase in the ionisation time. The plasma triple product shown in Figure 7 shows that $n_e \langle E_e \rangle \tau^q$ increases as a function of q (i.e. with the location of origin of charge state q ion population). It is "wisdom of the trade" that a higher triple product enables production of higher charge states, as hinted by the famous Golovanivsky diagram (see e.g. Ref. [1]). E.g. in the case of these experiments, an increase in the confinement time must compensate the spatially constant energy content — which causes an increase in the ionisation time — to allow HCI production. In this vein, parameter dependencies of the triple product could serve as a useful diagnostic when optimising the source for HCI production.

References

[1] R. Geller, *Electron cyclotron resonance ion sources and ECR plasmas.* IOP, 1996, ISBN: 9780750301077.

[2] R. Geller, T. Lamy, and P. Sortais, "Charge breeding of isotope on-line-created radioactive ions using an electron cyclotron resonance ion trap," *Review of Scientific Instruments*, vol. 77, no. 3, 03B107, 2006. DOI: `10.1063/1.2151896`. eprint: `https://doi.org/10.1063/1.2151896`. [Online]. Available: `https://doi.org/10.1063/1.2151896`.

[3] Y. Blumenfeld, T. Nilsson, and P. V. Duppen, "Facilities and methods for radioactive ion beam production," *Physica Scripta*, vol. T152, p. 014 023, Jan. 2013. DOI: `10.1088/0031-8949/2013/t152/014023`.

[4] R. Kronholm, T. Kalvas, H. Koivisto, J. Laulainen, M. Marttinen, M. Sakildien, and O. Tarvainen, "Spectroscopic study of ion temperature in minimum-b ECRIS plasma," *Plasma Sources Science and Technology*, vol. 28, no. 7, p. 075 006, 2019. DOI: `10.1088/1361-6595/ab27a1`. [Online]. Available: `https://doi.org/10.1088%2F1361-6595%2Fab27a1`.

[5] R. Kronholm, T. Kalvas, H. Koivisto, S. Kosonen, M. Marttinen, D. Neben, M. Sakildien, O. Tarvainen, and V. Toivanen, "Ecris plasma spectroscopy with a high resolution spectrometer," *Review of Scientific Instruments*, vol. 91, no. 1, p. 013 318, 2020. DOI: `10.1063/1.5128854`. eprint: `https://doi.org/10.1063/1.5128854`. [Online]. Available: `https://doi.org/10.1063/1.5128854`.

[6] O. Tarvainen, H. Koivisto, A. Galatà, J. Angot, T. Lamy, T. Thuillier, P. Delahaye, L. Maunoury, D. Mascali, and L. Neri, "Diagnostics of a charge breeder electron cyclotron resonance ion source helium plasma with the injection of ^{23}Na1+ ions," *Phys. Rev. Accel. Beams*, vol. 19, p. 053 402, 5 2016. DOI: 10.1103/PhysRevAccelBeams.19.053402. [Online]. Available: https://link.aps.org/doi/10.1103/PhysRevAccelBeams.19.053402.

[7] J. Angot, O. Tarvainen, T. Thuillier, M. Baylac, T. Lamy, P. Sole, and J. Jacob, "Charge breeding time investigations of electron cyclotron resonance charge breeders," *Phys. Rev. Accel. Beams*, vol. 21, p. 104 801, 10 2018. DOI: 10.1103/PhysRevAccelBeams.21.104801. [Online]. Available: https://link.aps.org/doi/10.1103/PhysRevAccelBeams.21.104801.

[8] V. Mironov, B. Sergey, A. Bondarchenko, A. Efremov, and V. Loginov, "Numerical model of electron cyclotron resonance ion source," *Physical Review Special Topics - Accelerators and Beams*, vol. 18, Jul. 2015. DOI: 10.1103/PhysRevSTAB.18.123401.

[9] H.-K. Chung, M. Chen, W. Morgan, Y. Ralchenko, and R. Lee, "Flychk: generalized population kinetics and spectral model for rapid spectroscopic analysis for all elements," *High Energy Density Physics*, vol. 1, no. 1, pp. 3–12, 2005, ISSN: 1574-1818. DOI: https://doi.org/10.1016/j.hedp.2005.07.001. [Online]. Available: http://www.sciencedirect.com/science/article/pii/S1574181805000029.

[10] R. C. Pardo, R. Harkewicz, and P. J. Billquist, "Time evolution of charge states in an electron cyclotron resonance ion source (abstract)a)," *Review of Scientific Instruments*, vol. 67, no. 3, pp. 881–881, 1996. DOI: 10.1063/1.1147232. eprint: https://doi.org/10.1063/1.1147232. [Online]. Available: https://doi.org/10.1063/1.1147232.

[11] R. Harkewicz, J. Stacy, J. Greene, and R. C. Pardo, "Solid material evaporation into an electron cyclotron resonance source by laser ablation," *Review of Scientific Instruments*, vol. 65, no. 4, pp. 1104–1106, 1994. DOI: 10.1063/1.1145078. eprint: https://doi.org/10.1063/1.1145078. [Online]. Available: https://doi.org/10.1063/1.1145078.

[12] R. Vondrasek, R. Scott, R. Pardo, and D. Edgell, "Techniques for the measurement of ionization times in ecr ion sources using a fast sputter sample and fast gas valve," *Review of Scientific Instruments*, vol. 73, pp. 548–551, Feb. 2002. DOI: 10.1063/1.1430273.

[13] D. Neben, J. Fogleman, D. Leitner, G. Machicoane, G. Parsey, A. Pham, S. Renteria, J. Stetson, I. Tobos, and J. Verboncoeur, "Fast Sputtering Measurement Studies using Uranium with the NSCL ECR Ion Sources," in *Proc. of International Workshop on ECR Ion Sources (ECRIS'16), Busan, Korea, August 28 - September 1, 2016*, (Busan, Korea), ser. International Workshop on ECR Ion Sources, https://doi.org/10.18429/JACoW-ECRIS2016-WEPP40, Geneva, Switzerland: JACoW, Oct. 2016, pp. 129–133, ISBN: 978-3-95450-186-1. DOI: https://doi.org/10.18429/JACoW-ECRIS2016-WEPP40. [Online]. Available: http://jacow.org/ecris2016/papers/wepp40.pdf.

[14] M. Marttinen, J. Angot, A. Annaluru, P. Jardin, T. Kalvas, H. Koivisto, S. Kosonen, R. Kronholm, L. Maunoury, O. Tarvainen, V. Toivanen, and P. Ujic, "Estimating ion confinement times from beam current transients in conventional and charge breeder ecris," *Review of Scientific Instruments*, vol. 91, no. 1, p. 013 304, 2020. DOI: 10.1063/1.5128546. [Online]. Available: https://doi.org/10.1063/1.5128546.

[15] V. Mironov, S. Runkel, K. E. Stiebing, O. Hohn, G. Shirkov, H. Schmidt-Böcking, and A. Schempp, "Plasma diagnostics at electron cyclotron resonance ion sources by injection of laser ablated fluxes of metal atoms," *Review of Scientific Instruments*, vol. 72, no. 5, pp. 2271–2278, 2001. DOI: `10.1063/1.1361087`.

[16] M. Imanaka, T. Nakagawa, H. Arai, I. Arai, and S. Lee, "Plasma diagnostics of liquid he-free sc-ecr ion source (shiva) with use of laser ablation technique," *Nuclear Instruments and Methods in Physics Research Section B: Beam Interactions with Materials and Atoms*, vol. 237, pp. 647–655, Aug. 2005. DOI: `10.1016/j.nimb.2005.04.105`.

[17] J. Angot, A. Galatà, L. Maunoury, T. Thuillier, M. Baylac, M. Migliore, and P. Sole, "Contaminants reduction in ecr charge breeders by lnl lpsc ganil collaboration," in *ECRIS 2020 proceedings WEZZO02*, 2020.

[18] G. Shirkov, C. Mühle, G. Musiol, and G. Zschornack, "Ionization and charge dispersion in electron cyclotron resonance ion sources," *Nuclear Instruments and Methods in Physics Research Section A: Accelerators, Spectrometers, Detectors and Associated Equipment*, vol. 302, no. 1, pp. 1–5, 1991, ISSN: 0168-9002. DOI: `https://doi.org/10.1016/0168-9002(91) 90485-9`. [Online]. Available: `http://www.sciencedirect.com/science/article/pii/ 0168900291904859`.

[19] G. Melin, A. G. Drentje, A. Girard, and D. Hitz, "Ion Behavior and Gas Mixing in Electron Cyclotron Resonance Plasmas as Sources of Highly Charged Ions," *Journal of Applied Physics*, vol. 86, no. 9, p. 4772, 1999.

[20] G. VORONOV, "A practical fit formula for ionization rate coefficients of atoms and ions by electron impact:z= 1–28," *Atomic Data and Nuclear Data Tables*, vol. 65, no. 1, pp. 1–35, 1997, ISSN: 0092-640X. DOI: `https://doi.org/10.1006/adnd.1997.0732`. [Online]. Available: `http://www.sciencedirect.com/science/article/pii/S0092640X97907324`.

[21] I. Izotov, O. Tarvainen, V. Skalyga, D. Mansfeld, T. Kalvas, H. Koivisto, and R. Kronholm, "Measurement of the energy distribution of electrons escaping minimum-b ECR plasmas," *Plasma Sources Science and Technology*, vol. 27, no. 2, p. 025 012, Feb. 2018. DOI: `10.1088/ 1361-6595/aaac14`.

[22] H. Knudsen, H. K. Haugen, and P. Hvelplund, "Single-electron-capture cross section for medium- and high-velocity, highly charged ions colliding with atoms," *Phys. Rev. A*, vol. 23, pp. 597–610, 2 Feb. 1981. DOI: `10.1103/PhysRevA.23.597`. [Online]. Available: `https: //link.aps.org/doi/10.1103/PhysRevA.23.597`.

[23] J. C. Slater, "Atomic shielding constants," *Phys. Rev.*, vol. 36, pp. 57–64, 1 Jul. 1930. DOI: `10.1103/PhysRev.36.57`. [Online]. Available: `https://link.aps.org/doi/10.1103/ PhysRev.36.57`.

[24] E. Clementi and D. L. Raimondi, "Atomic screening constants from scf functions," *The Journal of Chemical Physics*, vol. 38, no. 11, pp. 2686–2689, 1963. DOI: `10.1063/1.1733573`. eprint: `https://doi.org/10.1063/1.1733573`. [Online]. Available: `https://doi.org/10.1063/1. 1733573`.

[25] H. J. West, "Calculation of ion charge state distribution in ecr ion source," Lawrence Livermore National Laboratory, Tech. Rep., 1982.

[26] G. Douysset 1, H. Khodja, A. Girard, and J. P. Briand, "Highly charged ion densities and ion confinement properties in an electron-cyclotron-resonance ion source," *Phys. Rev. E*, vol. 61, pp. 3015–3022, 3 2000. DOI: `10.1103/PhysRevE.61.3015`. [Online]. Available: `https://link.aps.org/doi/10.1103/PhysRevE.61.3015`.

[27] T. Lamy, J. Angot, M. Marie-Jeanne, J. Médard, P. Sortais, T. Thuillier, A. Galatà, H. Koivisto, and O. Tarvainen, "Fine frequency tuning of the phoenix charge breeder used as a probe for ecris plasma," Jan. 2011.

[28] C. Perret, Ph.D. dissertation, Université Joseph Fourier, Grenoble, 1998.

[29] J. Angot, T. Lamy, M. Marie-Jeanne, P. Sortais, and T. Thuillier, "Lpsc phoenix ecr charge breeder beam optics and efficiencies," in *ECRIS 2012 proceedings THYO02*, 2012.

[30] T. Lamy, J. Angot, T. Thuillier, P. Delahaye, L. Maunoury, J. Choinski, L. Standylo, A. Galata, G. Patti, H. Koivisto, and O. Tarvainen, "Experimental activities with the lpsc charge breeder in the european context," *ECRIS 2014 Proceedings WEOBMH01*, 2014.

[31] J. L. Delcroix and A. Bers, *Physique des Plasmas 2*. (Paris:CNRS) p 357, 1994.

[32] L. Maunoury, O. Bajeat, C. Barthe-Dejean, P. Delahaye, M. Dubois, R. Frigot, P. Jardin, A. Jeanne, O. Kamalou, P. Lecomte, O. Osmond, G. Peschard, A. Savalle, J. Angot, T. Lamy, and P. Sole, "Spiral1 charge breeder : performances and status," *ECRIS 2016 Proceedings*, 2016. DOI: `https://doi.org/10.18429/JACoW-ECRIS2016-MOFO01`.

[33] J. Angot, T. Thuillier, O. Tarvainen, M. Baylac, J. Jacob, T. Lamy, M. Migliore, and P. Sole, "Recent improvements of the lpsc charge breeder," *poster*,

[34] O. Tarvainen, T. Lamy, J. Angot, T. Thuillier, P. Delahaye, L. Maunoury, J. Choinski, L. Standylo, A. Galatà, G. Patti, and H. Koivisto, "Injected 1+ ion beam as a diagnostics tool of charge breeder ECR ion source plasmas," *Plasma Sources Science and Technology*, vol. 24, no. 3, p. 035 014, May 2015. DOI: `10.1088/0963-0252/24/3/035014`.

[35] H. Tawara and T. Kato, "Total and partial ionization cross sections of atoms and ions by electron impact," *Atom. Data Nucl. Data Tabl.*, vol. 36, pp. 167–353, 1987. DOI: `10.1016/0092-640X(87)90014-3`.

[36] J. D. Huba, *NRL formulary*, Naval Research Laboratory, Washington, DC 20375, 2016. [Online]. Available: `https://www.nrl.navy.mil/ppd/content/nrl-plasma-formulary`.

[37] M. Guerra, P. Amaro, C. I. Szabo, A. Gumberidze, P. Indelicato, and J. P. Santos, "Analysis of the charge state distribution in an ECRIS ar plasma using high-resolution x-ray spectra," *Journal of Physics B: Atomic, Molecular and Optical Physics*, vol. 46, no. 6, p. 065 701, Mar. 2013. DOI: `10.1088/0953-4075/46/6/065701`. [Online]. Available: `https://doi.org/10.1088%2F0953-4075%2F46%2F6%2F065701`.

[38] C.-R. Du, S. A. Khrapak, T. Antonova, B. Steffes, H. M. Thomas, and G. E. Morfill, "Frequency dependence of microparticle charge in a radio frequency discharge with Margenau electron velocity distribution," *Physics of Plasmas*, vol. 18, no. 1, p. 014 501, 2011. DOI: `10.1063/1.3530439`. eprint: `https://doi.org/10.1063/1.3530439`. [Online]. Available: `https://doi.org/10.1063/1.3530439`.

[39] V. Mironov and J. Beijers, "Three-dimensional simulations of ion dynamics in the plasma of an electron cyclotron resonance ion source," *Physical Review Special Topics - Accelerators and Beams*, vol. 12, p. 073 501, Jul. 2009. DOI: `10.1103/PhysRevSTAB.12.073501`.

[40] M. A. Leitner, D. Wutte, and C. M. Lyneis, "Design of the extraction system of the superconducting ecr ion source venus*," in *Proceedings of the 2001 Particle Accelerator Conference, Chicago*, P. Lucas and S. Webber, Eds., Argonne National Laboratory, Fermi National Accelerator, and Laboratory Oak Ridge National Laboratory, vol. 5, Chicago, Illinois U.S.A.: IEEE, 2001, pp. 67–69.

[41] D. Wutte, S. Abbott, M. A. Leitner, and C. M. Lyneis, "High intensity metal ion beam production with ecr ion sources at the lawrence berkeley national laboratory," *Review of Scientific Instruments*, vol. 73, no. 2, pp. 521–524, 2002. DOI: 10.1063/1.1425781. eprint: https://doi.org/10.1063/1.1425781. [Online]. Available: https://doi.org/10.1063/1.1425781.

[42] J. Mandin, "Étude expérimentale et simulation des conditions d'extraction d'un faisceau d'ions multichargés d'une source à résonance cyclotronique électronique," Theses, Université de Caen, Dec. 1996. [Online]. Available: http://hal.in2p3.fr/in2p3-00008706.

[43] L. Panitzsch, M. Stalder, and R. F. Wimmer-Schweingruber, "Spatially resolved measurements of electron cyclotron resonance ion source beam profile characteristics," *Review of Scientific Instruments*, vol. 82, no. 3, p. 033 302, 2011. DOI: 10.1063/1.3553013. eprint: https://doi.org/10.1063/1.3553013. [Online]. Available: https://doi.org/10.1063/1.3553013.

[44] L. Panitzsch, T. Peleikis, M. Stalder, and R. F. Wimmer-Schweingruber, "Spatially resolved charge-state and current-density distributions at the extraction of an electron cyclotron resonance ion source," *Review of Scientific Instruments*, vol. 82, no. 9, p. 093 302, 2011. DOI: 10.1063/1.3637462. eprint: https://doi.org/10.1063/1.3637462. [Online]. Available: https://doi.org/10.1063/1.3637462.

[45] D. Neben, G. Machicoane, G. Parsey, A. Pham, J. Stetson, and J. Verboncoeur, "An Analysis of Fast Sputtering Studies for Ion Confinement Time," in *Proc. of Linear Accelerator Conference (LINAC'16), East Lansing, MI, USA, 25-30 September 2016*, (East Lansing, MI, USA), ser. Linear Accelerator Conference, https://doi.org/10.18429/JACoW-LINAC2016-TUPRC032, Geneva, Switzerland: JACoW, May 2017, pp. 475–477, ISBN: 978-3-95450-169-4. DOI: https://doi.org/10.18429/JACoW-LINAC2016-TUPRC032. [Online]. Available: http://jacow.org/linac2016/papers/tuprc032.pdf.

27

Figure 8 – The variation of the fitting parameters a_q, b_q and c_q as a function of the fitting range.

A   Supplementary material

A.1   Fitting range analysis

To study the variation in time of the fitting parameters a_q, b_q and c_q, the fitting range interval was increased incrementally from $t_0 = 0$ s to t_f, where t_f is the longest duration of an extracted transient. The fits were thus made in the intervals $[t_0, 0.2t_f]$, $[t_0, 0.4t_f]$, $[t_0, 0.6t_f]$, $[t_0, 0.8t_f]$ and $[t_0, t_f]$. Figure 8 shows the obtained fitting parameters as a function of the fitting range end percentile. It can be seen that as the fitting range is increased only the fitting parameters for charge states 2+ and 3+ change. This change is attributed to the in-flight ionised ions which are unaccounted for in the balance equation. Due to the time dependence found for the charge states 2+ and 3+, only the fitting parameters from 4+ onward were used in the analysis.

A.2   RK4 fitting curves

The fits resulting from the fitting procedure described in section 3 are plotted with the experimentally measured K^{n+} transients in Figure 9. The fits were all made using a 10 μs step size in the 4$^{\text{th}}$ order RK method. A close fit is obtained for all charge states.
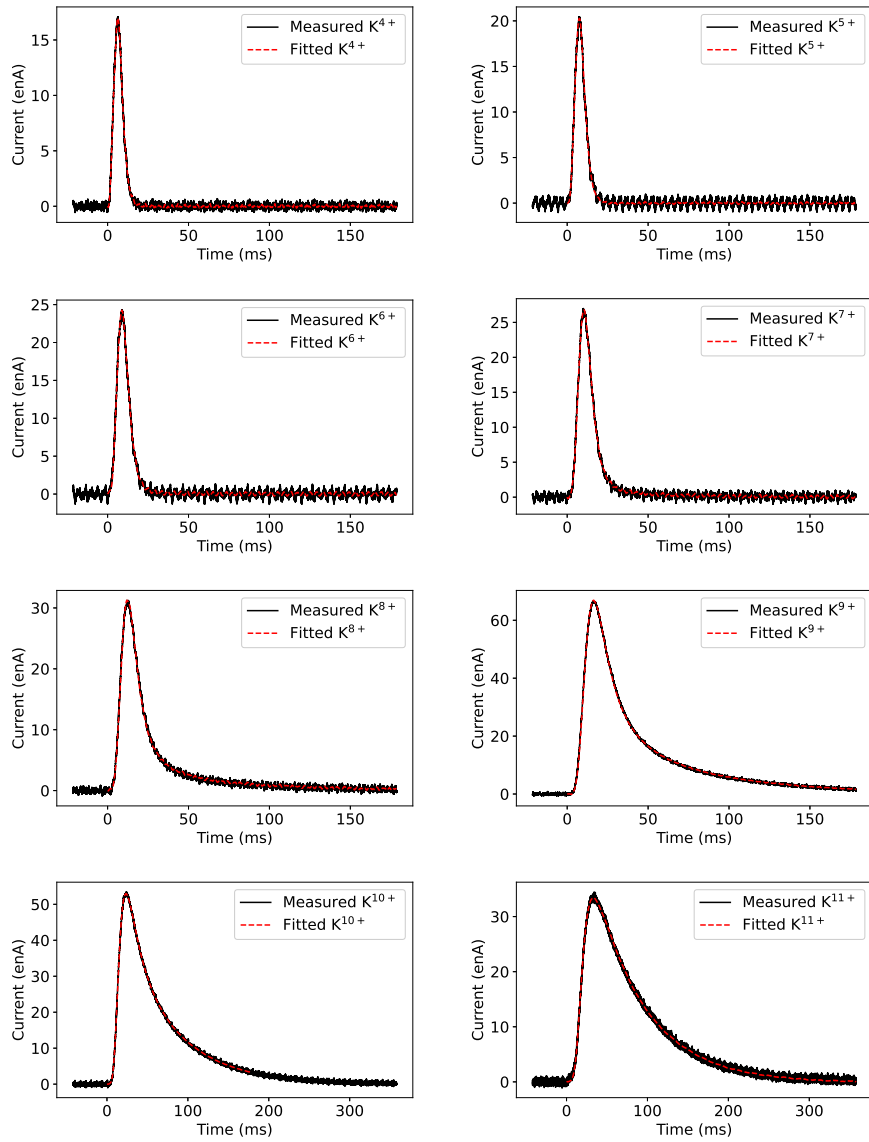
Figure 9 – Extracted K^{n+} pulse responses for charge states between $4+$ to $11+$ plotted with the RK4 fitting curves.

A.3   Numerical code

The python codes for obtaining the fitting parameters a_q, b_q and c_q and for determining the n_e, T_e solution set are provided. In addition, the experimental data used in this work is provided as
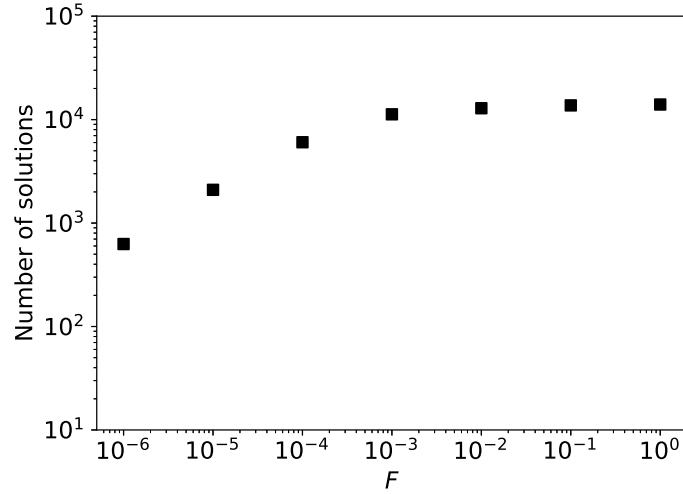
Figure 10 – The number of valid solutions with a given upper limit of the penalty function F for K^{7+}.

a sample data set. The code is publicly available on github at the URL: `https://github.com/misapema-jyfl/popTauPy`, and instructions for its use will be available there in the near future. The experimental data measured for this manuscript is available at doi:10.6084/m9.figshare.13602827.v1.

A.4   Penalty function limit analysis

In order to determine the precision required by the computation presented in section 3, the effect of constraining the maximum value of the penalty function F on the results obtained from the computation performed using 1000 Monte Carlo biases for the Voronov formula was studied. The smaller the maximum value of F, the more precisely the left-hand-side and right-hand-side of Eq. (18) match one another, and hence the more precise the solution. Figures 10, and 11 show the effect of constraining the maximum value of F on the number of valid solutions and the resultant values for the plasma parameters, respectively. The results of the analysis are plotted for K^{7+} as representative of all other charge states producing similar results. Based on the analysis, we choose $F < 10^{-4}$ as it is the highest precision for the solution of Eq. (18), while the number of valid solutions is still some thousands for all charge states, ensuring a thorough sampling of the solution set.

A.5   Neutral density deconvolution

The charge exchange times $\left[n_0 \left\langle \sigma v \right\rangle_{q \to q-1}^{\mathrm{cx}}\right]^{-1}$ were obtained via the method presented in this paper. Using the equations (5) and (6) presented in section 2, one can calculate the rate coefficient

30

(a)

(b)

(c)
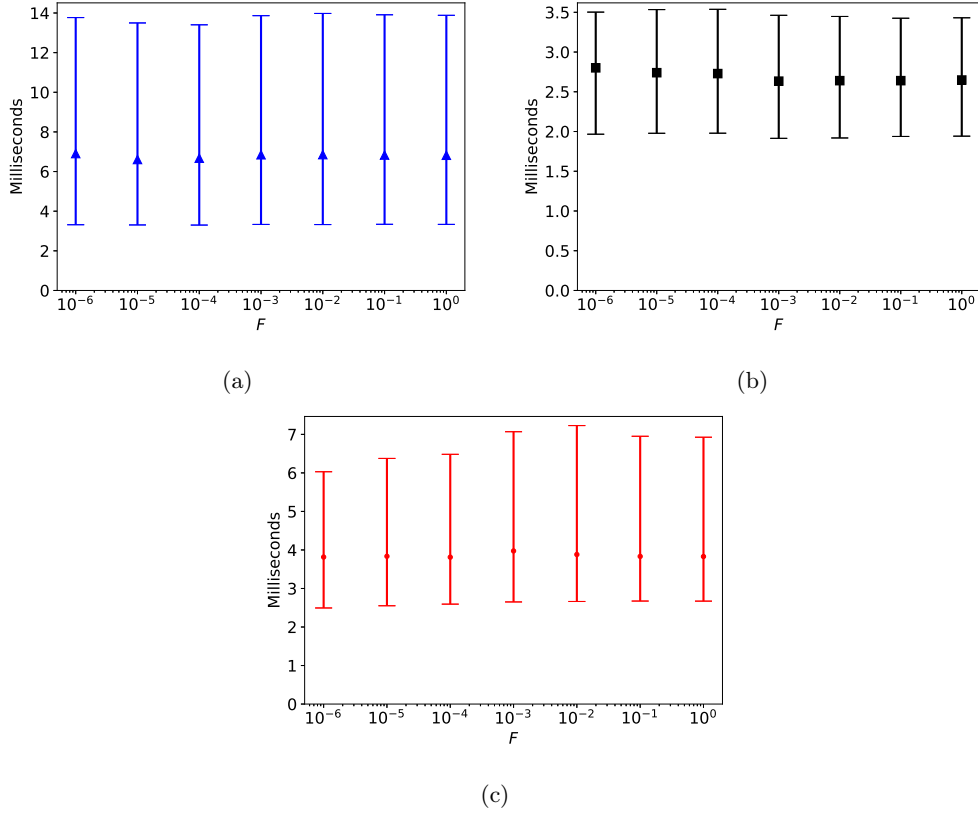
Figure 11 – The postdictions of the plasma characteristic times for charge exchange (a), ionisation (b) and ion confinement (c) as a function of the upper limit of the penalty function F for K^{7+}.

$\langle \sigma v \rangle^{\text{cx}}_{q \to q-1}$ as a function of the unknown ion temperature T_i^q according to

$$\langle \sigma v \rangle^{\text{cx}}_{q \to q-1} = \pi r_0^2 q \left(\frac{I_0}{I} \right)^2 Z_{\text{eff}} \sqrt{\frac{8T_i^q}{\pi m_i}}. \tag{28}$$

It should be noted that Eq. (28) assumes the neutral temperature to be low compared to the ion temperature. The effective charge state of neutral helium can be calculated by using the formulae provided in Ref. [24]

$$Z_{\text{eff}} = Z - \Sigma, \tag{29}$$

where Z is the proton number, and the screening coefficient Σ for the $1s$ electronic state is given by

$$\begin{aligned} \Sigma\,(1s) = {} & 0.3 \times (1s - 1) + 0.0072 \times (2s + 2p) \\ & + 0.0158 \times (3s + 3p + 4s + 3d + 4p), \end{aligned} \tag{30}$$
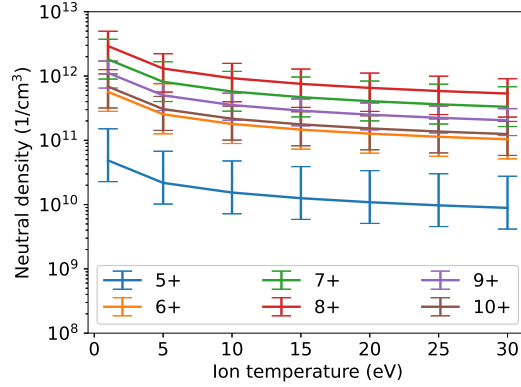
Figure 12 – The postdicted local neutral density as a function of ion temperature.

where the number of electrons in a given quantum state characterized by quantum numbers n and l is denoted by the terms $nl = (1s, 2s, 2p, \ldots)$. For ground state helium only the state $1s$ is occupied, and thus its effective charge is

$$Z_{\text{eff}} = 2 - 0.3 \times (2 - 1) = 1.7. \tag{31}$$

Reference [4] has found the ion temperatures to lie in the range $T_i^q \in [5, 28]$ eV. We calculate accordingly the charge exchange rate coefficient in the range $[1, 30]$ eV. The neutral density can then be obtained from the characteristic frequency for charge exchange by dividing by the corresponding rate coefficient. The results as a function of ion temperature are shown in Fig. 12.

A.6 Collision time calculations

The total collision frequency between the test particle α and particle species β present in the plasma can be obtained by taking a sum of Eq. (24). The ion-ion collision frequency between a K^{q+} ion and the helium buffer is thus obtained from

$$\sum_{\beta=\text{He}^+,\text{He}^{2+}} \nu_\epsilon^{\alpha/\beta} = 1.8 \cdot 10^{-19} \frac{\sqrt{m_\alpha m_\beta} q_\alpha^2 \ln \Lambda}{(m_\alpha T_\beta + m_\beta T_\alpha)^{3/2}} \sum_\beta n_\beta q_\beta^2 \qquad (s) \tag{32}$$

where T_β is assumed the same for both He charge states to allow moving it out of the summation. Because the helium CSD in plasma is not precisely known an alternative form is derived as follows:

The plasma effective (average) charge state is defined according to

$$\langle q \rangle \equiv \frac{\sum_q n^q q}{\sum_q n^q}. \tag{33}$$

where n^q is charge state q ion number density, and $\langle q \rangle$ is the effective charge state. In a multispecies plasma the summation is also carried over all ion species i. Due to quasi-neutrality of the plasma

$$n_e = \sum_q n^q q. \tag{34}$$

32

The mean square charge state is defined as,

$$\left\langle q^2 \right\rangle \equiv \frac{\sum_q n^q q^2}{\sum_q n^q}. \tag{35}$$

From Eq. (33) we solve

$$\sum_q n^q = \frac{n_e}{\langle q \rangle}, \tag{36}$$

where the substitution according to Eq. (34) was made. Substituting Eq. (36) to Eq. (35) one obtains

$$\left\langle q^2 \right\rangle = \frac{\sum_q n^q q^2}{n_e} \left\langle q \right\rangle, \tag{37}$$

which after rearranging gives

$$\sum_q n^q q^2 = n_e \frac{\left\langle q^2 \right\rangle}{\langle q \rangle}. \tag{38}$$

The averages in Eq. (38) can be approximated from the extracted beam currents as per

$$\left\langle q^2 \right\rangle \simeq \frac{\sum_q (I^q/q) q^2}{\sum_q (I^q/q)} \tag{39}$$

and

$$\langle q \rangle \simeq \frac{\sum_q (I^q/q) q}{\sum_q (I^q/q)} \tag{40}$$

since the extracted beam CSD provides a rough image of the CSD in plasma [37].

A.7 Fit to confinement time

A power fit of the form

$$y = A \times q^B \tag{41}$$

was fitted to the confinement times obtained as a result of the method presented in this work. The fitting procedure (nonlinear least squares with the Levenberg-Marquardt method) could not accept asymmetric uncertainties, so instead of the median values of τ^q presented in Fig. 5 (c), the average value of τ^q was used, and the uncertainties around it were assumed symmetric. The obtained best fit parameters were

$$\begin{cases} A = 0.04426 \pm 2 \cdot 10^{-5}, & \text{and} \\ B = 2.5 \pm 0.4 \end{cases} \tag{42}$$

with a reduced χ^2 value of 0.47. The resultant fit is plotted in Figure 13.
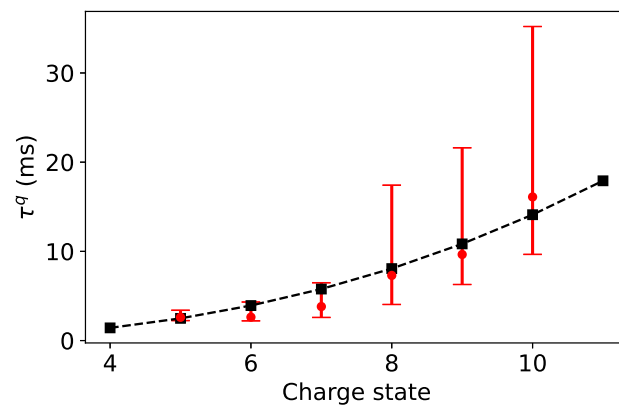
Figure 13 – A power fit to the obtained confinement times.

PII

MEASUREMENT OF IONIZATION, CHARGE EXCHANGE AND ION CONFINEMENT TIMES IN CHARGE BREEDER ECR ION SOURCES WITH SHORT PULSE 1+ INJECTION OF METAL IONS

by

M Luntinen, J Angot, O Tarvainen, V Toivanen, T Thuillier, H Koivisto

Measurement of ionization, charge exchange and ion confinement times in charge breeder ECR ion sources with short pulse 1+ injection of metal ions

M Luntinen[1], J Angot[2], O Tarvainen[3], V Toivanen[1], T Thuillier[2] and H Koivisto[1]

[1] University of Jyväskylä, Department of Physics, Survontie 9D, 40500 Jyväskylä, Finland
[2] Univ. Grenoble Alpes, CNRS, Grenoble INP, LPSC-IN2P3, 53 Avenue des Martyrs, 38000 Grenoble, France
[3] STFC ISIS Pulsed Spallation Neutron and Muon Facility, Rutherford Appleton Laboratory, Harwell, OX11 0QX, UK

E-mail: mailto:misapema@jyu.fi

Abstract. The Consecutive Transients (CT) method is used for estimating the characteristic times of ionization, charge exchange and confinement within the plasma of a Charge Breeder Electron Cyclotron Resonance Ion Source (CB-ECRIS). The method reveals differences in the characteristic times between different source configurations, with K^{9+} charge breeding efficiencies of 8.9 % and 20.4 %, and allows qualitative explanation of the improved breeding efficiency. The increase in K^{9+} efficiency is accompanied by a decrease in ionization time for low charge states, a decrease of charge exchange time for high charge states, and an overall decrease of the ion confinement time, which increases non-linearly with the charge state. The charge exchange time exhibits a minimum near charge state K^{8+}, indicating low neutral density near the plasma core. The CT-method yields a distribution of possible n_e and $\langle E_e \rangle$ corresponding to the spatial distribution of different charge state ions. The results hint at a non-uniform plasma electron density and energy distribution as well as a nested-layer distribution for the ion populations — hot and dense plasma with high charge state ions near the plasma core.

1. Introduction

The Consecutive Transients (CT) method has been used to obtain postdictions for the ionization, charge exchange and confinement times (τ_{inz}^q, τ_{cx}^q and τ^q) of charge state q ion populations in a CB-ECRIS plasma [1]. The method is based on measuring the extracted current transients prompted by short pulse injection of metal ions into the plasma, making fits to the transients of (minimum) five consecutive charge states, and an optimisation procedure to obtain the plasma electron density n_e and average energy $\langle E_e \rangle$ of the presumed Electron Energy Distribution (EED) as well as the times τ_{inz}^q, τ_{cx}^q and τ^q. The method is based on the balance equation [2, 3] describing the temporal evolution of the densities of each ion population. The method probes the plasma conditions (n_e, $\langle E_e \rangle$) of the support plasma, which determine τ_{inz}^q, τ_{cx}^q and τ^q of the injected ions. The results are spatially localised to the origin of the charge state q ion population. Measuring five consecutive charge state transients poses experimental limitations on the support/injected species combinations, since one must avoid q/m overlap in the Charge State Distribution (CSD). The method takes into account the uncertainty of the ionization cross section data and resulting

Table 1: The former (June 2020) and new (February 2021) charge breeder operating parameters.

	Configuration	
Parameter	Former	New
B_{inj} (T)	1.58	1.57
B_{min} (T)	0.45	0.44
B_{ext} (T)	0.83	0.84
μW power (W)	504	530
Support gas species	He	H_2
P_{inj} ($\times 10^{-8}$ mbar)	9.0	13.6
K^+ intensity (nA)	710	500
Injection pulse width (ms)	5	5

rate coefficients by the means of a Monte Carlo approach. No assumptions need to be made regarding the confinement scheme i.e. the functional dependence of τ^q.

Here we demonstrate that the CT-method can reveal the physical causes resulting in a change of the charge breeding efficiency. The comparison is made between the characteristic times obtained for potassium ions in the support plasma of a CB-ECRIS. The source configurations correspond to $^{39}K^{9+}$ efficiencies of 8.9 % and 20.4 %, respectively. Identifying the mechanisms underpinning the factor of > 2 improvement in the charge breeding efficiency of a stable isotope can guide the optimisation of Radioactive Ion Beam (RIB) production.

2. Experimental methods

The $1+\rightarrow N+$ test bench [4] at LPSC Grenoble is dedicated to the development and characterization of the Phoenix CB-ECRIS. The 1+ beam line is used for generating, characterizing and injecting the 1+ ion beam into the CB-ECRIS and the N+ beam line for analysing the extracted multicharged beams. The CB-ECRIS and the test bench are continuously upgraded to increase the global and charge state specific breeding efficiencies, Σ and η^q, and to reduce the charge breeding time and impurities in the N+ CSD. Short pulse injection of 1+ ions is used for the measurement of the charge breeding times τ_{CB}; the time when 90 % of all ions of charge state q have been extracted is designated as τ_{CB}[5]. In 2018-2019, the $1+\rightarrow N+$ test bench was upgraded to improve the vacuum and the alignment of the device [4]. The optimum efficiency of K^{10+} charge state measured in June 2020 was 10.6 % with τ_{CB}^{10+} of 132 ms. The first data using the CT-method to obtain the plasma parameters were taken in this configuration [1] with He support plasma.

The CB tuning and conditioning were then optimised to improve the CB efficiency to 20.4 % for K^{9+} with H_2 support gas (τ_{CB}^{9+} of 131 ms). The CT-method was applied in this configuration in February 2021 to estimate which parameters could have caused the efficiency improvement. Table 1 compares the two CB configurations. The main differences are the support gas species, the B_{min} value (+11.8%) and the microwave power (+5.2%). The charge breeding efficiencies η^q of the K charge states are shown in Table 2. A significant increase of K^{9+} efficiency was obtained (+11.5% absolute efficiency), accompanied by a small efficiency shift towards lower charge states. The extracted current transients of K^{3+}–K^{12+} were measured to obtain the characteristic times for K^{5+}–K^{10+} ion populations. The injected K^+ pulse was kept short (5 ms pulse width) and low in intensity (500 – 710 nA) to minimize the perturbance on the support plasma, while still resulting in high signal-to-noise ratio of the transient current.

Table 2: The charge breeding efficiencies η^q, charge breeding times τ^q_{CB} and the median values of the population confinement times τ^q. The global efficiency includes charge states $K^{4+} - K^{12+}$.

Ion	η^q (%)		τ^q_{CB} (ms)		τ^q (ms)	
	Former	New	Former	New	Former	New
K^{3+}	1.2	1.3	9	10		
K^{4+}	1.0	1.4	11	12		
K^{5+}	1.1	1.9	13	15	3	3
K^{6+}	1.2	3.0	16	49	3	4
K^{7+}	1.5	5.8	20	90	4	4
K^{8+}	2.7	11.1	45	119	15	12
K^{9+}	8.9	20.4	98	131	16	8
K^{10+}	10.6	11.8	132	138	24	12
K^{11+}	8.5	4.7	149			
K^{12+}	5.1	1.3	155			
Σ (%)	41.8	62.7				

3. Numerical methods

3.1. Principle of the method

The method for analyzing the measured beam current transients of the $q+$ ions has been extensively described in Ref. [1] and is only briefly recapitulated here: The balance equations [2, 3] governing the evolution in time of the ion population densities are defined by

$$
\begin{aligned}
\frac{\mathrm{d}n^q}{\mathrm{d}t} = &+n_e \left\langle \sigma v \right\rangle^{\text{inz}}_{q-1 \to q} n^{q-1} - n_e \left\langle \sigma v \right\rangle^{\text{inz}}_{q \to q+1} n^q \\
&+n_0 \left\langle \sigma v \right\rangle^{\text{cx}}_{q+1 \to q} n^{q+1} - n_0 \left\langle \sigma v \right\rangle^{\text{cx}}_{q \to q-1} n^q - \frac{n^q}{\tau^q},
\end{aligned}
\tag{1}
$$

where the ionization and charge exchange rate coefficients ($\left\langle \sigma v \right\rangle^{\text{inz/cx}}$) together with the plasma electron and neutral densities (n_e, n_0) determine the characteristic times

$$
\tau^q_{\text{inz}} \equiv \left[n_e \left\langle \sigma v \right\rangle^{\text{inz}}_{q \to q+1} \right]^{-1}
\tag{2}
$$

$$
\tau^q_{\text{cx}} \equiv \left[n_0 \left\langle \sigma v \right\rangle^{\text{cx}}_{q \to q-1} \right]^{-1}
\tag{3}
$$

and the loss term $-n^q/\tau^q$ defines the ion confinement time τ^q. Here n^q refer to the injected species, while n_e and n_0 are properties of the support plasma, which are assumed to be constant in time. Using the following identity [6, 7, 1] for the charge state q beam current

$$
I^q = \kappa F_B L S \frac{n^q q e}{\tau^q},
\tag{4}
$$

where κ is the beamline transmission efficiency, F_B a factor dependent on the mirror ratio of the ion source, L the length of the plasma chamber and S the area of the extraction aperture, one can recast the balance equation in the form

$$
\frac{\mathrm{d}}{\mathrm{d}t} I^q = a_q I^{q-1} - b_q I^q + c_q I^{q+1},
\tag{5}
$$

where I^{q-1}, and I^{q+1} are the beam currents of charge states $q-1$ and $q+1$, respectively, and the coefficients a_q, b_q and c_q are defined as

$$a_q = n_e \left\langle \sigma v \right\rangle^{\text{inz}}_{q-1 \to q} \frac{q}{q-1} \frac{\tau^{q-1}}{\tau^q} \tag{6}$$

$$b_q = \left(n_e \left\langle \sigma v \right\rangle^{\text{inz}}_{q \to q+1} + n_0 \left\langle \sigma v \right\rangle^{\text{cx}}_{q \to q-1} + 1/\tau^q \right) \qquad \text{and} \tag{7}$$

$$c_q = n_0 \left\langle \sigma v \right\rangle^{\text{cx}}_{q+1 \to q} \frac{q}{q+1} \frac{\tau^{q+1}}{\tau^q}. \tag{8}$$

The coefficients a_q, b_q and c_q can be determined by fitting Eq. 5 to the experimentally measured current I^q. The fitting is done by taking $I^{q-1}(t)$ and $I^{q+1}(t)$ as input parameters of Eq. 5, and solving the differential equation for the middle charge state current (numerical solution for the charge state q current denoted by $\mathfrak{J}^q(t)$). A least-squares method is then used to minimize the difference between $\mathfrak{J}^q$ and I^q to obtain a_q, b_q and c_q. Definitions 6, 7 and 8 then yield

$$\frac{q}{q+1} \frac{a_{q+1}}{n_e \left\langle \sigma v \right\rangle^{\text{inz}}_{q \to q+1}} = \frac{b_{q+1} - n_e \left\langle \sigma v \right\rangle^{\text{inz}}_{q+1 \to q+2} - \frac{a_{q+1} c_q}{n_e \left\langle \sigma v \right\rangle^{\text{inz}}_{q \to q+1}}}{b_q - n_e \left\langle \sigma v \right\rangle^{\text{inz}}_{q \to q+1} - \frac{a_q c_{q-1}}{n_e \left\langle \sigma v \right\rangle^{\text{inz}}_{q-1 \to q}}}, \tag{9}$$

which is an equation of two unknowns, n_e and $\langle E_e \rangle$, since the rate coefficients $\left\langle \sigma v \right\rangle^{\text{inz}}_{q' \to q''}$ may be calculated as a function of the average energy $\langle E_e \rangle$ of the EED. In lieu of experimental determination of the EED, we have thus far assumed the Maxwell-Boltzmann (MB) distribution. Equation 9 provides an infinitude of solutions for n_e and $\langle E_e \rangle$, which may be constrained on physical grounds such that

$$\begin{cases} \tau^q > 0, \\ \tau^{q+1} > 0, \\ 1/n_0 \left\langle \sigma v \right\rangle^{\text{cx}}_{q \to q-1} > 0, \\ n_{e,\text{low}} < n_e < n_{e,\text{co}}, \\ \langle E_e \rangle_{\text{low}} < \langle E_e \rangle < \langle E_e \rangle_{\text{high}}, \end{cases} \tag{10}$$

where τ^q, τ^{q+1} and $\left[n_0 \left\langle \sigma v \right\rangle^{\text{cx}}_{q \to q-1} \right]^{-1} \equiv \tau^q_{\text{cx}}$ can be calculated from the definitions of a_q, b_q and c_q (c.f. Ref. [1] Eqs. (16) and (19)). The upper bound of n_e is the cut-off frequency [8] $n_{e,\text{co}}$, while its lower bound $n_{e,\text{low}}$ is taken from the literature [9]. The lower limit of $\langle E_e \rangle$ is set to be on the order of the plasma potential, i.e., ~ 10 eV, while its upper limit can be constrained at 10 keV, since the fraction of electrons found with energies above a few keV is 20–50 % [7, 10]. We thus focus on the warm electron population, which is mainly responsible for the ionization.

3.2. Code enhancements

While the numerical method has remained unchanged in principle since the introduction of the method [1], the code has been updated improving the precision and speed of the algorithm: *(i)* The rate coefficients are now calculated as a function of the average energy $\langle E_e \rangle$ of the EED (not T_e), which facilitates the comparison between different EEDs in the future. *(ii)* In Ref. [1] we adopted an "umbrella" uncertainty bound of 60 % for the rate coefficient as reported by Voronov [11]. The code now uses the experimental uncertainties of the cross section data [12]. *(iii)* The handling of the constraints has been improved: The penalty function is first minimized within the n_e and $\langle E_e \rangle$ bounds. After the minimum has been found, the characteristic times are calculated and minima leading to negative (unphysical) characteristic times are discarded. All the following results have been computed using the improved version (v1.2) of the code.
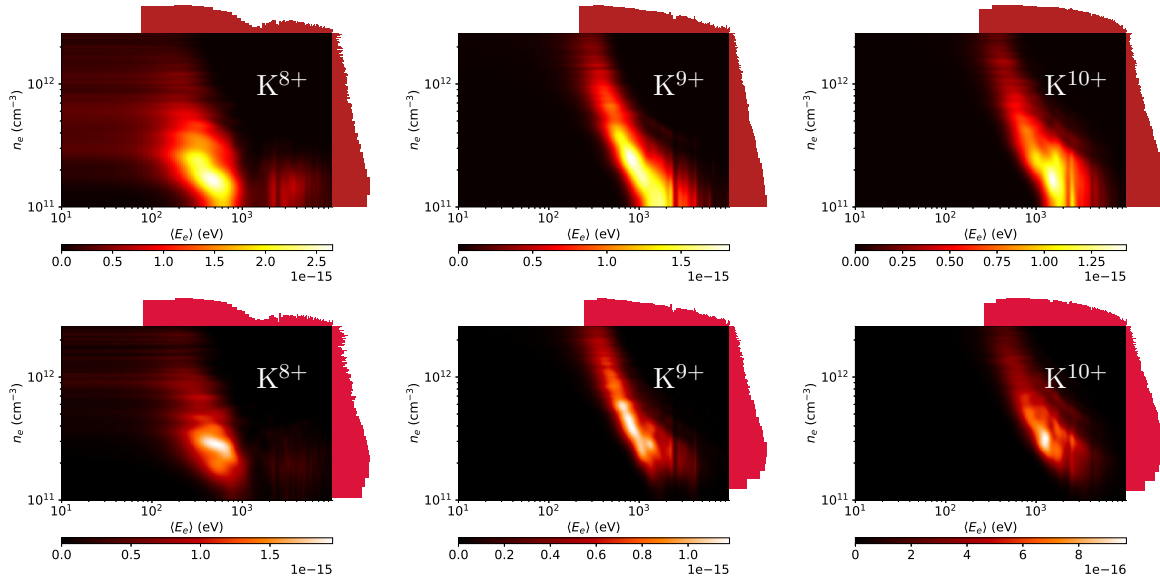
Figure 1: The $(n_e, \langle E_e \rangle)$ -solution sets of K8+–K10+ for the two charge breeder configurations Former (upper row) and New (lower row).
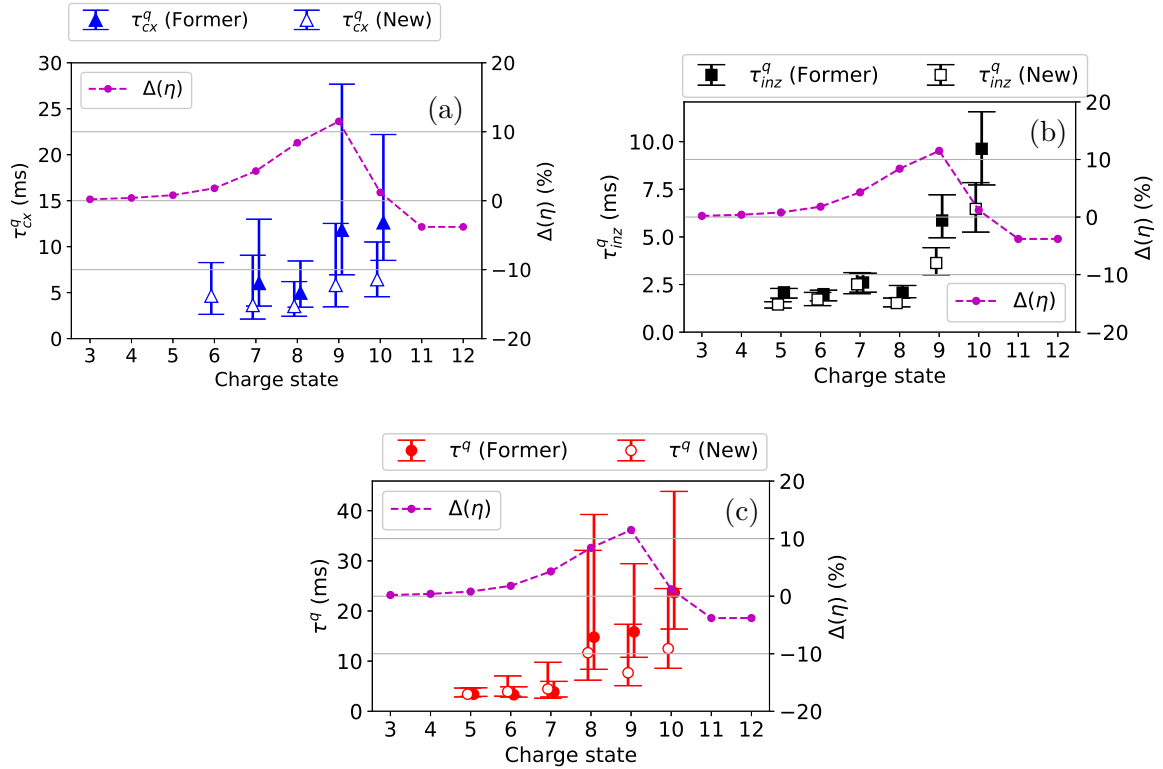
4. Results and analysis

Figure 2: Comparisons of τ_{cx}^q, τ_{inz}^q and τ^q and the absolute difference $\Delta(\eta)$ of CB efficiencies.

Figure 1 shows heatmaps of the $(n_e, \langle E_e \rangle)$ i.e. viable solutions of Eq. 9 in both CB

Table 3: The most probable values of n_e and $\langle E_e \rangle$ in the two CB configurations.

	n_e ($\times 10^{11}$ cm^{-3})		$\langle E_e \rangle$ (eV)	
Ion	Former	New	Former	New
K^{5+}	1.0	1.0	96	129
K^{6+}	1.3	1.4	124	115
K^{7+}	1.2	1.0	156	168
K^{8+}	1.4	2.1	150	214
K^{9+}	1.0	2.6	288	357
K^{10+}	1.4	2.5	353	518

configurations for K^{8+}–K^{10+}. These examples represent the set of (n_e, $\langle E_e \rangle$)-pairs satisfying Eq. 9 in the vicinity of their respective ion population n^q. It must be recalled, that the I^q beams are extracted from the whole plasma, and the n_e and $\langle E_e \rangle$ values represent averages for a given ion population. The variation of the n_e and $\langle E_e \rangle$ as a function of q thus reflects the average spatial variation of each n^q. Hence, the characteristic times calculated at these (n_e, $\langle E_e \rangle$) also yield a distribution of results. Further constraining (if possible) of the n_e and $\langle E_e \rangle$ spans, and the uncertainty of the ionization cross sections, would decrease the uncertainty of the results. Histograms of the solution sets are projected onto the n_e and $\langle E_e \rangle$ axes (note the logarithmic scale).

Comparison of the histograms and the most probable values of n_e and $\langle E_e \rangle$ — tabulated in Table 3 — reveals that in the new configurations the local n_e and $\langle E_e \rangle$ are higher in particular for the HCIs. This is commensurate with the decrease of their τ_{inz}^q. Increase of n_e is also to be expected from the increased neutral gas input compared to the former configuration, as the increased n_0 allows for a higher n_e, particularly in the core of the plasma where the highly charged ions (HCIs) are believed to be confined in the potential dip [3], which itself is generated by the higher concentration of hot, well-confined electrons.

Figure 2 shows τ_{inz}^q, τ_{cx}^q and τ^q as a function of q for the two data sets. The characteristic times are overlaid with the absolute charge breeding efficiency change between the CB configurations. The uncertainty bounds enclose a one sigma (34.1 %) fraction of all results around the median value, represented by the data point. The distribution of values is typically sharply peaked around the lower values, with the most probable value lying below the median. The size of the uncertainty bounds is affected by both, the uncertainty of the experimentally measured ionization cross sections (e.g. at worst for K^{8+} the uncertainty is $\delta\sigma_{q\rightarrow q+1}^{\mathrm{inz}}/\sigma_{q\rightarrow q+1}^{\mathrm{inz}} = 200$ %) and the limits imposable upon the solution space (n_e, $\langle E_e \rangle$). Especially the K^{9+} efficiency is improved between the two configurations. Each of the characteristic times, in particular τ_{cx}^q and τ^q have decreased for the HCIs, although in most cases the uncertainty bounds overlap.

Molecular hydrogen has a larger diameter and smaller ionization potential than helium, which may explain the decrease in τ_{cx}^q, the charge exchange cross section being inversely proportional to the square of the ionization potential [13], i.e. $\sigma_{q\rightarrow q-1}^{\mathrm{cx}} \propto I^{-2}$. Hence, switching to a H$_2$ support plasma increases $\sigma_{q\rightarrow q-1}^{\mathrm{cx}}$. There is a minimum in τ_{cx}^q around K^{7+} and K^{8+} for both of the data sets. This minimum is attributable to the increase of $\sigma_{q\rightarrow q-1}^{\mathrm{cx}}$ with q and the nested-layer structure of the ECRIS plasma. The latter is consistent with simulations and experiments [14, 15, 16, 17, 18] suggesting that the HCIs originate in the plasma core near the plasma chamber axis, while lower charge states originate from the peripheral plasma forming an overlapping layered structure. The increase of τ_{cx}^q towards the HCIs implies a decrease of neutral density toward the plasma core, since the $\sigma_{q\rightarrow q-1}^{\mathrm{cx}}$ increasing with q would otherwise imply a further decrease in τ_{cx}^q. The decreased τ_{cx}^q of the HCIs is in line with the increased

charge breeding efficiency of the lower charge states in the new configuration.

There is a small decrease of τ_{inz}^q of the low charge states, while a prominent decrease, attributed to the increase of n_e implied by the solution sets (Fig. 1.), is seen for the HCIs in the new configuration. The effect of the faster ionization is to feed the high charge state populations. The electron shell closure at K^{9+} causes a discrete jump between τ_{inz}^{8+} and τ_{inz}^{9+}.

The median of the confinement time τ^q solutions has decreased in particular for K^{9+} and K^{10+}. Especially the former data set shows a non-linear q-dependence for τ^q. A linear model for τ^q would yield negative confinement times for low charge states, while a power law fit is found to best represent the results [1]. In Ref. [7] a linearly increasing trend and much shorter values (~ 5 ms) of τ^q were found. Short τ^q has been used as an argument in favor of a predominantly collisional or ambipolar ion confinement[19]. However, recent optical measurements of the Doppler broadening of ion emission lines [20] have found $\sim$ 10 eV ion temperatures, unattainable with such short τ^q. There is mounting evidence from emittance [15] and current density measurements [17, 18], simulations [14, 3], and afterglow experiments [21, 22], that the HCIs are confined within a potential dip $\Delta\phi$ of the plasma potential distribution. The HCIs remain confined until they obtain enough energy to overcome the electrostatic barrier, i.e. in excess of $eq\Delta\phi$. The electrostatic confinement scheme is in accordance with the power law trend observed here.

It is important to note that it is the combination of τ_{inz}^q, τ_{cx}^q, and τ^q ($\forall q \in \{0, 1, 2, \ldots, q_{\mathrm{max}}\}$) that determines the steady-state CSD of the plasma. The change in the K^{9+} efficiency can thus be explained through the characteristic times: *(i)* The decrease in τ_{cx}^q for the HCIs indicates faster rate of charge exchange and a consequent shift of the CSD towards lower charge states. In effect, the K^{9+} population is fed from the HCIs via charge exchange; *(ii)* The decrease in τ^q allows the K^{9+} ions — once produced — to escape more rapidly, which increases the extracted beam intensity; *(iii)* The shorter ionization time of the low charge states supplies to the K^{9+} population (but is counteracted by the simultaneous decrease of τ_{cx}^q). In short, the increase of the K^{9+} CB efficiency is explicable by the pile-up into $q = 9$ and its shorter confinement time.

5. Conclusion

It has been shown, that the CT-method can be used to discern differences between the characteristic times in different CB configurations. It therefore enables the analysis of fundamental processes in the ion source plasma. Here, the source tune has been changed by varying multiple operating parameters, and the characteristic times are affected by multiple physical effects. In future experiments, the evolution of the characteristic times will be studied by varying one parameter at a time.

It must be noted that an infinitude of $(n_e, \langle E_e \rangle)$ pairs satisfies Eq. 9. It would be a great benefit to the method, if it were possible to set stricter constraints on n_e and $\langle E_e \rangle$, and if the ionization cross section were known more precisely. The presumed EED also being a source of possible error, its experimental measurement in plasma is desired. In short term we plan to study the sensitivity of the results on the assumed EED.

The CT-method provides a breakdown of τ_{CB}^q to its components: The characteristic times τ_{inz}^q, τ_{cx}^q determine the rate at which ions of different charge states are generated, while τ^q gives the rate at which ions of a given population exit the plasma. It is important to note that τ_{CB}^q is affected by the characteristic times of all charge states populations as a given particle may spend time as an ion at various different charge states before being extracted from the source. The τ_{CB}^q is thus a measure of the cumulative confinement time [23] of an ion, including its charge state history, while τ^q measures the confinement time of ion population at charge state q, and is directly affected by changes in the ion confinement conditions.

Based on the discussion of the causes underlying the change in K^{9+} efficiency, it can be said that in order to maximize the charge breeding efficiency of a given charge state one must maximize the pile-up into that charge state population the charge states both above and below,

i.e. one must minimize the ionization time from below, and minimize the charge exchange time from above. The best efficiencies can be obtained for charge states whose valence electron lies on a closed shell (such as K^{9+}), because the ionization from such a state is minimized and the population will not be depleted as much via ionization to higher states. At the same time one should minimize the confinement time of the desired charge state to efficiently extract the ions.

Data availability statement

The data that support the findings of this study are openly available at `DOI:10.6084/m9.figshare.14685432`, and the analysis code (release version 1.2.4) is publicly available at: `https://github.com/misapema-jyfl/popTauPy`.

Acknowledgments

References

[1] Angot J, Luntinen M, Kalvas T, Koivisto H, Kronholm R, Maunoury L, Tarvainen O, Thuillier T and Toivanen V 2020 *Plasma Sources Science and Technology* **30** 035018
[2] Shirkov G, Mühle C, Musiol G and Zschornack G 1991 *Nucl. Instrum. Methods Phys. Res. A: Accel. Spectrom. Detect. Assoc. Equip.* **302** 1 − 5 ISSN 0168-9002
[3] Shirkov G D 1993 *Plasma Sources Science and Technology* **2** 250–257
[4] Angot J, Galatà A, Maunoury L, Thuillier T, Baylac M, Migliore M and Sole P 2020 *ECRIS 2020 proceedings* WEZZO02
[5] Angot J, Tarvainen O, Thuillier T, Baylac M, Lamy T, Sole P and Jacob J 2018 *Phys. Rev. Accel. Beams* **21**(10) 104801
[6] West H J 1982 Calculation of ion charge state distribution in ecr ion source Tech. rep. Lawrence Livermore National Laboratory
[7] Douysset 1 G, Khodja H, Girard A and Briand J P 2000 *Phys. Rev. E* **61**(3) 3015–3022
[8] Geller R 1996 *Electron cyclotron resonance ion sources and ECR plasmas* (IOP) ISBN 9780750301077
[9] Tarvainen O, Koivisto H, Galatà A, Angot J, Lamy T, Thuillier T, Delahaye P, Maunoury L, Mascali D and Neri L 2016 *Phys. Rev. Accel. Beams* **19**(5) 053402
[10] Perret C 1998 *Caractérisation de la population électronique dans un plasma de source d'ions à résonance cyclotronique électronique* Ph.D. thesis Université Joseph Fourier, Grenoble
[11] Voronov G 1997 *At. Data Nucl. Data Tables* **65** 1 − 35 ISSN 0092-640X
[12] Lennon M A, Bell K L, Gilbody H B, Hughes J G, Kingston A E, Murray M J and Smith F J 1988 *Journal of Physical and Chemical Reference Data* **17** 1285–1363 ISSN 15297845
[13] Knudsen H, Haugen H K and Hvelplund P 1981 *Phys. Rev. A* **23**(2) 597–610
[14] Mironov V, Sergey B, Bondarchenko A, Efremov A and Loginov V 2015 *Physical Review Special Topics - Accelerators and Beams* **18**
[15] Wutte, D, Clark, D J, Laune, B, Leitner, M A, Lyneis C M 2001 *AIP Conference Proceedings* vol 445 pp 445–448
[16] Leitner M A, Wutte D and Lyneis C M 2001 *Proceedings of the 2001 Particle Accelerator Conference, Chicago* vol 5 ed Lucas P and Webber S Argonne National Laboratory and Fermi National Accelerator and Laboratory Oak Ridge National Laboratory (Chicago, Illinois U.S.A.: IEEE) pp 67–69
[17] Panitzsch L, Stalder M and Wimmer-Schweingruber R F 2011 *Rev. Sci. Instrum.* **82** 033302
[18] Panitzsch L, Peleikis T, Stalder M and Wimmer-Schweingruber R F 2011 *Rev. Sci. Instrum.* **82** 093302
[19] Melin G, Drentje A G, Girard A and Hitz D 1999 *Journal of Applied Physics* **86** 4772
[20] Kronholm R, Kalvas T, Koivisto H, Laulainen J, Marttinen M, Sakildien M and Tarvainen O 2019 *Plasma Sources Science and Technology* **28** 075006
[21] Sortais P 1992 *Rev. Sci. Instrum.* **63** 2801–2805
[22] Nakagawa T *et al.* 1998 *Review of Scientific Instruments* **69** 637–639
[23] Marttinen M *et al.* 2020 *Rev. Sci. Instrum.* **91** 013304

PIII

DIAGNOSTICS OF HIGHLY CHARGED PLASMAS WITH MULTICOMPONENT 1+ ION INJECTION

by

M Luntinen, V Toivanen, H Koivisto, J Angot, T Thuillier, O Tarvainen, G Castro

Physical Review E **106**, 055208 (2022) .

Author(s): Luntinen, M.; Toivanen, V.; Koivisto, H.; Angot, J.; Thuillier, T.; Tarvainen, O.; Castro, G.

Title: Diagnostics of highly charged plasmas with multicomponent 1+ ion injection

Year: 2022

Version: Published version

Please cite the original version:

Luntinen, M., Toivanen, V., Koivisto, H., Angot, J., Thuillier, T., Tarvainen, O., & Castro, G. (2022). Diagnostics of highly charged plasmas with multicomponent 1+ ion injection. Physical Review E, 106(5), Article 055208. https://doi.org/10.1103/PhysRevE.106.055208

Diagnostics of highly charged plasmas with multicomponent 1+ ion injection

M. Luntinen [ORCID],[*] V. Toivanen [ORCID], and H. Koivisto [ORCID]

Accelerator Laboratory, Department of Physics, University of Jyväskylä, FI-40014 Jyväskylä, Finland

J. Angot [ORCID][†] and T. Thuillier [ORCID]

Univ. Grenoble Alpes, CNRS, Grenoble INP, LPSC-IN2P3, 38000 Grenoble, France

O. Tarvainen [ORCID]

*UK Science and Technology Facilities Council, ISIS Pulsed Spallation Neutron and Muon Facility,
Rutherford Appleton Laboratory, Harwell Campus, OX11 0QX, United Kingdom*

G. Castro [ORCID]

INFN-LNS, Via S. Sofia 62, 95123, Catania, Italy

We establish multicomponent 1+ injection into a charge breeder electron cyclotron resonance ion source and an associated computational procedure as a noninvasive probe of the electron density n_e, average electron energy $\langle E_e \rangle$, and the characteristic times of ionization, charge exchange, and ion confinement of stochastically heated, highly charged plasma. Multicomponent injection allows refining the n_e, $\langle E_e \rangle$ ranges, reducing experimental uncertainty. Na/K injection is presented as a demonstration. The $\langle E_e \rangle$ and n_e of a hydrogen discharge are found to be 600^{+600}_{-300} eV and $8^{+8}_{-3} \times 10^{11}$ cm^{-3}, respectively. The ionization, charge exchange, and confinement times of high charge state alkali ions are on the order of 1 ms–10 ms.

I. INTRODUCTION

In past decades, the nuclear and astrophysics communities have migrated toward the use of radioactive ion beams (RIBs) for the study of nuclear structures far from stability [1]. The RIB production methods (e.g., the ISOL method [2]) generate low-intensity beams of singly charged, radioactive ions, which need to be postaccelerated to attain an energy required for nuclear physics experiments. The 1+ ions are usually further ionized before postacceleration in a process referred to as charge breeding [3,4].

In a charge breeder electron cyclotron resonance ion source (CB-ECRIS) [5] the radioactive 1+ species are injected at low energy and captured by the plasma, where the magnetically confined electrons are stochastically heated by microwave radiation. The electrons attain energies in the 10 eV to 100 keV range through resonant interaction with the microwave and are able to ionize the injected particles in a stepwise manner. The ionization is counteracted by charge exchange with the neutral atoms of the plasma, whereby the highly charged ion captures a valence electron from the neutral atom.

The electron impact ionization process is dominated by electrons at 10^2–10^3 eV energies. The high-energy electrons at 10^4–10^5 eV range are well confined and form a 3D dip in the positive ambipolar plasma potential profile [6,7], confin-

ing the highly charged ions. Consequently, the different ion populations form a nested layer structure, with higher charge states originating near the axis of the plasma chamber, and lower charge states from the peripheral plasma (see, e.g., simulations in Refs. [8,9]). The plasma loss processes (e.g., random-walk [10], ambipolar diffusion [11], rf scattering [12], and instabilities [13]) determine the rate at which ions escape confinement and become available for beam formation. The ion confinement time needs to be long compared to the ionization time for the ions to reach a high charge state. If the charge-bred species is radioactive, the confinement time must also be short compared to its half-life.

The charge-breeding process needs to be fast and efficient to enable the—usually quite low intensity—injected radioactive 1+ ion beam to be charge bred to high charge states before radioactive decay causes significant losses. The ion production efficiency and breeding time must be understood to discern which radioactive isotopes are accessible for charge breeding and postacceleration, and to guide further development of the CB-ECRIS to access RIBs of short-lived isotopes. The total breeding time is relatively well understood phenomenologically [14] but the underlying physical causes have not yet been revealed by experiment. The diagnostic methods used to probe these properties must be noninvasive to avoid perturbing the tenuous plasma state. In effect, this constrains the methods to those usable in the same conditions as when delivering the RIB to the user.

We have recently developed a method which satisfies these conditions. The so-called consecutive transients (CT) method

---

[*]miha.s.p.luntinen@jyu.fi
[†]julien.angot@lpsc.in2p3.fr

055208-1

[15,16] for estimating the ECR-heated plasma properties, i.e., the electron density, average energy of the EED, characteristic times of ionization, charge exchange, and ion confinement. It is based on causing a small perturbation and monitoring the response of the complex system to it, requiring fewer *a priori* assumptions than any previous method and, uniquely, accounts for the experimental uncertainty of the electron-impact ionization cross sections employed in the calculations involved in this and similar methods [17–21]. Stable alkali metal ions are used as a proxy for the true RIBs. Here we expound an experimental and computational methodology relying on multicomponent probing of the plasma. This allows physically constraining the results, circumventing the uncertainty of the ionization cross sections inherited by the CT method.

II. METHOD

The working principle of the CT method is as follows: A continuous beam of singly charged metallic ions is injected into the plasma of a CB-ECRIS from the 1+ ion source [22]. Metallic ions are chosen to prevent recirculation from the plasma chamber walls [23]. The operating parameters (neutral gas input rate, microwave heating power, magnetic mirror ratios, etc.) of the ECRIS are then optimized for the production of a desired charge state of the injected species in a process colloquially referred to as tuning.

Once the tune is established, the injected 1+ beam is pulsed by means of an electrostatic chopper to produce square 1+ ion pulses. It is important to minimize the perturbation on the plasma by selecting an appropriate pulse width (on the order of 10 ms) and injected 1+ current (∼100–500 nA), limiting the rate of particles injected into the device to roughly two orders of magnitude less than the total rate of particles extracted from the plasma. It was shown in Ref. [15] that the modification of the high charge states' beam currents in the support plasma charge state distribution (CSD) was at most ∼5 % when injecting the 1+ species continuously at an intensity of 710 nA. The perturbation is even smaller in the pulsed injection mode with lower 1+ currents.

The temporal evolution of the volumetric density of charge state q in the plasma is described by the balance equation [7]

$$
\begin{aligned}
\frac{dn^q}{dt} = &+ n_e \langle \sigma v \rangle^{\text{inz}}_{q-1 \to q} n^{q-1} - n_0 \langle \sigma v \rangle^{\text{cx}}_{q \to q-1} n^q \\
&+ n_0 \langle \sigma v \rangle^{\text{cx}}_{q+1 \to q} n^{q+1} - n_e \langle \sigma v \rangle^{\text{inz}}_{q \to q+1} n^q \\
&- \frac{n^q}{\tau^q},
\end{aligned}
\tag{1}
$$

where $\langle \sigma v \rangle^{\text{inz/cx}}$ are the rate coefficients of ionization from the ground state and charge exchange (functions of the average energy of the electron or ion energy distribution, see Ref. [15]), n_0, n^q, and n_e the neutral, ion, and electron densities, respectively. The final term $-n^q/\tau^q$ represents the rate of ion losses and defines the confinement time τ^q.

Since the injected beam is pulsed, the time series of the extracted beam is a transient whose shape is determined by Eq. (1). We measure the beam current time series (I^q) and fit

them with an equation derived from Eq. (1),

$$
\frac{dI^q}{dt} = a_q I^{q-1} - b_q I^q + c_q I^{q+1},
\tag{2}
$$

where the fit coefficients a_q, b_q, and c_q are functions of n_e and $\langle E_e \rangle$. At least five consecutive charge states' currents are required for the analysis.

Using an optimization procedure [15], it is possible to determine a range of n_e and $\langle E_e \rangle$ values consistent with the coefficients a_q, b_q, and c_q, and to calculate the characteristic times of ionization (from q to $q + 1$) $\tau^q_{\text{inz}} = [n_e \langle \sigma v \rangle^{\text{inz}}_{q \to q+1}]^{-1}$, charge exchange (from q to $q - 1$) $\tau^q_{\text{cx}} = [n_0 \langle \sigma v \rangle^{\text{cx}}_{q \to q-1}]^{-1}$, and ion confinement τ^q.

Similarly to the n_e and $\langle E_e \rangle$ values, a range of solutions is obtained for the characteristic times, and in lieu of additional constraints (e.g., the cutoff density [24] for n_e) the range may be very broad. There is evidence from both simulations and experiments that highly charged ions originate from the same plasma volume near the central axis of the plasma chamber [8,9,25–28] and, consequently, these ion populations probe the same plasma conditions, i.e., they have a common n_e $\langle E_e \rangle$ value. We may thus take the intersection of two or more solution sets of highly charged ion populations which constrains the results on the aforementioned physical basis. The intersection is obtained by multiplying the two-dimensional histograms generated from the distributions of the n_e, $\langle E_e \rangle$ points within the solution sets of the two populations.

The $\langle E_e \rangle$ dependence of the a_q, b_q, c_q coefficients arises via the rate coefficients, which are calculated under the assumption of a Maxwell-Boltzmann electron energy distribution (EED) for the warm electrons, since the actual EED is unknown. Experiments measuring the lost electron energy indicate a non-Maxwellian tail for the EED [29], but results with the kappa-distribution [30] have shown that the characteristic times obtained via the CT method are unaffected by even a large distortion of the shape of the EED.

There are three possibilities for applying the overlap-method: (i) overlap of different charge states of the same ion species (e.g., K^{9+}, K^{10+}, ...), (ii) overlap of the same charge states of different isotopes (e.g., $^{39}K^{9+}$ and $^{41}K^{9+}$), and (iii) overlap of high charge states of different ion species (e.g., K and Na). Each case is justified for HCIs for the reasons mentioned in the previous paragraph. Additionally, case (ii) is justified whenever the two isotopes' masses are similar enough not to cause a significant difference in their spatial distribution. We will focus on category (iii) as a sample case, since the different ionization cross sections of the two species help mitigate the effects of the large experimental uncertainty of the ionization cross sections currently available; data from Refs. [31,32] are used in this paper. Results for cases (i) and (ii) are presented in the Appendices alongside additional discussion.

A. Overlap analysis of Na and K

The data [33] were collected on the LPSC 14.5 GHz CB-ECRIS test bench [5,15] (see also Appendix A). The experimental setup was amended by loading the 1+ ion source

with a Na/K composite pellet, which enables producing a beam of Na^+ and K^+ and quickly switching between them by retuning the injection beam line, without having to adjust the CB-ECRIS parameters. Due to the internal uncertainties involved in tuning the CB-ECRIS, no-stop component switching is paramount to ensure that the same plasma conditions are probed by both injected species. The CB-ECRIS was tuned for Na^{8+} production, and pulsed beams of 100 nA and 200 nA of $^{23}Na^+$ and $^{39}K^+$, respectively, were injected in 10 ms pulses into the hydrogen discharge sustained in the source. The injection beamline optics were tuned for each injected 1+ species, and the extracted highly charged ion beam currents were measured at the N+ Faraday Cup, downstream of the CB-ECRIS (see Appendix A). The experimental parameters are tabulated in Table III in Appendix B.

The time series of the charge bred K and Na beam current transients (the N+ currents) were analyzed using the CT-analysis codes (the CT analyzer) [34] and the n_e, $\langle E_e \rangle$ postdictions consistent with the measured time series—and the corresponding characteristic times—were obtained. Each $(n_e, \langle E_e \rangle)$ pair of the solution set satisfies the fitting parameters a_q, b_q, c_q and is thus a possible value of the plasma density and average energy within the plasma volume whence the K and Na ions originate. On the order of 10^4 postdictions were obtained in each set. The n_e, $\langle E_e \rangle$ range where solutions were sought was limited on physical grounds. The density was constrained to the range 10^{11} cm^{-3} < n_e < 2.6×10^{12} cm^{-3}, where the upper limit is the cutoff density for 14.5 GHz microwaves and the lower limit is a conservative estimate based on results from Ref. [13]. 3D Monte Carlo simulations [35] suggest that the plasma within the ECR zone may be overdense (i.e., n_e greater than the cutoff density). However, there is no direct experimental evidence of this. The average energy of the EED was set to the range 10 eV < $\langle E_e \rangle$ < 10 keV, where the lower limit is the order of magnitude of the plasma potential [36] and the upper limit was chosen based on Ref. [11].

Based on simulation results for the spatial distribution of ions [9], it can be argued that ions having a charge state above the peak in the CSD can be said to originate from the same plasma volume. Figure 1 shows the CSD (continuous 1+ injection) of K and Na, which indicates that the peak occurs for Na^{6+} and K^{9+}. It was found that in the data set presented here, a mutual overlap of $(n_e, \langle E_e \rangle)$ can be found for the populations of K^{9+}, K^{10+}, and Na^{7+}.

To obtain the overlap set, a 2D histogram was generated out of each $(n_e, \langle E_e \rangle)$ solution set (with 200×200 bins). These histograms were then multiplied binwise by one another, and the product histogram was normalized to the maximum density of solutions within the set, i.e., the region which contributes most to the characteristic times calculated within the set. Finally, only those $(n_e, \langle E_e \rangle)$ pairs falling into the nonzero bins of the product set were kept out of the original solution sets. This constrains the set of viable solutions significantly, as demonstrated hereafter.

III. RESULTS

Figure 2 shows the outlines of the individual solution sets of K^{9+}, K^{10+}, and Na^{7+} in $(\langle E_e \rangle, n_e)$ space, restricted on the
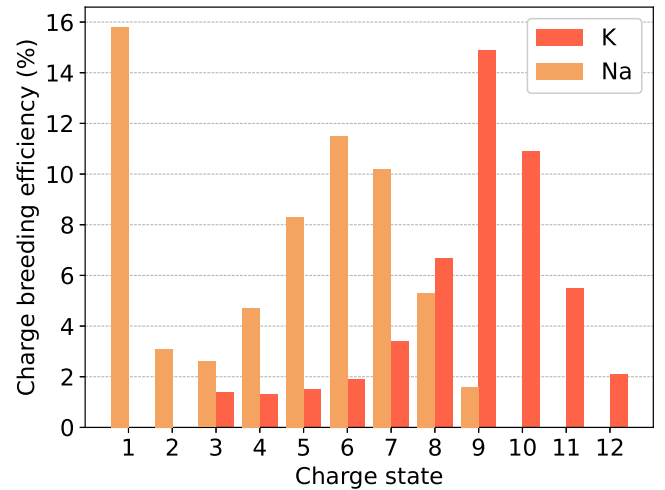

FIG. 1. Continuous mode charge breeding efficiencies of K and Na.

physical grounds discussed above, and Fig. 3 shows the heat map of their mutual overlap. The distributions of n_e and $\langle E_e \rangle$ values are projected as histograms on the margins of Fig. 3. To characterize the distributions, we tabulate the median value and in superscript and subscript we indicate the upper and lower confidence bounds, respectively, which enclose 34.1% of all solutions above and below the median. For example, the value $n_e = 4^{+10}_{-3}$ (10^{11}cm^{-3}) would describe a distribution whose median value is 4 (10^{11}cm^{-3}) and 68.2% of all n_e values would fall in the interval [1, 14] (10^{11}cm^{-3}). Figure 5 in Appendix C shows an example distribution obtained for the confinement time from the CT analyzer, with the median and the 34.1% bounds plotted as vertical lines.

Table I shows the median values of n_e and $\langle E_e \rangle$ as well as their 34.1% bounds for both the individual solution sets as well as the overlap. Similarly, Table II shows the median as well as the minimum characteristic times calculated from the individual solution sets, and within their mutual overlap. The
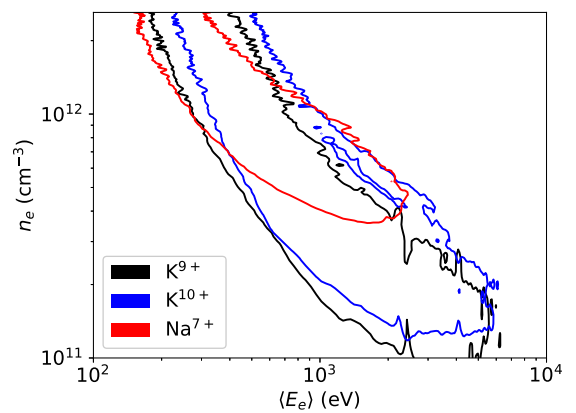

FIG. 2. The limits of the solution sets for K^{9+}, K^{10+}, and Na^{7+}. The threshold of the drawn contours has been set to 0.1 of the maximum density. The solution set ranges have been constrained based on physical considerations as described in the text. The image has been modified by an applied Gaussian filter for improved clarity.
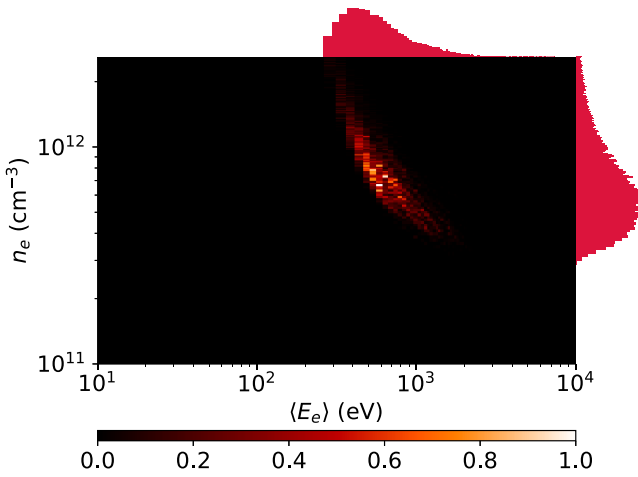
FIG. 3. Heat map of the overlap of the K^{9+}, K^{10+}, and Na^{7+} solution sets. Densities are normalized to the maximum density. Margin histograms show the distribution of n_e and $\langle E_e \rangle$ values within the overlap set.

minimum values are tabulated for the characteristic times to highlight their order of magnitude in particular in the case of the confinement time.

We find that the uncertainty is reduced in almost all cases, and that in particular the n_e, and $\langle E_e \rangle$ distributions benefit from the overlap: For example, the median of $\langle E_e \rangle$ corresponding to the K^{10+} population decreases from 1300 eV to 600 eV, and the relative uncertainty from 200% to 150% when applying the overlap. The n_e median increases from 4×10^{11} cm^{-3} to 8×10^{11} cm^{-3}, and the relative uncertainty decreases from 300% to 140%.

The characteristic time estimates are also generally improved, in particular the confinement times. The relative uncertainty of K^{10+} confinement time decreases from 140% to 100% with the overlap. Similar reduction in the error bars of the charge exchange times can be seen. We note also that the minimum confinement times are significantly longer than those suggested by Ref. [11].

IV. DISCUSSION

The CT method yields a postdiction for the range of electron densities and average energies (for the presumed EED), which can serve as a guide for plasma modeling. We have shown it to be possible to reduce the breadth of the n_e, $\langle E_e \rangle$ region by overlapping two or more solution sets—in partic-

TABLE I. Medians and 34.1% bounds of n_e and $\langle E_e \rangle$ calculated from the individual solution sets and within the overlap of K and Na. Applying the overlap (two-element injection) reduces the uncertainty.

	n_e (10^{11}cm^{-3})	$\langle E_e \rangle$ (eV)
K^{9+}	4^{+10}_{-3}	1000^{+1900}_{-600}
K^{10+}	4^{+9}_{-3}	1300^{+1800}_{-800}
Na^{7+}	7^{+6}_{-3}	900^{+4600}_{-500}
Overlap	8^{+8}_{-3}	600^{+600}_{-300}

TABLE II. The characteristic times of confinement, ionization, and charge exchange (τ^q, τ^q_{inz}, τ^q_{cx}, respectively) for K^{9+}, K^{10+}, and Na^{7+} within their mutual overlap and individually. The minimum value (Min.) of the distribution is given along with the median (Med.) and the upper and lower bounds enclosing 34.1% of solutions above and below the median. All data in units of ms.

		τ^q		τ^q_{inz}		τ^q_{cx}	
	Ion	Min.	Med.	Min.	Med.	Min.	Med.
Overlap	K^{9+}	5	8^{+6}_{-2}	2	$3.5^{+.5}_{-.6}$	3	16^{+14}_{-8}
	K^{10+}	8	16^{+11}_{-5}	4	7^{+2}_{-2}	4	9^{+4}_{-3}
	Na^{7+}	4	$5.3^{+1.7}_{-.8}$	2	$2.8^{+.3}_{-.4}$	5	19^{+11}_{-8}
No overlap	K^{9+}	5	10^{+10}_{-4}	2	$3.8^{+.9}_{-.7}$	3	9^{+13}_{-5}
	K^{10+}	8	19^{+20}_{-7}	4	8^{+2}_{-2}	4	8^{+5}_{-3}
	Na^{7+}	4	$5.4^{+2.1}_{-.9}$	2	$2.8^{+.3}_{-.4}$	5	20^{+11}_{-8}

ular, the overlap of two different species (K/Na) limits the range of solutions. This reduction in the n_e, $\langle E_e \rangle$ uncertainty is reflected to the characteristic times.

Of the three overlap methods (i)–(iii), the overlap of two isotopes of the same element [case (ii)] had next to no effect, as could be expected: Since the plasma properties were unchanged, with two-nucleon mass difference there shouldn't be large deviations between the solution sets. Overlapping multiple charge states of a given species, or multiple species [cases (i) and (iii)], led to noticeable decrease in the uncertainty. The overlap of two different species [case (iii)] has the added benefit that the different ionization cross sections (and their different experimental uncertainties) reduce the effect of the uncertainty of the cross section on the method results. The results for cases (i) and (ii) are presented in Appendices D and E.

In Ref. [15], it was shown that the CT-method can be used to identify bottlenecks in the charge breeding process; e.g., an electron shell closure inhibits the production of higher charge states, and must be compensated by a higher plasma energy content to decrease the ionization time. Multicomponent injection helps in identifying these bottlenecks by decreasing the possible range of $\langle E_e \rangle$ and n_e, which leads to decreased uncertainty of the characteristic time values.

The method precision is still limited by the uncertainty of the ionization cross sections, whose literature values carry in some cases an experimental uncertainty in excess of 100%. This uncertainty is partly inherited by the CT- method through the evaluation of the ionization rate coefficients. Arbitrarily curtailing the cross section uncertainty in the data analysis leads to a further reduction in the width of the distribution of the characteristic times, which motivates improving the cross-section data either experimentally or through modeling.

The confinement times found by means of the CT method support recent findings [37] where ion temperatures in ECR-heated plasma were found to be an order of magnitude higher than conventionally believed. Long confinement times—consistent with electrostatic confinement in a potential dip within the plasma potential profile—were hypothesized as a potential explanation. According to Table II, highly charged ions have a confinement time $\gtrsim 5$ ms.
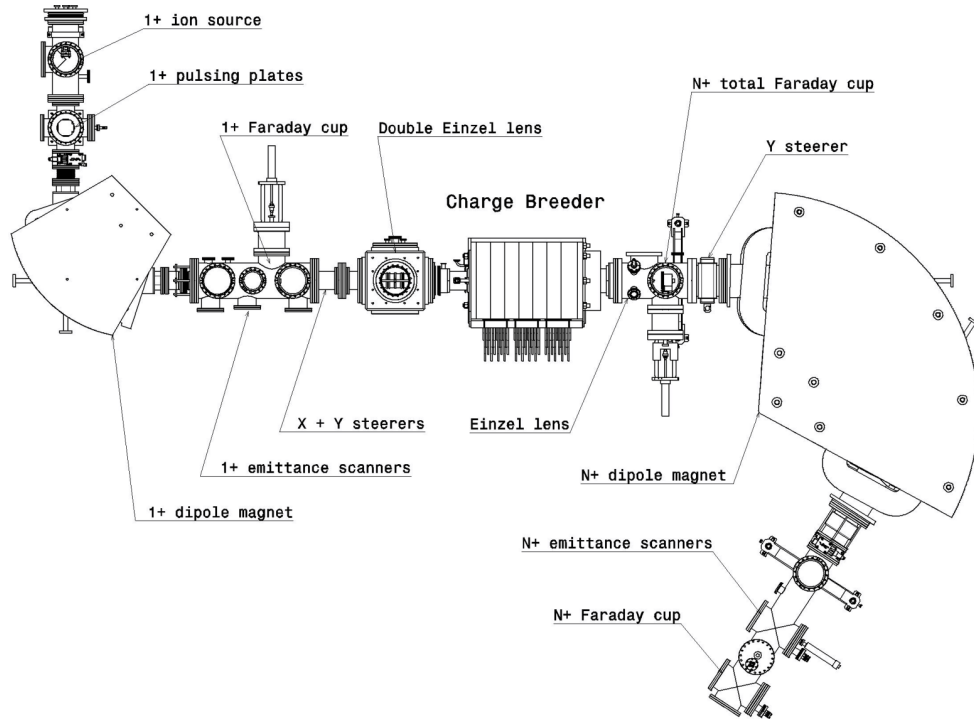
FIG. 4. Schematic layout of the $1+ \rightarrow N+$ PHOENIX-type 14.5 GHz CB-ECRIS test bench at LPSC.

Similarly long confinement time estimates have been found via other methods [19–21], with some simulations placing the total residence time of an ion inside the plasma at up to 100 ms [38]. The 100 ms residence time estimate is in agreement with the charge-breeding time measurements [14].

Reference [11] determined ion confinement times from the extracted beam currents via quasisimultaneous measurements of bremsstrahlung and Kα emissions from the plasma, and found much shorter confinement times than those presented in this paper (at most <4 ms for Ar^{16+}) with a linear charge state dependence. However, their analysis may be influenced

FIG. 5. The resultant confinement time distribution obtained for ^{41}K^{9+} in the helium discharge corresponding to the operating parameters of Table IV. The solid red line corresponds to the median and the dotted lines are the upper and lower bounds enclosing in total 68.2% of all results within the distribution.

by a circular reasoning as they fix the net ion density to obtain the EED from the bremsstrahlung emission, and later use the EED to compute the ion densities from the Kα emissions. The linear dependency, and an assumption of 1 eV temperature for all ions, was used to conclude that the ambipolar diffusion model is the best candidate for ion confinement in an ECRIS. In Ref. [15], confinement times found via the CT method were shown to be best fitted by a power law rather than a linear fit. This and the charge state dependent ~ 10 eV ion temperatures found in Ref. [37] suggest ion confinement in the potential dip instead—the ions trapped in the dip would stay there until they attain the energy required to overcome the potential barrier $qe\Delta\phi$.

By solving Eq. (1) as a function of time, it is possible to obtain the plasma CSD, and from there one may estimate the intensity of extracted N+ ions. In the case of RIB production, one must amend Eq. (1) with a term describing loss rates to radioactive decay, allowing the estimation of extracted RIB intensity. Doing this requires knowledge of the characteristic times of stable proxy elements, for which the presented method provides improved information.

APPENDIX A: THE EXPERIMENTAL SETUP

The experimental campaign was conducted on the Laboratory of Subatomic Physics and Cosmology (LPSC) $1+ \rightarrow$

TABLE III. ECRIS operating parameters for the Na/K overlap data set. The source was tuned for Na^{8+} production.

B_{inj}	1.54 T
B_{min}	0.45 T
B_{ext}	0.83 T
Microwave power	540 W (14.5 GHz)
Support gas species	H_2
P_{inj}	11–12 (10^{-8} mbar)
P_{ext}	13–15 (10^{-8} mbar)
1+ pulse width	10 ms
$^{39}K^{1+}$ injection intensity	200 nA
$^{23}Na^{1+}$ injection intensity	100 nA
Extraction HV	20 kV

N+ test bench, schematically pictured in Fig. 4. Starting from the top left of the figure, the 1+ ion source, based on thermionic emission of positive ions from a heated sample, was used to produce the singly charged ions for injection into the charge breeder: the amount of injected material was controlled by adjusting the heating power on the pellet. The pulsing was achieved by the 1+ pulsing plates, which deflected the beam electrostatically. The 1+ dipole magnet was used to select the desired 1+ ion species based on the charge-to-mass ratio, and the 1+ Faraday cup enabled the precise measurement of the injected 1+ current. The PHOENIX-type 14.5 GHz CB-ECRIS was assembled with a hexapole providing a 0.8 T radial magnetic field strength at the plasma chamber wall, on the poles. The plasma electrode aperture size was 8 mm. After extraction from the ECRIS, the N+ dipole magnet allowed the selection of the charge-bred, highly charged ions based on their charge-to-mass ratio. The N+ Faraday cup was used to measure the transient time series of the N+ currents.

APPENDIX B: ECRIS OPERATING PARAMETERS

The CB-ECRIS operating parameters used in the campaign to produce the Na/K-overlap data set are tabulated in Table III. The operating parameters used in the campaign to produce the isotope overlap data set are tabulated in Table IV.

TABLE IV. Source operating parameters for the isotope overlap data set.

B_{inj}	1.52 T
B_{min}	0.41 T
B_{ext}	0.83 T
Microwave power	540 W (14.5 GHz)
Support gas species	He
P_{inj}	8–10 (10^{-8} mbar)
P_{ext}	9–15 (10^{-8} mbar)
1+ pulse width	10 ms
$^{39}K^{1+}$ injection intensity	270 nA
$^{41}K^{1+}$ injection intensity	55 nA
Extraction HV	20 kV

TABLE V. The characteristic times of confinement, ionization, and charge exchange (τ^q, τ^q_{inz}, τ^q_{cx}, respectively) for $^{39}K^{9+}$ and $^{41}K^{9+}$ within their mutual overlap, and individually. The minimum value of (Min.) of the distribution is given along with the median (Med.) and the upper and lower bounds enclosing 34.1% of solutions above and below the median. All data in units of ms.

		τ^q		τ^q_{inz}		τ^q_{cx}	
	Ion	Min.	Med.	Min.	Med.	Min.	Med.
Overlap	$^{39}K^{9+}$	6	11^{+7}_{-3}	3	$5.4^{+.9}_{-.8}$	4	13^{+15}_{-6}
	$^{41}K^{9+}$	7	16^{+19}_{-6}	3	$4.5^{+.9}_{-.7}$	4	9^{+8}_{-4}
No overlap	$^{39}K^{9+}$	6	13^{+12}_{-4}	3	6^{+1}_{-1}	4	10^{+12}_{-4}
	$^{41}K^{9+}$	7	16^{+20}_{-6}	3	4^{+1}_{-1}	4	9^{+8}_{-3}

APPENDIX C: EXAMPLE CHARACTERISTIC TIME DISTRIBUTION

Figure 5 shows the confinement time values of $^{41}K^{9+}$ individually using the ECRIS operating parameters tabulated in Table IV. The median value 14.2 ms is plotted in solid red, while the lower bound at 9.5 ms and the upper bound at 28.8 ms are plotted with dotted lines. The upper and lower bounds enclose 34.1% of the solutions above and below the median, respectively, i.e., the uncertainty is given with a confidence of 68.2%.

APPENDIX D: ISOTOPE OVERLAP

The potassium isotopes ^{39}K and ^{41}K were selectively injected into the helium plasma of the charge breeder (the source operating parameters tabulated in Table IV). The resultant continuous injection mode CSDs are shown in Fig. 6. Although there is an apparent absolute difference in the charge breeding efficiencies of the two isotopes, it turns out that by multiplying the ^{39}K distribution by 1.16 yields the same shape as for ^{41}K. We can thus be assured that the plasma properties are not markedly changed by the differing 1+ injection intensities: One expects more or less the same CSD for two

TABLE VI. The characteristic times of confinement, ionization, and charge exchange (τ^q, τ^q_{inz}, τ^q_{cx}, respectively) for $^{39}K^{10+}$ and $^{41}K^{10+}$ within their mutual overlap, and individually. The minimum value of (Min.) of the distribution is given with the median (Med.) along with the upper and lower bounds enclosing 34.1% of solutions above and below the median. All data in units of ms.

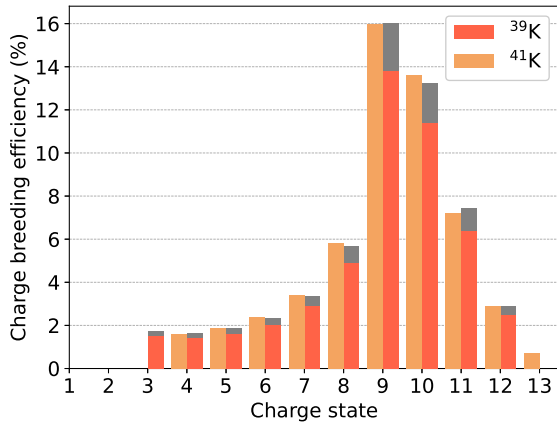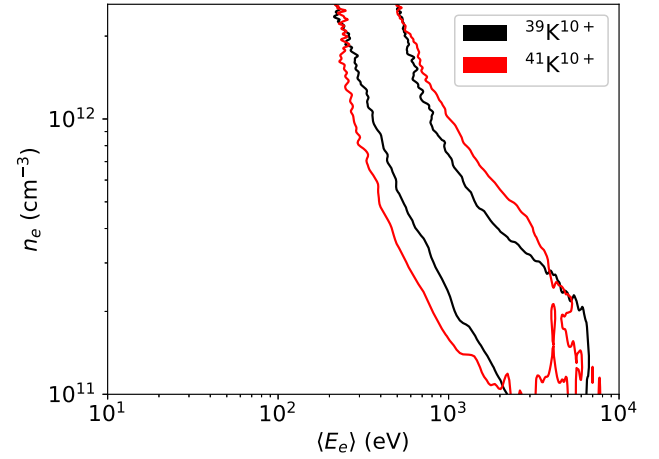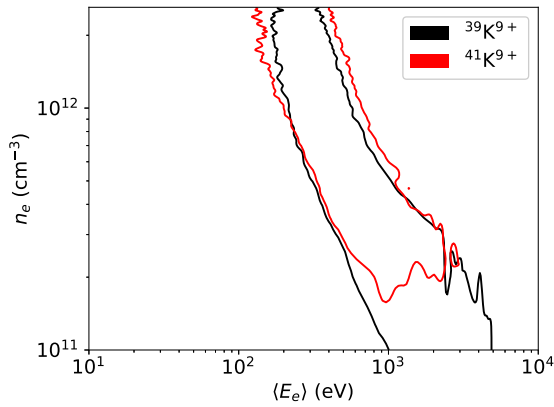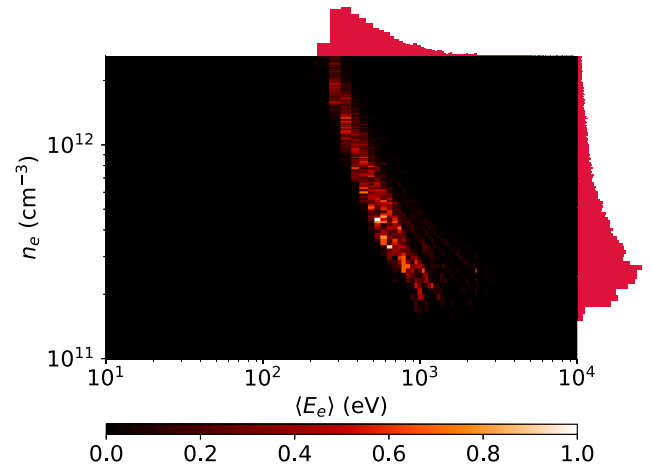|		τ^q		τ^q_{inz}		τ^q_{cx}	
	Ion	Min.	Med.	Min.	Med.	Min.	Med.
Overlap	$^{39}K^{10+}$	13	35^{+43}_{-14}	4	$5.8^{+.9}_{-.9}$	6	11^{+6}_{-3}
	$^{41}K^{10+}$	10	18^{+12}_{-5}	5	13^{+3}_{-3}	6	12^{+7}_{-4}
No overlap	$^{39}K^{10+}$	13	36^{+44}_{-14}	4	6^{+1}_{-1}	6	11^{+6}_{-3}
	$^{41}K^{10+}$	10	18^{+15}_{-5}	5	13^{+4}_{-3}	5	12^{+8}_{-4}

FIG. 6. The continuous mode charge breeding efficiencies of ^{39}K and ^{41}K. The gray bars represent the ^{39}K efficiency multiplied by 1.16, resulting in a distribution having the same shape as for ^{41}K.
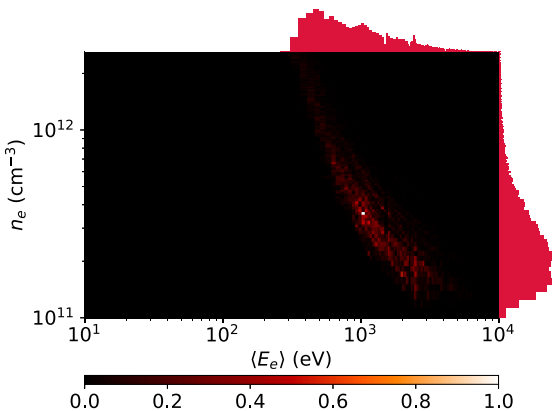

(a)

(a)

(b)

FIG. 8. Outermost contours of the solution sets of $^{39}K^{10+}$ and $^{41}K^{10+}$ (a) and the heat map of their overlap (b). (a) has been modified by an applied Gaussian filter for clarity. The margin histograms show the distribution of n_e and $\langle E_e \rangle$ values within the solution set.

(b) Overlap

FIG. 7. Outermost contours of the solution sets of $^{39}K^{9+}$ and $^{41}K^{9+}$ (a), and the heat map of their overlap (b). (a) has been modified by an applied Gaussian filter for clarity. The margin histograms show the distribution of n_e and $\langle E_e \rangle$ values within the solution set.

isotopes of the same ion species if the plasma properties are unchanged, since they have the same electron configuration. Figures 7 and 8 present the solution sets of $^{39}K^{9+/10+}$ and $^{41}K^{9+/10+}$ and heat maps of their respective overlaps.

The characteristic time results for $^{39}K^{9+}$ and $^{41}K^{9+}$ are tabulated in Table V and the results for $^{39}K^{10+}$ and $^{41}K^{10+}$ in Table VI. The corresponding values for the obtained n_e, $\langle E_e \rangle$ distributions are found in Tables VII and VIII for the overlaps of $^{39/41}K^{9+}$ and $^{39/41}K^{10+}$, respectively.

APPENDIX E: CHARGE-STATE OVERLAP

Three different overlap sets of the high charge states of ^{41}K were taken: The charge states $^{41}K^{10+}$–$^{41}K^{11+}$ were overlapped in set A, $^{41}K^{9+}$–$^{41}K^{11+}$ in set B, and $^{41}K^{8+}$–$^{41}K^{11+}$ in

TABLE VII. The electron densities n_e and averages energies of the EED $\langle E_e \rangle$ of the helium discharge obtained from $^{39}K^{9+}$ and $^{41}K^{9+}$ within their mutual overlap and individually. The median along with the upper and lower bounds enclosing 34.1% of solutions above and below the median is tabulated.
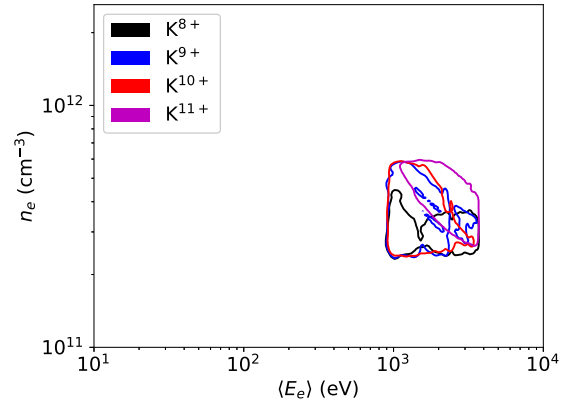
	n_e (10^{11}cm^{-3})	$\langle E_e \rangle$ (eV)
$^{39}K^{9+}$	$3.2^{+8.6}_{-1.7}$	890^{+1350}_{-520}
$^{41}K^{9+}$	$7.8^{+9.5}_{-4.6}$	510^{+580}_{-190}
Overlap	$5.9^{+9.9}_{-3.2}$	560^{+600}_{-230}

set C. The ECRIS operating parameters were the ones given in Table IV, and the CSD is the one shown in Fig. 6.

To obtain better statistics, the CT analyzer was run twice: First, the analysis was done as usual in the range $\langle E_e \rangle \in [10, 10\,000]$ eV, $n_e \in [1 \times 10^{11}, 2.6 \times 10^{12}]$ cm^{-3}. The overlap was then taken, and the minimum and maximum $\langle E_e \rangle$ and n_e values common to each population in the set were selected as the new limits. The CT analyzer was then run with the new, constrained limits. The resultant contours of sets A, B, and C are presented in Fig. 9, and the estimates of n_e and $\langle E_e \rangle$ are presented in Table IX. The characteristic times computed within each of the overlaps are plotted in Fig. 10. We find that there is a reduction in the uncertainty when more charge states are overlapped. However, the uncertainty of the confinement time of $^{41}K^{9+}$ markedly increases when $^{41}K^{8+}$ is included in the overlap. This may indicate that $^{41}K^{8+}$ originates from a region of plasma with different plasma conditions, and we note that $^{41}K^{8+}$ is indeed below the CSD peak, and hence may correspond to a different plasma volume. In the case of the ionization time and the charge exchange time, inclusion of $^{41}K^{8+}$ leads to further reduction in the uncertainty.

An interesting phenomenon in the ionization times emerges from the charge-state overlap: It appears that the ionization time of $^{41}K^{11+}$ is shorter than that of $^{41}K^{10+}$, which is unexpected considering that the ionization potential increases with charge state. We note that K^{11+} has three metastable excited states with lifetimes on the order of a few milliseconds, while K^{10+} only has one (see Table X). The greater number of metastable states could decrease the ionization time of K^{11+} compared to K^{10+} if the ionization occurs in a two-step process such that an electron first ionizes K^{11+} to a metastable


(a)

(b)

(c)

FIG. 9. The outermost contours of the solution sets for $^{41}K^{8+}$, $^{41}K^{9+}$, $^{41}K^{10+}$, and $^{41}K^{11+}$. Set A in (a), set B in (b), and set C in (c). The image has been modified by an applied Gaussian filter for improved clarity.

TABLE VIII. The electron densities n_e and averages energies of the EED $\langle E_e \rangle$ of the helium discharge obtained from $^{39}K^{10+}$ and $^{41}K^{10+}$ within their mutual overlap and individually. The median along with the upper and lower bounds enclosing 34.1% of solutions above and below the median is tabulated.

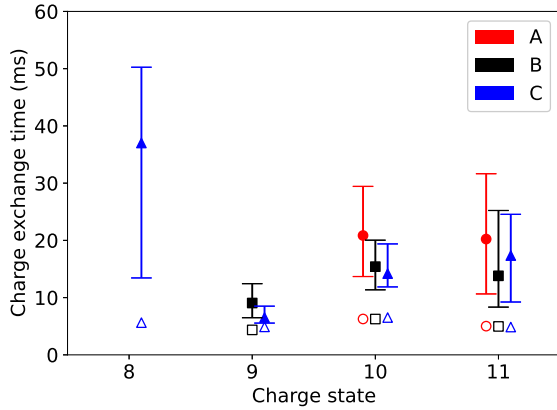|	n_e (10^{11}cm^{-3})	$\langle E_e \rangle$ (eV)
$^{39}K^{10+}$	$3.4^{+8.8}_{-1.7}$	1410^{+2240}_{-880}
$^{41}K^{10+}$	$4.1^{+7.5}_{-2.0}$	1240^{+1690}_{-690}
Overlap	$3.7^{+7.6}_{-1.8}$	1310^{+1760}_{-740}

state, and a subsequent electron impact leads to ionization before the metastable state de-excites. This is, however, speculative, as possible processes leading to premature quenching of the metastable states are unknown.
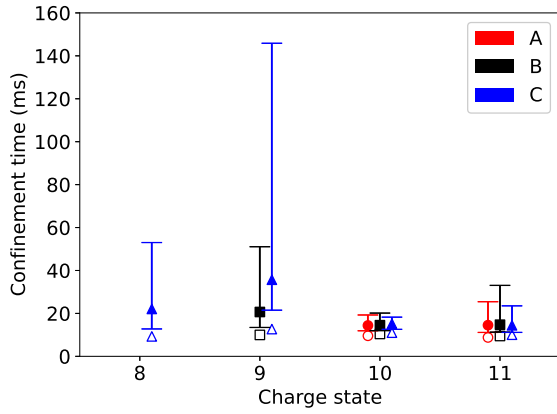
(a)
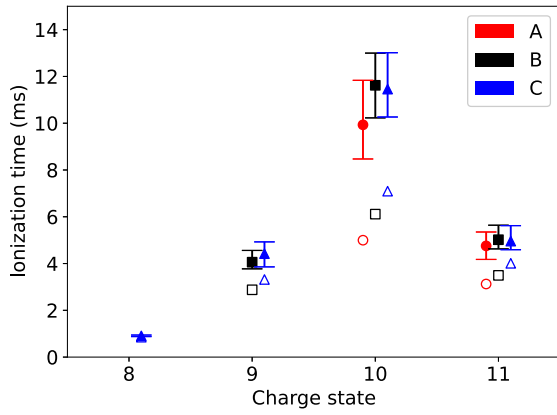
(b)

(c)

FIG. 10. The characteristic times of confinement (a), ionization (b), and charge exchange (c) obtained from the overlap sets of $^{41}K^{10+}$–$^{41}K^{11+}$ (set A), $^{41}K^{9+}$–$^{41}K^{11+}$ (set B), and $^{41}K^{8+}$–$^{41}K^{11+}$ (set C). The median values of the distributions are plotted in solid markers, and the error bars enclose 34.1% of all solutions above and below the median. The minimum values are plotted by empty markers. The x-axis values have been slightly displaced for clarity.
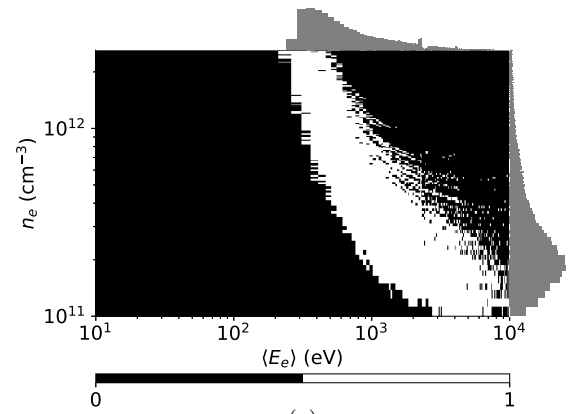
(a)
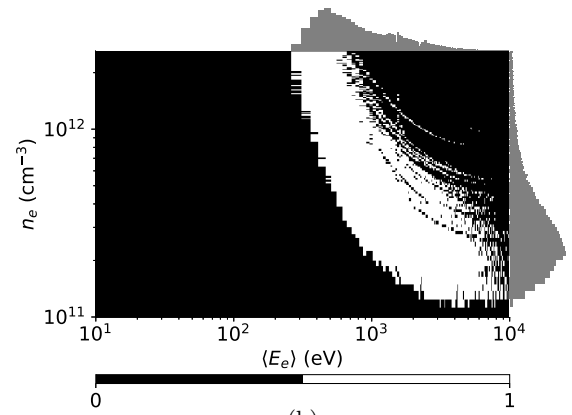
(b)
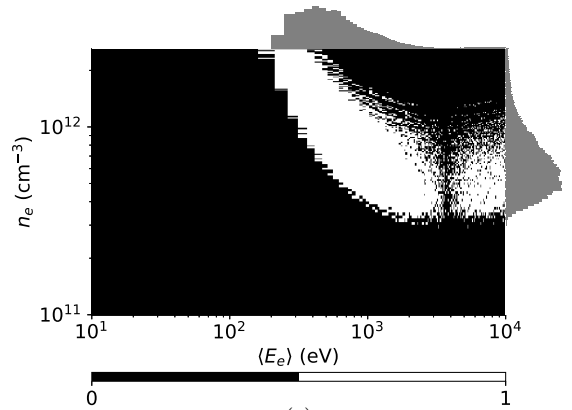
(c)

FIG. 11. Binary heat map of the solution sets of K^{9+} (a), K^{10+} (b), and Na^{7+} (c). Margin histograms show the distribution of n_e and $\langle E_e \rangle$ values within the solution set.

APPENDIX F: SOLUTION SETS

Figure 11 shows two-dimensional histograms of the solution sets of $K^{9+/10+}$ and Na^{7+} obtained from the CT analysis code. The histogram plots have been generated with
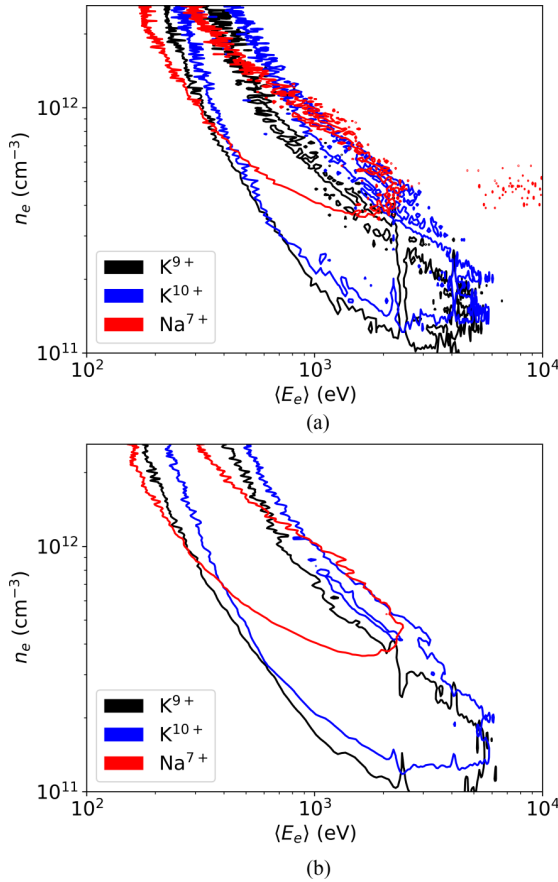
FIG. 12. Example of the effect of Gaussian filtering on the overlap contours. (a) has no applied Gaussian filter, while in (b) a Gaussian filtering with a standard deviation $\sigma = 1$.

TABLE IX. The electron densities n_e and averages energies of the EED $\langle E_e \rangle$ obtained with different charge state overlaps of ^{41}K within their mutual overlap. The median along with the upper and lower bounds enclosing 34.1% of solutions above and below the median is tabulated.

Set	n_e (10^{11}cm^{-3})	$\langle E_e \rangle$ (eV)
A	$7.4^{+1.2}_{-3.5}$	1100^{+1300}_{-500}
B	$4.9^{+1.7}_{-1.2}$	1400^{+800}_{-400}
C	$3.6^{+0.9}_{-0.5}$	2400^{+700}_{-700}

TABLE X. Spontaneous metastable transitions of K^{10+} and K^{11+} [40,41].

Ion	Upper state	Lower state	Lifetime (ms)
K^{10+}	$2s^2 2p^5\ ^2\mathrm{P}^o_{1/2}$	$2s^2 2p^5\ ^2\mathrm{P}^o_{3/2}$	4.4
K^{11+}	$2s^2 2p^4\ ^1\mathrm{S}_0$	$2s^2 2p^4\ ^3\mathrm{P}_1$	0.2
	$2s^2 2p^4\ ^1\mathrm{D}_2$	$2s^2 2p^4\ ^3\mathrm{P}_2$	2.4
	$2s^2 2p^4\ ^3\mathrm{P}_1$	$2s^2 2p^4\ ^3\mathrm{P}_2$	6.7

is illustrated in Fig. 12. The filtering is done using the `gaussian_filter` function from Python's `scipy.ndimage` module, and its effect is to blur high-noise regions of the contour, which result from few non-zero regions outside of the general grouping. Without filtering, the contour is jagged, and applying the filter allows the reader to more easily see the general tendencies in the data. The effect is the same as when filtering noisy current signals in experimental measurements. We have taken great care to ensure that relevant portions of data are not obscured by the filtering—this is confirmed by eyeballing the produced images and adjusting the standard deviation σ of the Gaussian kernel accordingly. Only the contour images are affected by the filtering, and any (all) analysis of the overlap data sets is carried out using unfiltered data. The experimental data and codes required to reproduce the images in the paper are freely available and links to them are referenced within the paper. This includes all postprocessing routines such as plotting the contour images with or without the Gaussian filtering.

200×200 bins so if any solutions at all are found in a given bin, the histogram takes there the value 1. The distributions of the n_e and $\langle E_e \rangle$ values are plotted on the y and x margins, respectively.

APPENDIX G: GAUSSIAN FILTERING

Gaussian filtering is a classical method for removing noise from 2D photos and images, and its effect on our images

[1] W. Gelletly, Radioactive ion beams: A new window on atomic nuclei, Proc. Am. Philos. Soc. **145**, 519 (2001).

[2] M. Lindroos, Review of ISOL-type radioactive beam facilities, in *Proceedings of the EPAC'04* (JACoW Publishing, Geneva, Switzerland, 2004).

[3] R. Geller, T. Lamy, and P. Sortais, Charge breeding of isotope on-line-created radioactive ions using an electron cyclotron resonance ion trap, Rev. Sci. Instrum. **77**, 03B107 (2006).

[4] F. J. C. Wenander, Charge breeding of radioactive ions, edited by R. Bailey, arXiv:1404.0945.

[5] J. Angot, A. Galatã, L. Maunoury, T. Thuillier, M. Baylac, M. Migliore, P. Sole (LNL LPSC GANIL Collaboration), Contaminants reduction in ECR charge breeders, in *Proceedings of ECRIS 2020* (JACoW Publishing, MI, USA, 2020).

[6] G. Melin, F. Bourg, P. Briand, J. Debernardi, M. Delaunay, R. Geller, B. Jacquot, P. Ludwig, T. K. N'Guyen, L. Pin, M. Pontonnier, J. C. Rocco, and F. Zadworny, Some particular aspects of the physics of the ECR sources for multicharged ions, Rev. Sci. Instrum. **61**, 236 (1990).

[7] G. Shirkov, A classical model of ion confinement and losses in ECR ion sources, Plasma Sources Sci. Technol. **2**, 250 (1993).

[8] V. Mironovand J. P. Beijers, Three-dimensional simulations of ion dynamics in the plasma of an electron cyclotron resonance ion source, Phys. Rev. ST Accel. Beams **12**, 073501 (2009).

[9] V. Mironov, S. Bogomolov, A. Bondarchenko, A. Efremov, and V. Loginov, Numerical model of electron cyclotron resonance ion source, Phys. Rev. ST Accel. Beams **18**, 123401 (2015).

[10] G. Melin, A. G. Drentje, A. Girard, and D. Hitz, Ion behavior and gas mixing in electron cyclotron resonance plasmas as sources of highly charged ions, J. Appl. Phys. **86**, 4772 (1999).

[11] G. Douysset, H. Khodja, A. Girard, and J. P. Briand, Highly charged ion densities and ion confinement properties in an electron-cyclotron-resonance ion source, Phys. Rev. E **61**, 3015 (2000).

[12] M. Sakildien, O. Tarvainen, R. Kronholm, I. Izotov, V. Skalyga, T. Kalvas, P. Jones, and H. Koivisto, Experimental evidence on microwave induced electron losses from ECRIS plasma, Phys. Plasmas **25**, 062502 (2018).

[13] O. Tarvainen, T. Kalvas, H. Koivisto, J. Komppula, R. Kronholm, J. Laulainen, I. Izotov, D. Mansfeld, V. Skalyga, V. Toivanen, and G. Machicoane, Limitation of the ECRIS performance by kinetic plasma instabilities (invited), Rev. Sci. Instrum. **87**, 02A703 (2016).

[14] J. Angot, O. Tarvainen, T. Thuillier, M. Baylac, T. Lamy, P. Sole, and J. Jacob, Charge breeding time investigations of electron cyclotron resonance charge breeders, Phys. Rev. Accel. Beams **21**, 104801 (2018).

[15] J. Angot, M. Luntinen, T. Kalvas, H. Koivisto, R. Kronholm, L. Maunoury, O. Tarvainen, T. Thuillier, and V. Toivanen, Method for estimating charge breeder ECR ion source plasma parameters with short pulse 1+ injection of metal ions, Plasma Sources Sci. Technol. **30**, (2021).

[16] M. Luntinen, J. Angot, O. Tarvainen, V. Toivanen, T. Thuillier, and H. Koivisto, Measurement of ionization, charge exchange and ion confinement times in charge breeder ECR ion sources with short pulse 1+ injection of metal ions, J. Phys.: Conf. Ser. **2244**, 012009 (2022).

[17] R. C. Pardo, R. Harkewicz, and P. J. Billquist, Time evolution of charge states in an electron cyclotron resonance ion source, Rev. Sci. Instrum. **67**, 1602 (1996).

[18] M. Imanaka, T. Nakagawa, H. Arai, I. Arai, and S. M. Lee, Plasma diagnostics of liquid He-free SC-ECR ion source (SHIVA) with use of laser ablation technique, Nucl. Instrum. Methods Phys. Res., Sect. B **237**, 647 (2005).

[19] D. E. Neben *et al.*, Fast sputtering measurement studies using uranium with the NSCL ECR ion sources, in *Proceedings of ECRIS'16* (JACoW Publishing, Busan, Korea, 2016), pp. 128–132.

[20] D. E. Neben, G. Machicoane, A. N. Pham, J. W. Stetson, G. Parsey, and J. P. Verboncoeur, An analysis of fast sputtering studies for ion confinement time, in *Proceedings of LINAC'16* (JACoW Publishing, MI, USA, 2016), pp. 475–477.

[21] M. Marttinen, J. Angot, A. Annaluru, P. Jardin, T. Kalvas, H. Koivisto, S. Kosonen, R. Kronholm, L. Maunoury, O. Tarvainen, V. Toivanen, and P. Ujic, Estimating ion confinement times from beam current transients in conventional and charge breeder ECRIS, Rev. Sci. Instrum. **91**, 013304 (2020).

[22] T. Lamy *et al.*, Experimental activities with the LPSC charge breeder in the European context, in *Proceedings of ECRIS'14* (JACoW Publishing, Geneva, Switzerland, 2014), pp. 120–126.

[23] R. Geller, P. Ludwig, and G. Melin, Metal ion production in ECRIS (invited), Rev. Sci. Instrum. **63**, 2795 (1992).

[24] R. Geller, *Electron Cyclotron Resonance Ion Sources and ECR Plasmas* (Institute of Physics Publishing, Bristol and Philadelphia, 1996).

[25] S. Biri, A. Valek, T. Suta, E. Takcs, C. Szab, L. T. Hudson, B. Radics, J. Imrek, B. Juhsz, and J. Plinks, Imaging of ECR plasmas with a pinhole x-ray camera, Rev. Sci. Instrum. **75**, 1420 (2004).

[26] L. Panitzsch, T. Peleikis, M. Stalder, and R. F. Wimmer-Schweingruber, Spatially resolved charge-state and current-density distributions at the extraction of an electron cyclotron resonance ion source, Rev. Sci. Instrum. **82**, 093302 (2011).

[27] L. Panitzsch, T. Peleikis, M. Stalder, and R. F. Wimmer-Schweingruber, Experimental results: Charge-state and current-density distribution at the plasma electrode of an ECR ion source, in *Proceedings of ECRIS'12* (JACoW Publishing, Sydney, Australia, 2012), pp. 101–105.

[28] R. Vondrasek, Diagnostics for multiple frequency heating and investigation of underlying processes, Rev. Sci. Instrum. **93**, 031501 (2022).

[29] I. Izotov, O. Tarvainen, V. Skalyga, D. Mansfeld, T. Kalvas, H. Koivisto, and R. Kronholm, Measurement of the energy distribution of electrons escaping minimum-B ECR plasmas, Plasma Sources Sci. Technol. **27**, 025012 (2018).

[30] V. Pierrardand M. Lazar, Kappa distributions: Theory and applications in space plasmas, Sol. Phys. **267**, 153 (2010).

[31] K. L. Bell, H. B. Gilbody, J. G. Hughes, A. E. Kingston, and F. J. Smith, Recommened data on the electron impact ionization of light atoms and ions, J. Phys. Chem. **12**, 891 (1983).

[32] M. A. Lennon, K. L. Bell, H. B. Gilbody, J. G. Hughes, A. E. Kingston, M. J. Murray, and F. J. Smith, Recommended data on the electron impact ionization of atoms and ions: Fluorine to nickel, J. Phys. Chem. Ref. Data **17**, 1285 (1988).

[33] The experimental data are openly available at https://doi.org/10.6084/m9.figshare.20071925.

[34] CT-analyzer release ct-analyzer-v2.0. Openly available at https://github.com/misapema-jyfl/ct-analyzer.

[35] D. Mascali, S. Gammino, L. Celona, and G. Ciavola, Towards a better comprehension of plasma formation and heating in high performances electron cyclotron resonance ion sources (invited), Rev. Sci. Instrum. **83**, 02A336 (2012).

[36] O. Tarvainen, P. Suominen, and H. Koivisto, A new plasma potential measurement instrument for plasma ion sources, Rev. Sci. Instrum. **75**, 3138 (2004).

[37] R. Kronholm, T. Kalvas, H. Koivisto, J. Laulainen, M. Marttinen, M. Sakildien, and O. Tarvainen, Spectroscopic study of ion temperature in minimum-B ECRIS plasma, Plasma Sources Sci. Technol. **28**, 075006 (2019).

[38] D. Mascali, L. Neri, L. Celona, G. Castro, G. Torrisi, S. Gammino, G. Sorbello, and G. Ciavola, A double-layer based model of ion confinement in electron cyclotron resonance ion source, Rev. Sci. Instrum. **85**, (2014).

[39] Persistent identifier urn:nbn:fi:research-infras-2016072533.

[40] A. Kramida, Yu. Ralchenko, J. Reader, and NIST ASD Team, NIST Atomic Spectra Database (Ver. 5.9), https://physics.nist.gov/asd (accessed June 17, 2022), National Institute of Standards and Technology, Gaithersburg, MD, 2021.

[41] A. Kramida, Yu. Ralchenko, J. Reader, and NIST ASD Team, NIST Atomic Spectra Database (Ver. 5.9), https://physics.nist.gov/asd (accessed June 17, 2022), National Institute of Standards and Technology, Gaithersburg, MD, 2021.

PIV

THE EFFECTS OF ELECTRON ENERGY DISTRIBUTION AND IONIZATION CROSS SECTION UNCERTAINTY ON CHARGE BREEDER ION SOURCE DIAGNOSTICS WITH PULSED 1+ INJECTION

by

M Luntinen, J Angot, H Koivisto, O Tarvainen, T Thuillier, G Castro

The effects of electron energy distribution and ionization cross section uncertainty on charge breeder ion source diagnostics with pulsed 1+ injection

M Luntinen,[1, a)] J Angot,[2] H Koivisto,[1] O Tarvainen,[3] T Thuillier,[2] and V Toivanen[1]

[1)] *Accelerator Laboratory, Department of Physics, University of Jyväskylä, FI-40014 Jyväskylä, Finland*

[2)] *Univ. Grenoble Alpes, CNRS, Grenoble INP, LPSC-IN2P3, 38000 Grenoble, France*

[3)] *UK Science and Technology Facilities Council, ISIS Pulsed Spallation Neutron and Muon Facility, Rutherford Appleton Laboratory, Harwell Campus, OX11 0QX, United Kingdom.*

(Dated: 21 May 2023)

The consecutive transients (CT) method is a plasma diagnostic technique of Charge Breeder Electron Cyclotron Resonance Ion Source plasmas. It is based on short-pulse injection of singly charged ions and the measurement of the resulting transients of the extracted multi-charged ion beams. Here we study the origin of the large uncertainty bounds yielded by the method to reveal avenues to improve its accuracy. We investigate the effects of the assumed electron energy distribution (EED) and the uncertainty inherited from the ionization cross section data of K^{4+}–K^{12+} ions on the resulting plasma electron density n_e, average energy $\langle E_e \rangle$, and the characteristic times of ion confinement τ^q, electron impact ionization τ_{inz}^q, and charge exchange τ_{cx}^q provided by the CT method. The role of the EED was probed with Kappa and double-Maxwellian distributions, the latter resulting in a shift of the n_e and $\langle E_e \rangle$ distributions. The uncertainty of the ionization cross section $\sigma_{q \to q+1}^{\mathrm{inz}}$ was artificially curtailed to investigate its impact on the values and uncertainties of the plasma parameters. It is demonstrated that hypothetical perfect knowledge of $\sigma_{q \to q+1}^{\mathrm{inz}}$ significantly reduces the uncertainties of τ^q, τ_{inz}^q, and τ_{cx}^q, which motivates the need for improved cross section data.

[a)]miha.s.p.luntinen@jyu.fi

1

I. INTRODUCTION

Electron cyclotron resonance ion sources (ECRIS)[1] are used worldwide for the production of stable, high intensity beams of medium to high charge state ions for the purposes of accelerator based nuclear physics[2,3], heavy ion based radiotherapy[4,5], and various industrial applications (e.g.[6,7]). ECRIS operation is based on the magnetic confinement and microwave heating of electrons, which break up and ionize neutral gas supplied into the plasma chamber at near vacuum pressure.

ECRIS based charge breeders[8] are a vital component of ISOL facilities exploring the boundaries of the nuclear chart. They enable efficient conversion of the low intensity 1+ beam of rare and short-lived isotopes to high charge state ions required for post-acceleration. Due to the diminishing reaction cross sections involved in the nuclear physics experiments (i.e. production of the heavy isotopes), ever greater beam intensities are demanded. As the 1+ intensities yielded by the ISOL method are typically low, the charge breeder efficiency needs to be as high as possible to realize this. Fundamental nuclear physics research hence benefits from the continued improvements in ECRIS technology, which in turn requires the development of state-of-the art plasma diagnostics methods for R&D purposes and benchmarking of simulations[9–11].

One of the keys to ECRIS development for charge breeding lies in optimizing the electron density n_e and average energy $\langle E_e \rangle$ in the plasma. These parameters affect directly the rate of ionization — a higher electron density implies more collisions, and a higher impact energy enables higher charge states to be produced. The electron density and energy also modify the ion confinement properties. The energetic electrons also experience improved confinement within the minimum-B structure of the ECRIS magnetic field. This leads to a buildup of a hot electron component in the plasma core, which causes a negative potential dip $\Delta\Phi$ in the otherwise positive plasma potential profile Φ[1,12,13]. This dip presents an electrostatic barrier to the positive highly charged ions in the central plasma, improving their confinement. The electron energy distribution of ECR ion sources has been studied e.g. using escaping electron spectroscopy[14,15] while singly charged ion beam injection[16,17], microwave interferometry[18], and bremsstrahlung emissions[19] can be used for studying the electron density. On the other hand, plasma diamagnetism[20,21] diagnostic yields information on the plasma energy content $n_e \langle E_e \rangle$.

2

Decreasing charge exchange rate between ions and neutral atoms also leads to improvements in charge breeding efficiency of high charge states. Here the ion captures a valence electron from the valence orbital of the neutral atom, leading to a decrease of its charge state. Charge exchange can be counteracted by decreasing the neutral density, i.e. decreasing the input of the neutral gas and hence the pressure, or by using a gas with a high first ionization potential.

The characteristic times of ion confinement, ionization and charge exchange (τ^q, τ^q_{inz}, and τ^q_{cx}, respectively) are measures for their respective processes. These have been probed by means of beam current transient measurements[22–26], which are based on the modeling of the beam current through the balance equation of ion densities. The consecutive transients (CT) method discussed in this work is the latest improvement in this lineage of diagnostics methods. The major improvements over the previous techniques are that (i) the CT method requires fewer assumptions — in particular no assumptions need to be made regarding the functional dependence of the confinement time on the ion charge state — and (ii) while the previous methods equate the in-plasma ion density to the extracted beam current (i.e. $qn^q \propto I^q$) the CT method incorporates the confinement time dependence (i.e. $I^q \propto qn^q/\tau^q$) similar to Ref.[25].

We have shown[27–29] that the Consecutive Transients method (CT) can be used to obtain postdictions for n_e, $\langle E_e \rangle$, τ^q, τ^q_{inz}, and τ^q_{cx} with a parsimony of assumptions. The working principle of the CT method is recounted in Section II. The downside of the technique is the considerable uncertainty associated with the results – e.g. for the confinement time of potassium $\tau^{8+}_{\text{K}} = 14.4^{+23.1}_{-5.9}$ ms or an uncertainty of 200 % (see Table IV). We investigate here the method's intrinsic uncertainty originating from parameters which need to be either assumed or taken from the literature, as opposed to uncertainty involved with the experimental setup such as the perturbation caused on the support plasma or the source tuning error due to e.g. hysteresis of the yoke magnetic material. The study of the effect of the intrinsic error sources is critical, as they are beyond the control of the experimenter and play a deciding role in the estimation of the robustness of the method.

Two sources of uncertainty are computationally relevant: (1) The method requires the user to presume a certain EED, which is used to evaluate the ionization rate coefficients, thus affecting the resulting n_e and $\langle E_e \rangle$ values. In Section III A we probe the sensitivity of the method to the EED with a particular focus on the high-energy tail of the presumed

distribution; (2) The electron impact rate coefficients are computed using literature values of the cross sections, some of which are subject to considerable experimental uncertainty (for example, the cross section of the ground state electron-impact ionization of K^{8+} to K^{9+}, $\sigma_{8+\to9+}^{\text{inz, K}}$, carries a reported relative uncertainty of 200%[30]). In absence of more precise literature values we investigate here the effect of arbitrarily curtailing the uncertainty limits to simulate more precise knowledge of the cross sections (Section III B). In short, the purpose of this work is to establish what is the effect of varying the presumed EED on the method results, and whether or not more precise cross section data could lead to an improvement in the result precision.

II.   THE CT METHOD

The experimental methodology of the CT method is illustrated schematically in Fig. 1. Short ($\lesssim 10$ ms) pulses of 1+ ions of a probe element (metallic, to minimize wall recycling effects) are injected into a support gas plasma sustained within the ECRIS. The injected ions are captured by the plasma where they experience ionization by electron-impact and charge exchange with neutral atoms, until escaping confinement. A portion of the escaped ions form the N+ beam, i.e. the extracted beam comprised of the various charge states' ions. The N+ beam is m/q analyzed using a dipole magnet, and the beam transient time series of consecutive charge states (minimum of 5) are measured with a Faraday cup.
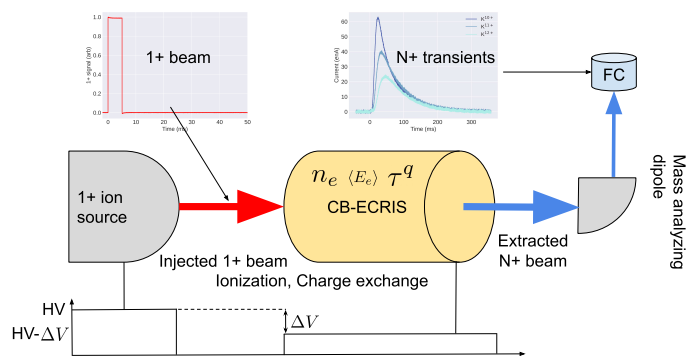
FIG. 1: The experimental principle of the consecutive transients method.

A. Analysis procedures

The time evolution of the plasma charge state distribution of the injected material is described by the balance equation[12]

$$
\begin{aligned}
\frac{\mathrm{d}n^q}{\mathrm{d}t} = {} &+n_e \left\langle \sigma v \right\rangle^{\mathrm{inz}}_{q-1 \to q} n^{q-1} - n_e \left\langle \sigma v \right\rangle^{\mathrm{inz}}_{q \to q+1} n^q \\
&+n_0 \left\langle \sigma v \right\rangle^{\mathrm{cx}}_{q+1 \to q} n^{q+1} - n_0 \left\langle \sigma v \right\rangle^{\mathrm{cx}}_{q \to q-1} n^q - n^q/\tau^q,
\end{aligned}
\tag{1}
$$

where $\left\langle \sigma v \right\rangle^{\mathrm{inz/cx}}$ are the rate coefficients of ionization/charge exchange. Here it is assumed that electron impact ionization dominates over photoionization and double (and other higher order) ionization reactions have been omitted. Charge exchange takes place with neutral atoms of the support plasma (density n_0). Ion-ion charge exchange is neglected as it becomes increasingly unlikely with q due to the increasing ionization potentials[31-33] and the Coulomb repulsion between like-charged ions. Furthermore, the balance equation assumes that owing to their high collisionality, the ions are in Maxwellian thermal equilibrium. The term $-n^q/\tau^q$ defines the n^q population confinement time τ^q through diffusive processes, i.e. ion losses caused by instabilities are ignored. The ionization and charge exchange times are defined through the corresponding rates:

$$
\tau^q_{\mathrm{inz}} = \left(n_e \left\langle \sigma v \right\rangle^{\mathrm{inz}}_{q \to q+1} \right)^{-1}, \quad \text{and} \tag{2}
$$

$$
\tau^q_{\mathrm{cx}} = \left(n_0 \left\langle \sigma v \right\rangle^{\mathrm{cx}}_{q \to q-1} \right)^{-1}. \tag{3}
$$

We combine the balance equation with a model for the extracted beam current[27,34,35]

$$
I^q = \kappa F_B L S \frac{n^q q e}{\tau^q}, \tag{4}
$$

where κ, L, and S are the beamline transmission efficiency, length of the plasma, and area of the extraction aperture, respectively. For generality, we have introduced the mirror ratio dependent factor F_B which determines the fraction of the ions escaping confinement that are lost towards the extraction. The κ, F_B, L, S, and elementary charge e cancel out upon substitution into Eq. 1, giving us the time evolution of the extracted and detected beam as

$$
\dot{I}^q = a_q I^{q-1} - b_q I^q + c_q I^{q+1}, \tag{5}
$$

5

where

$$a_q = n_e \left\langle \sigma v \right\rangle^{\mathrm{inz}}_{q-1 \to q} \frac{q}{q-1} \frac{\tau^{q-1}}{\tau^q}, \tag{6}$$

$$b_q = \left(n_e \left\langle \sigma v \right\rangle^{\mathrm{inz}}_{q \to q+1} + n_0 \left\langle \sigma v \right\rangle^{\mathrm{cx}}_{q \to q-1} + 1/\tau^q \right), \tag{7}$$

$$c_q = n_0 \left\langle \sigma v \right\rangle^{\mathrm{cx}}_{q+1 \to q} \frac{q}{q+1} \frac{\tau^{q+1}}{\tau^q}. \tag{8}$$

Fitting Eq. 5 to the measured time series data, the coefficients a_q, b_q and c_q are obtained as the fitting parameters. It is emphasized that these coefficients are not affected by the uncertainties of the ionisation or charge exchange cross sections, but merely carry the uncertainty associated to the fitting procedure, which contributes to the uncertainty of the results only when the signal-to-noise ratio of the data is poor. By algebraic manipulation it is possible to construct an equation depending only on the coefficients a_q, b_q, c_q, and n_e and $\langle E_e \rangle$:

$$\frac{q}{q+1} \frac{a_{q+1}}{n_e \left\langle \sigma v \right\rangle^{\mathrm{inz}}_{q \to q+1}} = \frac{b_{q+1} - n_e \left\langle \sigma v \right\rangle^{\mathrm{inz}}_{q+1 \to q+2} - \frac{a_{q+1} c_q}{n_e \left\langle \sigma v \right\rangle^{\mathrm{inz}}_{q \to q+1}}}{b_q - n_e \left\langle \sigma v \right\rangle^{\mathrm{inz}}_{q \to q+1} - \frac{a_q c_{q-1}}{n_e \left\langle \sigma v \right\rangle^{\mathrm{inz}}_{q-1 \to q}}} \tag{9}$$

Solving Eq. 9 requires the parameters a_q, a_{q+1}, b_q, b_{q+1}, c_{q-1} and c_q, which dictates that the transients of five consecutive charge states must be measured.

Equation 9 has an infinitude of solutions, and the acceptable solution set is obtained by defining a penalty function

$$F^q(n_e, \langle E_e \rangle) =$$

$$\left| \frac{q}{q+1} \frac{a_{q+1}}{n_e \left\langle \sigma v \right\rangle^{\mathrm{inz}}_{q \to q+1}} - \frac{b_{q+1} - n_e \left\langle \sigma v \right\rangle^{\mathrm{inz}}_{q+1 \to q+2} - \frac{a_{q+1} c_q}{n_e \left\langle \sigma v \right\rangle^{\mathrm{inz}}_{q \to q+1}}}{b_q - n_e \left\langle \sigma v \right\rangle^{\mathrm{inz}}_{q \to q+1} - \frac{a_q c_{q-1}}{n_e \left\langle \sigma v \right\rangle^{\mathrm{inz}}_{q-1 \to q}}} \right|$$

$$\left/ \frac{q}{q+1} \frac{a_{q+1}}{n_e \left\langle \sigma v \right\rangle^{\mathrm{inz}}_{q \to q+1}} \right. \tag{10}$$

and minimizing it as a function of $\langle E_e \rangle$ in a dense array of n_e points. Here the dependence on $\langle E_e \rangle$ comes from the ionization rate coefficients, defined as

$$\left\langle \sigma v \right\rangle^{\mathrm{inz}}_{q \to q+1} = \int_0^\infty g(v; \langle E_e \rangle) \sigma^{\mathrm{inz}}_{q \to q+1}(v) v \mathrm{d}v \tag{11}$$

where $g(v; \langle E_e \rangle)$ is the EED as a function of speed, and parameterized by the average energy of the distribution. Strictly speaking v is the relative speed of the electrons and ions, but owing to the much smaller mass and greater energy of the electrons, the ions can be considered stationary. The $\sigma^{\mathrm{inz}}_{q \to q+1}$ of potassium in our work are taken from the literature

6

values for the ground state electron-impact ionization reported in Refs.[30,36]. The upper limit of F is selected to be low enough that each solution set contains on the order of 10^3 solutions for sufficient statistics. In this work we set $F \leq 10^{-6}$. The effect of restricting the upper limit of F is elaborated in Appendix A.

The solution sets depend on the EED presumed in the calculation of the rate coefficients $\langle \sigma v \rangle^{\mathrm{inz}}$. Since the rate coefficients directly inherit the experimental uncertainty carried by $\sigma^{\mathrm{inz}}_{q \rightarrow q+1}$, as can be seen from Eq. 11, this is reflected in the uncertainty of the method results.

The characteristic times can then be computed within the solution set according to[37]

$$\tau^q = \left(b_q - n_e \langle \sigma v \rangle^{\mathrm{inz}}_{q \rightarrow q+1} - \frac{a_q c_{q-1}}{n_e \langle \sigma v \rangle^{\mathrm{inz}}_{q-1 \rightarrow q}} \right)^{-1}, \tag{12}$$

$$\tau^q_{\mathrm{cx}} = \left(b_q - n_e \langle \sigma v \rangle^{\mathrm{inz}}_{q \rightarrow q+1} - 1/\tau^q \right)^{-1}, \quad \text{and} \tag{13}$$

$$\tau^q_{\mathrm{inz}} = 1/n_e \langle \sigma v \rangle^{\mathrm{inz}}_{q \rightarrow q+1} \tag{14}$$

We eliminate unphysical results by demanding that the characteristic times are positive. As we obtain a set of solutions for $\langle E_e \rangle$ and n_e, we obtain also a distribution for τ^q, τ^q_{cx}, and τ^q_{inz}. To plot the results, we take the median value between the upper and lower uncertainty limits so that they enclose 34.1% of all solutions, respectively (reflecting a one sigma confidence interval for a Gaussian distribution).

In this work the determination of the coefficients a_q, b_q, and c_q was conducted by solving Eq. 5 with a 4$^{\mathrm{th}}$ order Runge-Kutta method using a time step of 10^{-4} s, and minimizing the least squares difference between the measured time series for I^q and the numerical solution. The $\langle E_e \rangle$, n_e optimization (i.e. the minimization of the penalty function) was performed in a 1000 element array of logarithmically spaced n_e values, and 1000 Monte Carlo (MC) iterations for the uncertainty were performed. A small random displacement was added to the elements in the n_e array between each MC iteration to better cover the search space.

B. Experimental data

The data analysed in this work are from the experimental campaign conducted for Ref.[27] on the 14.5 GHz CB-ECRIS at the LPSC. The relevant source operating parameters are summarized in Table I. The corresponding characteristic times and charge breeding efficiencies of potassium in helium plasma are tabulated in Table II. Singly charged potassium ions

7

TABLE I: Main CB-ECRIS operating parameters.

Support gas species	He
P_{inj} (background)	2.5×10^{-8} mbar
P_{inj} (operation)	8.7×10^{-8} mbar
Extraction voltage	20 kV
Injected 1+ intensity	710 nA
B_{inj}	1.58 T
B_{min}	0.45 T
B_{ext}	0.83 T
Microwave power	500 W (14.5 GHz)
ΔV	-3.9 V

TABLE II: The charge breeding efficiencies η^q and the characteristic times obtained in Ref.[27]. The relative uncertainties are computed from the absolute upper and lower uncertainty limits ($\hat{\delta}$ and $\check{\delta}$, resp.) according to $\delta = (\hat{\delta} + \check{\delta})/\tau$ for each τ.

Charge state	τ^q (ms)	δ (%)	τ^q_{inz} (ms)	δ (%)	τ^q_{cx} (ms)	δ (%)	η^q (%)
1	—	—	—	—	—	—	9.7
2	—	—	—	—	—	—	2.7
3	—	—	—	—	—	—	1.2
4	—	—	—	—	—	—	1.0
5	$2.6^{+0.8}_{-0.4}$	46	$2.6^{+0.5}_{-0.5}$	38	360^{+410}_{-250}	183	1.1
6	$2.6^{+1.7}_{-0.4}$	81	$2.5^{+0.7}_{-0.7}$	56	26^{+26}_{-17}	165	1.2
7	4^{+4}_{-2}	150	$2.6^{+0.9}_{-0.8}$	65	7^{+7}_{-4}	157	1.5
8	7^{+10}_{-4}	200	$3.1^{+1.4}_{-0.8}$	71	4^{+5}_{-2}	175	2.7
9	10^{+13}_{-4}	170	10^{+4}_{-3}	70	9^{+7}_{-3}	111	8.9
10	16^{+19}_{-7}	163	13^{+3}_{-4}	54	13^{+15}_{-5}	154	10.6
11	—	—	—	—	—	—	8.5
12	—	—	—	—	—	—	5.1
							$\Sigma_q \eta^q = 54.2$ %

8

were injected in 10 ms pulses into a helium support plasma sustained within the ECRIS. The N+ beam was mass analyzed using a dipole magnet, and the transient time series were collected at the N+ Faraday cup. The experimental setup and methods are discussed in detail in Ref.[27].

The key results of Ref.[27] can be summarized as follows: We showed that the method can be used to obtain postdictions for the electron density and average energy, i.e. the energy content of the plasma, as well as the characteristic times; The closed electron shell of K^{9+} is visible in the ionization times; The charge exchange time exhibits a minimum at K^{8+} from which it was inferred that although the cross section of charge exchange increases with charge state, the decreasing neutral density towards the plasma core mitigates its effects for high charge states; The confinement time was found to satisfy a power law within the uncertainty bounds, with the long confinement times of the high charge states implying that at the charge breeder ECRIS plasma conditions the highly charged ions are indeed electrostatically confined with the low charge states being magnetized; The energy content $n_e \langle E_e \rangle$ was found to be constant as a function of charge state (within the uncertainty limits) and the plasma triple product $n_e \langle E_e \rangle \tau^q$ was seen to increase with q — in agreement of the Golovanivsky diagram for ECRIS performance[1,38].

Importantly, we identified the EED as a possible source of error for the method. Although this is not directly reflected in the uncertainty bounds, it is used in the evaluation of the ionization rate coefficients and thus inherently affects the resultant n_e, $\langle E_e \rangle$ values. In the analysis in Ref.[27] the EED was presumed to be a simple Maxwell-Boltzmann distribution. Other error sources — including the support plasma perturbation — are discussed in Ref.[27] and in Appendix C.

We also found that the method yields considerable uncertainty bounds for the characteristic times. For high charge states the relative uncertainty (68.2% confidence interval) of τ^q and τ_{cx}^q was > 100 %. It was speculated that this uncertainty originates largely from the uncertainty of the ionization cross sections. In Ref.[27] the rate coefficients were obtained using the semi-empirical Voronov formula[39] and an umbrella uncertainty of 60% was applied to all charge states based on Ref.[39]. This is incorrect as the uncertainty varies charge state to charge state. Thereafter[28,29] we have adopted the cross sections and the corresponding uncertainties from the semi-empirical formula and data reported in Refs.[30,36]. We compute the rate coefficients using a chosen EED, and apply each charge state the appropriate un-

certainty as given in the literature. Understanding how the selection of the EED and the uncertainties of the ionization cross sections affect the results of the CT method (topic of this paper) can be considered a prerequisite for using the method in parametric studies of charge breeder ECRIS plasma parameters in upcoming measurement campaigns.

III.   ANALYSIS METHODS AND RESULTS

A.   Changing the EED

To study the effects of presuming different EEDs in computing the rate coefficients, we employed three different distributions: The default Maxwell-Boltzmann distribution, the kappa distribution[40] and a double Maxwell-Boltzmann distribution. Often, theoretical approaches in ECRIS physics employ the Maxwell-Boltzmann distribution. It presumes thermodynamic equilibrium in the ensemble of particles, which is not necessarily a rigorous assumption in the case of the non-equilibrium plasma of the ECRIS. The true EED remains unknown but experimental measurements of the lost electron energy distribution (LEED) imply that the EED is non-Maxwellian[14]. In particular, there appears to exist a population of hot ~ 100 keV electrons which appear as a pronounced "hump" in the LEED[15].

It is therefore interesting to investigate the effect of varying the high energy tail of the EED. The kappa distribution provides a mathematically convenient way to do this by varying the value of the spectral parameter κ, which has the effect of increasing the relative weight of the high energy tail as κ decreases. For $\kappa \to \infty$ the kappa distribution approaches a Maxwell-Boltzmann distribution. The aforementioned LEED experiments, however, suggest that a double MB distribution might better describe the EED. We thus construct a double Maxwell-Boltzmann distribution with hot and warm electron populations, so that the hot population has a fixed $\langle E_e \rangle_h$ and the $\langle E_e \rangle_c$ is allowed to vary. This is justified as the ionization cross section is greater in the energy range corresponding to the warm electron population, and hence the rate coefficient is more sensitive to variations of $\langle E_e \rangle_c$. The double MB distribution allows us to assign arbitrary fractions of the total electron population to either the warm or the hot population. We assume the EEDs to be isotropic although it could be argued that this does not hold for the hot electron population of the double MB distribution.

10

The Maxwell-Boltzmann distribution as a function of speed v is

$$g(v) = \left(\frac{m}{2\pi kT}\right)^{3/2} 4\pi v^2 e^{-\frac{mv^2}{2kT}} \tag{15}$$

where k is the Boltzmann constant, T is the temperature, and m is the particle mass.

The kappa distribution was taken from Ref.[40], and converted to speed formalism by integrating over the solid angle in velocity space ($v^2 \mathrm{d}v \mathrm{d}\Omega$) which amounts to multiplication by $4\pi v^2$ thanks to the symmetry of the distribution. We have then

$$g_\kappa(v) = \frac{2v^2}{(\kappa w_\kappa^2)^{3/2}} \frac{\Gamma(\kappa+1)}{\Gamma(\kappa-1/2)\Gamma(3/2)} \left(1 + \frac{v^2}{\kappa w_\kappa^2}\right)^{-(\kappa+1)} \tag{16}$$

where the thermal velocity $w_\kappa = \sqrt{(2\kappa-3)kT_{eq}/\kappa m}$, T_{eq} is the so-called equivalent temperature, Γ is the Gamma function, and the spectral index $\kappa > 3/2$.

The double Maxwell-Boltzmann distribution was defined so that

$$g(v; \langle E_{e,c}\rangle) = n_e \left[f_c g_c(v; \langle E_{e,c}\rangle) + f_h g_h(v; \langle E_{e,h}\rangle)\right] \tag{17}$$

where $g_h(v; \langle E_{e,h}\rangle)$ represents the hot electron population with a fixed average energy set to $\langle E_{e,h}\rangle = 100$ keV. The average energy of the warm population — the main provider of ionizing collisions — described by $g_c(v; \langle E_{e,c}\rangle)$ was allowed to vary. The coefficients $0\% \leq f_c \leq 100\%$, and $f_h = 100\% - f_c$ define the fraction of electrons assigned to the warm and hot population, respectively.

According to Ref.[41] switching off the microwave heating power leads to an abrupt 50% decrease in the electron flux escaping through the magnetic mirror. It was inferred that this occurs due to the elimination of rf-induced pitch angle scattering of electrons. The actual fractions of electrons in any given population are unknown, but since the rf-induced pitch angle scattering primarily affects the warm and hot electrons (with energies on the order of 10 keV–100 keV[41]), we infer that in the "worst-case-scenario" $f_h = 50\%$. In the following analysis, the hot population energy was set to $\langle E_e\rangle_h = 100$ keV. Another analysis was conducted with $\langle E_e\rangle_h = 200$ keV, but there were no significant deviations in the results.

To facilitate comparisons between the different EEDs, we use average energy of the distribution instead of the temperature or equivalent temperature. For the Maxwell-Boltzmann distribution this amounts to the substitution $kT \to \frac{2}{3}\langle E_e\rangle$, but for the kappa distribution we need to solve for a given $\langle E_e\rangle$

$$\langle E_e\rangle = \int_0^\infty (\frac{1}{2}mv^2)g_\kappa(v;T)\mathrm{d}v \tag{18}$$

11
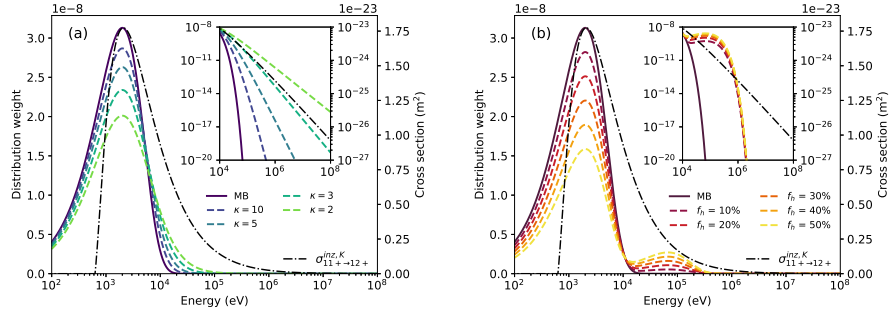
FIG. 2: Different EEDs plotted with a fixed most probable energy of 2 keV. The Maxwell-Boltzmann (MB) distribution and the kappa distribution for different values of κ are plotted in subplot (a); The MB distribution and double-MB distribution with different assignments of electrons to the warm and hot populations are plotted in (b). In (a) $\kappa = 2, 3, 5, 10$ and in (b) the most probable energy of the warm population is fixed to 2 keV while the fraction of electrons in the hot, 100 keV population gets values of $f_h = 10\%, 20\%, 30\%, 40\%, 50\%$. The ground state electron-impact ionization cross section $\sigma^{\mathrm{inz,\ K}}_{11+\rightarrow12+}$ is depicted by the black dashed line and is overlaid with the distributions. The insets highlight the high-energy behavior.

as a function of T, to obtain the equivalent temperature which yields the desired $\langle E_e \rangle$. The rate coefficients are then computed according to Eq. 11 substituting the distributions from Eqs. 15, 16, and 17. Note that we use classical equations throughout the analysis.

Figure 2 (a) plots the Maxwell-Boltzmann (MB) distribution together with the kappa distribution (for $\kappa = 2, 3, 5, 10$) as a function of the electron energy for a constant most probable energy of 2 keV. In subfigure (b) the MB distribution is compared to a double-Maxwellian distribution. In 2 (b), the warm population most probable energy is fixed to 2 keV and the $\langle E_e \rangle_h = 100$ keV. The double-Maxwellian is plotted with different fractions of electrons assigned to the hot population, $f_h = 10\%, 20\%, 30\%, 40\%, 50\%$. The high energy behavior of the distributions is highlighted by the log-log inset plots. The particle number in each distribution is normalized, i.e. an integral over each distribution yields unity.

Figure 3 shows $\langle \sigma v \rangle^{\mathrm{inz,\ K}}_{8+\rightarrow9+}$ with different EEDs as a function of $\langle E_e \rangle$. We observe that the maximum rate coefficient is reached at a higher $\langle E_e \rangle$ as κ decreases. The double MB

12

distribution on the other hand yields a flat low-$\langle E_e \rangle$ component to the rate coefficient at energies below 100 eV, thanks to the constant high energy population whose EED overlaps with a non-zero part of the ionization cross section. The small cross section at high energy is in part compensated by the large v. At high $\langle E_e \rangle$ the double MB distribution yields a smaller rate coefficient, because while the less energetic population approaches optimum energy the contribution of the hot population remains constant.

Examples of the CT-method ($\langle E_e \rangle$,n_e) solution sets obtained using different EEDs are plotted for K^{8+}, K^{9+}, and K^{10+} in Fig. 4. The contour encloses all bins for which the density of solutions is greater than 10% of the maximum. For lower values of κ, we find that the postdicted ($\langle E_e \rangle$, n_e) sets have shifted towards higher electron energy and density compared to the standard MB. In the case of the double MB EED we find that a higher proportion of hot electrons reduces the n_e domain at low $\langle E_e \rangle$ — consistent with the higher rate coefficient in that region. In the high energy range the double MB distribution yields nearly identical solutions as with the simple MB, which is to be expected as the rate coefficients deviate much less. For lower charge states ($K^{7+,6+,5+}$) the double MB distribution yields slightly higher n_e values at low $\langle E_e \rangle$ than the standard MB. N.B. that we do not expect each charge state population to yield the same n_e and $\langle E_e \rangle$ due to the spatial distribution of electrons as discussed in detail in Ref.[27].

Figure 5 shows the characteristic times as a function of the charge state obtained using different EEDs. The only major deviations are observed in the case of the confinement time of K^{8+}, K^{9+} and K^{10+}. Both the double MB and kappa distribution results indicate, that a presumed larger hot electron population postdicts a greater confinement time. The deviations remain within the uncertainty bounds, however. The similarity between the characteristic times obtained with the kappa distribution and a standard MB can be attributed to the similarity of the rate coefficients given by them (see Fig. 3). The double MB on the other hand has a significant contribution from the hot electron population even when the warm population has a moderate or low energy.

B. Curtailing the cross section uncertainty

To investigate the effect of having more precise information of $\sigma_{q \to q+1}^{\text{inz}}$, we perform an artificial curtailment of its experimental uncertainty. Because the ionization rate coefficients
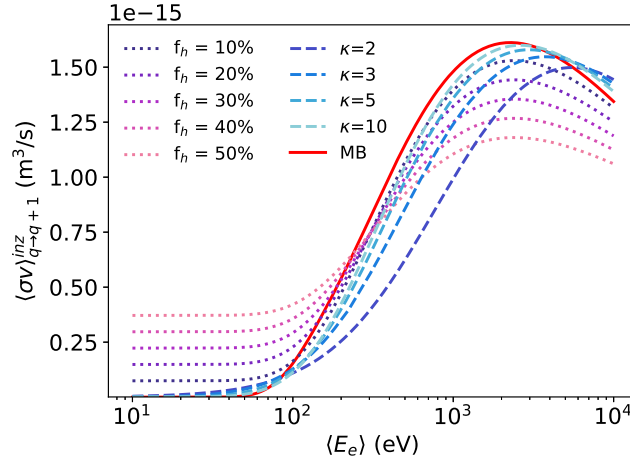
FIG. 3: The $\langle \sigma v \rangle^{\mathrm{inz}}_{8+\to 9+}$ for the reaction $e^- + \mathrm{K}^{8+} \to \mathrm{K}^{9+} + 2e^-$ as a function of $\langle E_e \rangle$ using different EEDs: Maxwell-Boltzmann (MB), kappa distribution ($\kappa = 2, 3, 5, 10$) and a double-Maxwellian distribution with the hot population fixed to $\langle E_e \rangle_h = 100$ keV and $f_h = 10\%, 20\%, 30\%, 40\%, 50\%$ of electrons assigned to the hot population.

directly inherit the uncertainty of the cross sections, the uncertainty of $\sigma^{\mathrm{inz}}_{q\to q+1}$ is taken into account by repeating the $n_e, \langle E_e \rangle$ optimization multiple times (~ 1000) and adding a random bias to the rate coefficients $\langle \sigma v \rangle^{\mathrm{inz}}_{q\to q+1}$ in each iteration. That is

$$\langle \sigma v \rangle^{\mathrm{inz}}_{q\to q+1} \to \langle \sigma v \rangle^{\mathrm{inz}}_{q\to q+1} \left(\mathcal{A} + \mathcal{B}_q \right) \tag{19}$$

where $\mathcal{A}$ is a constant offset and $\mathcal{B}_q$ is selected by a random, uniform sample from within the bounds of the experimental uncertainty of $\sigma^{\mathrm{inz}}_{q\to q+1}$. Effectively, we limit the range from which $\mathcal{B}_q$ is sampled to a fraction of the reported uncertainty. Simultaneously, we vary the constant offset $\mathcal{A}$ to account for possible systematic errors in the cross section measurement. We constrain the selection of $\mathcal{A}$ and $\mathcal{B}_q$ so that the original uncertainty limits are never exceeded. As an example, if the added offset is 50% (i.e. $\mathcal{A} = 150\%$), then $\mathcal{B}_q \sim U(-50, 50)\% \times \delta\sigma^{\mathrm{inz}}_{q\to q+1}$, where U is the uniform distribution, is the largest extent of $\mathcal{B}_q$. Figure 6 shows the effect of varying the offset and the random bias. The different sets of $\mathcal{A}$ and $\mathcal{B}_q$ analyzed are tabulated in Table III.

14
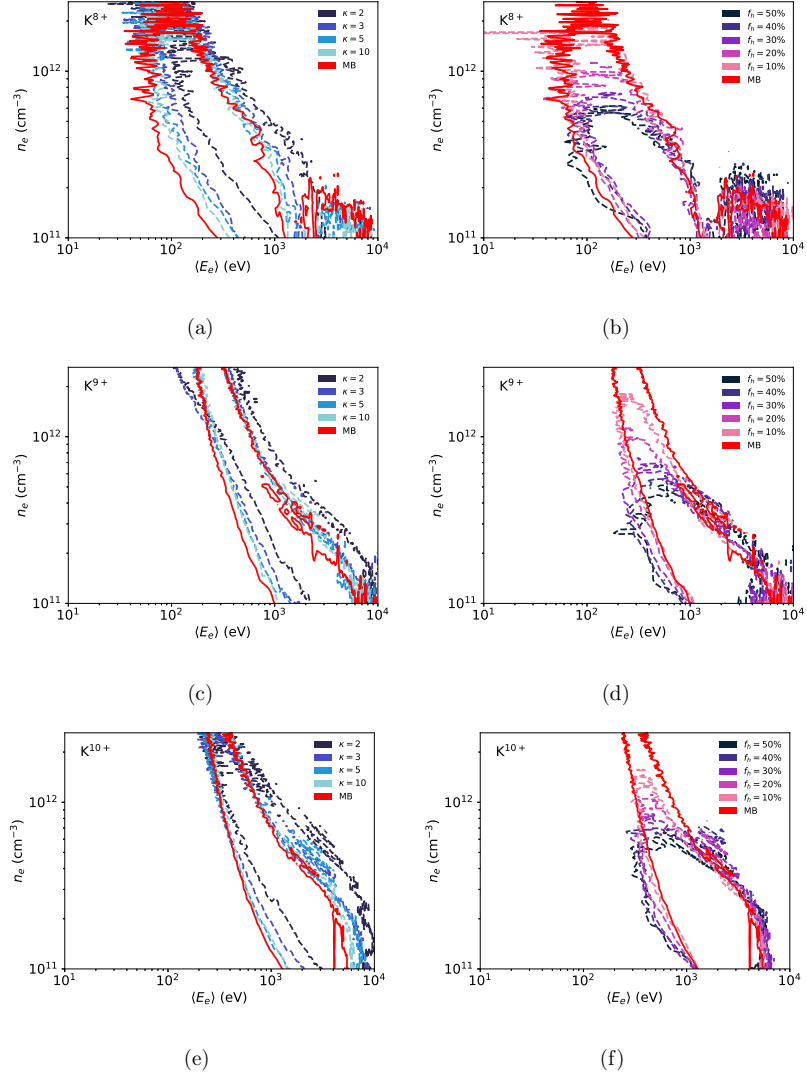
FIG. 4: Outer contours of the solution sets for K^{8+}, K^{9+}, and K^{10+} with different EEDs. (a), (c), (e) compare the results obtained with the kappa distributions, while (b), (d), (f) show the sets obtained with the different double MB distributions. The standard MB distribution is plotted for reference in each figure. A Gaussian filter was applied to smooth the contours, improving legibility.

15

(a)

(b)

(c)

(d)

(e)

(f)
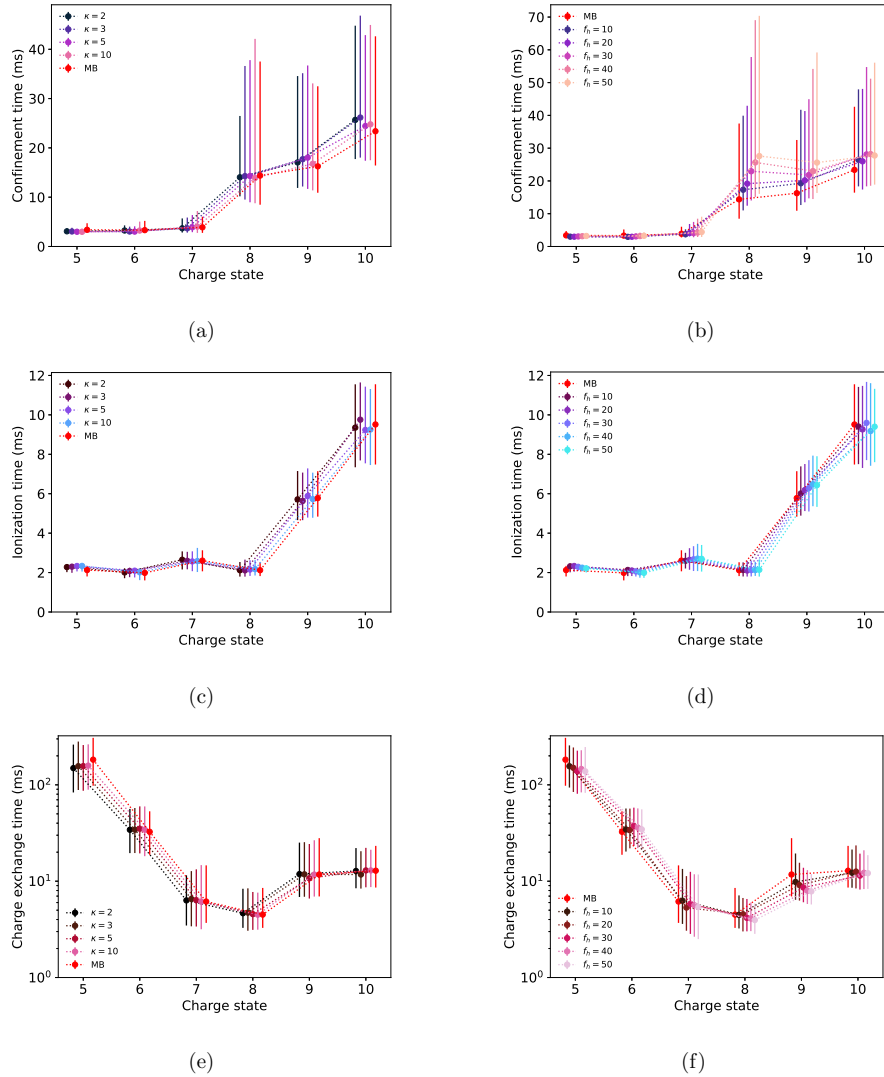
FIG. 5: The characteristic times of confinement, ionization, and charge exchange using different EEDs. (a), (c), (e) plot solutions obtained using the kappa distribution, while (b), (d), (f) plot solutions with the double MB distribution. The results for a standard MB distribution are plotted for reference in each subfigure.
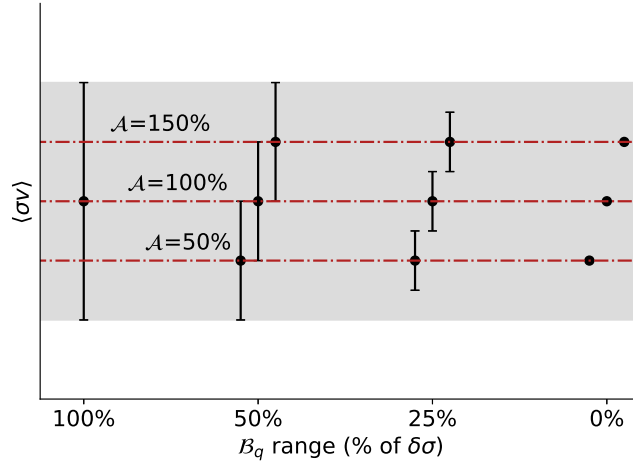
FIG. 6: Schematic illustration of artificially curtailing the rate coefficient / cross section uncertainty. The gray region shows the original experimental uncertainty. Applying the offset $\mathcal{A}$ shifts the center of $\langle \sigma v \rangle$ while curtailing the range of the random variable $\mathcal{B}_q$ narrows the uncertainty bounds. That is, $\mathcal{A}$ represents systematic error and $\mathcal{B}_q$ relative uncertainty.

Figure 7 shows the effect of curtailing the cross section (rate coefficient) uncertainty limits, with K^{8+} used as an example case. The solution sets become progressively narrower as the uncertainty limits are tightened. The effect of decreasing $\mathcal{A}$ is to shift sets towards higher n_e. This is because the resulting lower value of $\langle \sigma v \rangle^{\text{inz}}$ needs to be compensated by a higher n_e, in order to obtain the ionization rate which minimizes the penalty function (Eq. 10). Similar effects are seen for all charge states.

Figure 8 plots the characteristic times resulting from the curtailed solution sets. We can see that in general, the decreased uncertainty yields smaller uncertainty bounds. The characteristic times obtained for K^{8+}, which has the largest associated uncertainty of the cross section ($\delta\sigma_{8+\rightarrow 9+}^{\text{K,inz}} = 200$ %), from the different analyses are tabulated in Table IV. NB that the set 100-50 yields, counterintuitively, a greater uncertainty than the uncurtailed analysis. This happens when the decreased uncertainty range prohibits certain $\langle E_e \rangle$, n_e values resulting in a greater variance in the resultant characteristic time distributions. In general,

17

TABLE III: The combinations of offset $\mathcal{A}$ and percentage range for the random bias $\mathcal{B}_q$ used in the analysis. The $\mathcal{B}_q$ is selected from a random uniform distribution as a percentage of the original uncertainty of the ionization cross section $\delta\sigma$. The combination $\mathcal{A} = 100\%$, $\mathcal{B}_q \sim U(0,0)\%$ corresponds to perfect knowledge of $\sigma_{q \to q+1}^{\text{inz}}$.

Set label	$\mathcal{A}$ (%)	$\mathcal{B}_q$ (% $\times \delta\sigma$)
150-50	150	$\sim U(-50, 50)$
150-25	150	$\sim U(-25, 25)$
150-10	150	$\sim U(-10, 10)$
150-00	150	$\sim U(0, 0)$
100-50	100	$\sim U(-50, 50)$
100-25	100	$\sim U(-25, 25)$
100-10	100	$\sim U(-10, 10)$
100-00	100	$\sim U(0, 0)$
50-50	50	$\sim U(-50, 50)$
50-25	50	$\sim U(-25, 25)$
50-10	50	$\sim U(-10, 10)$
50-00	50	$\sim U(0, 0)$

however, the curtailed uncertainty decreases the relative uncertainty of the characteristic times.

We note that the uncertainty of the confinement time of K^{10+} increases across the board even though the uncertainty is decreased. Although the solution sets become narrower, they still cover a large swathe of the $\langle E_e \rangle$, n_e space, which permits the broad distribution of τ^q. That is, the remaining solutions in the solution set contain a great range of postdictions for τ^q. In appendix B a further constraint on n_e and $\langle E_e \rangle$ is shown to lead to the desired improved precision also for K^{10+}. Furthermore, we cannot rule out the low beam current of K^{10+} from contributing to the seemingly counter-intuitive increase of the uncertainty.

18

IV. DISCUSSION

A. EED effects

The effect of the double MB distribution on the confinement time results is a consequence of the constant contribution from the hot electron population to the rate coefficients. Due to the presumed hot electron population, the high charge states' rate coefficient is many orders of magnitude greater than that computed using a single MB or kappa distribution, and the penalty function minimum is obtained at a lower n_e, which cuts off the high density region from the solution sets. Consequently, only a subset of characteristic time solutions is found using the double MB distribution as compared to the standard MB distribution (see Fig. 4).

The effect of varying κ can also be seen in Fig. 4. Decreasing κ causes the distribution to deviate more from the standard MB EED, and to increase the relative weight of the high energy tail. Here, the differences at low energy are relatively lesser than in the case of a double MB EED, and larger differences are seen at high $\langle E_e \rangle$. The resultant characteristic times are not affected significantly by the variation of κ.

TABLE IV: The characteristic times of K^{8+} and the corresponding relative uncertainties for different selections of $\mathcal{A}$ and $\mathcal{B}_q$. The uncurtailed set corresponds to full uncertainty range of $\sigma_{q \to q+1}^{\mathrm{inz}}$ and the sets 100-50, 100-25, 100-10, 100-00 to those tabulated in Table III. The relative uncertainties are computed from the absolute upper and lower uncertainty limits ($\hat{\delta}$ and $\check{\delta}$, resp.) according to $\delta = (\hat{\delta} + \check{\delta})/\tau$ for each τ.

Set	τ^q (ms)	δ (%)	τ_{inz}^q (ms)	δ (%)	τ_{cx}^q (ms)	δ (%)
Uncurtailed	$14.4_{-5.9}^{+23.1}$	200	$2.1_{-0.3}^{+0.4}$	33	$4.5_{-1.2}^{+4.0}$	120
100-50	$13.3_{-5.3}^{+42.3}$	360	$2.2_{-0.3}^{+0.5}$	34	$4.6_{-1.6}^{+3.7}$	110
100-25	$10.4_{-2.9}^{+10.9}$	130	$2.1_{-0.2}^{+0.4}$	28	$5.8_{-2.1}^{+3.4}$	100
100-10	$9.1_{-1.6}^{+7.3}$	100	$2.0_{-0.2}^{+0.1}$	16	$6.5_{-1.0}^{+1.5}$	40
100-00	$8.7_{-1.4}^{+5.9}$	80	$2.0_{-0.2}^{+0.1}$	14	$6.7_{-0.1}^{+0.3}$	6

(a) Set: 50-50   (b) Set: 50-25   (c) Set: 50-00

(d) Set: 100-50   (e) Set: 100-25   (f) Set: 100-00

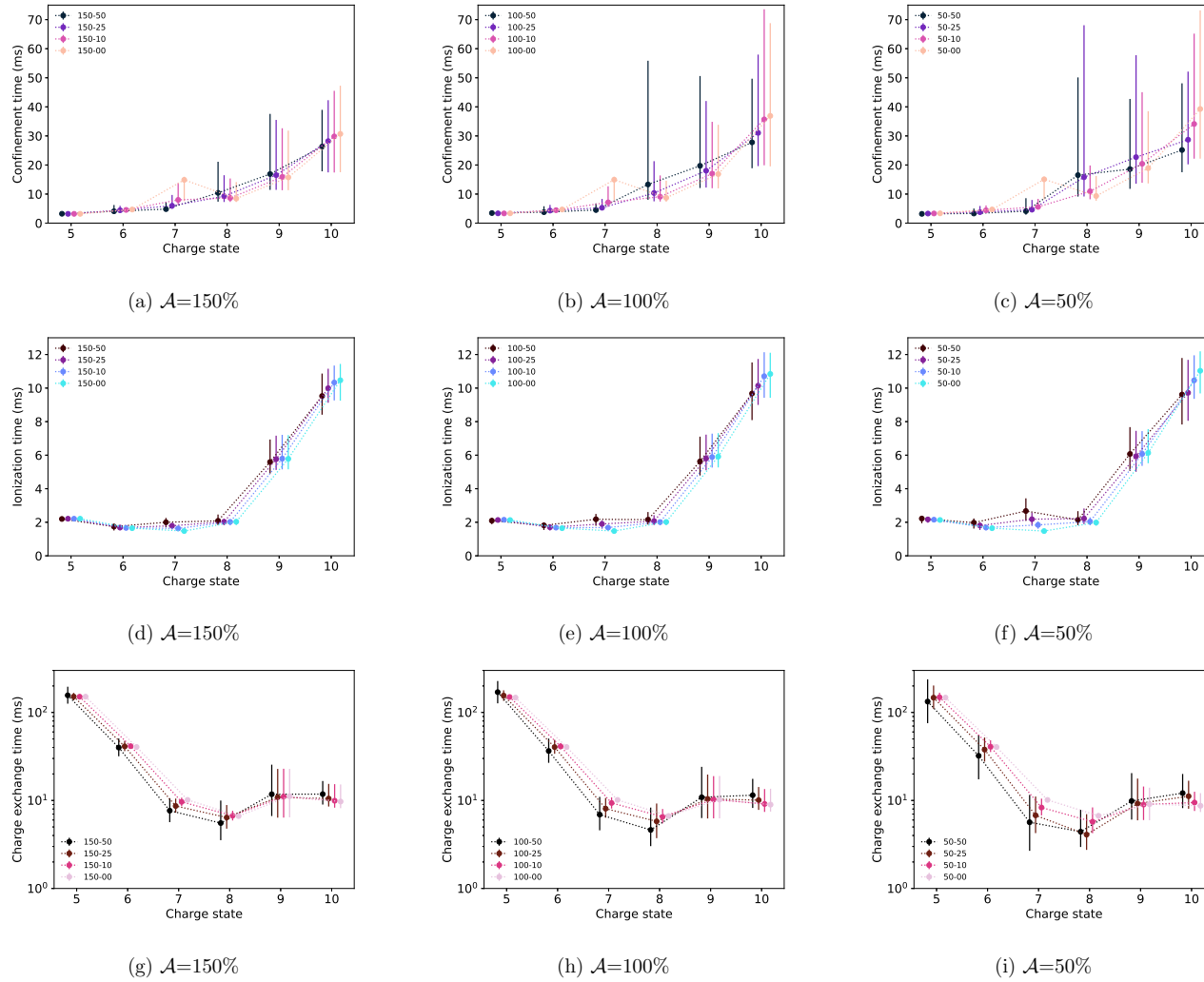(g) Set: 150-50   (h) Set: 150-25   (i) Set: 150-00

FIG. 7: Solution sets for K^{8+} using curtailed uncertainty ranges (denoted by the set number from Table III) and a simple Maxwell-Boltzmann EED.

20

(a) $\mathcal{A}=150\%$

(b) $\mathcal{A}=100\%$

(c) $\mathcal{A}=50\%$

(d) $\mathcal{A}=150\%$

(e) $\mathcal{A}=100\%$

(f) $\mathcal{A}=50\%$

(g) $\mathcal{A}=150\%$

(h) $\mathcal{A}=100\%$

(i) $\mathcal{A}=50\%$

FIG. 8: Characteristic times using curtailed uncertainty ranges. Top row shows the confinement times, middle row the ionization times and bottom row the charge exchange times. In each column the offset $\mathcal{A}$ is fixed and the data points represent varying $\mathcal{B}_q$ range.

21

B. Curtailed uncertainty

It was observed that artificially reducing the uncertainty associated with the experimental values of $\sigma_{q \to q+1}^{\text{inz}}$ yields — in general — an improvement in the precision of the CT method results. The $(\langle E_e \rangle, n_e)$ solution sets become narrower, although they still trace a long path in the $(\langle E_e \rangle, n_e)$-space, i.e. we find a broad distribution of $(\langle E_e \rangle, n_e)$ pairs which are consistent with the measured transient time series. We also obtain a concomitant improvement in the precision of the characteristic times, and the confinement and charge exchange times benefit the most, as is evident from Table IV. The uncertainty which remains after setting $\mathcal{B}_q \sim U(0,0)\%$ can be further reduced by a prior measurement of $\langle E_e \rangle$ and n_e, as indicated by the case study in Appendix B. These findings motivate a revisit of the electron impact ionization cross sections to improve their precision, and performing a measurement of $\langle E_e \rangle$ and/or n_e in conjunction with the CT method experiments.

The most straightforward method for the determination of the electron density is probably through the combined bremsstrahlung emission and beam current spectroscopy -method expounded in Ref.[19]. It requires, however, the EED to be known/presumed beforehand, as well as knowledge of the ion confinement times. In Ref.[19] the confinement times are assumed to be weakly dependent on q based on findings in Ref.[34]. The τ^q found through the CT method imply, that such an assumption underestimates the density of the high charge state ions, causing n_e to be overestimated. Such an estimate could, however, be used as an upper limit for n_e. The bremsstrahlung detector should also be chosen so that the measurement is sensitive to the electron population with energy $\lesssim 1$ keV, as the warm electron population is dominant in determining $\langle \sigma v \rangle_{q \to q+1}^{\text{inz}}$. Altogether, we identify simultaneous measurement of the bremsstrahlung emission (spectral temperature) and application of the CT method as the most straightforward method for reducing the uncertainty bounds of the obtained plasma parameters.

In Ref.[29] we showed that multi-species 1+ injection can also be used to reduce the uncertainty of the results. We used a composite Na/K pellet at the 1+ ion source which produced Na^+ and K^+ ions via thermal emission, enabling us to switch between the two ion species without switching off the ECRIS, and hence to probe the same support plasma conditions with both 1+ ions. The high charge states of the two ions can be argued to originate from the same plasma volume, and an overlap of the respective solution sets is justified. Tak-

ing the overlap reduces the $\langle E_e \rangle, n_e$ space, leading to a reduction in the characteristic time uncertainties as well. For example, the uncertainties of τ^{9+}, τ_{inz}^{9+}, and τ_{cx}^{9+} for potassium were reduced by 40, 11, and 62 percentage points, respectively. This implies that better knowledge of the ionisation cross section uncertainties could be expected to yield a more significant improvement. Despite the usefulness of the overlap method it carries the weight of the additional assumption regarding the volume of origin of the ion populations, and only the high charge states benefit from it.

C. Conclusion

The effect of the EED on the CT method results can be summarized to arise from the modification of the $\langle \sigma v \rangle_{q \to q+1}^{\mathrm{inz}}$ it causes. The deviations in τ^q, τ_{inz}^q, and τ_{cx}^q due to the variation of the EED are well within the uncertainty bounds, but we expect that an increase in the precision of $\sigma_{q \to q+1}^{\mathrm{inz}}$ would show that the characterization of the EED is important in particular for determining τ^q of highly charged ions.

To determine the uncertainty originating from the EED in any real experimental setting, the experimenter should characterize the uncertainty related to their knowledge of the EED, and test the effect on the results by varying the shape of the EED within the limits of that uncertainty (e.g. the fraction of electrons in the hot/warm population of a double MB distribution, or the precise value of κ of a kappa distribution). The LEED measurement offers a route for the above, but the confined plasma EED may be different from the escaping one, as discussed in Ref.[15].

To our knowledge, the CT method is unique among ECRIS related plasma diagnostics, in that it accounts for the uncertainty of the electron-impact ionization cross section. The results in this work indicate that $\delta\sigma_{q \to q+1}^{\mathrm{inz}}$ has a significant effect on the CT method results' precision, and there is no reason to believe that other research where the ionization cross sections are employed would not be likewise affected. Its effects should thus be considered for example in simulations of the temporal evolution of the CSD in an ECRIS plasma (e.g. Refs.[10,12]) and k-α measurements (e.g. Ref.[42]). Such research would hence benefit greatly from a revisit of the cross sections — either through theoretical approaches or experimental measurement. We emphasize that the conclusion about the necessity of improved cross section data of high charge state electron impact ionization is not specific to potassium but

23

would likewise reduce the uncertainty bounds for all 1+ probe beams (elements).

CONFLICT OF INTEREST

The authors have no conflicts to disclose.

DATA AVAILABILITY STATEMENT

The data[43] that support the findings of this study are openly available at the following URL/DOI: https://doi.org/10.6084/m9.figshare.13602827.v1; The analysis codes employed in this work are openly available in the repository at: https://github.com/misapema-jyfl/ct-analyzer (Release: ct-analyzer-v2.0). The cross section curtailment was performed on a customized version of the released code, which is available upon reasonable request from the corresponding author.

AUTHOR CONTRIBUTIONS

The author contributions have been tabulated in Table V.

ACKNOWLEDGMENTS

Appendix A: Penalty function upper limit variation and number of solutions with curtailed cross sections

The number of solutions in a given data set is plotted as a function of the upper limit of the penalty function of Eq. 10, F, in Figure 9. The value $F \leq 10^{-6}$ ensures that sufficient statistics are obtained for each solution set, while at the same time eliminating sources of crude error. The figure shows the number of solutions only for Maxwellian EED as similar behavior was found regardless of the assumed EED, i.e. $F \leq 10^{-6}$ was deemed appropriate

TABLE V: Author contributions for M. Luntinen (ML), J. Angot (JA), O. Tarvainen (OT), V. Toivanen (VT), H. Koivisto (HK), and T. Thuillier (TT).

Role	ML	JA	OT	VT	HK	TT
Conceptualization	Equal	Equal	Equal			
Data curation	Lead			Supporting		
Formal analysis	Lead	Supporting	Supporting	Supporting	Supporting	
Funding acquisition					Equal	Equal
Investigation		Lead				
Methodology	Equal	Equal				
Project administration	Lead			Supporting	Supporting	Supporting
Resources						Lead
Software	Lead					
Supervision			Equal		Equal	Equal
Validation	Lead					
Visualization	Lead					
Writing – original draft	Lead	Supporting	Supporting	Supporting	Supporting	Supporting
Writing – review & editing	Lead	Supporting	Supporting	Supporting	Supporting	Supporting

in each case. Figure 10 shows the solution set of K^{10+} for using different upper limits of F. It can be seen that requiring smaller values of F rarefies the solution set uniformly in $(\langle E_e \rangle, n_e)$-space, i.e. valid results are found throughout the optimisation bounds.

In addition to the penalty function value, the number of solutions in $(\langle E_e \rangle, n_e)$-space is affected by the the choice of the offset $\mathcal{A}$ and random bias $\mathcal{B}_q$ used in the analysis. As an example, Table VI lists the number of solutions for K^{8+} (assuming Maxwellian EED), i.e. the case presented in Fig. 7, when $\mathcal{A}$ and $\mathcal{B}_q$ are varied. We observe that (i) the number of solutions decreases as $\mathcal{A}$ is decreased keeping $\mathcal{B}_q$ constant, and (ii) the number of solutions increases as $\mathcal{B}_q$ is decreased keeping $\mathcal{A}$ constant. We associate (i) to the shift of the solutions in the $(\langle E_e \rangle, n_e)$-space, in particular fewer solutions are found at high n_e when $\mathcal{A}$ is decreased. There is no apparent reason for (ii) other than the decrease in the number of 'pathological' (unphysical) solutions outside the allowed $(\langle E_e \rangle, n_e)$-domain with
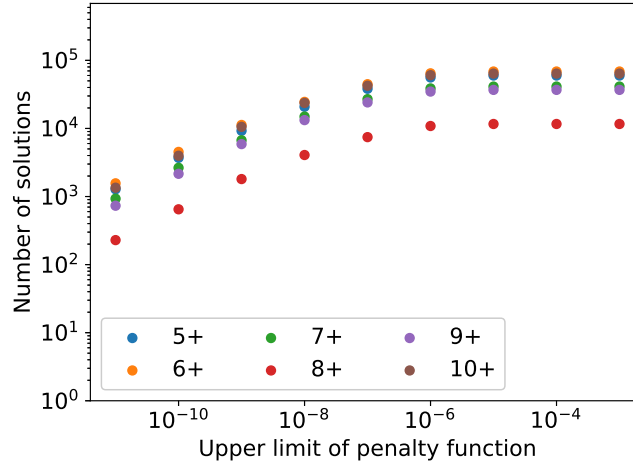
FIG. 9: The number of solutions in the solution sets obtained for different charge states as a function of the upper limit of the penalty function. The plot corresponds to data from the data set using a single Maxwell-Boltzmann EED.
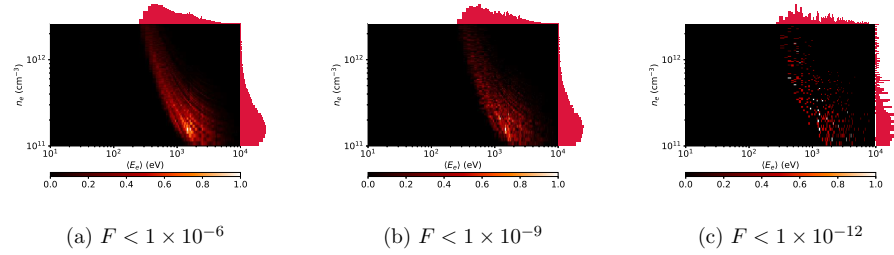

(a) $F < 1 \times 10^{-6}$ (b) $F < 1 \times 10^{-9}$ (c) $F < 1 \times 10^{-12}$

FIG. 10: The effect of varying the upper limit of the penalty function value on the solution set obtained for K^{10+}.

decreasing $\mathcal{B}_q$. Altogether the number of solutions is always significant (9000-19000 for K^{8+}, even higher for other charge states), which guarantees statistical significance of the analysis.

26

TABLE VI: The number of ($\langle E_e \rangle$, n_e)-solutions for K^{8+} for various $\mathcal{A}$ and $\mathcal{B}_q$ with Maxwellian EED. The corresponding solution spaces are illustrated in Fig. 7(a)-(i)

$\mathcal{A}$-$\mathcal{B}_q$	Number of solutions	Figure
50-50	9420	7(a)
50-25	11933	7(b)
50-00	14358	7(c)
100-50	14293	7(d)
100-25	16832	7(e)
100-00	17574	7(f)
150-50	15543	7(g)
150-25	18344	7(h)
150-00	18758	7(i)

Appendix B: Curtailing the solution set range

It was found that the curtailment of the ionization cross section uncertainty led to a broadening of the error estimate for the confinement time of K^{10+}. Therefore, in addition to the artificial curtailment of the cross section uncertainty, we performed a case study on K^{10+} where we imposed further (arbitrary) limitations also on the $\langle E_e \rangle$ and n_e values. This was done in the post-processing phase on the solution sets obtained for both an uncurtailed analysis using the standard MB EED, and the set 100-00 ($\mathcal{A} = 100\%$ and $\mathcal{B}_q \sim U(0,0)$ %, i.e. presumed perfect knowledge of the $\sigma_{q \to q+1}^{\mathrm{inz}}$). This extra analysis simulates the hypothetical effect of having a more precise knowledge of the plasma conditions prior to applying the CT method. The limitation on the $\langle E_e \rangle$ and n_e values was applied as shown in Fig. 11. We select solutions from a region in ($\langle E_e \rangle$, n_e)-space so that $\langle E_e \rangle \in [1, 2]$ keV, and $n_e \in [1, 2] \times 10^{11}$ cm^{-3} — plotted in the figure in cyan. Table VII tabulates the results. It can be seen that decreasing $\delta\sigma_{q \to q+1}^{\mathrm{inz}}$ and applying the further constraint on the density and average energy yields a considerable decrease in the uncertainty of τ^q, which goes from the 117% of the standard, non-limited MB set, to the 30% for the limited set 100-00. On the other hand, merely limiting either the $\delta\sigma_{q \to q+1}^{\mathrm{inz}}$ or the $\langle E_e \rangle$, n_e values does not appear to be as effective in the case of K^{10+}. The τ_{inz}^q and τ_{cx}^q also benefit from the additional limitation on
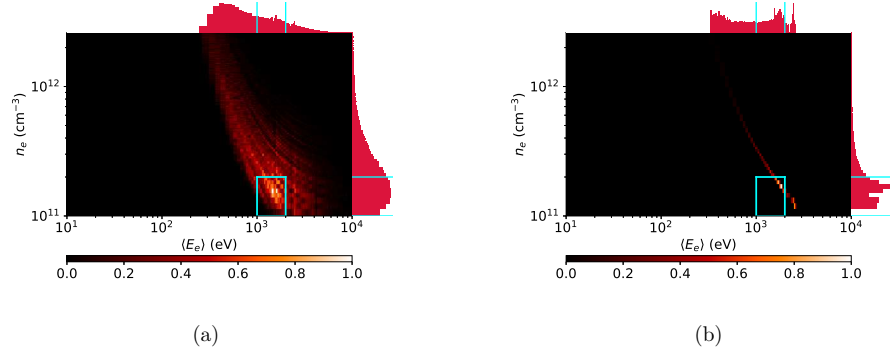
27

(a) (b)

FIG. 11: The solution sets for K^{10+} using a Maxwell-Boltzmann EED with the default uncertainty ranges (a) and using arbitrarily curtailed uncertainty (from Set 100-00) (b). The region $n_e \in [1, 2] \times 10^{11}$ cm^{-3} and $\langle E_e \rangle \in [1, 2]$ keV is highlighted in cyan.

TABLE VII: The characteristic time results for K^{10+} using a Maxwell-Boltzmann EED without curtailing the cross section uncertainty (MB); with cross section uncertainty curtailed to $\mathcal{A} = 100\%$ and $\mathcal{B}_q \sim U(0,0)$ (Set 100-00); and with their ranges limited to $\langle E_e \rangle \in [1, 2]$ keV, $n_e \in [1, 2] \times 10^{11}$ cm^{-3} (limited MB and limited Set 100-00, respectively). The relative uncertainties are computed from the absolute upper and lower uncertainty limits ($\hat{\delta}$ and $\check{\delta}$, resp.) according to $\delta = (\hat{\delta} + \check{\delta})/\tau$ for each τ.

Set	τ^q (ms)	δ (%)	τ^q_{inz} (ms)	δ (%)	τ^q_{cx} (ms)	δ (%)
MB	23^{+20}_{-7}	117	10^{+2}_{-2}	40	13^{+11}_{-5}	123
100-00	37^{+32}_{-18}	135	9^{+5}_{-2}	78	11^{+2}_{-2}	36
Limited MB	36^{+31}_{-11}	116	12^{+2}_{-2}	33	9^{+2}_{-2}	44
Limited 100-00	46^{+8}_{-6}	30	11^{+1}_{-1}	18	8^{+1}_{-1}	25

the solution set ranges.

Appendix C: The effect of the 1+ pulse length

The reliability of the characteristic times obtained with the CT method is subject to uncertainties other than the intrinsic ones discussed in detail in this paper. In particular,

28
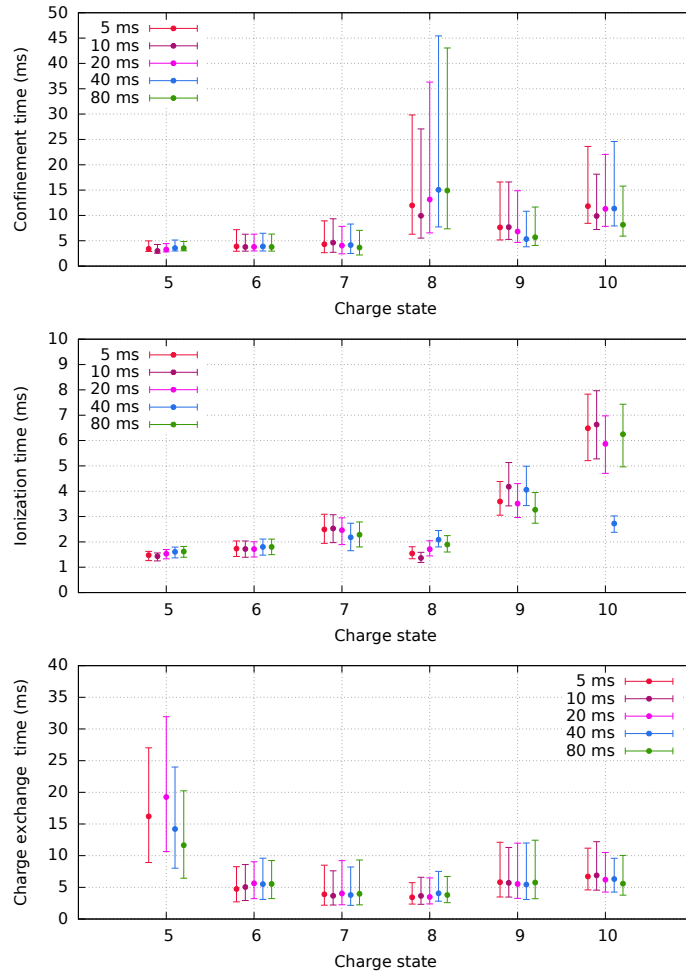
FIG. 12: Confinement times, ionization times and charge exchange times of potassium charge states from 5+ to 10+ with varied pulse length of the injected 1+ beam.

the potential perturbation caused by the 1+ injection is a relevant concern. The level of the charge breeder plasma perturbation is proportional to the number of injected particles, i.e. the 1+ beam current (see Ref.[16]) and the length of the 1+ beam pulse. The pulse length is more relevant for the CT method as it profoundly affects the shape of the high charge

state beam current transients and, thus, the resulting fitting parameters a_q, b_q and c_q. The usable pulse length is limited by two factors: (a) the 1+ pulse needs to be long enough to ensure the intensities of the highest charge state ions (K^{10+} in our case) are sufficiently above the noise level of the measurement, and (b) the 1+ pulse needs to be shorter than the saturation time of the high charge state ion signals (often referred to as the breeding time) to preserve the transient nature of the measurement and to avoid excessive perturbation of the charge breeder plasma. These two conditions render the 1+ beam pulse duration, t_{1+} to be in the range of 5 ms $\leq t_{1+} \leq$ 100 ms as found through a series of experiments. In this range the 1+ beam pulse length does not affect the results, namely the characteristic times, obtained with the CT method, i.e. the characteristic times computed from the data at different 1+ pulse lengths are within the uncertainty resulting from the cross section data. This is demonstrated in Fig. 12 where the confinement, ionization and charge exchange times of potassium (charge states 5+ to 10+) are plotted at 5 different 1+ beam pulse lengths ranging from 5 ms to 80 ms. It is evident that the results are within the uncertainty bounds with a single exception of the ionization time of K^{10+} at 40 ms 1+ pulse length, which we attribute to experimental error. Here we note that the data with varying 1+ pulse length was recorded at a different time from the data discussed in the main text of this paper and hydrogen (H_2) was used as a buffer gas instead of helium. The choice of the buffer gas does not change the conclusion that within the above limits of the 1+ pulse length the uncertainties related to the EED and ionization cross section are greater than those arising from the experiment itself.

REFERENCES

[1] R. Geller, Electron Cyclotron Resonance Ion Sources and ECR Plasmas (Institute of Physics Publishing, Bristol and Philadelphia, 1996).

[2] R. Geller, T. Lamy, and P. Sortais, "Charge breeding of isotope on-line-created radioactive ions using an electron cyclotron resonance ion trap," Review of Scientific Instruments **77**, 3–6 (2006).

[3] Y. Blumenfeld, T. Nilsson, and P. V. Duppen, "Facilities and methods for radioactive ion beam production," Physica Scripta **2013**, 014023 (2013).

[4] A. Kitagawa, T. Fujita, M. Muramatsu, S. Biri, and A. G. Drentje, "Review on heavy ion radiotherapy facilities and related ion sources (invited)," Review of Scientific Instruments **81**, 02B909 (2010).

[5] A. Kitagawa, T. Fujita, and M. Muramatsu, "Present Status and Future Prospect of Heavy Ion Radiotherapy," in Proc. 23rd International Workshop on ECR Ion Sources (ECRIS'18), International Workshop on ECR Ion Sources No. 23 (JACoW Publishing, Geneva, Switzerland, 2019) pp. 49–52.

[6] S. Biri, R. Racz, J. Palinkas, C. Hegedus, and S. Kokenyesi, "Application of the atomki-ecris for materials research," Journal of Electrical and Electronics Engineering **2**, 113–116 (2009).

[7] T. Uchida, H. Minezaki, K. Tanaka, M. Muramatsu, T. Asaji, Y. Kato, A. Kitagawa, S. Biri, and Y. Yoshida, "Bio-nano ecris: An electron cyclotron resonance ion source for new materials production," The Review of scientific instruments **81**, 02A306 (2010).

[8] F. J. C. Wenander, "Charge Breeding of Radioactive Ions," (2013), comments: 30 pages, contribution to the CAS-CERN Accelerator School: Ion Sources, Senec, Slovakia, 29 May – 8 June 2012, edited by R. Bailey, CERN-2013-007, arXiv:1404.0945.

[9] A. Galatà, D. Mascali, L. Neri, and L. Celona, "A new numerical description of the interaction of an ion beam with a magnetized plasma in an ecr-based charge breeding device," Plasma Sources Science and Technology **25**, 045007 (2016).

[10] V. Mironov, S. Bogomolov, A. Bondarchenko, A. Efremov, and V. Loginov, "Numerical model of electron cyclotron resonance ion source," Physical Review Special Topics - Accelerators and Beams **18**, 1–23 (2015).

[11] V. Mironov, S. Bogomolov, A. Bondarchenko, A. Efremov, V. Loginov, and D. Pugachev, "Spatial distributions of plasma potential and density in electron cyclotron resonance ion source," Plasma Sources Science and Technology **29**, 065010 (2020).

[12] G. Shirkov, "A classical model of ion confinement and losses in ECR ion sources," Plasma Sources Science and Technology **2**, 250–257 (1993).

[13] V. P. Pastukhov, "Classical longitudinal losses of of plasma in open adiabatic traps (russian)," Voprosy Teorii Plazmy , 160–204 (1984).

[14] I. Izotov, O. Tarvainen, V. Skalyga, D. Mansfeld, T. Kalvas, H. Koivisto, and R. Kronholm, "Measurement of the energy distribution of electrons escaping minimum-B ECR

plasmas," Plasma Sources Science and Technology **27** (2018), 10.1088/1361-6595/aaac14.

[15]I. Izotov, O. Tarvainen, V. Skalyga, D. Mansfeld, H. Koivisto, R. Kronholm, V. Toivanen, and V. Mironov, "Measurements of the energy distribution of electrons lost from the minimum b-field—the effect of instabilities and two-frequency heating," Review of Scientific Instruments **91**, 013502 (2020).

[16]O. Tarvainen, T. Lamy, J. Angot, T. Thuillier, P. Delahaye, L. Maunoury, J. Choinski, L. Standylo, A. Galatà, G. Patti, and H. Koivisto, "Injected 1+ ion beam as a diagnostics tool of charge breeder ECR ion source plasmas," Plasma Sources Science and Technology **24** (2015), 10.1088/0963-0252/24/3/035014.

[17]O. Tarvainen, T. Kalvas, H. Koivisto, J. Komppula, R. Kronholm, J. Laulainen, I. Izotov, D. Mansfeld, V. Skalyga, V. Toivanen, and G. Machicoane, "Limitation of the ECRIS performance by kinetic plasma instabilities (invited)," Review of Scientific Instruments **87** (2016), 10.1063/1.4931716.

[18]D. Mascali, E. Naselli, and G. Torrisi, "Microwave techniques for electron cyclotron resonance plasma diagnostics," Review of Scientific Instruments **93**, 033302 (2022).

[19]A. Gumberidze, M. Trassinelli, N. Adrouche, C. I. Szabo, P. Indelicato, F. Haranger, J.-M. Isac, E. Lamour, E.-O. Le Bigot, J. Mérot, C. Prigent, J.-P. Rozet, and D. Vernhet, "Electronic temperatures, densities, and plasma x-ray emission of a 14.5 ghz electron-cyclotron resonance ion source," Review of Scientific Instruments **81**, 033303 (2010).

[20]C. Barué, M. Lamoureux, P. Briand, A. Girard, and G. Melin, "Investigation of hot electrons in electron-cyclotron-resonance ion sources," Journal of Applied Physics **76**, 2662–2670 (1994).

[21]J. Noland, O. Tarvainen, J. Benitez, D. Leitner, C. Lyneis, and J. Verboncoeur, "Studies of electron heating on a 6.4 ghz ecr ion source through measurement of diamagnetic current and plasma bremsstrahlung," Plasma Sources Science and Technology **20**, 035022 (2011).

[22]R. C. Pardo, R. Harkewicz, and P. J. Billquist, "Time evolution of charge states in an electron cyclotron resonance ion source," Review of Scientific Instruments **67**, 1602–1605 (1996).

[23]M. Imanaka, T. Nakagawa, H. Arai, I. Arai, and S. M. Lee, "Plasma diagnostics of liquid He-free SC-ECR ion source (SHIVA) with use of laser ablation technique," Nuclear Instruments and Methods in Physics Research, Section B: Beam Interactions with Materials and Atoms **237**, 647–655 (2005).

[24]D. Neben, J. Fogleman, D. Leitner, G. Machicoane, G. Parsey, A. Pham, S. Renteria, J. Stetson, L. Tobos, and J. Verboncoeur, "Fast Sputtering Measurement Studies using Uranium with the NSCL ECR Ion Sources," in Proc. ECRIS'16 (JACoW Publishing, Geneva, Switzerland, 2016) pp. 128–132.

[25]D. E. Neben, G. Machicoane, A. N. Pham, J. W. Stetson, G. Parsey, and J. P. Verboncoeur, "An Analysis of Fast Sputtering Studies for Ion Confinement Time," in Proc. LINAC'16 (JACoW Publishing, Geneva, Switzerland, 2016) pp. 475–477.

[26]M. Marttinen, J. Angot, A. Annaluru, P. Jardin, T. Kalvas, H. Koivisto, S. Kosonen, R. Kronholm, L. Maunoury, O. Tarvainen, V. Toivanen, and P. Ujic, "Estimating ion confinement times from beam current transients in conventional and charge breeder ECRIS," Review of Scientific Instruments 91 (2020), 10.1063/1.5128546.

[27]J. Angot, M. Luntinen, T. Kalvas, H. Koivisto, R. Kronholm, L. Maunoury, O. Tarvainen, T. Thuillier, and V. Toivanen, "Method for estimating charge breeder ECR ion source plasma parameters with short pulse 1+ injection of metal ions," Plasma Sources Science and Technology 30 (2021), 10.1088/1361-6595/abe611.

[28]M. Luntinen, J. Angot, O. Tarvainen, V. Toivanen, T. Thuillier, and H. Koivisto, "Measurement of ionization, charge exchange and ion confinement times in charge breeder ECR ion sources with short pulse 1+ injection of metal ions," Journal of Physics: Conference Series 2244 (2022), 10.1088/1742-6596/2244/1/012009.

[29]M. Luntinen, V. Toivanen, H. Koivisto, J. Angot, T. Thuillier, O. Tarvainen, and G. Castro, "Diagnostics of highly charged plasmas with multicomponent 1+ ion injection," Phys. Rev. E 106, 055208 (2022).

[30]M. A. Lennon, K. L. Bell, H. B. Gilbody, J. G. Hughes, A. E. Kingston, M. J. Murray, and F. J. Smith, "Recommended data on the electron impact ionization of atoms and ions: Fluorine to nickel," Journal of Physical and Chemical Reference Data 17, 1285–1363 (1988).

[31]A. Müller and E. Salzborn, "Scaling of cross sections for multiple electron transfer to highly charged ions colliding with atoms and molecules," Physics Letters A 62, 391–394 (1977).

[32]H. Knudsen, H. K. Haugen, and P. Hvelplund, "Single-electron capture by highly charged ions colliding with atomic and molecular hydrogen," Phys. Rev. A 24, 2287–2290 (1981).

[33]R. Kronholm, T. Kalvas, H. Koivisto, J. Laulainen, M. Marttinen, M. Sakildien, and O. Tarvainen, "Spectroscopic study of ion temperature in minimum-b ecris plasma,"

Plasma Sources Science and Technology **28**, 075006 (2019).

[34] G. Douysset, H. Khodja, A. Girard, and J. P. Briand, "Highly charged ion densities and ion confinement properties in an electron-cyclotron-resonance ion source," Phys. Rev. E **61**, 3015–3022 (2000).

[35] H. I. W. Jr., "Calculation of ion charge-state distribution in ecr ion sources," Tech. Rep. UCRL-53391 (Lawrence Livermore National Laboratory, 1982).

[36] K. L. Bell, H. B. Gilbody, J. G. Hughes, A. E. Kingston, and F. J. Smith, "Recommened Data on the Electron Impact Ionization of Light Atoms and Ions," J. Phys. CHem. **12**, 891–916 (1983).

[37] We note here that in Ref.[27] the equation of τ_{cx}^q has a typographical error, but the correct equation was implemented in the numerical analysis and the results were not affected.

[38] K. S. Golovanivsky, Instruments and Experimental Techniques **28**, 989 (1986).

[39] G. Voronov, "A practical fit formula for ionization rate coefficients of atoms and ions by electron impact: Z=1-28," Atomic Data and Nuclear Data Tables **65**, 1–35 (1997).

[40] V. Pierrard and M. Lazar, "Kappa Distributions: Theory and Applications in Space Plasmas," Solar Physics **267**, 153–174 (2010), arXiv:1003.3532.

[41] M. Sakildien, O. Tarvainen, R. Kronholm, I. Izotov, V. Skalyga, T. Kalvas, P. Jones, and H. Koivisto, "Experimental evidence on microwave induced electron losses from ecris plasma," Physics of Plasmas **25**, 062502 (2018).

[42] M. Sakildien, O. Tarvainen, T. Kalvas, H. Koivisto, R. Kronholm, R. Thomae, J. Mira, F. Nemulodi, and P. Jones, "Investigation into the gas mixing effect in ecris plasma using kα and optical diagnostics," AIP Conference Proceedings **2011**, 040010 (2018).

[43] J. Angot and M. Luntinen, "Consecutive_Transients_Sample_Data," (2021), 10.6084/m9.figshare.13602827.v1.

34

PV

DIAGNOSTICS OF CHARGE BREEDER ELECTRON CYCLOTRON RESONANCE ION SOURCE PLASMA WITH CONSECUTIVE TRANSIENTS METHOD

by

J Angot, O Tarvainen, H Koivisto, M Luntinen, T Thuillier, V Toivanen

Diagnostics of charge breeder electron cyclotron resonance ion source plasma with consecutive transients method

J. Angot[*] and T. Thuillier

Univ. Grenoble Alpes, CNRS, Grenoble INP, LPSC-IN2P3, 38000 Grenoble, France

O. Tarvainen

UK Science and Technology Facilities Council, ISIS Pulsed Spallation Neutron and Muon Facility, Rutherford Appleton Laboratory, Harwell Campus, OX11 0QX, United Kingdom

H. Koivisto, M. Luntinen, and V. Toivanen

Accelerator Laboratory, Department of Physics, University of Jyväskylä, FI-40014 Jyväskylä, Finland

(Dated: October 18, 2023)

The consecutive transients (CT) method is a diagnostics approach combining experimental and computational techniques to probe the plasma parameters of Charge Breeder Electron Cyclotron Resonance Ion Sources (CB-ECRIS). The method is based on short pulse injection of singly charged ions into the charge breeder plasma, and the measurement of the resulting transients of the charge bred multiply charged ions. Estimates for plasma density, average electron energy and characteristic times of ion confinement, electron impact ionization and charge exchange are then computationally derived from the experimental data. Here the CT method is applied for parametric studies of CB-ECRIS plasma. Potassium ions were charge bred with hydrogen support plasma, and the effects of varied microwave power, neutral gas pressure and magnetic field strength on the plasma parameters and charge breeding efficiency are presented. It is shown that the method is sufficiently sensitive to provide relevant information on changing plasma conditions with the control parameters. The neutral gas pressure had the strongest impact on the plasma parameters, and the results agree with trends obtained by using other diagnostic methods, e.g. the increase of plasma density with increased neutral gas pressure. Furthermore, the method can provide information inaccessible with other methods, such as the characteristic times of ion confinement, ionization and charge exchange — and the hierarchy between them. The results show that the peak charge breeding efficiency is obtained for the highest ion charge state for which the ionization time remains shorter than the charge exchange and the ion confinement times.

I. INTRODUCTION

Charge Breeder Electron Cyclotron Resonance Ion Sources (CB-ECRIS) are used in Isotope Separation On-Line (ISOL) -facilities for post-acceleration of radioactive nuclei [1, 2]. The charge breeding process involves deceleration and capture of the incident 1+ ion beam, stepwise electron impact ionization to high charge state in the magnetically confined minimum-B ECRIS plasma, and extraction of the charge bred ions together with buffer (or support) gas ions. Optimising the charge breeding efficiency and time benefits from dedicated plasma diagnostics for the CB-ECRIS plasma parameters affecting these steps.

ECRIS plasmas are unique in many aspects. The electron energy distribution (EED) is strongly non-Maxwellian (see e.g. Ref. [3]) owing to the efficient energy transfer from the microwave electric field to the electrons on a closed magnetic isosurface where the relativistic resonance condition $\omega_{RF} = \omega_{ce} = eB/\gamma m_e$ is met. The resulting electron energies range from a few eV to several hundred keV with the high energy electrons being strongly confined magnetically. The high charge state ions remain relatively cold, i.e. $5-30\,\mathrm{eV}$ as indicated by the Doppler broadening of their emission lines [4], and are confined electrostatically in a local potential minimum caused by the accumulation of hot electrons in the centre of the trap [5, 6]. In fact, simulations [7, 32] allude the presence of two (small) potential dips, along the plasma chamber axis, at the mirror points for hot electrons near the ECR-zone. Non-invasive diagnostics methods applied for studying minimum-B ECRIS plasmas (not necessarily charge breeders) include, bremsstrahlung and x-ray diagnostics, microwave interferometry, plasma diamagnetism measurement, optical emission spectroscopy, measurement of the plasma potential, detection of kinetic instabilities, and escaping electron spectroscopy [9–17].

The consecutive Transient (CT) method [18, 19] is a recently developed method combining computational techniques and experiments for probing the plasma density n_e, (warm) electron average energy $\langle E_e \rangle$, and characteristic times of ion confinement τ_{conf}, charge exchange τ_{cex} and electron impact ionization τ_{ion} in CB-ECRIS plasmas. The CT method is based on short pulse 1+ injection into the ECRIS plasma and the analysis of the resulting N+ ion beam transients extracted from the ECRIS. As such, the CT method has both benefits and drawbacks. The positives are: the method can be considered non-invasive, the magnitude of the perturbation it causes can

---

be controlled by adjusting the injected 1+ pulse width and intensity, and the equipment required for the 1+ injection and pulsing as well as N+ current measurement is readily available in all CB-ECRIS facilities. The downsides of the method are: limited combinations of 1+ ions and plasma species (clean charge state distribution spectrum with minimum of 5 consecutive charge states without m/q-overlap is necessary for the method), the complexity of data analysis, and the large uncertainties of the characteristic times due to the lack of accurate cross section data for high charge state ionisation. As such, the method either complements existing CB-ECRIS diagnostics while requiring fewer assumptions, or provides information inaccessible through other techniques. For example, it has been shown with the CT method that the ion confinement time is not a linear function but rather increases exponentially with the charge state [18, 19], which is commensurate with electrostatic ion confinement in a local potential dip [5, 6]. It has been shown that the inherent uncertainties of the CT method can be reduced e.g. by two-component injection or overlapping the $(\langle E_e \rangle, n_e)$ solution sets of neighbouring charge states albeit with the caveat of additional assumption [20]. Furthermore, it has been demonstrated that the main contributor to the large relative uncertainty of the CT method is the lack of precise ionization cross section data whereas the presumed EED has a smaller effect [21].

In this paper we apply the CT method for parametric studies of the CB-ECRIS plasma. We do not detail the method itself but rather refer the reader to the literature [18–21] for a comprehensive account of the assumptions, computational details and data analysis.

In the following sections we describe the experimental setup, and present the measured plasma energy content and characteristic times along with the charge breeding efficiency of potassium as a function of the CB-ECRIS microwave power, neutral (hydrogen) pressure and magnetic field strength. These sweeps are carried out to demonstrate that the CT method is sensitive enough to pick up trends in the above plasma parameters (observables) responding to the change of the control parameters. The results of the CT method are placed in context comparing them to the outcomes of other ECRIS plasma diagnostics.

II. EXPERIMENTAL SETUP AND PROCEDURE

The experiments were carried out on the LPSC 1+→N+ test bench, shown in Fig. 1, dedicated for the development of the PHOENIX CB-ECRIS [22] — in particular measurements of the charge breeding efficiency, charge breeding time and m/q-contamination.

Delivering on this remit requires generating a stable 1+ beam with fine tuning of the ion injection energy, a good base vacuum on the order of 10^{-8} mbar or better, the hardware for pulsing of the 1+ beam and beam di-

agnostics. Hence, the 1+ beam line is equipped with a surface ionisation source producing alkali metal beams, a dipole magnet for mass separation, a Faraday cup to measure the beam intensity, beam optics and deflecting plates for 1+ injection optimisation and pulsing. The 1+ source potential is typically set to HV=20 kV. The CB-ECRIS plasma chamber is then biased to HV-ΔV with a negative supply floating at the 1+ source potential. This configuration allows fine-tuning the 1+ ion energy, which is essential for the 1+ beam capture by the CB plasma through electrostatic deceleration by the charge breeder and its plasma potential, and subsequent thermalization of the injected ions in ion-ion collisions with the buffer gas ions. The beams extracted from the charge breeder are analysed in the N+ beam line with a mass spectrometer and diagnostics including a Faraday cup for beam intensity measurement.

The current incarnation of the LPSC charge breeder is a 14.5 GHz minimum-B ECR ion source equipped with three coils to create the axial magnetic profile with two magnetic mirrors at the injection and extraction, respectively [23]. Typical operational values of the injection, minimum-B and extraction axial magnetic fields are $B_{inj} \approx 1.6$ T, $B_{min} \approx 0.4$ T, and $B_{ext} \approx 0.8$ T. A permanent magnet sextupole surrounding the plasma chamber creates the radial magnetic mirror of 0.8 T at the plasma chamber wall, in front of the pole (the total radial field then being affected by the radial component of the solenoid field). A 2 kW klystron microwave amplifier for plasma (electron) heating is connected to the plasma chamber through a direct waveguide port. The vacuum pumping system assures a base pressure of approximately 3×10^{-8} mbar at the source injection.

Here we apply the CT method to observe the influence of different charge breeder tuning parameters on the plasma characteristics i.e. n_e, $\langle E_e \rangle$ and τ_{conf}, τ_{cex} and τ_{ion} of potassium (^{39}K) ions. We chose K as the injected element because it is an alkali element, thus minimising the wall recycling, with several (consecutive) charge states from K$^+$ to K^{12+} found in the m/q spectrum without overlap with the support or residual gas ions. Hydrogen was chosen as plasma support gas to obtain high charge breeding efficiencies of high charge state K ions. The ion source control parameters varied systematically in this study were: (i) the microwave power as it presumably influences the EED and plasma density (see e.g. Refs. [11, 24, 25]), (ii) the support gas feed rate (pressure) which acts on the neutral and electron densities (see e.g. Refs. [24, 26]), (iii) the magnetic field minimum B_{min} as it affects the tail of the EED and the occurrence of kinetic plasma instabilities [27–29], and (iv) the extraction magnetic field B_{ext}, which allegedly affects the trapping of the hot electrons and the global plasma confinement [30]. For each parameter sweep, a $500 - 900$ nA K$^+$ beam was produced with the 1+ ion source. The beam line optics and the CB parameters were optimized for the charge breeding of K^{9+} resulting in 19-20% efficiency at best. The 1+ pulsing was then used to generate 10 ms
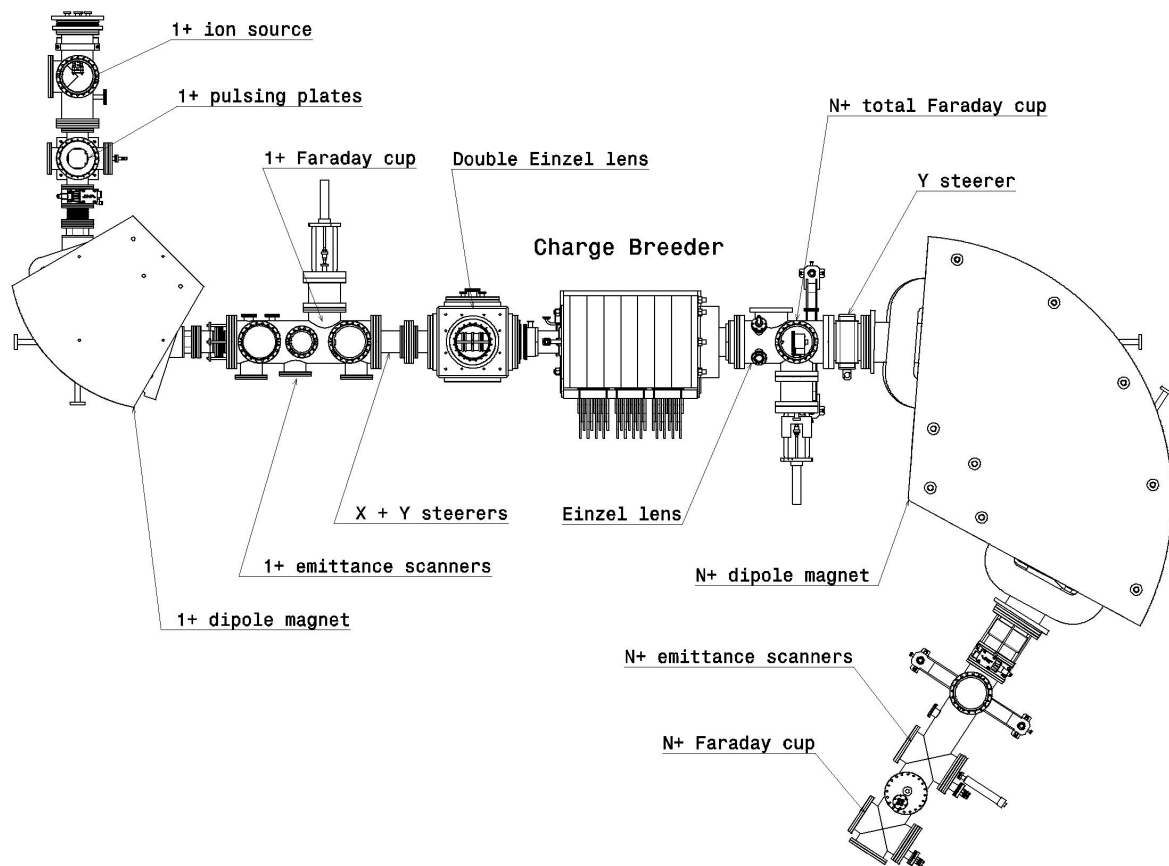
FIG. 1. Schematic view of the 1+→N+ CB-ECRIS test bench.

bunches of injected ions at $1\,\mathrm{Hz}$ repetition rate allowing the ion current transients to decay before the onset of the subsequent 1+ pulse. The multi-charged K beam intensity responses (transients) were measured from the Faraday cup of the N+ beam line averaging over 64 waveforms for each charge state to improve the signal-to-noise ratio of the measurement. The microwave power and gas feed rate studies were carried out in the control parameter ranges yielding a stable CB regime i.e. the magnetic field was chosen accordingly to avoid kinetic instabilities. Only one CB-ECRIS control parameter was varied during each sweep. The B_{min} and B_{ext} values corresponding to certain combinations of coil currents were simulated with Radia3D [31]. The coil currents were then adjusted so that in each sweep only either B_{min} or B_{ext} varied while other field values remained constant. The parameter settings for each sweep are given in Section III along with the data plots. For each setting, the ΔV value was adjusted to optimize the K^{9+} breeding efficiency.

III. RESULTS

In the following subsections we present the results of the CB-ECRIS parameter sweeps. We first describe the $K^+ \rightarrow K^{n+}$ charge breeding efficiencies as a function of each parameter. The $(\langle E_e \rangle, n_e)$ solution sets derived from the transients of each ion charge state are used for calculating the plasma energy content $n_e \langle E_e \rangle$, which is then presented along with the characteristic times.

For clarity, we present two examples of the $(\langle E_e \rangle, n_e)$ solution sets for K^{10+} in Figs. 2(a) and 2(b) highlighting the change of the calculated plasma energy content from $3.5 \times 10^{14}\mathrm{eV/cm^3}$ to $6.9 \times 10^{14}\mathrm{eV/cm^3}$ with the notable shift of the $(\langle E_e \rangle, n_e)$ solution space towards higher plasma density. The energy content value is taken as the median value of the product of the $(\langle E_e \rangle, n_e)$ solutions from the CT-method. These examples were measured as a part of the gas pressure sweep discussed later. The n_e and $\langle E_e \rangle$ values were restricted to $10^{11}\,\mathrm{cm^{-3}} \leq n_e \leq 2.6 \times 10^{12}\,\mathrm{cm^{-3}}$ and $10\,\mathrm{eV} \leq E_e \leq 10\,\mathrm{keV}$. These limits are based on experimental evidence and simulations of the electron density, and electron energy as explained in
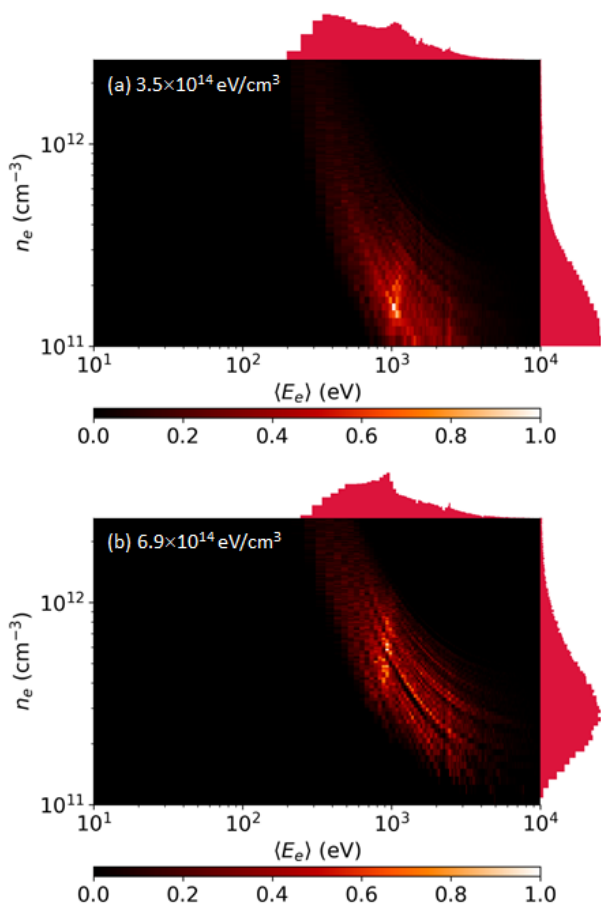
FIG. 2. Examples of the $(\langle E_e \rangle, n_e)$ solution sets for K^{10+} and the corresponding plasma energy contents. The H_2 gas pressure was increased from 6.8×10^{-8} mbar in (a) to 2.3×10^{-7} mbar in (b). The energy content increases due to increased median plasma density from 3.8×10^{11} cm^{-3} to 1.5×10^{12} cm^{-3}.

Ref. [18] and references therein.

The plasma energy contents and characteristic times are presented in Sections III A - III D without the estimated uncertainties for the sake of illustration clarity. The uncertainties are discussed separately in Section III E.

A. Microwave power

The charge breeding efficiencies of K^{4+}-K^{12+} as a function of the microwave power are shown in Fig. 3. Increasing the power increases the average charge state of K ions, which causes the breeding efficiency of K^{9+}-K^{11+} to improve significantly with this control parameter. In contrast, the efficiency of charge states $\leq K^{8+}$ exhibit a maximum efficiency at 350 W and then a decrease as the power is ramped up. Two sweeps were made to ensure
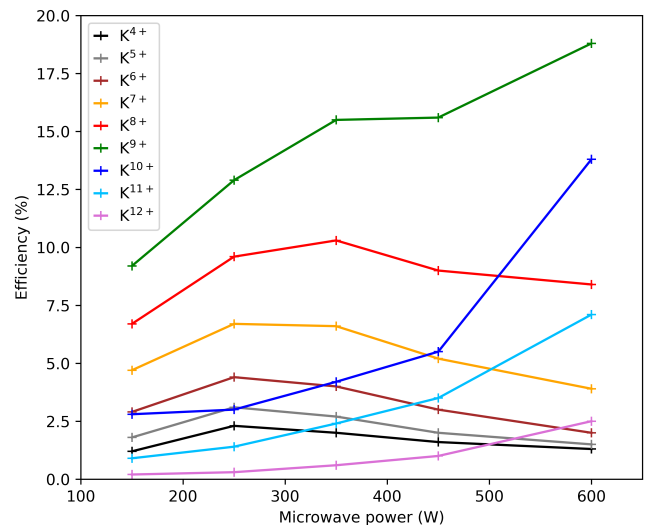
FIG. 3. The charge breeding efficiency of K^{4+} - K^{12+} as a function of the microwave power.

the reproducibility of the observed trends but are only shown for the plasma energy content plots. The increase of the high charge state breeding efficiency with the microwave power was observed in both microwave power sweeps. The other source settings in these sweeps were as follows: neutral gas pressure $1.2 \times 10^{-7} - 1.3 \times 10^{-7}$ mbar, B_{inj} $1.57 - 1.58$ T, B_{min} $0.44 - 0.45$ T and B_{ext} 0.84 T.

Figure 4 shows the (median) energy content as a function of the microwave power for potassium charge states from K^{8+} to K^{10+} in the two microwave power sweeps. Three observations can be made; (i) the calculated energy content depends on the charge state, which is attributed to the highest charge states originating from the core of the plasma where the plasma density and electron energies can be argued to be higher, (ii) the trend of the plasma energy content is to increase with microwave power by 20-40% (ignoring a single outlier data point for K^{10+} at 350 W), and (iii) the trend of the energy content was found to be similar for both microwave power sweeps.

Figure 5 shows τ_{conf}, τ_{cex} and τ_{ion} for charge states K^{6+}-K^{10+} as a function of the microwave power. The confinement time of the high charge states K^{8+}-K^{10+} is longer than the confinement time of the charge states K^{6+}-K^{7+}, which is commensurate with the spatial distribution of the ions found in simulations and experiments [32–34] suggesting that the highest charge states are highly collisional and electrostatically confined (as opposed to magnetically confined electrons). The trend of τ_{conf} with the microwave power is to decrease for charge states K^{6+}-K^{7+} and to increase for charge states K^{8+}-K^{10+}. Admittedly there are data points deviating from the trend, and altogether the variation of τ_{conf} is not drastic. Nevertheless, we draw the attention to the fact that the confinement time of the highest charge states,
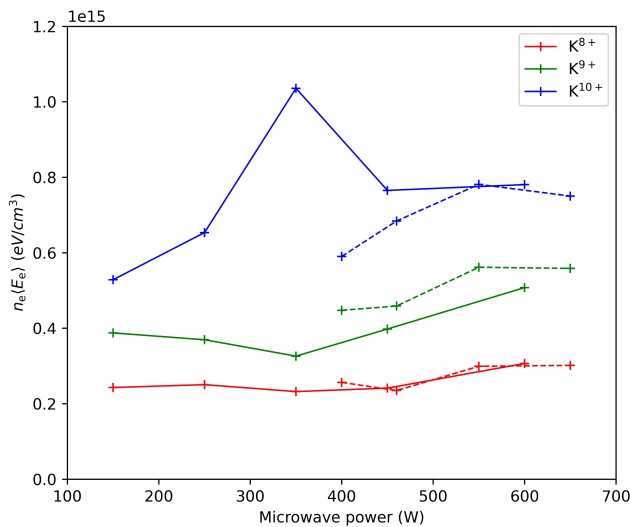
FIG. 4. The (local) plasma energy content of K^{8+}, K^{9+} and K^{10+} as a function of the microwave power. The solid and dashed lines represent two different power sweeps.

i,e. K^{8+}-K^{10+}, are always longer than their ionization times. Furthermore, in the case of K^{10+} the notable increase of τ_{conf} at high microwave power is correlated with significant increase of the corresponding charge breeding efficiency. The charge exchange time is found longest for the high charge state ions and the trend of τ_{cex} is to decrease with the microwave power, but again, the changes are very small. Finally, τ_{ion} does not exhibit a clear trend with the microwave power, but is shorter for the lower charge states than for the higher ones. This is probably due to very low neutral gas density in the core plasma (potential dip) where the highest charge states reside as discussed in Ref. [32]. The ionization rate coefficient first increases and then typically plateaus towards high $\langle E_e \rangle$ (e.g. > 1000 eV for K^{8+}), so improved electron heating is not expected to affect τ_{ion} by much assuming sufficiently high $\langle E_e \rangle$ as indicated by the solution sets. Generally speaking, high charge state production requires τ_{ion} to be shorter than τ_{cex}, which is the case found throughout the power sweep for most of the charge states, especially those below the K^{9+} peak charge state of the CB-efficiency. Finally, we note that the continuous increase of the K^{9+} efficiency with the microwave power is accompanied with a decrease of τ_{ion} of $K^{6+/7+}$ and an increase of τ_{conf} of the higher charge state ions. This highlights the importance of the hierarchy of the characteristic times in regards to the optimum charge state for the highest CB efficiency.

B. Neutral gas pressure

The effect of the neutral H_2 pressure (gas feed rate) on the charge breeding efficiency and plasma parame-

ters was studied through two sweeps with otherwise almost identical configuration, i.e. $530 - 560$ W microwave power, 1.57 T B_{inj}, $0.44 - 0.45$ T B_{min} and $0.83 - 0.84$ T B_{ext}. Fig. 6 shows the charge breeding efficiencies of K^{4+}-K^{12+} for one of the sweeps. The behaviour is rather complex but can be summarized as follows; the higher the charge state, the lower the optimum pressure for maximising the charge breeding efficiency.

The effect of the H_2 neutral pressure on the plasma energy content is shown in Fig. 7 for potassium charge states from K^{8+} to K^{10+}. Here the results of both sweeps are displayed (either solid or dashed lines). It is seen that the trend of the plasma energy content is to increase with the gas pressure (with the exception of the highest pressure), which is attributed to higher plasma density as indicated by the histograms of the solution sets shown as projections to the axes in Fig. 2. The finding is commensurate with diamagnetic loop experiments reporting the plasma energy content to increase with the neutral gas pressure (saturating at high pressures) [11]. Figure 7 also shows the evolution of the ΔV-value. The ΔV appears to follow the same trend as the energy content. This is consistent as the optimum energy (tuned with ΔV) for 1+ beam capture relies on the plasma potential [35], which presumably depends on the low energy electron density as implied by the data in Ref. [14].

Figure 8 shows τ_{conf}, τ_{cex} and τ_{ion} for charge states K^{6+}-K^{10+} as a function of the H_2 neutral gas pressure. All these characteristic times tend to decrease with the neutral (buffer) gas pressure, with only the ionisation time of K^{10+} breaking the trend. We note that obvious outlier points, e.g. >1 s τ_{cex} for K^{6+} arising from poor fits to experimental transient data are not shown in the figure, which explains 'missing data points' at low pressure.

C. Magnetic field minimum, B_{min}

The charge breeding efficiencies of K^{4+}-K^{12+} at different B_{min} are shown in Fig. 9. The other source parameters, i.e. magnetic field maxima, microwave power and H_2 gas pressure were kept constant at B_{inj} of 1.51 T, B_{ext} of 0.82 T, 530 W and 1.1×10^{-7} mbar, respectively. The CB efficiency of charge states $\leq K^{7+}$ decreases, and the efficiency of charge states $\geq K^{8+}$ increases with increasing B_{min}.

The plasma energy content at three different B_{min} settings is presented for K^{8+}-K^{10+} in Fig. 10. The highest energy content is systematically found at the strongest B_{min}.

The characteristic times τ_{conf}, τ_{cex} and τ_{ion} for charge states K^{6+}-K^{10+} are shown in Fig. 11 as a function of B_{min}. There are no systematic trends except the confinement time of the highest K^{10+} charge state approximately doubling from the weakest to strongest B_{min} value, which together with the enhanced CB efficiency of even higher charge states implies improved (electro-
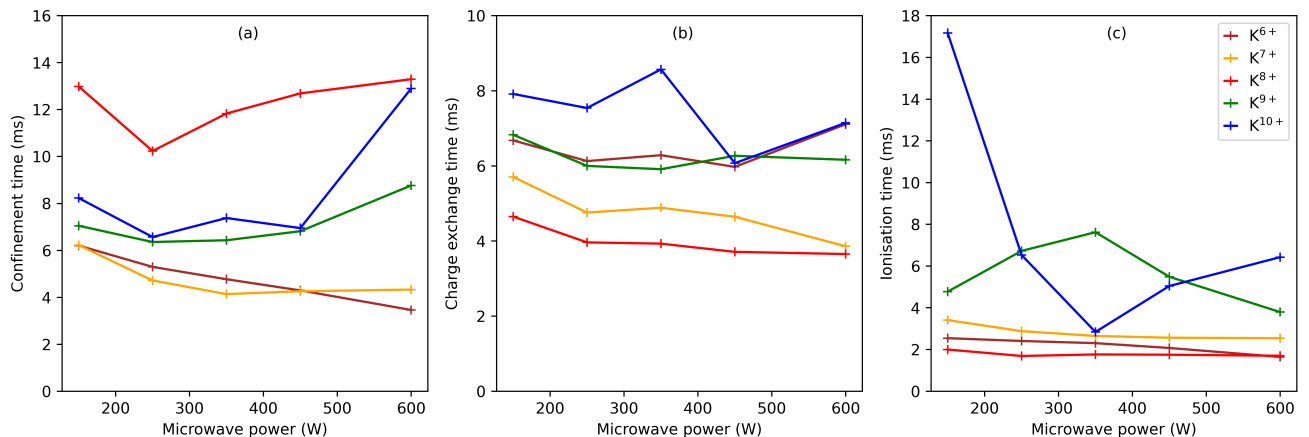
FIG. 5.   The confinement, charge exchange and ionisation times (τ_{conf}, τ_{cex} and τ_{ion}) of K^{6+} - K^{10+} ions as a function of the microwave power.
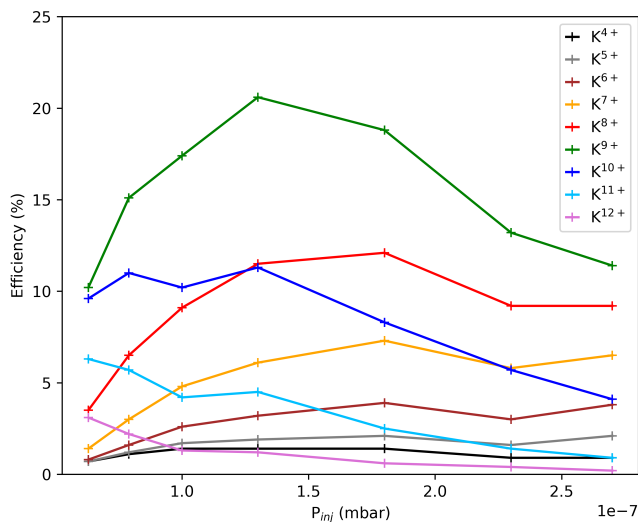

FIG. 6.   The charge breeding efficiency of K^{4+} - K^{12+} as a function of the H_2 (buffer) gas pressure.
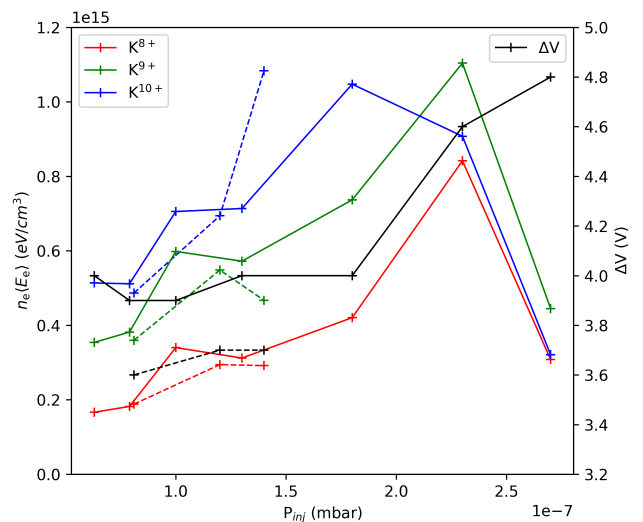

FIG. 7.   The (local) plasma energy content of K^{8+}, K^{9+} and K^{10+} together with the optimum ΔV value as a function of the H_2 (buffer) gas pressure. The solid and dashed lines represent two different pressure sweeps.

static) ion confinement.

D.   Extraction mirror magnetic field, B_{ext}

The effect of the extraction mirror field B_{ext} on the charge breeding efficiencies of K^{4+}-K^{12+} is illustrated in Fig. 12. Here the other source parameters were as follows: B_{inj} of $1.58\,\mathrm{T}$, B_{min} of $0.45\,\mathrm{T}$, $530\,\mathrm{W}$ microwave power and $1.4 \times 10^{-7}\,\mathrm{mbar}$ H_2 pressure. The CB efficiency of high charge state ions, i.e. K^{9+} and higher, exhibits a clear optimum at $0.83-0.84\,\mathrm{T}$ while the efficiency of lower charge states decreases monotonically with increasing B_{ext}.

Figure 13 shows the plasma energy content (for K^{8+}-K^{10+}) as a function of B_{ext}. The extraction field has very little effect on the energy content, i.e. there is no trend observed with this parameter.

The characteristic times τ_{conf}, τ_{cex} and τ_{ion} of charge states K^{6+}-K^{10+} measured with different B_{ext} are shown in Fig. 14. There are no clear trends, which is in line with B_{ext} having little effect on the CB efficiency compared to e.g. the neutral gas pressure. Nevertheless, we note that the efficiency increase of the optimum charge state K^{9+} at B_{ext} between $0.822\,\mathrm{T}$ and $0.852\,\mathrm{T}$ corresponds to an increase of the confinement time.
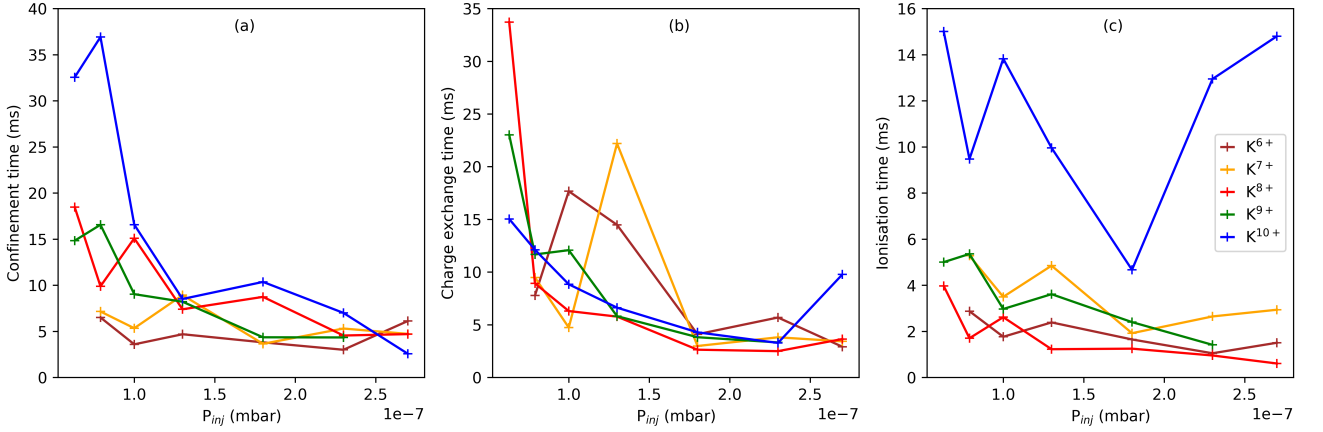
FIG. 8. The confinement, charge exchange and ionisation times of K^{6+} - K^{10+} as a function of the H_2 (buffer) gas pressure.
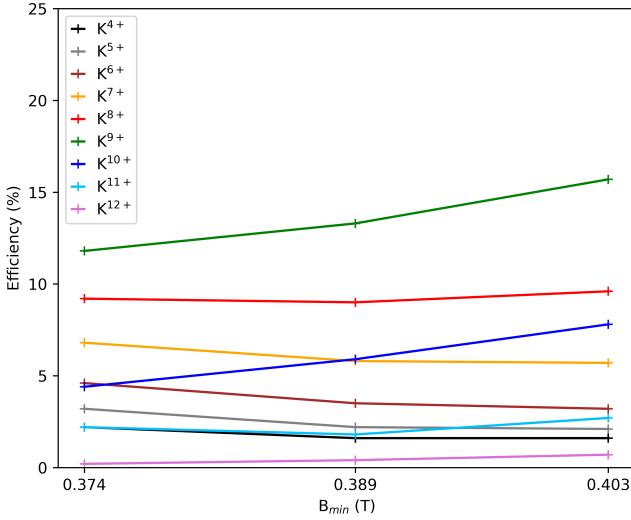

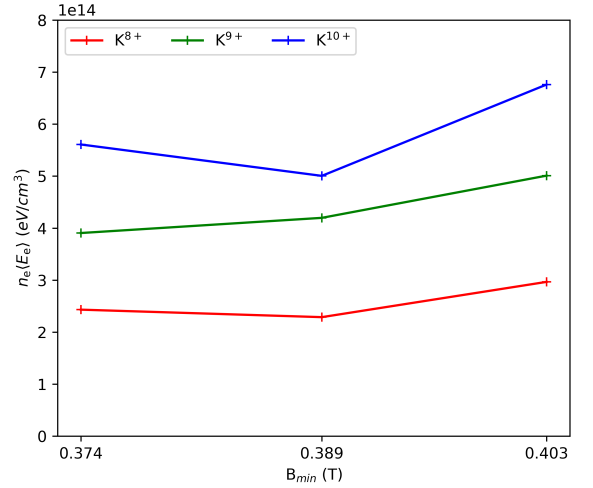FIG. 9. The charge breeding efficiency of K^{4+} - K^{12+} as a function of B_{min}.

FIG. 10. The (local) plasma energy content of K^{8+}, K^{9+} and K^{10+} as a function of B_{min}.

E. On the uncertainty of τ_{conf}, τ_{cex} and τ_{ion}

As stated earlier, the most prominent downside of using the CT method for estimating the characteristic times τ_{conf}, τ_{cex} and τ_{ion} of the high charge state ions is the large uncertainty. Typical uncertainties of high charge state potassium confinement and charge exchange times are 100-200% while the ionization times can be estimated more accurately, i.e. with 40-70% relative uncertainty [18–21], which raises the concern that the CT method might not be able to detect small variations of the plasma parameters. Thus, the statistical relevance of the measurement results presented above could be questioned. However, it has been shown in Ref. [21] that the large uncertainties are inherited from the ionization cross section data [36]. This allows us to argue that the CT method can reveal trends of the characteristic times as a function of a control parameter, such as microwave power, gas pressure and magnetic field strength, although the absolute values of the times are subject to systematic errors of the cross section data. In other words, the conclusions based on the trends of the characteristic time median values displayed in Figs. 5, 8, 11 and 14 are not affected by the uncertainties of the individual data points. Hence, the data are presented without the corresponding uncertainties for the clarity of the illustration.
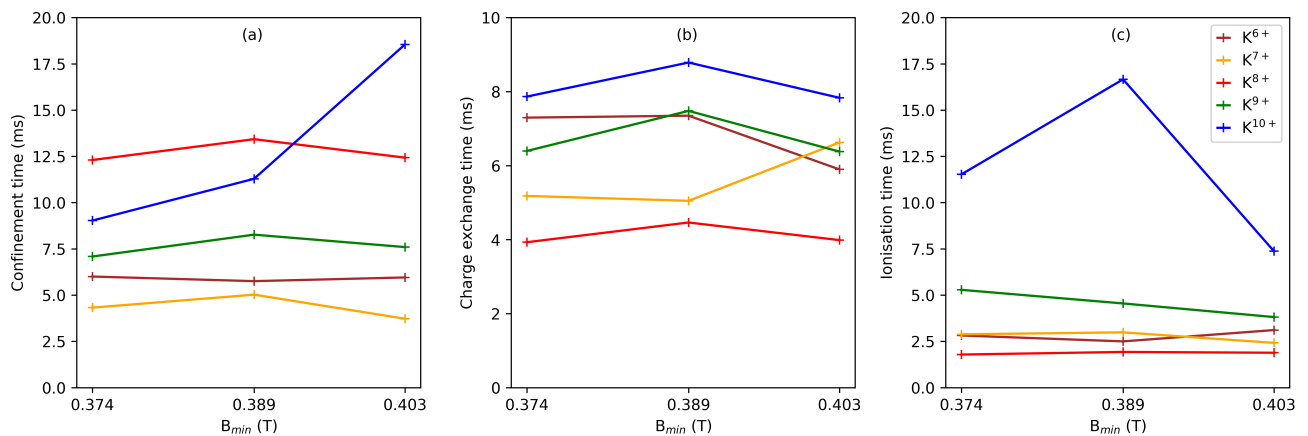
FIG. 11. The confinement, charge exchange and ionisation times of K^{6+} - K^{10+} as a function of B_{min}.
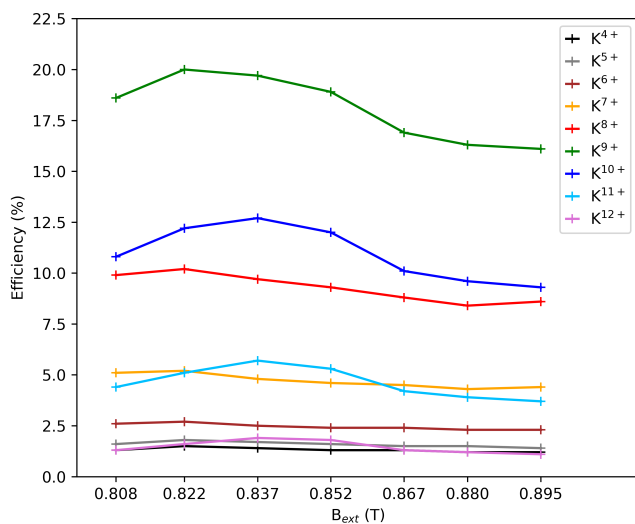

FIG. 12. The charge breeding efficiency of K^{4+} - K^{12+} as a function of B_{ext}.
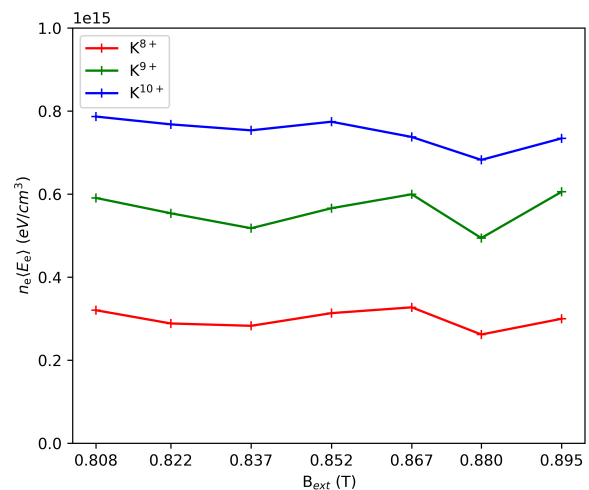

FIG. 13. The (local) plasma energy content of K^{8+}, K^{9+} and K^{10+} as a function of B_{ext}.

IV. CONCLUSIONS AND DISCUSSION

It was found that the charge breeding efficiency of high charge state K ions and the plasma energy content in the core of the ECR discharge increases with the microwave power. Closer inspection of the solution set histograms reveals that this is most likely due to increase of the median $\langle E_e \rangle$ rather than n_e as illustrated in Fig. 15 showing the $(\langle E_e \rangle, n_e)$ solution sets for K^{10+} at microwave powers of 150 W (a) and 600 W (b) as a representative example. This interpretation is commensurate with the shift of the charge state distribution (charge breeding efficiency vs. charge state) as the peak of the ionisation cross section is at higher energy for the high charge ions. The increase of the plasma energy content with the microwave

power has been observed earlier with diamagnetic loop diagnostic [11]. No sound conclusions can be made from the characteristic times as a function of the microwave power.

Neutral gas pressure was found to be the control parameter producing the clearest trends of the plasma energy content and characteristic times. The increase of the plasma energy content with the neutral gas pressure is attributed to the increase of the plasma density rather than the average energy of the warm electrons (see Fig. 2). Similar conclusion, i.e. increase of n_e with the neutral gas pressure, has been drawn when probing ECRIS plasmas with diamagnetic loop [11], K-alpha x-ray emission [24] or 1+ in-flight ionisation in a charge breeder [34]. The behavior of the charge breeding efficiency with the buffer gas pressure can be explained as follows: as the
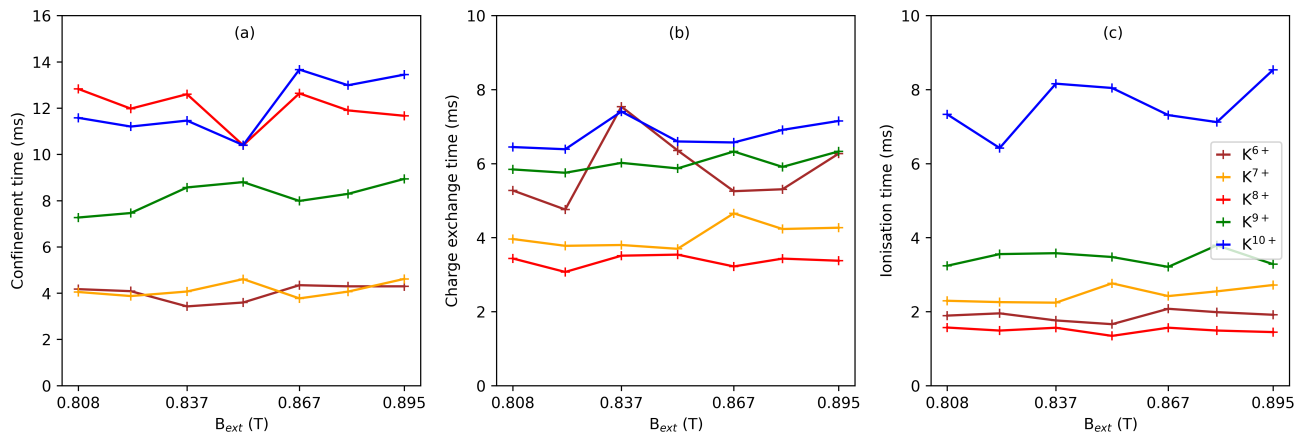
FIG. 14. The confinement, charge exchange and ionisation times of K^{6+} - K^{10+} as a function of B_{ext}.
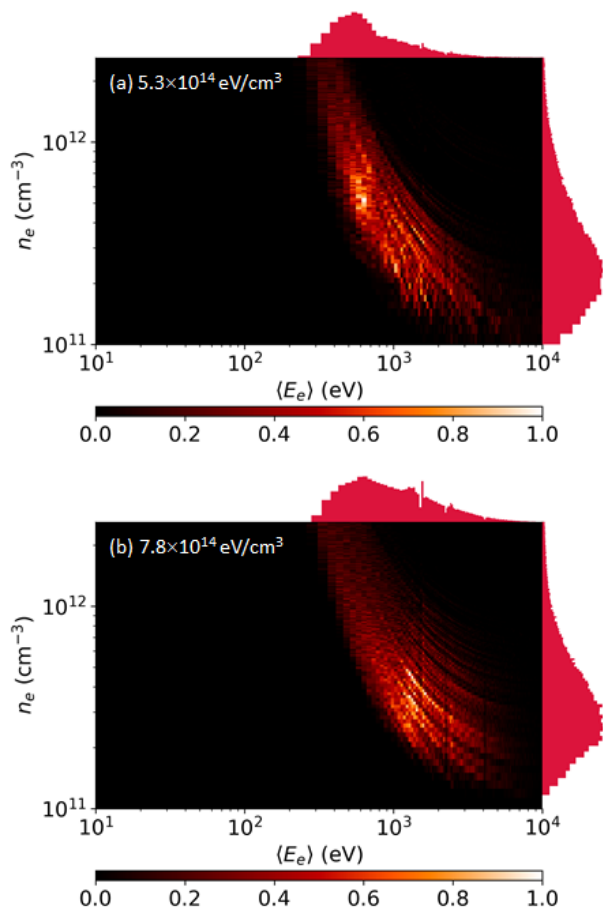

FIG. 15. The $(\langle E_e \rangle, n_e)$ solution sets for K^{10+} and the corresponding plasma energy contents. The microwave power was increased from 150 W in (a) to 600 W in (b). The energy content increases due to increase in the median electron energy from 1.0 keV to 1.5 keV.

neutral gas feed rate is increased, the enhanced charge exchange rate limits the high charge state ion production whereas ions with low or medium charge state first benefit from the increased plasma density (electron impact ionisation rate) and only at very high neutral gas pressure their production is limited by the charge exchange. This interpretation is supported by the fact that the charge exchange times have a decreasing trend with the pressure. It is worth noting that the ionisation time of the highest charge states is shorter than their charge exchange time only at the lowest pressure, which matches the observed trend of the charge breeding efficiency. The decrease of the confinement time with the pressure is attributed to higher plasma density, which increases the electron flux and ambipolar plasma potential (see e.g. [14]), thus reducing the average ion confinement time as the fluxes of negative and positive charge carriers are equal in equilibrium condition (i.e. $n_e/\tau_e = \Sigma q n_i^q/(\tau_{conf}^q)$ where q refers to the charge state of the ion). The decrease of the charge exchange and ionisation times with the neutral gas pressure are presumably due to increased neutral and plasma (electron) densities affecting the charge exchange and electron impact ionisation rates $n_n n_i \langle \sigma_{cex} v_i \rangle$ and $n_e n_i \langle \sigma_{ion} v_e \rangle$, respectively.

Examining the solution sets obtained in the extremes of the minimum-B magnetic field sweep reveals that the small increase of the plasma energy content with B_{min} is most likely due to increasing $\langle E_e \rangle$ rather than n_e as illustrated in Fig. 16 showing the $(\langle E_e \rangle, n_e)$ solution sets for K^{10+} at B_{min} of 0.37 T (a) and 0.40 T (b). This is consistent with B_{min} being the most influential parameter affecting the plasma bremsstrahlung spectral temperature [37] and the occurrence of kinetic instabilities [29] driven by the anisotropy of the hot electron component [38]. Finally, B_{ext} sweep yielded very similar solution sets (not shown for brevity) and median n_e and $\langle E_e \rangle$ -values regardless of the absolute strength of the extraction mirror field, i.e. B_{ext} appears to have a smaller effect on the
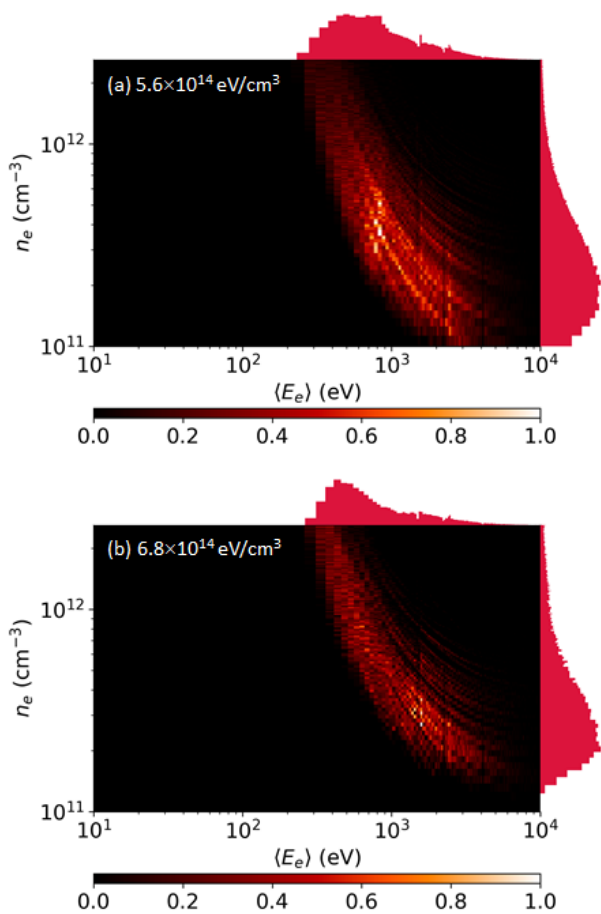
FIG. 16. The $(\langle E_e \rangle, n_e)$ solution sets for K^{10+} and the corresponding plasma energy contents. The $B_{\min}$ was increased from 0.37 T in (a) to 0.40 T in (b). The energy content increases slightly due to increase in the median electron energy from 1.1 keV to 1.3 keV.

plasma parameters than $B_{\min}$ as discussed in Ref. [30].

Besides the parametric trends of the plasma energy content and characteristic times we can make some general observations. The conditions for producing fully stripped ions in ECRIS plasma have been postulated in Ref. [39] presenting the so-called Golovanivsky plot displaying the required product $n_e \tau_{\mathrm{conf}}$ at the optimum electron temperature T_e of a Maxwellian distribution with $kT_e = \langle E_e \rangle 2/3$ to produce various fully stripped ions. For argon, which is the neighbouring element to potassium, the triple product $n_e \tau_{\mathrm{conf}} T_e$ required for fully stripped ions is approximately $3.2 \times 10^{15} \mathrm{eVs/cm^3}$. In

this work we have found that the plasma energy content $n_e \langle E_e \rangle$ ranges from $0.2 \times 10^{15} \mathrm{eV/cm^3}$ to $1.0 \times 10^{15} \mathrm{eV/cm^3}$ with $10-15$ ms confinement times for the highest charge states of potassium. These values translate to triple product of 0.1-$1.0 \times 10^{13} \mathrm{eVs/cm^3}$ suggesting that fully stripped K^{19+} ions cannot be produced with the CB-ECRIS, which is commensurate with the extracted charge state distribution where the maximum detectable charge state of potassium is K^{12+}.

Further to the absolute scale of the triple product (plasma parameters) we note that the results reveal a hierarchy of characteristic times relevant for high charge state ion production. The peak of the charge breeding efficiency distribution is at K^{9+}, which is the highest charge state for which we find consistently $\tau_{\mathrm{ion}} < \tau_{\mathrm{cex}}$ and $\tau_{\mathrm{ion}} < \tau_{\mathrm{conf}}$. In other words, for charge states 9+ and lower, the ionisation time is shorter than the charge exchange time or the ion confinement time, which causes ions to "pile-up" on that charge state making its charge breeding efficiency the highest. For charge states above the peak of the breeding efficiency distribution the time hierarchy appears to convert to $\tau_{\mathrm{cex}} < \tau_{\mathrm{conf}}$ and $\tau_{\mathrm{cex}} < \tau_{\mathrm{ion}}$, i.e. charge exchange limits the production of very high charge state ions.

Overall, the results discussed here have demonstrated that despite of the large relative uncertainty (see Ref. [21] for thorough discussion) the CT method is sensitive enough to identify trends in the plasma parameters, e.g. the increase of the plasma density with the neutral gas pressure. Importantly, these trends are similar to those inferred from other diagnostics such as diamagnetic loop experiments and K-alpha emission [11, 24]. The advantage of the CT method over other diagnostics techniques arises from its simplicity; practically all charge breeders are readily equipped with 1+ beam pulsing and N+ beam current (transient) detection apparatus. The computational analysis tools required to translate the beam current transients into $(\langle E_e \rangle, n_e)$ solution sets and corresponding characteristic times, τ_{conf}, τ_{cex} and τ_{ion}, are open source and available through GitHub [40].

ACKNOWLEDGMENTS

[1] Blumenfeld Y, Nilsson T and Van Duppen P 2013, Phys. Scr. T152 014023
[2] Wenander F 2004 Nucl. Phys. A 746 40–6
[3] I. Izotov, V. Skalyga and O. Tarvainen, Rev. Sci. Instrum., 043501 (2022).
[4] R Kronholm et al 2019 Plasma Sources Sci. Technol. 28 075006
[5] G. Melin et al., Rev. Sci. Instrum. 61, 236 (1990).

[6] G. Shirkov, Plasma Sources Sci. Technol. 2, 250 (1993).

[7] D Mascali *et al.* 2013 Plasma Sources Sci. Technol. 22 065006.

[8] V Mironov *et al.* 2020 Plasma Sources Sci. Technol. 29 065010

[9] T. Thuillier, J. Benitez, S. Biri, and R. Rácz, Rev. Sci. Instrum. 93, 021102 (2022).

[10] D. Mascali, E. Naselli, and G. Torrisi, Rev. Sci. Instrum. 93, 033302 (2022).

[11] J. Noland, O. Tarvainen, J. Benitez, D. Leitner, C. Lyneis and J. Verboncoeur, Plasma Sources Sci. Technol. 20 035022, (2011).

[12] R. Kronholm, T. Kalvas, H. Koivisto, S. Kosonen, M. Marttinen, D. Neben, M. Sakildien, O. Tarvainen and V. Toivanen, Rev. Sci. Instrum., 91, 013318 (2020).

[13] D. Hitz, Advances in imaging and electron physics 144, 1 (2006).

[14] Tarvainen O, Suominen P and Koivisto H 2004 Rev. Sci. Instrum. 75 3138

[15] V. Toivanen, B. S. Bhaskar, I. V. Izotov, H. Koivisto, and O. Tarvainen, Rev. Sci. Instrum. 93, 013302 (2022).

[16] I. Izotov, O. Tarvainen, V. Skalyga, D. Mansfeld, H. Koivisto, R. Kronhom, V. Toivanen and V. Mironov, Rev. Sci. Instrum. 91, 013502 (2020).

[17] O. Tarvainen, T. Kalvas, H. Koivisto, R. Kronholm, M. Marttinen, M. Sakildien, V. Toivanen, I. Izotov, V. Skalyga and J. Angot, Rev. Sci. Instrum. 90, 113321 (2019).

[18] J. Angot, M. Luntinen, T. Kalvas, H. Koivisto, R. Kronholm, L. Maunoury, O. Tarvainen, T. Thuillier and V. Toivanen, Plasma Sources Sci. Technol. 30 035018, (2021).

[19] M. Luntinen, J. Angot, O. Tarvainen, V. Toivanen, T. Thuillier and H. Koivisto, J. Phys.: Conf. Ser. 2244 012009 (2022).

[20] M. Luntinen, V. Toivanen, H. Koivisto, J. Angot, T. Thuillier, O. Tarvainen, G. Castro, Phys. Rev. E 106, 055208, (2022).

[21] M. Luntinen, J. Angot, H. Koivisto, O. Tarvainen, T. Thuillier, and V. Toivanen, The effects of electron energy distribution and ionization cross section uncertainty on charge breeder ion source diagnostics with pulsed 1+ injection, Physics of Plasmas 30, 073904 (2023).

[22] T. Lamy, J. L. Bouly, J. C. Curdy, R. Geller, A. Lacoste, P. Sole, P. Sortais, T. Thuillier, and J. L. Vieux-Rochaz, Rev. Sci. Instrum. 73, 717 (2002)

[23] J. Angot, T. Thuillier, M. Baylac, M. Migliore, P. Sole, A. Galatà, L. Maunoury, ECRIS2020 proceedings, doi:10.18429/JACoW-ECRIS2020-WEZZO02

[24] M. Sakildien, R. Kronholm, O. Tarvainen, T. Kalvas, P. Jones, R. Thomae and H. Koivisto, Nucl. Instrum. Meth. Phys. A, 900, pp. 40–52 (2018).

[25] T. Ropponen *et al.* 2011 Plasma Sources Sci. Technol. 20 055007, (2011).

[26] I. Izotov, O. Tarvainen, V. Skalyga, D. Mansfeld, T. Kalvas, H. Koivisto and R. Kronholm, Plasma Sources Sci. Technol. 27, 025012 (2018).

[27] I. Izotov *et al.*, Plasma Phys. Control. Fusion 63 (2021) 045007.

[28] B. Bhaskar, H. Koivisto, O. Tarvainen, T. Thuillier, V. Toivanen, T. Kalvas, I. Izotov, V. Skalyga, R. Kronholm and M. Marttinen, Plasma Phys. Control. Fusion 63 095010, (2021).

[29] O. Tarvainen, I. Izotov, D. Mansfeld, V. Skalyga, S. Golubev, T. Kalvas, H. Koivisto, J. Komppula, R. Kronholm, J. Laulainen and V. Toivanen, Plasma Sources Sci. Technol. 23, 025020, (2014).

[30] V. Toivanen, B. Bhaskar, H. Koivisto, L. Maunoury, O. Tarvainen and T. Thuillier, Phys. Plasmas 29, 013501 (2022).

[31] P. Elleaume, O. Chubar, J. Chavanne, Proc. PAC97, Vancouver, Canada, 12–16 May 1997, pp. 3509–3511.

[32] V. Mironov, S. Bogomolov, A. Bondarchenko, A. Efremov, and V. Loginov, Phys. Rev. Special Topics - Accelerators and Beams 18, 1 (2015).

[33] L. Panitzsch, T. Peleikis, M. Stalder, and R. F. Wimmer-Schweingruber, Rev. Sci. Instrum. 82, 1 (2011).

[34] O. Tarvainen, T. Lamy, J. Angot, T. Thuillier, P. Delahaye, L. Maunoury, J. Choinski, L. Standylo, A. Galatà, G. Patti and H. Koivisto, Plasma Sources Sci. Technol. 24 035014, (2015).

[35] O. Tarvainen, J. Angot, T. Thuillier, M. Migliore, L. Maunoury and P. Chauveau, 2022 Plasma Sources Sci. Technol. 31 125003.

[36] M. A. Lennon, K. L. Bell, H. B. Gilbody, J. G. Hughes, A. E. Kingston, M. J. Murray, and F. J. Smith, Journal of Physical and Chemical Reference Data 17, 1285–1363 (1988).

[37] J. Benitez, C. Lyneis, L. Phair, D. Todd, and D. Xie, IEEE Trans. Plasma Sci. 45, 1746–1754 (2017).

[38] Golubev S V and Shalashov A G 2007 Phys. Rev. Lett. 99 205002

[39] K. S. Golovanivsky, Instruments and experimental techniques, vol. 28 no. 5 part 1 pag 989, New York: Plenum.

[40] 4] CT-analyzer release ct-analyzer-v2.0. Openly available at https: //github.com/misapema-jyfl/ct-analyzer